Integration of Interspecies Data for Developing Tissue-Level Brain Injury Risk Functions

---

A Dissertation

Presented to

the faculty of the School of Engineering and Applied Science

University of Virginia

---

in partial fulfillment
of the requirements for the degree

Doctor of Philosophy

by

Taotao Wu

May 2019

APPROVAL SHEET

This Dissertation
is submitted in partial fulfillment of the requirements
for the degree of
Doctor of Philosophy

Author Signature: Tao Tao Wu

This Dissertation has been read and approved by the examining committee:

Advisor: Jeff R. Crandall

Committee Member: Matthew B. Panzer

Committee Member: Robert S. Salzar

Committee Member: Jacobo Antona-Makoshi

Committee Member: Chia-Yi (Alex) Kuan

Committee Member: _____

Accepted for the School of Engineering and Applied Science:

Craig H. Benson, School of Engineering and Applied Science

May 2019

ABSTRACT

Traumatic brain injuries (TBI) are a significant public health burden occurring in automotive crashes, accidents, sports, and in military training and combat. There is a significant interest in understanding the tolerance of the human brain to external mechanical loads with the ultimate objective of mitigation and prevention of TBI. Early TBI research focused on understanding the injury mechanisms in animals, and the latest research focus has been on collecting exposure data in humans that routinely experience head impacts to quantify injury risks. Both research approaches have major limitations when studied in isolation, but when integrated they may provide a complete picture on TBI mechanisms and risk. One of the biggest challenges to forming a more comprehensive understanding of TBI risk is the applicability of animal brain injury data to humans. Therefore, the objective of this dissertation was to integrate human and animal brain injury data to establish a unique brain injury dataset that will be used to develop tissue-level brain injury risk functions. Finite element (FE) simulations were used to bridge the interspecies gap between human and non-human primate (NHP) injury data, assuming the equivalence of tissue-level metrics across primates.

To achieve the goals, advanced multi-scale FE models of the human and NHP (macaque and baboon) brains were developed by explicitly incorporating mesoscopic anatomical details (axonal tracts) using a novel embedding method. Mechanical behaviors of the brain tissue were modeled with a hyper-viscoelastic constitutive model, calibrated with available multi-modal testing data of *in vitro* brain tissue and extensively validated for *in situ* and *in vivo* intracranial deformations under various loading conditions. The numerical methods, anatomical features (axonal tractography), and constitutive models in these FE models were harmonized to facilitate the study of tissue-level responses across models of different species.

Utilizing these computational tools, this dissertation presents two new methods to derive brain injury risk functions by integrating NHP and human brain injury data. First, a cross-species scaling method was formulated to correlate animal exposure data to humans, specifically to find the equivalent biomechanical impact conditions that result in similar tissue-level mechanical responses for different

species. Recognizing the resonance of the brain deformation under rotational motion, a new brain injury scaling method was developed based on scaling the natural frequency of the brain. The results of this work indicate that previously described biomechanical scaling methods, often based on the relative mass of each species, were poor predictors of the equivalent biomechanical impact conditions between NHP and human. The physically-bounded frequency-based scaling method improved the accuracy of scaling the equivalent loading conditions and provided insight to account for the interspecies differences in brain physical morphology, anatomy and tissue properties.

Second, a methodology for integrating interspecies injury data to derive human brain injury risk functions was developed through the harmonized brain FE models of the human, macaque and baboon. The efficacy of the tissue-level injury metrics for predicting injury was evaluated computationally by simulation of an integrated dataset of sub-injurious human volunteer sled tests, laboratory reconstructed head impacts from professional football, and *in vivo* NHP tests. The current analysis lends some favor to Von Mises stress and maximum principal strain over other existing tissue-level metrics as good predictors of injury, while no evidence was shown that the global axonal strain was a better predictor of injury than the global principal strain. Associated injury risk functions for mild and severe TBI were proposed through integrated data. Efficacy of the proposed injury risk functions was first verified by an independent test dataset and eventually applied to automotive crash scenarios to ensure the proper usage of the risk functions.

The main contributions of this dissertation were the new methods for developing tissue-level brain injury risk functions using injury data of multiple species. The findings and the developed methods could be of critical importance in guiding the technical innovation of more effective safety countermeasures, thereby, reducing the incidences, consequences, and societal burden of TBI.

DEDICATION

This dissertation is dedicated to

my parents and grandparents for their endless love and support.

临行密密缝 意恐迟迟归

CONTENTS

LIST OF FIGURES

LIST OF TABLES

ACKNOWLEDGMENTS

The completion of this dissertation would not have been possible without the guidance and support of my advisors Dr. Matthew B. Panzer and Dr. Jeff R. Crandall. I feel so lucky that I had the opportunity to learn from the great minds, their passion for science and exploration inspired me to become a better researcher. I would also like to express my gratitude to the members of my advisory committee, Dr. Robert S. Salzar, Dr. Alex Kuan, and Dr. Jacobo Antona-Makoshi, for their precious expertise and time. Their help truly improved the quality of this dissertation.

I owed a debt of gratitude to almost every person that has worked at the UVA Center for Applied Biomechanics since I started my graduate work in 2014. The friendship of Ahmed Alshareef and J. Sebastian Giudice is much appreciated and has led to many interesting discussions relating to this research. Special thanks to my office mates, Hamed Joodaki and Jacek Toczyski, who are always considerate and supportive. Especially helpful to me during my early time in the Center were Taewung Kim, Bingbing Nie, Lee Gabler, Huipeng Chen and Varun Bollapragada, who taught me the skills required to finish this work. Jason Kerrigan, Greg Shaw, Jason Forman, and David Lessley deserve my gratitude for their willingness to help me with their specialties. Thanks also to Kevin Kong, Zhaonan Sun, Qi Zhang, Carolyn Roberts, Gwansik Park, Kristen Reynier, Daniel Perez-Rapela, and the rest of my friends at the Center for making my stay in Charlottesville that much more pleasurable.

I gratefully acknowledge the thoughtful review of Alayna Panzer and Tim Gillispie for this dissertation. My friends in China have also been generous with their love and encouragement despite the long distance between us. I was so fortunate to have my former roommates to set up my life in a new culture, for that I will always be grateful.

CHAPTER 1 : INTRODUCTION

1.1 Statement of Problem

Despite the significant scientific emphasis on reducing their societal cost, traumatic brain injuries (TBI) remain a significant public health issue. The Centers for Disease Control and Prevention (CDC) estimates that TBI accounts for approximately 2.5 million emergency department (ED) visits, 282,000 hospitalizations, and 56,000 deaths annually in the United States (CDC, 2015). Nearly one-third of all injury-related deaths in the United States included a TBI as a cause of death (Faul and Coronado, 2015). From 2006 to 2013, the rate of TBI-related ED visits increased by 54.7%, although this trend might reflect the increased awareness of TBI among the general public (Taylor et al., 2017). Nevertheless, the public health and economic burden of TBI is substantial, which warrants continued injury prevention efforts and public awareness.

Currently, major injury prevention efforts have focused on improving motor vehicle safety and safe play in sports to target a large proportion of the population (CDC, 2015), and there is a significant interest in designing better protective head equipment and safety countermeasures. What is not well known are the quantitative thresholds of the external loads that lead to cognitive and physical dysfunction. Consequently, the current testing protocols and standards to assess a product may not reflect its protective performance in the field. On the other hand, the design of protective equipment may undergo changes through trial and error without adequate understanding of the rule of thumb for good protection; thus, this hampers technical innovation for injury prevention. Understanding the mechanism and the biomechanical tolerances of TBI is the cornerstone of the design and development of effective countermeasures.

The biomechanical understanding of TBI is, unfortunately, still at the initial stages. Fundamental questions and challenges associated with TBI research remain unanswered. From the biomechanical perspective, how does the tissue in the brain respond when an external load is applied to the head? How does the intracranial tissue response relate to the TBI? How does the risk of TBI injury vary with external head motion? Data from animal experiments have been used to define the probability of injury concerning the level of physical impact, but how do scientists relate the animal-derived relationship between loading conditions and neurological responses to humans? The focus of this dissertation was to answer some of these questions.

1.2 Motivation

For biomechanical engineers who seek answers to the lingering questions associated with TBI, the tissue-level metrics of the brain are considered the critical components to link external mechanical loads to subsequent development of pathological consequences. However, the relationship between tissue-level metrics and injury has not been thoroughly studied, mainly due to the lack of a uniformly well-characterized *in vivo* injury data.

A complete set of *in vivo* injury data should include both external loads (e.g., head kinematics) and clinical outcomes. Typically, the existing sources of injury data come from animal tests, human volunteer tests, field measurements, and reconstructed field impacts. Human data generally are gathered at the low-severity end (e.g., sub-injurious volunteer tests, and sports-related impacts) and do not permit evaluation of injury metrics and injury risk for more severe TBI (e.g., DAI). Animal data have the advantages of a broader range of injury severities, well-controlled loading conditions, and accessibility to pathophysiological mechanisms. The mechanical response associated with trauma characterized in these animal studies is difficult to translate to humans considering the differences in brain morphology and physiology across species

(Panzer et al., 2014). In general, each dataset has inherent limitations, and currently, no single type of test data is sufficient to develop a robust correlation between tissue-level metrics and TBI.

Therefore, new methods are required to address the potential issues with current tissue-level metrics and overcome the present challenges associated with the integration of injury data.

1.2.1 Limitations of Existing FE-Derived Tissue-Level Metrics

Because of a lack of noninvasive accessibility to the brain tissue in the head, tissue-level injury metrics are difficult to develop with *in vivo* or *in vitro* models. Finite element (FE) modeling is a powerful tool for studying the internal biomechanical responses of human or animal brain to external loadings. However, the biofidelity of current brain FE models was only partially validated for tissue responses (brain deformation) using experimental data that was not "totally suited" or "designed" for model evaluation (Yang et al., 2006). Several tissue-level metrics (e.g., Kleiven, 2007; Deck and Willinger, 2008; Takhounts et al., 2003) have been developed based on homogeneous FE models (region-dependent but homogeneous in the region) with isotropic material models even though the brain is widely considered to be heterogeneous and anisotropic (Chatelin et al., 2010). Acknowledging that the (axonal) tract-oriented strains cannot be easily correlated to the tissue strain without considering the axonal orientations (Cloots et al., 2013), recent attempts to incorporate white matter anisotropy in brain FE models have been made based on diffusion-weighted magnetic resonance imaging (DWI) information. Most of these studies have implicitly incorporated fiber tractography to inform anisotropic, fiber-reinforced constitutive models (Giordano and Kleiven, 2014, Zhao and Ji, 2018, Ganpule et al., 2017, Wright et al., 2013). However, this approach over-simplifies the heterogeneity of the brain parenchyma and requires the use of weighted-average fiber orientation for each element, which may not be aligned with the actual direction of the axonal fiber bundles (Zhao and Ji, 2018).

Since the reliability of inferences drawn from these models depends on the model biofidelity and the accuracy of the mesoscopic fiber architecture, improved FE models are required to evaluate whether certain tissue-level metric (e.g., axonal strain) is a better predictor of TBI.

1.2.2 Challenges of Correlating Animal Brain Data to The Human Brain

Because of the limited availability of human injury data, animal injury data is being used for the development of human brain injury risk functions. The challenges of the application of animal brain injury data in human TBI studies can be identified in the following three aspects.

1. The similarity of material and cellular properties.

Regardless of the underlying ambiguities in the behavioral and physiological differences, the challenge in establishing a link between the human and the animal starts at the tissue level. The notion of seeking a correlation between tissue responses and injury outcomes through animal data assume interspecies equivalence for brain tissue. In other words, the equal tissue-level stimulus would cause similar severities of injury for both animal and human. The necessary but not sufficient condition for that requirement is that the brain tissue of both species is similar in mechanical properties and has a similar cellular composition. While the most commonly used animal models to study brain injury, such as mice (Sauerbeck et al., 2018), rats (Davidsson et al., 2011; Marmarou et al., 1994) and porcine models (Browne et al., 2011; Coats et al. 2016) do not have similar cellular compositions with the human brain (Figure 1-1). Non-human primates (Gennarelli et al., 1982; Ommaya and Hirsch, 1971; Ono et al., 1980) are considered as a more representative human surrogate because human and non-human primates have similar cellular compositions, mechanical properties (Estes and McElhaney, 1970), and brain anatomy.

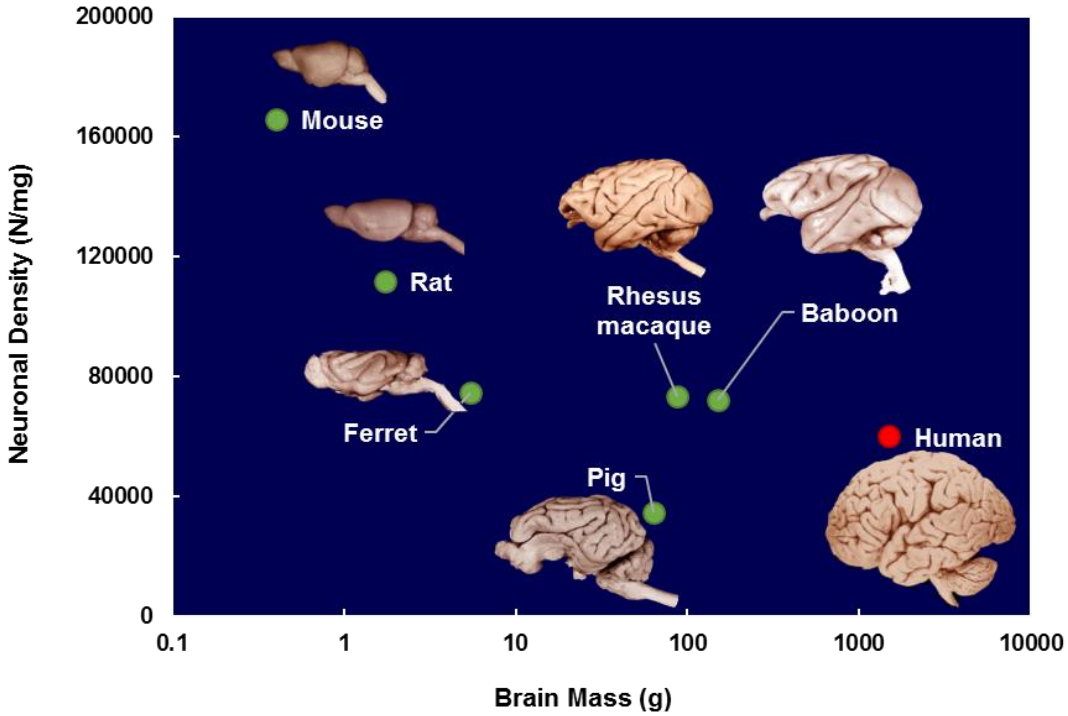

Brain anatomy images (not to scale) were adapted from the University of Wisconsin and Michigan State Comparative Mammalian Brain Collections (www.brainmuseum.org).

Figure 1-1. Neuronal density (number of neuron cells per microgram), based on data from (Herculano-Houzel and Dos Santos, 2018).

2. Scaling.

Simplified scaling methods (e.g., mass scaling method, Ommaya et al., 1967) based on dimensional analysis have guided the interpretation of animal data in the context of humans. They were explicitly theorized to find the equivalent biomechanical impact conditions that result in similar tissue-level mechanical responses (shear strain) for different species, but the existing scaling methods have not been validated and fail to account for the anatomical and morphological complexity of the brains of different species.

3. FE model resolution.

Brain FE models have shown potential for addressing the limitation of scaling methods by establishing dimensionless tissue-level equivalence from the animal to the human (Antona-Makoshi, 2016). Compared to human models, current animal brain FE models are not as advanced and are not suited for the investigations of specific injury mechanisms or the development of tissue-level injury risk functions (see Chapter 2). The model inconsistency observed in the literature (Giudice et al., 2018) also undermines the direct comparison between different models for tissue responses.

1.2.3 Need for Interspecies Data Integration

Numerous brain injury risk functions derived from different data sources have indicated considerable variability in the literature (Sanchez et al., 2017). These discrepancies may be caused by issues including but not limited to, the bias and possible errors involving the data sources themselves, the limitation of small sample size, the scaling techniques used to involve animal data, and the low predictability of the metrics. A unified methodology for the integration of the data from different sources would potentially address many of these issues.

1.3 Objectives and Outline

The goal of this study was to investigate methods to integrate human and animal brain injury data and develop tissue-level injury risk functions for predicting human brain injury. The integration of non-human primate (NHP) and human injury data were explored for the demonstration of concept, partially because the similarity between primates likely fulfills the requirements for the tissue-level equivalence. This work will focus on using computational methods to understand brain injury and brain tissue responses in closed-head impact scenarios. The goal will be accomplished through the following specific aims:

1) Develop advanced computational tools for assessing tissue-level brain injury metrics for both human and non-human primate models;

2) Develop methods to correlate biomechanical responses of the animal model with the human model by scaling the exposure data (head kinematics);

3) Integrate interspecies injury data, assess the correlation between tissue-level metrics and injury outcomes, develop and evaluate injury risk functions for predicting brain injury.

As outlined in Figure 1-2, following an overview of the background research in the literature, eight chapters are presented to achieve these aims. The results from this work will advance the collective understanding of TBI injury mechanisms. The significance of this work will contribute to addressing two persistent questions associated with TBI research: How do researchers derive human injury tolerance based on animal experiments? What are the quantitative thresholds of mechanical stimuli that lead to injury (or dysfunction) in the brain? In a practical sense, the resulting injury risk functions would motivate and guide the technical innovation for brain injury mitigation and prevention.

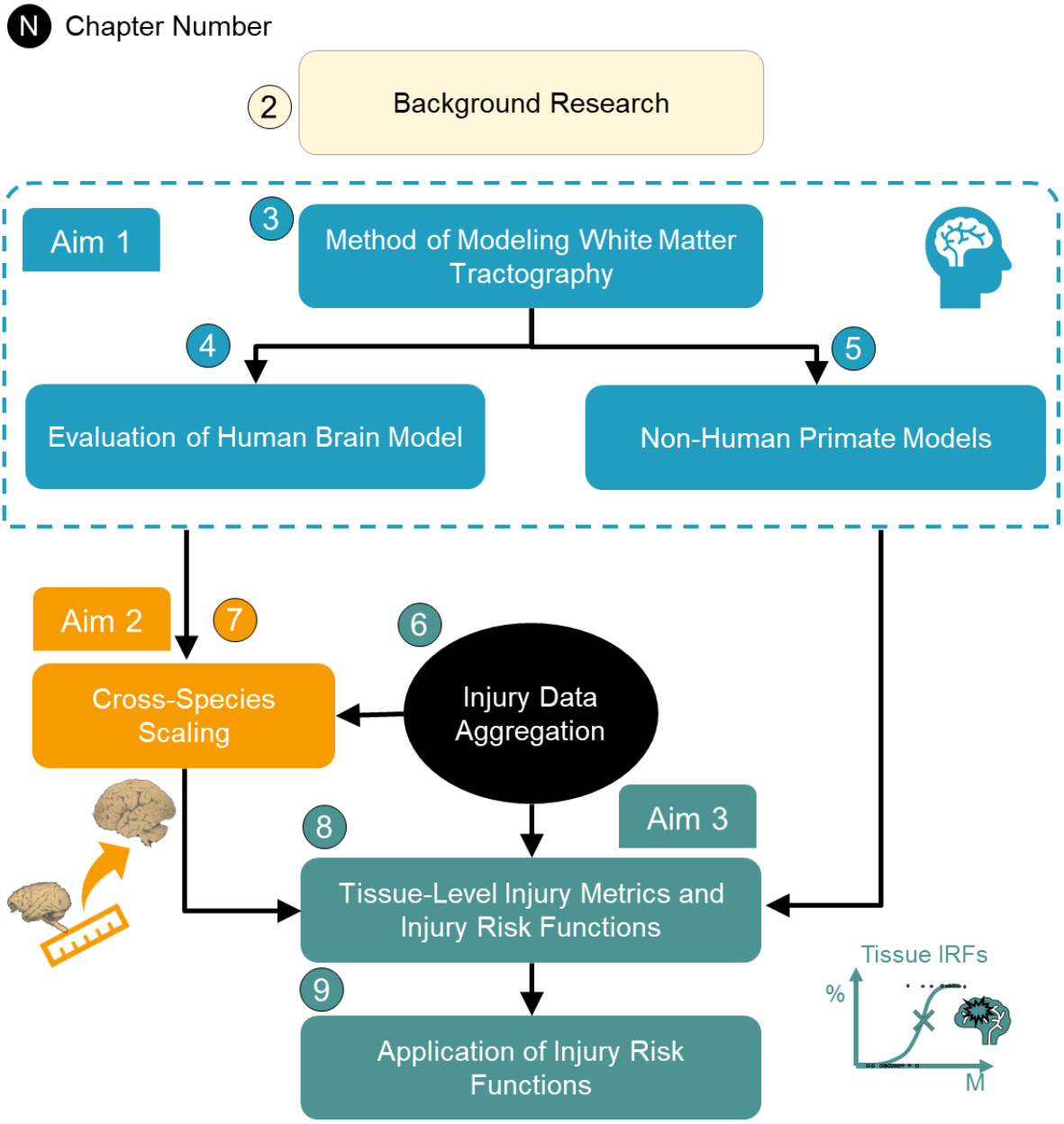

Figure 1-2. Overview of this dissertation

CHAPTER 2 : BACKGROUND

This chapter presents background research relevant to this dissertation. Topics include information on human brain anatomy, existing TBI mechanisms, injury criteria, and computational brain models. Each subsection contributes to the biomechanical understanding of brain injury.

2.1 Human Neuroanatomy: from Macro to Micro

The brain, which is contained within the cranium, is the center of the nervous system and the most complex organ in the human body. Knowledge of the anatomy of the brain would help to understand the biomechanical response and injury mechanism of the brain. A brief biomechanical background of the structure and composition of the brain is discussed in this section.

At the macroscale, the brain is divided into five parts (Figure 2-1), as follows: cerebrum, the basal ganglia, the diencephalon, the brainstem, and the cerebellum (Nolte, 2002). They are constrained and stabilized in the skull through three meninges/membranes, which are the dura mater, the arachnoid mater, and the pia mater from the outermost layer inward. There are several places where the inner dural layer separates from its external counterpart and protrudes into the cranial cavity. The primary dural extensions are the falx cerebri between the two cerebral hemispheres, and the tentorium cerebelli between the cerebral hemispheres and the cerebellum. The spaces between meninges and the brain are filled with a clear cerebrospinal fluid (CSF) that is produced within the ventricles. From the perspective of biomechanics, the brain is protected from injury by meninges and CSF, which provide complex boundary conditions for the brain tissues and influence the mechanical responses of the brain as a whole in the skull.

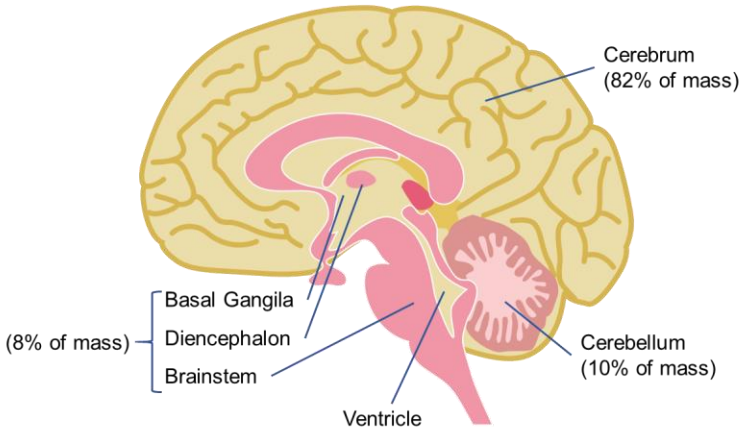

Figure 2-1. Mid-sagittal view of the brain (basal ganglia and diencephalon are blocked by the ventricle in this view).

At the mesoscale (~1 mm), the brain's structure is not always evident. At this scale, the organization of the structural connections (connectome) in the brain can be observed through advanced imaging techniques. Different brain regions are connected to each other through axons at the cellular level to form an enormously complicated network system (Figure 2-2). This structural connection serves as a critical constraint on brain functionality and provides fundamental insight into the understanding of the pathophysiology underlying the different brain injury.

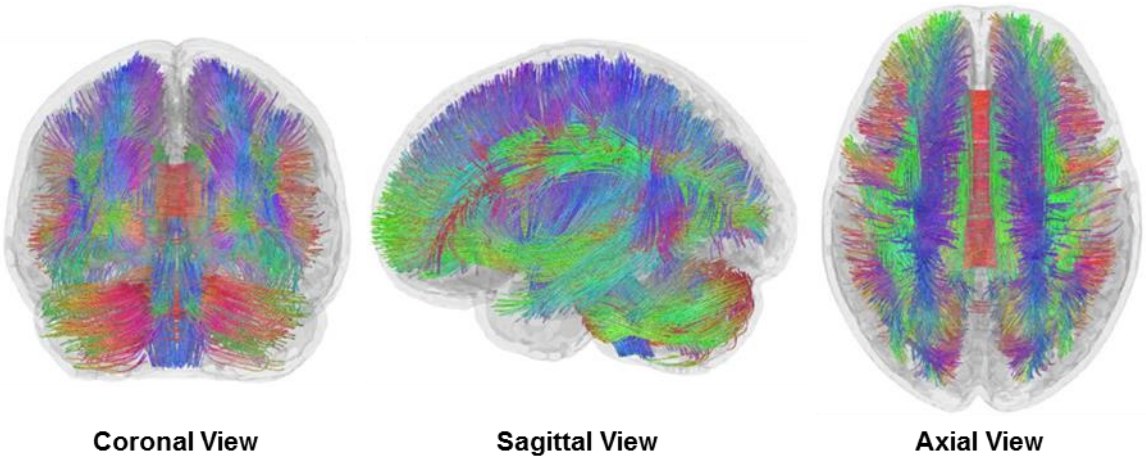

Figure 2-2. Mesoscale axonal fiber architecture in three views. Each tube is a nerve tract consisting of bundles of axons (Yeh et al., 2018).

At the microscale, nervous tissue is primarily composed of neurons and glial cells (Figure 2-3). Neurons are the information-processing and signaling elements, while glial cells play a variety of supporting roles. There are around 100 billion neurons in the human nervous system and a similar number of glial cells (von Bartheld et al., 2016). The brain at the macroscale is easily divisible into gray matter and white matter. This distinction is a result of the underlying microstructural architecture: White matter is mainly composed of myelinated axons, the myelin sheath gives white matter the whitish appearance, while in gray matter there is a preponderance of unmyelinated cell bodies and dendrites.

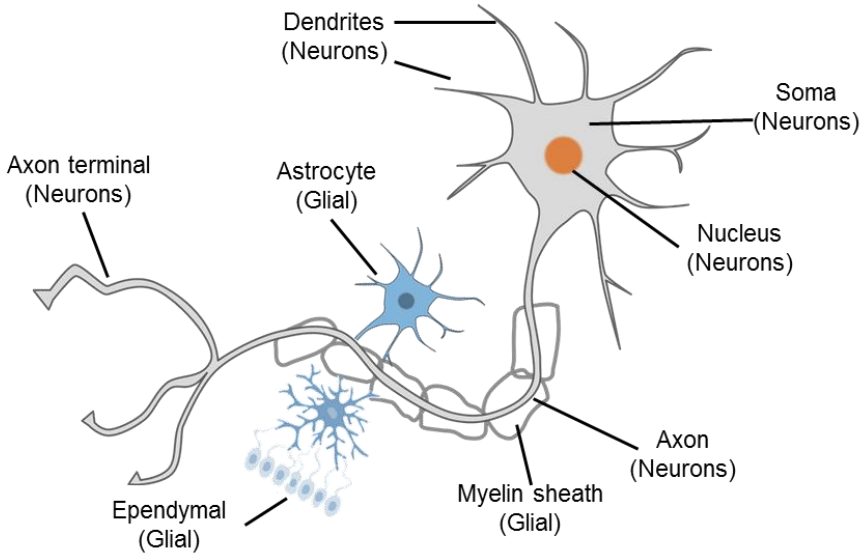

Figure 2-3. Neurons and glial cells.

2.2 Injury Mechanism

Because of the complexity of brain anatomy, TBI is a multiplex injury with a broad spectrum of symptoms and dysfunctions. Controversy regarding the mechanisms of TBI exists, and injuries with different damage patterns may be caused by different or multiple mechanisms. Unlike an open head injury when an object penetrates the skull and brain, over 90% of common brain injuries are closed-head injuries without skull penetration (Santiago et al., 2012), including

concussion, contusion, intracranial hemorrhage, diffuse axonal injury, and brainstem injuries. These injuries can be diffuse (also called multifocal), meaning they affect tissues throughout the brain; or focal, meaning the damage is localized in one area. Amongst the closed-head injuries, diffuse-type TBIs are the most frequent, and they account for 81% of all brain injuries, according to the National Automotive Sampling System Crashworthiness Data System (NASS CDS) database (Takahashi and Yanaoka, 2017). Diffuse-type injuries were the focus of this dissertation. The mechanisms that can cause these types of injuries were discussed as follows.

Brain injury or dysfunction is believed to be caused by shear deformation in the brain due to the rapid rotation of the head (Holbourn, 1943). While few experiments were able to confirm Holbourn's hypothesis directly, numerous animal and human studies support the claim that both brain deformation (Alshareef et al., 2018; Meaney et al., 1995) and TBI (Gennarelli et al., 1972; Ommaya and Gennarelli, 1974) were more easily induced by the rotational head motion than the translational head motion. One important anatomic phenomenon of TBI was the findings of disrupted white matter tracts and normal gray matter in autopsy (Strich, 1956). This type of injury was later called Diffuse Axonal Injury (DAI). DAI is thought to be caused by mechanical disruption of axonal cytoskeletons resulting in axonal swelling, retraction bulb, axonal degeneration, and downstream deafferentation. Histopathology studies on animal models (Gennarelli et al., 1982; Ibrahim et al., 2010) also found proteolysis, swelling, and other microscopic changes to the neuronal structure in injured subjects. Similar abnormalities of axons were recreated *in vitro* through tissue deformation in experimental conditions (Nakadate et al., 2017; Tang-Schomer et al., 2010), indicating a possible correlation between strain and injury.

The concussion injury is a complex pathophysiological process affecting the brain induced by biomechanical forces. Currently, a concussion is diagnosed when the patient appears to be

confused or has transient brain dysfunction, but the loss of consciousness or amnesia is not required. Pathological findings in standard imaging are not expected. A concussion is a milder form of DAI (Browne et al., 2011), with mainly physiological disruption of brain function. However, current imaging techniques cannot detect the extent of minor axon injury.

Subarachnoid hemorrhage (SAH) and intraventricular hemorrhage (IVH) might also be caused by the same shearing mechanism that underlies severe DAI (Mata-Mbemba et al., 2018, 2015). Myriad other hypothesized injury mechanisms also exist to explain blast-induced TBI associated with small deformation from fast events. Notable examples of these mechanisms are cavitation in brain tissue (Panzer et al., 2012; Salzar et al., 2017), the systemic response of the whole body to blast exposure (Cernak, 2010), and the secondary injury caused by blood-brain barrier disruption (Hay et al., 2015). However, these examples are based on different scenarios, and their applicability to blunt trauma is yet to be confirmed.

2.3 Injury Metrics and Brain Injury Tolerance

Based on an understanding of injury mechanisms, various injury metrics or criteria were utilized to predict TBI and characterize the human biomechanical tolerance to TBI (Gabler et al., 2016; Sanchez et al., 2017). Considering the variability in the population, the tolerance is generally expressed as a risk function (statistical modeling of the occurrence of injury) of an injury metric(s) in response to external mechanical load. These injury metrics for the brain can be categorized into two types, kinematics-based (Gadd, 1966; Versace, 1971), and tissue-level injury metrics (Sahoo et al., 2016; Zhang et al., 2004). Ideally, both the kinematics-based and tissue-level injury metrics should be developed based on their capability of predicting brain injury. However, the current kinematics-based injury metrics were developed based on their correlation to tissue-level metrics

(e.g., strain) because of limited injury data (Gabler et al., 2018a; Takhounts et al., 2013), with the underlying assumption that corresponding tissue-level metrics are good predictors of brain injury.

As summarized in Table 2-1, numerous tissue-level metrics have been derived from FE simulations of reconstructed real-world events. Notable examples of tissue-level injury metrics include maximum principal strain (MPS) (Kleiven, 2007; Viano et al., 2005), Von Mises stress (VMS) (Ueno et al., 1995) and the cumulative strain damage measure (CSDM) (Bandak and Eppinger, 1994; Takhounts et al., 2003). Recognizing the mechanism of axonal injury, recent studies suggested a new metric: tract-oriented strain (TOS, also called 'axonal strain' or 'axonal elongation' in the literature) (Giordano and Kleiven, 2014a; Sahoo et al., 2016; Sullivan et al., 2015). However, the correlation between the current tissue-level metrics and brain injury has yet to be validated or invalidated with reliable experimental TBI data.

Table 2-1. Summary of FE-derived tissue-level injury metrics in the literature.

Reference	Metric*	Injury Description	Data Source
(Ward et al., 1980)	PRS	Severe brain injury	Animal tests
(Trosseille et al., 1992)	Strain	Irreversible brain injury	Accident reconstruction
(Ueno et al., 1995)	VMS	Contusion	Animal tests
(Kang et al., 1997)	VMS	Severe brain injury	Accident reconstruction
(Takhounts et al., 2003)	CSDM	Concussion	Animal tests
(King et al., 2003)	SR	Concussion	Football reconstruction
(Zhang et al., 2004)	PRS, Shear Stress	Concussion	Football reconstruction
(Viano et al., 2005)	MPS, SR	Concussion	Accident reconstruction
(Kleiven, 2007)	PRS, MPS	Concussion	Football and Accident Reconstruction
(Yao et al., 2008)	PRS, VMS, Shear Stress	Mild TBI	Accident reconstruction
(Deck and Willinger, 2008)	VMS, MPS, VM Strain, CSF PRS	DAI	Football and Accident Reconstruction
(Giordano and Kleiven, 2014a)	Axonal Strain	Concussion	Football and Accident Reconstruction
(Sullivan et al., 2015)	TOS, SR, S×SR	DAI	Animal tests
(Sahoo et al., 2016)	Axonal Strain	DAI	Football and Accident Reconstruction

*PRS: pressure, SR: strain rate, S×SR: the product of strain and strain rate, VM Strain: Von Mises Strain.

In vitro models (e.g., dissociated cells and organotypic tissue slices) would also be useful in developing tissue-level metrics and provide insights into understanding the cellular mechanism of brain injury. Numerous *in vitro* models have been developed to understand the mechanical stimuli of impact and the following responses of tissue and cells (Cater et al., 2006; Elkin and Morrison, 2007; Nakadate et al., 2017). Representative in vitro studies and tissue-level tolerance in the literature are provided in Table 2-2.

Table 2-2. Summary of in vitro tissue-level injury metrics in the literature.

Reference	Injury Description	Strain (Strain Rate 1/s)	Data
(Gray and Ritchie, 1954)	Structural failure	0.33 (10)	A single myelinated fiber dissected from frog motor nerve
(Galbraith et al., 1993)	Structural failure	0.25 – 0.30 (10)	An isolated squid giant axon
(Bain and Meaney, 2000)	Electrophysiological impairment	0.18 (30-60)	Optic nerve of guinea pig
(Geddes et al., 2003)	Significant membrane permeability	0.3 (10)	Cortical neuronal cultures of rats
(Morrison et al., 2003)	Cell death	0.2 (5-50)	Organotypic slice culture of rat hippocampus
(LaPlaca et al., 2005)	Cell death	0.25-0.5 (20-30), shear strain	Neuronal and astrocyte cell culture
(Elkin and Morrison, 2007)	Cell death	0.1-0.2 (0.1-50)	Organotypic slice culture of rat cortex
(Tang-Schomer et al., 2010)	Undulation,8% length increase	0.75 (44)	Isolated axon culture
(Nakadate et al., 2017)	Axonal swellings and bulbs	0.15 (50), 0.20 (30)	Cultured neurons

The correlations between deformation (e.g., strain, axonal elongation) and the onset of damage (i.e., the degree of electrophysiological impairment, morphological damage, and cell death of neurons) have been established (Morrison et al., 2003), but researchers have not reached an agreement on strain rate (Cater et al., 2006; Elkin and Morrison, 2007). Axonal tolerance to deformation has also been studied (Bain and Meaney, 2000; Nakadate et al., 2017), but slice cultures that contain intact white-matter tracts have yet to be tested with *in vitro* models of injury. Another unanswered question concerns the threshold of damage needed to cause brain dysfunction or injury, although one may correlate strains at the tissue level to different levels of axonal damage

at the microscopic level. Furthermore, the application of those *in vitro* injury thresholds in computational models would also be challenging. For instance, strains at the element level (~10^0 mm) are not equivalent to strains at the microscopic level (~106 mm) (Giudice et al., 2018).

2.4 FE Models

To investigate the relationship between mechanical loads, brain tissue responses, and the resulting brain injury, numerous human and animal brain FE models have been developed and extensively used to study brain injury. A summary of state-of-the-art human brain FE models is provided in Table 2-3. Although these computational models can provide an accurate representation of the macroscale brain anatomy based on computed tomography (CT) and magnetic resonance imaging (MRI) scans, these models vary in numerical methods (element type, mesh size, element formulation, hourglass control methods, etc.) and material models. Many models used in TBI research are still based on isotropic material, although recent studies have attempted to incorporate white matter anisotropy into the model. Most of them have been validated using the same experimental data (Hardy et al., 2007, 2001), while producing discordant tissue-level responses (e.g., strain) under identical loading conditions (Giordano and Kleiven, 2016; Miller et al., 2017; Zhao and Ji, 2018). Compared with human models, animal brain FE models (as summarized in Table 2-4) usually are less advanced with only primary macroscale anatomical features modeled. Most current animal brain FE models are not validated for intracranial deformation since there is currently no well-characterized experimental dataset. In all surveyed animal models used in traumatic brain injury research, brain tissue was modeled as isotropic material using a linear viscoelastic model. In general, the number of elements (3,000-250,000) was fewer than that in the surveyed human models (13,000-2,100,000).

Table 2-3. Summary of state-of-the-art human brain finite element models.

Model	Reference	Elements			Material Models			Geometry
		Number	Resolution	Type	Anisotropy	Viscoelasticity	Hyperelasticity	
WSUBIM	(Zhang et al., 2001)	314,000	1.8 mm	Hex. Quad.	No	Yes	No	50th percentile male
KTH	(Kleiven and von Holst, 2002)	21,000	5.8 mm	Hex. Quad.	No[1]	No[2]	Yes	Visible Human Database
UCD	(Horgan and Gilchrist, 2003)	28,000	5.5 mm	Hex. Quad.	No	Yes	No	Visible Human Database (Male)
THUMS	(Kimpara et al., 2006)	50,000	3.8 mm	Hex. Quad.	No	Yes	No	50th percentile male
SUFEHM	(Deck and Willinger, 2008)	13,000	7.7 mm	Hex. Quad.	No[3]	Yes	Yes	Human adult male
SIMon	(Takhounts et al., 2008)	46,000	3.2 mm	Hex. Quad.	No	Yes	No	50th percentile male
KTH-V	(Ho et al., 2009)	2,000,000	0.9 mm	Voxs. Quad.	Yes	Yes	Yes	--
DSSM	(McAllister et al., 2012)	--	--	Hex. Quad.	No	Yes	Yes	Subject-specific (male)
GHBMC	(Mao et al., 2013)	270,000	2.5 mm	Hex. Quad.	No	Yes	No	50th percentile male
Singapore	(Yang et al., 2014)	1,170,000	1.6 mm	Tet. Tri.	No	Yes	No	50th percentile Chinese male
DHIM	(Ji et al., 2015)	115,000	3.3 mm	Hex. Quad.	No[4]	Yes	Yes	Subject-specific (male)
WFUABM	(Miller et al., 2016)	2,100,000	1 mm	Vox. Quad.	No	Yes	No	ICBM brain template
Imperial	(Ghajari et al., 2017)	1,250,000	1.8 mm	VoxS. Quald.	No	Yes	Yes	34-year-old male
JHU	(Ganpule et al., 2017)	--	--	Meshless	Yes	Yes	Yes	Subject-specific
Toyota	(Atsumi et al., 2018)	62,000	3.0 mm	Hex. Quad.	Yes	Yes	Yes	TURBO SQUID human brain
YEAHM	(Fernandes et al., 2018)	--	--	Tet. Tri.	No	Yes	Yes	65-year-old male
PSU	(Garimella and Kraft, 2017)	153,000	2.1 mm	Hex. Truss	Yes	Yes	Yes	Subject-specific (male)

[1]Updated to include white matter anisotropy (Giordano and Kleiven, 2014b)
[2]Updated to include viscoelasticity (Kleiven, 2006)
[3]Updated to include white matter anisotropy (Sahoo et al., 2014)
[4]Updated to include white matter anisotropy (Zhao and Ji, 2018)
Hex., hexahedral; Quad., quadrilateral; Pent., pentahedral; Tet., tetrahedral; Tri., triangular; Vox., voxel; VoxS., smoothed voxels

Table 2-4. Summary of state-of-the-art animal brain finite element models.

Species	Reference	Elements			Material Models			Geometry
		Number	Resolution	Type	Anisotropy	Viscoelasticity	Hyperelasticity	
Macaque	(Ng et al., 2017)	--	--	Hex. Quad.	No	Yes	No	Brain Atlas & CT
Macaque	(Antona-Makoshi, 2016)	77,000	1.8 mm	Hex. Quad.	No	Yes	No	brain Atlas & CT
Pig	(Coats et al., 2012)	30,000	2 mm	Hex.	No	Yes	No	CT
Pig	(Jean et al., 2014)	37,000	--	Tet.	No	Yes	No	CT
Sheep	(Anderson et al., 2003)	3,000	--	Hex.	No	Yes	No	MRI & CT
Ferret	(Panzer, 2012)	24,000	0.56 mm	Hex.	No	Yes	No	CT
Rat	(Antona-Makoshi, 2016)	145,000	0.35 mms	Hex.	No	Yes	No	Brain Atlas & CT
Rat	(Ren et al., 2014)	180,000	0.25 mm	Hex.	No	Yes	No	MRI & CT
Rat	(Mao et al., 2006)	250,000	0.1-0.3 mm	Hex.	No	Yes	No	Brain Atlas
Mouse	(Jean et al., 2014)	91,778	--	Tet.	No	Yes	No	CT

Hex., hexahedral; Quad., quadrilateral; Pent., pentahedral; Tet., tetrahedral; Tri., triangular.

Overall, the substantial model inconsistency in the current brain FE models of the human and animals precludes effective comparisons in the simulation results and significantly hampers the collective efforts in the investigation of TBI. Efforts to improve human and animal brain models in this dissertation are presented in the following three chapters.

CHAPTER 3 : EXPLICIT METHOD TO MODEL AXONAL FIBER TRACTS

Many brain finite element models lack mesoscopic (~1 mm) white matter structures, which may limit their capability in predicting TBI and assessing tissue-based injury metrics such as axonal strain. To address these limitations and to improve existing FE models, this chapter investigated a novel embedded method to incorporate axonal fiber tracts of white matter explicitly into existing isotropic brain FE models. The axon-based model will be a useful tool for understanding the mechanisms of TBI, evaluating tissue-based injury metrics, and developing injury mitigation systems. This chapter was published previously (Wu et al., 2019. Explicit Modeling of White Matter Axonal Fiber Tracts in a Finite Element Brain Model. *Annals of Biomedical Engineering*, DOI: 10.1007/s10439-019-02239-8) and was adapted for this dissertation with permission from the publisher.

3.1 Introduction

Computational models are crucial to understanding the mechanisms of TBI at the tissue level, because of their ability to link external head impact conditions to the mesoscopic and even microscopic (cellular level) responses of brain tissue that leads to injury. While the microstructure of the brain white matter (WM) is heterogeneous and anisotropic, most current computational brain models (Mao et al., 2013; Miller et al., 2016; Takhounts et al., 2008) have adopted an isotropic representation of the material. More importantly, the lack of mesoscopic WM structures may limit their capability in predicting TBI because the damage to axons is believed to be one of the critical mechanisms of TBI (Meaney and Smith, 2011). The significance of WM anisotropy on brain tissue responses has been recently studied (Sahoo et al., 2014; Wright et al., 2013; Zhao and Ji, 2018) and it is believed that the incorporation of WM anisotropy is necessary for the development of more precise injury metrics (Giordano and Kleiven, 2014a; Sahoo et al., 2016).

The axonal fiber architecture of human WM can be characterized *in vivo* through diffusion-weighted magnetic resonance imaging (DWI) and subsequent deterministic tractography analyses by exploiting the Brownian motion of water molecules in tissues (Jones et al., 2013). Recent attempts to incorporate WM anisotropy in brain FE models (Table 3-1) have been made based on tractography information. The majority of these studies have implicitly incorporated fiber tractography to inform anisotropic, fiber-reinforced constitutive models (Chatelin et al., 2013; Ganpule et al., 2017; Giordano and Kleiven, 2014b; Wright et al., 2013; Zhao and Ji, 2018). However, this approach over-simplifies the brain parenchyma heterogeneity and requires the use of weighted-average fiber orientation for each element, which may not be aligned with the actual orientation of the axonal fiber bundles (Zhao and Ji, 2018). Garimella and Kraft (Garimella and Kraft, 2017) discussed the limitations associated with this technique in detail and instead suggested that axonal fibers be explicitly modeled as embedded elements. This method allows for the incorporation of multiple fiber orientations for a single element and takes advantage of the full axonal fiber tractography. However, the embedding method introduces new challenges associated with, but not limited to, mechanical characterization of axonal fibers and interaction between fibers and the ground substance. Also, deterministic tractography can be an erroneous process due to differences in reconstruction methods and tracking algorithms (Maier-Hein et al., 2017). While most studies (Table 3-1) obtain WM tracts from a single subject, a population-based atlas is preferred for increasing the validity of the fiber tractography and modeling representative topological interconnectivity in the general population (Yeh et al., 2018).

Table 3-1. 3-D anisotropic brain FE models.

Studies	*Anisotropy Modeling Method*	*Tractography Source*	*Number of Solid Elements*
(Sahoo et al., 2016)	Anisotropic Constitutive Model	12 volunteers	13,000
(Giordano and Kleiven, 2014b)	Anisotropic Constitutive Model	1 volunteer	21,000
(Ganpule et al., 2017)	Anisotropic Constitutive Model	Subject-specific	-
(Garimella and Kraft, 2017)	Embedded Elements	Subject-specific	150,000
(Zhao and Ji, 2018)	Anisotropic Constitutive Model	Subject-specific	53,378

The first objective of this chapter was to develop a methodology to incorporate axonal fibers into an existing isotropic FE human brain model. The Global Human Body Models Consortium (GHBMC) owned 50th percentile male (M50) brain model (Mao et al., 2013) was used to demonstrate the applicability of this methodology. The second objective was to improve the biofidelity and prediction capability of the original model. From a broad perspective, this study provides a novel and generalized framework for incorporating mesoscopic anatomical details in multi-scale FE models.

3.2 Methods

3.2.1 Baseline Model

The GHBMC M50 v4.3 brain model (Mao et al., 2013) has been used extensively in TBI research (Gabler et al., 2018a, 2018c, 2016; Sanchez et al., 2018, 2017). The geometry of the model was based on CT and MRI scans of an adult male representing the 50^{th} percentile height and weight of the population. The brain model has 82,083 hexahedral elements in total and includes anatomical representation of the cerebrum, cerebellum, brainstem, corpus callosum, ventricles, thalamus, bridging veins, CSF, and membranes (falx, tentorium, pia, arachnoid, dura). Brain model responses, including pressure and relative brain-skull motion, were previously validated (Mao et al., 2013). In this study, the GHBMC baseline model was modified to include axonal WM fiber 1-D elements, and new constitutive material models were applied to the ground

substance and fiber components. Finally, the brain deformation response was validated under a battery of impact cases. The updated model is hereafter referred to as the 'axon-based' model.

3.2.2 Fiber Tractography Model and Embedded Element Method

A combination of open-source medical imaging tools and in-house scripts were utilized to embed the baseline model with axonal tract elements. Figure 3-1 shows a schematic of the process, which involves 5 steps: 1) a FE mesh of fiber networks is created based on a population-based tractography template; 2) the axon tract mesh is morphed from the geometry of the tractography template to the geometry of the baseline brain FE model; 3) the morphed fiber mesh is mathematically embedded into solid elements of the baseline model; 4) the brain elements (cable) are categorized based on the fractional anisotropy (FA) values of the tracts; 5) mechanical properties of both the axon tract elements and the isotropic solid element are assigned based on multi-modal tissue data in the literature. Each step of this process is explained in detail below.

The deterministic whole-brain fiber tractography process was performed using a freely available, pre-processed, group-averaged (N = 842; M: 372 F; 470; Ages: 20-40 yr) tractography dataset (HCP-842 tractography template) consisting of DWI data from the Human Connectome Project (Yeh et al., 2018). Data were accessed under the WU-Minn HCP open access agreement and were initially acquired using a multi-shell diffusion scheme (b-values: 1000, 2000, and 3000 sec/mm^2; diffusion sampling directions: 90, 90, and 90; in-plane resolution and the slice thickness: 1.25 mm). The tractography reconstruction was conducted using DSI Studio (http://dsi-studio.labsolver.org) in the standard MNI atlas space. After 5,000 randomized seeding attempts, the resulting tractography included in the model had 3,446 fiber tracts with a maximum length of 297.0 mm, a minimum length of 29.3 mm and a mean length of 78.6 ± 38.24 mm. An in-house script was used to convert the axonal tractography data obtained from DSI Studio into a FE mesh

using a network of 1-D cable (tension-only) elements. The axonal fiber tractography FE mesh had a total of 104,866 cable elements with an element size of around 2.5 mm. The elements were then categorized into ten groups based on their FA values (Figure 3-2). FA is a widely used metric of diffusion anisotropy and ranges from 0, representing an isotropic movement of water molecules (e.g., CSF), to 1, highly anisotropic movement of water molecules (e.g., fiber bundles).

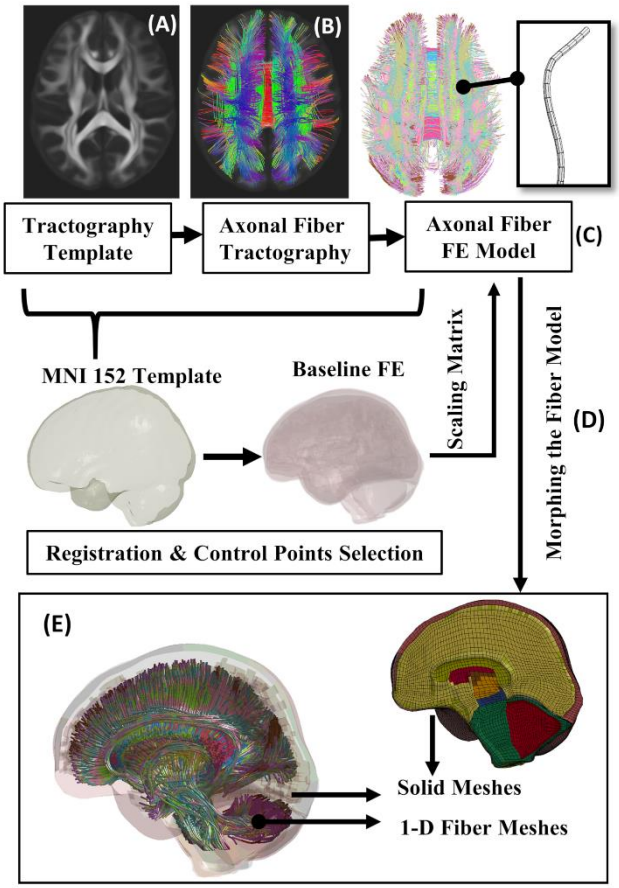

Figure 3-1. Procedural flowchart adopted to embed axonal fibers in the baseline brain FE model. (A) Diffusion MRI template; (B) Reconstructed axonal fiber tractography; (C) Fiber tractography FE model; (D) Morphing process; (E) Embedding fibers into the baseline model.

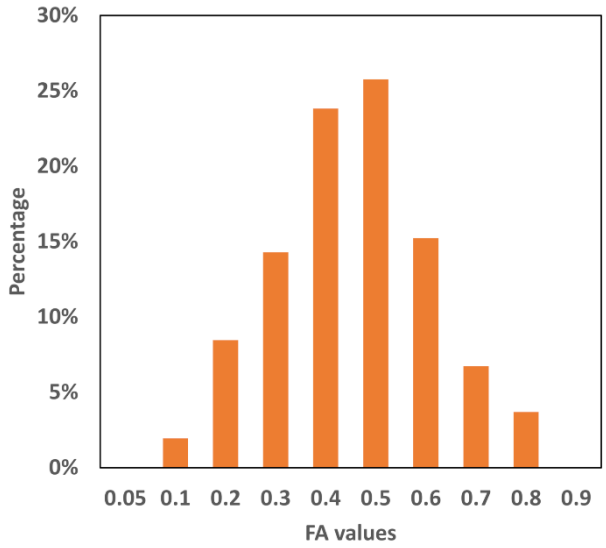

Figure 3-2. FA distribution for the cable fiber elements.

Matching the tractography mesh with the brain FE model is a challenging procedure because they are originally in different spatial orientations and are associated with brains that have different shapes and sizes. Here, a morphing technique was adopted to align the fiber FE model with the baseline model, based on a technique by Park et al. (Park et al., 2017). First, the geometry of the template MNI brain and CSF surface was aligned and scaled to the target geometry of the baseline model using iterative closest point approximation. Next, the MNI surface nodes served as landmarks and were mapped to the baseline model brain surface using an iterative registration method (Burr's elastic registration) to match the external geometry of the two surfaces. The same transformation in this step is then applied to the tractography mesh using a thin-plate spline method with radial basis function to interpolate and smooth to match the axonal tracts to the internal geometry of the baseline model brain. The results of the morphing can be visually checked in Figure 3-3. The mean distance between the MNI surface nodes and the baseline model surface after registration was less than 0.1 mm.

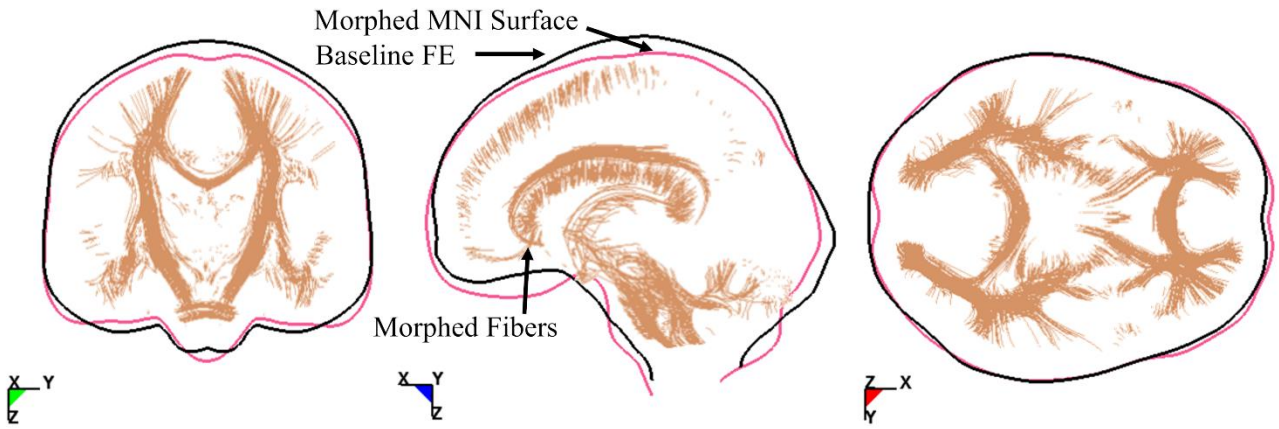

Figure 3-3. Morphing results demonstrating the morphed MNI surface and morphed fiber tractography model. The baseline model dura surface is shown in black.

Once the tractography mesh was in the same anatomical space as the volumetric baseline model brain, they were constrained as embedded elements using the *CONSTRAINED_BEAM_IN_SOLID Keyword in LS-DYNA (v971 R9.2.0, LSTC, Livermore, CA). This technique has been applied previously to model rebar-reinforced concrete composites (Bermejo et al., 2017) and ensures that the axonal fibers and volumetric ground substance are continuous and have the same accelerations and velocities. Steps were taken to ensure this method would satisfy the structural conditions of equilibrium, energy balance, and compatibility.

3.2.3 Constitutive Model

The brain tissue response was decomposed into an isotropic ground substance and an anisotropic component governed by the myelinated axons. The isotropic ground substance was assumed to have material properties the same as gray matter (GM). Therefore, the distinguishing feature between WM and GM was the presence of the myelinated axons. Both the ground substance and fiber materials were modeled as hyper-viscoelastic and implemented in LS-DYNA as user-defined materials. For the ground substance material, the isotropic hyper-elastic strain energy density function is based on the Holzapfel-Gasser-Ogden (HGO) model (Gasser et al., 2006):

$$W = \frac{G}{2}(\tilde{I}_1 - 3) + K\left(\frac{J^2 - 1}{4} - \frac{1}{2}\ln(J)\right) + \frac{k_1}{2k_2}(e^{k_2\tilde{E}_a{}^2} - 1) \quad [3\text{-}1]$$

$$\tilde{E}_a = \frac{1}{3}(\tilde{I}_1 - 3) \quad [3\text{-}2]$$

$\tilde{I}_1$ is the first invariant of the isochoric right Cauchy-Green deformation tensor and $J = \det F$ is the volume change ratio. G is the shear modulus, K is the bulk modulus, k_1 is a stress-like parameter, and k_2 is a dimensionless parameter.

While the strain energy density function for the axonal fiber was formulated as Equation [3-3], which is also based on the HGO model (Gasser et al., 2006).

$$W = \frac{k_1}{2k_2}(e^{k_2 E_a{}^2} - 1) \quad [3\text{-}3]$$

$$E_a = \kappa(I_1 - 3) + (1 - 3\kappa)(I_{4a} - 1) \quad [3\text{-}4]$$

The Green-Lagrange strain-like quantity E_a is a function of $I_{4a} = \tilde{C}: n_{0a} \otimes n_{0a}$ (where $\tilde{C}$ is the isochoric part of the right Cauchy–Green strain tensor and n_{0a} is the unit vector of fiber direction in the undeformed configuration) and κ. The dimensionless structure parameter κ accounts for the orientation distribution of the axons in a voxel-scale fiber bundle and can be related with FA through Equation [3-5] by assuming similarity between mechanical and diffusion anisotropy (Giordano and Kleiven, 2014b; Wright et al., 2013). At the lower limit, κ = 0 (FA = 1), axons are perfectly aligned and at the upper limit, κ = 1/3 (FA = 0), axons are randomly oriented and isotopically distributed.

$$\kappa = \frac{1}{2}\frac{-6 + 4\mathrm{FA}^2 + 2\sqrt{3\mathrm{FA}^2 - 2\mathrm{FA}^4}}{-9 + 6\mathrm{FA}^2} \quad [3\text{-}5]$$

The temporal response of the deviatoric stress component was modeled using a quasi-linear viscoelastic (QLV) mathematical framework (Fung, 2013), and the volumetric behavior was assumed to be independent of time.

$$\sigma^d(t) = \int_0^t [G_\infty + \sum_{i=1}^{4} G_i e^{-\beta_i(t-\tau)}] \frac{\partial \sigma_e^d}{\partial \tau} d\tau \qquad [3\text{-}6]$$

In which σ_e^d is the instantaneous, deviatoric elastic response. A Prony series with four time-constants was chosen to model the relaxation behavior. G_∞ and G_i are the linear coefficients of the reduced relaxation coefficients, and β_i are the relaxation time constants.

3.2.4 Parameters Calibration: Matrix

A single set of coefficients for the ground substance material model was first calibrated using available human GM tissue material testing data (Jin et al., 2013). These data were obtained from experiments conducted at a set of constant strain rates (0.5/s, 10/s, 30/s) under various loading modes including simple shear, compression, tension in terms of engineering stress and engineering strain. The explicit constitutive relations were derived analytically and formulated in terms of Cauchy stress and deformation gradient (***F***) during calibration. The calibration process was performed through a generalized reduced gradient nonlinear optimization to minimize the sum of squared error (SSE) between the experimental data and model predicted stress. The instantaneous and viscoelastic coefficients were optimized simultaneously.

3.2.5 Parameters Calibration: Fiber

The fiber properties were calibrated based on the composite response of the axonal fibers and the ground substance material, i.e., the mechanical properties of white matter. Since the stiffness of white matter in the model will be region dependent due to the heterogeneity of fiber architecture, the effective shear stiffness of the model at the corona radiata region was used as a

benchmark. The calibration of fiber parameters was conducted using a single element inverse FE approach, as detailed below. The same set of coefficients identified for the ground substance were used to model the relaxation behavior of the fibers.

Despite the differences in loading conditions, regions tested, and testing techniques from the literature (Braun et al., 2014; Budday et al., 2015; Clayton et al., 2012; Jin et al., 2013; Johnson et al., 2013; Johnson and Telzer, 2018; Kruse et al., 2008; Pervin and Chen, 2009; Prange and Margulies, 2002; Velardi et al., 2006; Zhang et al., 2011), the stiffness of the white matter ranged from 0 – 2.2 times stiffer than the gray matter stiffness, and in most of the studies this ratio is around 0.3 (Figure 3-4). The stiffness ratio was defined as $(\sigma_{WM} - \sigma_{GM})/\sigma_{GM}$, in which σ_{WM} and σ_{GM} are stress measured at the same strain level for white matter and gray matter respectively.

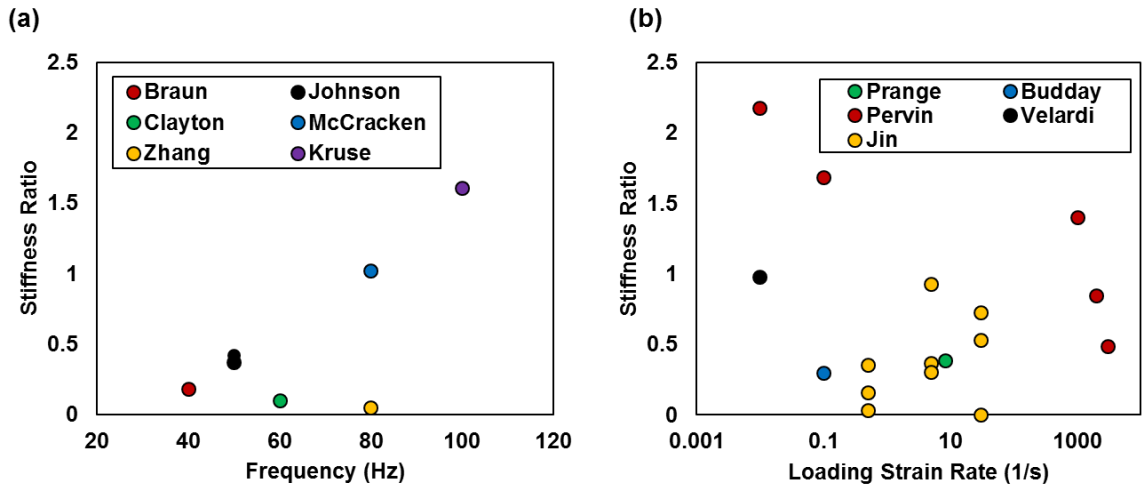

Figure 3-4. Stiffness ratio between the white matter and the gray matter in the literature. (a) Magnetic resonance elastography studies; (b) Mechanical tissue testing.

Unlike the continuum models of fiber-reinforced materials, the fiber contribution in the embedded model is not only determined by the constitutive model of the fiber but is also affected by the fiber architecture, including the numbers of fibers embedded, fiber distributions, and degree of anisotropy in the fibers. So, to identify the coefficients of the constitutive model for the fiber, those features of fiber architecture need to be determined first. Since not all the factors listed above

are explicitly accessible, we attempted to quantify their effects through a simplified model, a single solid element embedded with a fiber. Figure 3-5 illustrates the process of simplification and summarizes the calibration procedure in three steps：

a) Identify the basic structural parameters for the simplified model. The simplified model was built to replicate the same volume ratio between the fibers and the ground substance in the brain model, which was globally estimated to be 0.456 by dividing the volume of cable elements by the volume of white matter solid elements in the brain model. The degree of fiber dispersion (κ) in the simplified model was to match with those in the corona radiata region (mean $FA = 0.5$) because corona radiata was the common region tested in the literature to characterize the white matter material properties.

b) Initiate calibration based on the uniaxial tension loading condition. Since the fiber can only sustain tension, the fiber contribution was expected to be the largest under the tensile tests in which the fiber orientation was aligned with the stretch direction. In other words, the stiffness ratio should be at the upper bound of the range in the literature [0 – 2.2].

c) Estimate fiber properties based on the simple shear loading condition. Simulations with fiber (WM) and without fiber (GM) were then conducted respectively under the same simple shear loading condition, as shear is the primary loading scenario for brain tissue under impacts. The stiffness ratio under this condition should match the common ratio (0.3) found in the literature.

3.2.6 Initial Model Validation Data

Experiments from two separate studies were simulated to assess the biofidelity of the axon-based and baseline model brain deformations. The first study was a series of cadaveric impact tests conducted by Hardy et al. (2001, 2007) to measure relative brain-skull displacements under high-

rate impacts using embedded radiopaque, neutral density targets (NDT). Although not designed for model validation, these experiments have been widely used to validate brain FE models (Mao et al., 2013; Miller et al., 2017, 2016; Sahoo et al., 2014; Zhao and Ji, 2018). Recently, Alshareef et al. (2017) introduced a novel method for quantifying 3-D human brain deformation using sonomicrometry (SONO). These tests were conducted specifically to obtain validation targets for brain FE models. The axon-based and baseline models were simulated using a subset of 12 loading cases from a single cadaver (male; 53 years old; height of 173 cm). The loading cases (n=17) are summarized in Figure 3-6 and represent an array of loading severities, impact durations, and impact directions. The simulation performed in this chapter is only the first step to evaluate the biofidelity of the baseline and axon-based FE model. A comprehensive evaluation study will be presented in the next chapter.

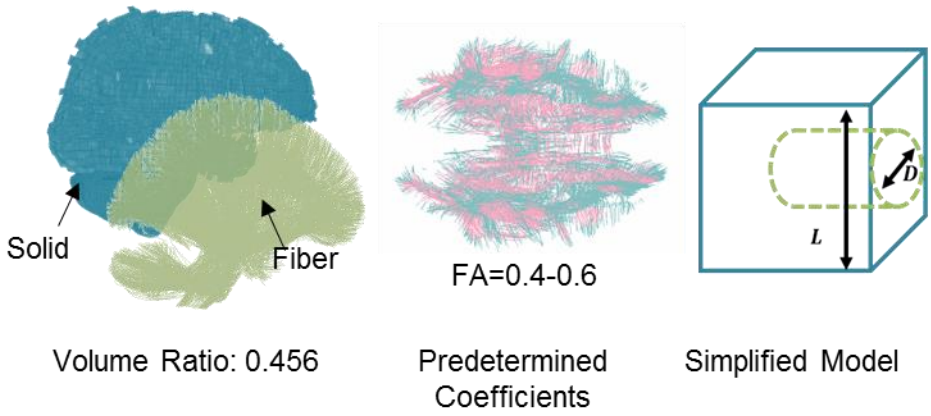

Figure 3-5. Calibration procedure used to identify material coefficients for the axonal fiber constitutive model.

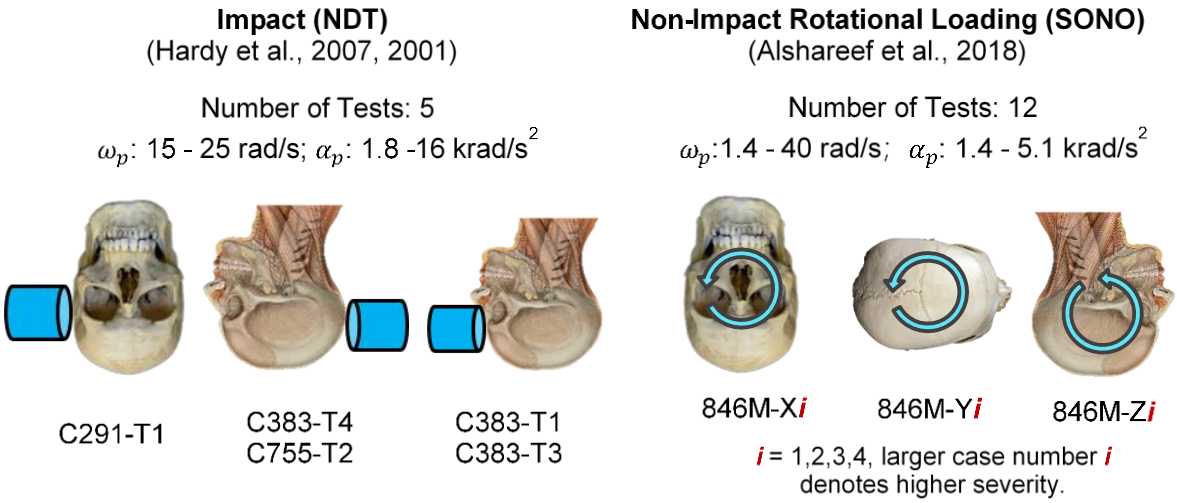

Figure 3-6. Summary of experimental test conditions.

3.2.7 Data Analysis

All simulations in this dissertation were performed using LS-DYNA (v971 R9.2.0, double precision; LSTC, Livermore, CA). Six-degree-of-freedom (DOF) head kinematics were applied to the rigid dura through the center of gravity of the head in both brain models. For each validation case, the predicted displacement-time histories of the relevant nodes were compared with the experimental measurements. Model biofidelity was quantified using the CORrelation and Analysis objective rating system (CORA) (Gehre et al., 2009). For each validation case, an overall score was computed by averaging the individual signal scores.

In this study, further investigation of strain-based metrics was performed using the SONO loading cases. The element-wise MPS for the solid brain tissue and the element-wise maximum axonal strain (MAS, the tensile strain sustained by axonal fiber tracts) were calculated.

Finally, to study the effect of the anisotropy on the tissue response, the element-wise MPS response of the baseline model was compared with those from its isotropic derivative model that only included the ground substance material (referred as GS-based model).

3.3 Results

3.3.1 Calibration Results

The optimized constitutive model for the ground substance material compared with experimental corridors are shown in Figure 3-7 (a). To verify the response of the calibrated constitutive model, hypothetical shear oscillation tests were analytically computed and the stress output from the constitutive model was compared to frequency sweep data available in the literature (Arbogast and Margulies, 1997; Bilston et al., 2001; Brands et al., 1999; Garo et al., 2007; Hrapko et al., 2006; Lippert et al., 2004; Nicolle et al., 2004; Peters et al., 1997; Shen et al., 2006; Thibault and Margulies, 1998). These results are shown in Figure 3-7 (b). This figure also demonstrates the differences between the calibrated model and the baseline model materials. The suitable coefficient was found, as illustrated in Figure 3-8, the element with fiber is around 0.3 times stiffer than the one without fiber at 30% strain with a strain rate of 30/s. The simulation results also correlate well with the experimental results (Jin et al., 2013) for the corona radiata at the same loading conditions.

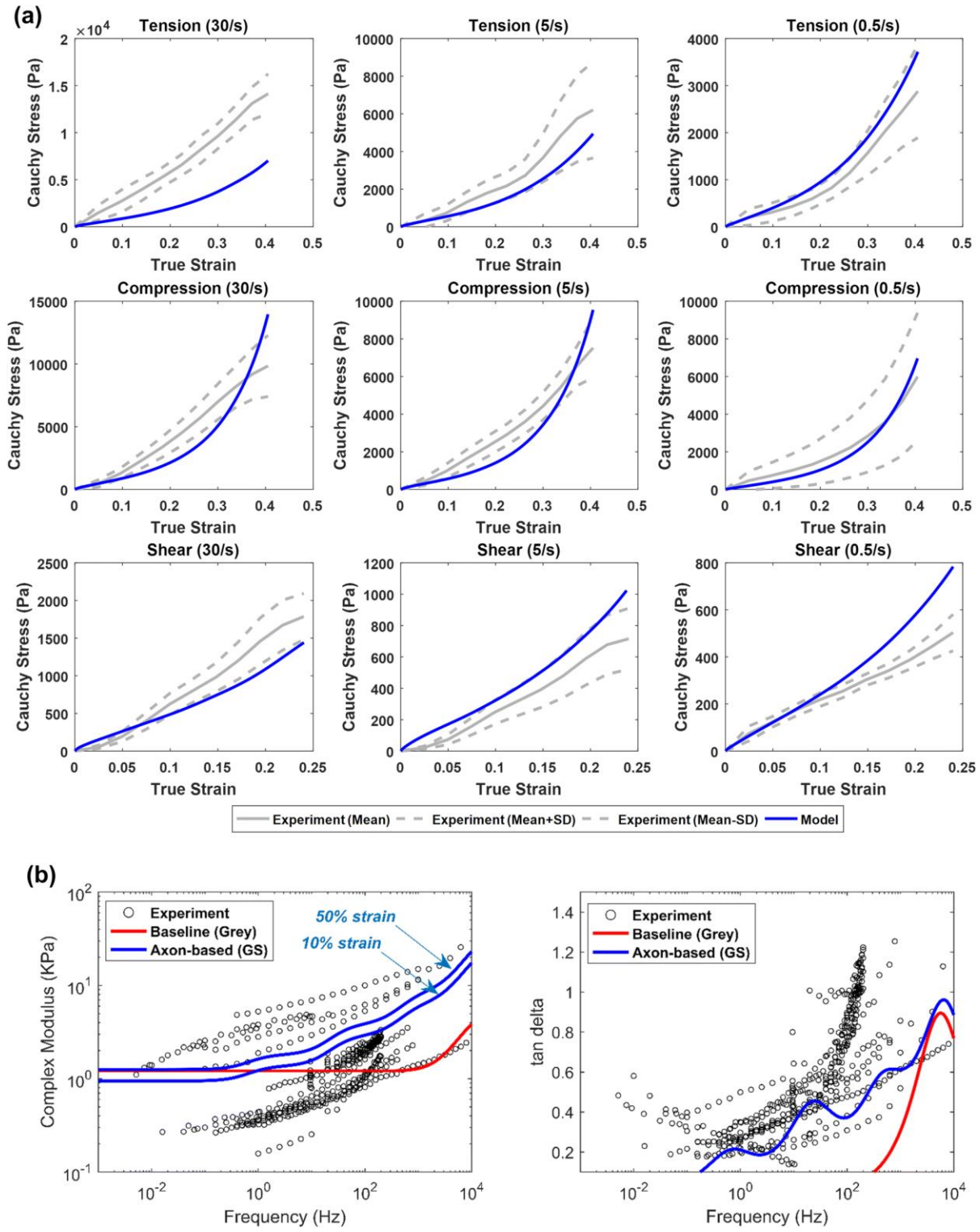

Figure 3-7. Constitutive model and experimental tissue tests results. (a) Constant strain rate mechanical tests; (b) Complex shear modulus and tan delta of brain tissue from shear oscillation tests in the literature between 0.01 and 10,000 Hz.

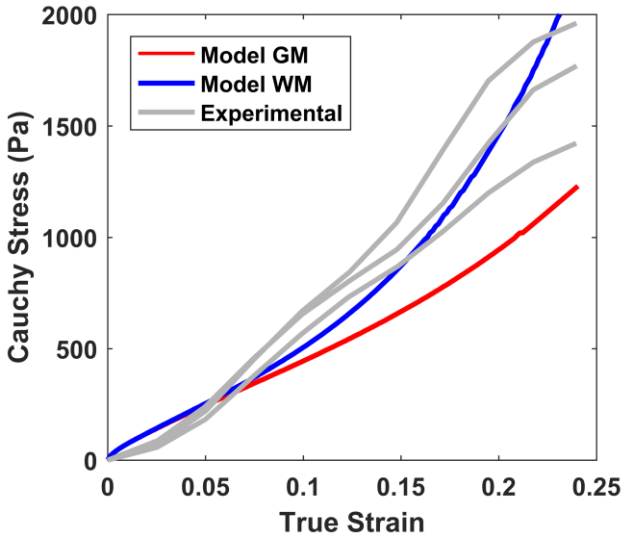

Figure 3-8. Stress responses of the gray matter (GM) and white matter (WM) for the single element tests under simple shear, compared with the experimental study (Jin et al., 2013).

Table 3-2 summarizes the detailed material properties employed in the axon-based model. The thickness of the falx, tentorium, and pia was modified based on recently published experimental data (Golman et al., 2013; Jin et al., 2006). Material properties of other brain regions remained identical to the unmodified baseline model.

Table 3-2. Material properties used in the axon-based model.

Anatomical component	Material model	Instantaneous material coefficients	Viscoelastic coefficients	Experimental references
Brain tissue (ground substance)	HGO Hyperelastic+ Quasilinear Viscoelastic	$G = 27.5$ kPa $K = 2.19$ GPa $k_1 = 203$ kPa $k_2 \to 0$	$G_1 = 0.8087$ $G_2 = 0.1005$ $G_3 = 0.047$ $G_4 = 0.0133$ $G_\infty = 0.0305$ $\tau_1 = 0.01$ ms $\tau_2 = 0.23$ ms $\tau_3 = 5$ ms $\tau_3 = 200$ ms	(Jin et al., 2013; Nicolle et al., 2004)
Axonal fibers	HGO Hyperelastic+ Quasilinear Viscoelastic	$k_1 = 900$ kPa $k_2 \to 0$ κ is a function of FA		(Budday et al., 2017; Jin et al., 2013)
Pia	Elastic	$E = 12.5$ MPa Thickness= 0.10 mm	-	(Jin et al., 2013)
Falx	Elastic	E =31.5 MPa Thickness= 0.45 mm	-	(Golman et al., 2013)
Tentorium	Elastic	E =31.5 MPa Thickness= 0.36 mm	-	

3.3.2 Nodal Displacements and CORA Score

All the FE models in this study were stable and terminated normally. The simulation with the axon-based model requires approximately 2.4 times more computational cost than that of the baseline model. For the NDT impacts, the axon-based and baseline models had overall CORA scores of 0.450 and 0.430, respectively, based on the average of the five tests (Figure 3-9, individual plots reported in the Appendix, Figure A1 – Figure A5). These performed as well as other state-of-the-art FE models for this particular experimental dataset. For the SONO cases, the performance of the axon-based and baseline models will be discussed in detail in the next chapter. Overall, the axon-based model reported a higher CORA score for 16 out of 17 total NDT and SONO cases (the only exception is the C383-T4 case).

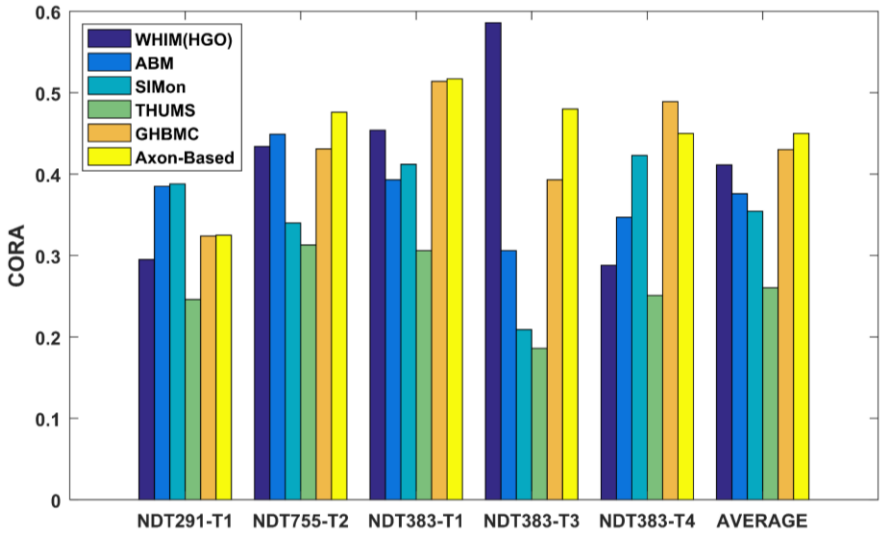

Figure 3-9. Comparison of validation performance of the axon-based model with other brain models. CORA scores for THUMS, SIMon, and ABM were adapted from (Miller et al., 2017), CORA scores for WHIM (HGO) were adapted from (Zhao and Ji, 2018).

3.3.3 Strain Results

Although the axon-based and baseline models demonstrated similar CORA scores, the strain responses in the two models were significantly different, especially in more severe loading conditions. For the SONO simulations, the MPS predicted by the baseline model, the MPS

predicted by the axon-based model, and the MAS predicted by the axon-based model are illustrated in Figure 3-10 as cumulative distributions across all brain tissue elements. In the most severe loading case (SONO 846M-Z4, $\omega_p = 40\, rad/s, \alpha_p = 5.1\, krad/s$), the maximum MPS of all elements predicted by the baseline model is more than 90%, while the axon-based model reported a maximum MPS of 56%.

3.3.4 Effects of Anisotropy

The element-wise MPS response of the axon-based model was compared with those from the isotropic GS-based model using linear regression. This result is illustrated in Figure 3-11 (a) showing the element-wise MPS under the most severe SONO loading case (SONO 846M-Z4, $\omega_p = 40\, rad/s, \alpha_p = 5.1\, krad/s$). Globally, the effects of anisotropy on strain responses were not significant. However, the inclusion of anisotropy does lead to some local differences in the strain pattern for the inner WM region (Figure 3-11 (b)), which were mainly composed of highly aligned axonal fibers.

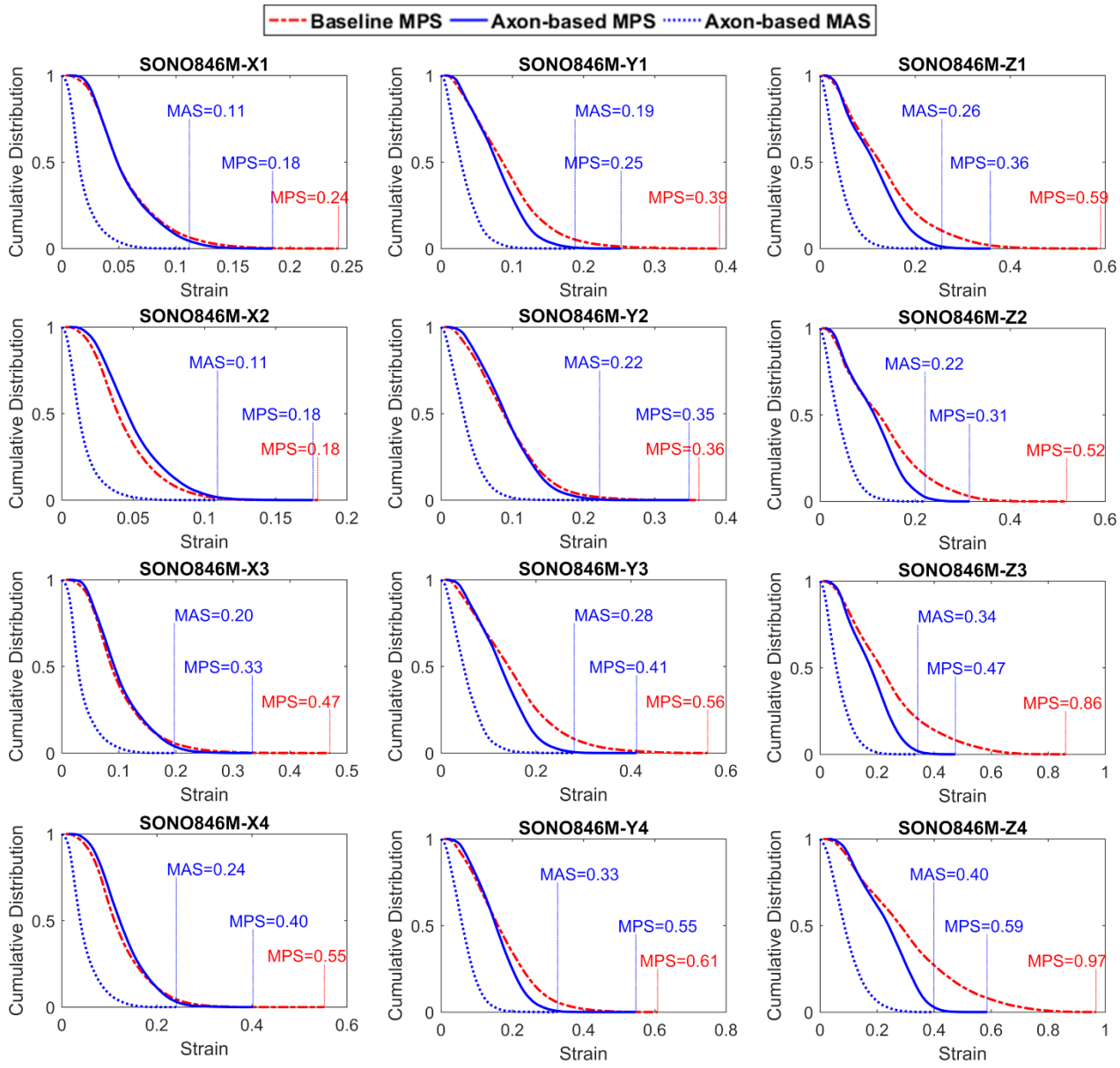

Figure 3-10. Comparison of strain results of the FE models in SONO simulations. The cumulative distributions show the percentage of elements above specific peak strain values.

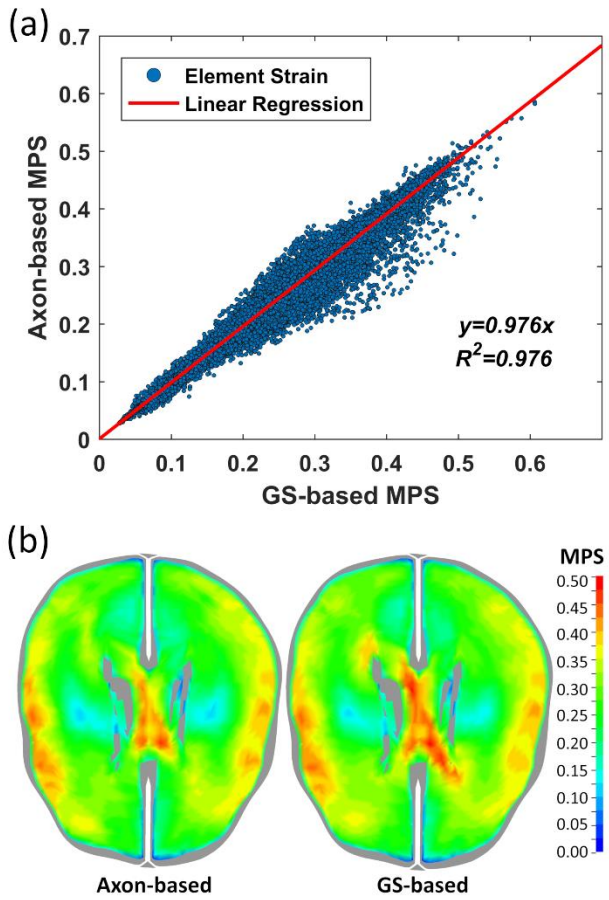

Figure 3-11. Effect of anisotropy on strain results for the SONO 846M-Z case. (a) Comparison of strain results of solid elements for the whole brain; (b) Comparison of strain distributions.

3.4 Discussion

Advanced brain FE models are fundamental for investigating TBI. With increasing interest in understanding injury mechanisms at the mesoscale, the biofidelity of the brain models needs to be improved in both anatomical representation and predicting biomechanical responses. In this study, we developed a novel framework based on an embedded element method for incorporating axonal fiber tracts into the existing isotropic brain FE models. We demonstrated the applicability of this framework on an existing brain model without extra efforts on mesh refinements.

3.4.1 Brain Material Properties

Most of the current brain models (Ganpule et al., 2017; Garimella and Kraft, 2017; Giordano and Kleiven, 2014b; Wright et al., 2013; Zhao and Ji, 2018) utilize material properties that have been calibrated using experimental brain tissue mechanical data obtained from a single loading mode, which might not fully capture the various aspects of the complex response of human brain tissue. Moreover, significant disparities in testing protocols and results reported in the literature complicate the selection of a single experimental dataset that accurately represents the mechanical behavior of the brain (Chatelin et al., 2010). It has been shown that, because of the vast variations in material properties, the resulting constitutive models will lead to significant disparities in strain-based injury metrics (Zhao et al., 2018). These disparities could be partly attributed to the viscoelasticity and frequency dependence of brain tissue as different studies have characterized brain tissue at different rates of deformation. To address these limitations, we have simultaneously identified a single parameter set for shear, compression, and tension at a series of constant strain rates, and verified the same parameter set with shear oscillation tests across a broad range of frequencies (0.01 to 10,000 Hz).

3.4.2 Constitutive Model for Axonal Fibers

One challenge inherent to explicitly modeling axonal fiber tracts is isolating the material properties of axonal fibers since the mechanical properties of axons, and WM directional-dependence are ambiguous in the literature (Ning et al., 2006). Even if reliable axon material property data is available, it would be challenging to incorporate it into the model because the stiffness contribution from the axonal fibers depends on structural features (such as cross-sectional area, element size, etc.), as well as the underlying ground substance constitutive model. Therefore,

instead of calibrating the axonal fiber constitutive material model directly, the fiber properties were calibrated based on the stiffness differences between the WM and GM in this study.

Individual axons in the axonal fiber tracts are not perfectly aligned but dispersed around some referential, preferred direction. In the axon-based model, these fibers were represented as 'cable' elements. Depending on the dispersion, the cables should have different mechanical properties. To account for the dispersion of the axons, most studies assume a probability distribution of the axons and perform a pre-integration of the distribution to achieve improved computational efficiency. The best-known model of this kind is the Holzapfel-Gasser-Ogden (HGO) model, which has been widely used for modeling anisotropic brain tissue (Ganpule et al., 2017; Giordano and Kleiven, 2014b; Zhao and Ji, 2018). As recognized by Holzapfel and Ogden (Holzapfel and Ogden, 2015), the limiting issue of using the HGO model in fiber-reinforced anisotropic materials is the tension-compression switch criterion. This switch criterion is required because fibers do not support compression. Also, compressive axonal strains should not be included when using strain-based metrics to relate brain deformation to injury. The switch used by previous studies (Ganpule et al., 2017; Giordano and Kleiven, 2014b) was based on an averaged structure invariant: E_a (denoted as 'axonal strain' in those studies). That is to say:

$$\begin{cases} w_{fiber} = \dfrac{k_1}{2k_2}\left(e^{k_2 {E_a}^2} - 1\right) & E_a > 0 \\ w_{fiber} = 0 & E_a \leq 0 \end{cases} \qquad \textit{[3-7]}$$

$$E_a = \kappa(I_1 - 3) + (1 - 3\kappa)(I_{4a} - 1) \qquad \textit{[3-8]}$$

However, this switch can give erroneous results, as deformation states may exist for which the axon family is extended according to the averaged structure invariant ($E_a > 0$), but the fiber in the corresponding preferred direction is under compression ($\lambda < 0$). This is apparent in Figure

3-12, which illustrates the dependence of E_a on λ for several values of κ. As shown, $E_a > 0$ does not necessarily require stretch $\lambda > 1$. In the current application, the effects of using different switches on the mechanical responses of brain tissue might not be significant (because the effect of anisotropy is small). However, using E_a, instead of the strain in the main fiber direction, as an injury metric (Giordano et al. 2016) might lead to erroneous results, because E_a cannot differentiate compressive and tensile strains.

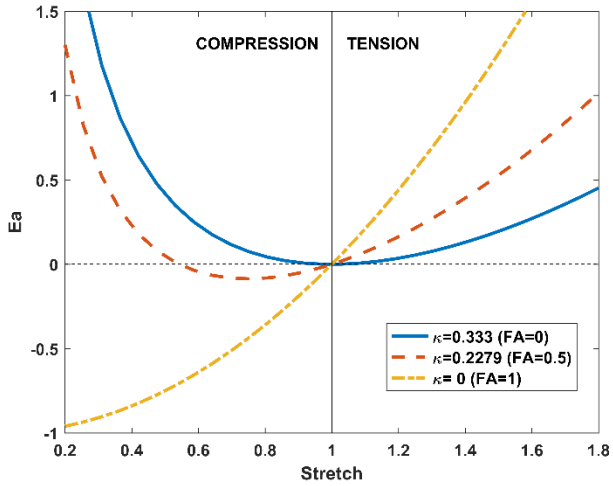

Figure 3-12. The plot of the function E_a for different dispersion values. Note that $E_a > 0$ exists under compressive loading.

I further noticed this criterion was not the original proposal of Gasser et al. (2006) as per Equation [3-10].

$$w_{fiber} = \frac{k_1}{2k_2}\left(e^{k_2 {E_a}^2} - 1\right) \qquad [3\text{-}9]$$

$$\begin{cases} E_a = \kappa(I_1 - 3) + (1 - 3\kappa)(I_{4a} - 1) & I_{4a} > 1 \\ E_a = \kappa(I_1 - 3) & I_{4a} \leq 1 \end{cases} \qquad [3\text{-}10]$$

However, this original criterion was also criticized for resulting in non-physical stress discontinuities (Latorre and Montáns, 2016). To our knowledge, there is no simple correction for this issue from a constitutive perspective (Holzapfel and Ogden, 2017). In this study, since the fibers and ground substance were explicitly modeled, and the nonlinear behavior of the fibers was

decoupled from the ground substance, the exclusion of the compressive strain and stress for these 1-D elements was straightforward and did not cause any stress discontinuities.

3.4.3 Embedded Elements Method

The embedding between the fibers and the ground substance was assumed to be no-slip, and the initial structure of the fiber is non-undulated. The no-slip assumption may be appropriate, as brain tissues can remain intact under large deformation (up to 50% strain) (Prange and Margulies, 2002). Axonal undulation is present in some intracranial nervous tissue as a physiological adaptation, such as the optic nerve, the root of the trigeminal nerve and cranial nerves VI-XII (Nilsson et al., 2012). Axon tracts in most other WM regions were fully coupled to the surrounding tissue, at least in porcine brain tissue (Dave Meaney, personal communication, October 13, 2017).

The embedded elements method was developed before its application in modeling soft tissue (Fish, 1992). In general, two issues should be considered when implementing embedded elements on a fiber-reinforced composite: the interpenetration of the contacting fibers and volume redundancy (Tabatabaei and Lomov, 2015). In this study, the first issue was irrelevant, because physically the fibers cannot come into contact with each other unless the surrounding tissues were damaged. TBI injuries typically present without visible physical damage or gross tissue disruption (Gennarelli et al., 1972). However, the volume redundancy issue needed special consideration to correct the resulting mass and stiffness redundancy. In the embedded element method, the ground substance occupies the full volume of the brain, including the volume under the fiber reinforcement. The addition of reinforcing axonal fibers that have finite cross-sectional area leads to mass and stiffness redundancies. To resolve this volume redundancy, I artificially decreased the mass density of the fibers to be negligible. To address the stiffness redundancy, the constitutive

contribution of the ground substance material was subtracted from the constitutive contribution of the axonal fibers (Tabatabaei and Lomov, 2015).

3.4.4 Effects of Anisotropy

In this study, we found the effects of anisotropy on strain responses were not substantial. Previous studies have also noted minimal effects of anisotropy on strain outcomes (Wright et al., 2013; Zhao and Ji, 2018). However, varying conclusions exist depending on how the fiber-reinforcement term was defined. In fact, the relative stiffness contribution of the fibers defined in constitutive model approaches varies in the literature. For example, Sahoo et al. (2014) concluded that the inclusion of DTI parameters (anisotropy) to the brain FE model had a significant influence on local brain deformation. This was expected since the contribution ratio between the fiber and ground substance terms in their constitutive model was relatively large; the fiber term contributes up to 70% of the overall stiffness under 1.5 stretch at the corona radiata region. Cloots et al. (2013), Giordano et al. (2014), and Zhao and Ji (2018) reported conflicting findings on the significance of anisotropy despite using fiber material properties based on the same experimental study (Ning et al., 2006). Nevertheless, a direct comparison with these previous studies was not feasible, because they modeled the axon contribution through a fiber reinforcement term in the strain energy function (not a physical fiber in the model). In this study, the fiber contribution was not solely determined by the constitutive model but was also related to the physical fiber architecture (e.g., distribution, cross-section area, numbers of cable elements).

Although the effects of anisotropy on mechanical responses were subtle, the fact that the MAS was significantly different from the MPS in values and distribution revealed the potential importance of incorporating anisotropic axonal fibers into brain FE models. For the SONO simulations using the axon-based model, the MAS was significantly lower than the MPS, and large

strains were occurring either in non-fiber directions or non-fiber regions (e.g., cerebral cortex). If axonal damage were indeed an injury mechanism of TBI, the differences between the MPS and the MAS could result in different injury risk outcomes. Several studies have explored the correlation between axonal strain and TBI. Sahoo et al. (2016) showed that axonal strain was the most appropriate parameter for predicting DAI, based on 109 reconstructed pedestrian accident cases. Giordano and Kleiven (2014a) found that strain in the axonal direction was a better injury predictor than MPS for a data set of 58 mild TBI reconstructions. Nevertheless, whether the axonal strain in an FE model is a better injury predictor requires further investigation.

3.4.5 Limitations

This study assumed correlations between the mechanical properties of nervous tissue and its underlying microstructure. The regional dependence or mechanical heterogeneity was typically found in biomechanical tests (Jin et al., 2013), indentation tests (Budday et al., 2015), and *in-vivo* magnetic resonance elastography (Johnson et al., 2013). Fiber-rich regions like the brainstem and corona radiata were generally stiffer than fiber-deficient regions such as the cortex and thalamus. However, the authors acknowledge the contrary evidence in the literature on the mechanical anisotropy of WM. Velardi et al. (2006) found a significantly stiffer response in the fiber direction than perpendicular to it under uniaxial tests. Prange and Margulies (2002), Arbogast and Margulies (1997), Feng et al. (2013), and Jin et al. (2013) found significant anisotropy in shear but their conclusions were contradictory, and the directional dependence did not correlate well with expected fiber orientation. Pervin and Chen (2009), Nicolle et al. (2004), and Budday et al. (2017) revealed no statistically significant dependencies on fiber orientation. The contradictory experimental results could be due to the complexity of the microstructure in the brain, as more than 80% of the white matter voxels in the HCP-842 template had more than one fiber orientation,

even at 2.5-mm^3 resolution (Yeh et al., 2018), and extracting specimens that exhibit distinct fiber direction would be difficult. Understanding the directional and regional dependence of brain mechanical properties both *in vitro* and *in vivo* is still a topic of ongoing research and inconclusive.

Another limitation is the fundamental ambiguities inherent in tract reconstruction techniques. The group-averaged whole-brain fiber tractography was obtained from DWI and subsequent deterministic tractography analyses. Group-averaged tractography would potentially reduce random errors associated with individual fiber tracking process, but there would still be an error between the tractography and the true fiber architecture. It has been shown recently that invalid bundles occur systematically across different research groups using different tract reconstruction methods when evaluated with ground truth bundles (Maier-Hein et al., 2017). The encouraging finding reported in the evaluation study is that the deterministic fiber tracking method used to obtain the current tractography template (HCP-842) has achieved the highest valid connection among 96 methods, at 92%. There were also limitations associated with the CORA objective rating system and its widespread use for validating brain FE models, particularly for brain deformation with nodal displacement-time histories (Zhao and Ji, 2018). For example, the axon-based and baseline models yielded very similar nodal responses for the cadaveric impacts, and these were reflected in the CORA scores. However, they differed significantly in strain outputs, and these differences were not reflected in the CORA score. This discrepancy is vital as most injury metrics (e.g., MPS and CSDM) are strain-based metrics.

3.4.6 Summary

In summary, this chapter developed an anisotropic and heterogeneous brain model by explicitly incorporating axonal fibers as embedded cable elements into the previously validated brain model. The initial evaluation demonstrated good biofidelity, a more comprehensive

evaluation of the newly developed human model using the latest biomechanical data is provided in Chapter 4. The novel method presented to incorporate FE meshes of highly complex tractography into the brain model provides advantages over the traditional (implicit) method that oversimplified the fiber network. The framework presented can also be generalized to include other mesoscopic anatomical details in finite element models without additional mesh generation.

CHAPTER 4 : EVALUATION OF HUMAN BRAIN FINITE ELEMENT MODEL

In Chapter 3, a method for modeling axonal fiber tracts in the brain FE model was developed. The human brain FE models were partially evaluated with legacy brain deformation data. Recently, the advancement of experimental methods enhanced our understanding of brain deformation under rotational loads and thus enables a more comprehensive evaluation of the biofidelity of computation models. The objective of this chapter was to extensively evaluate both the baseline human model and newly developed axon-based human model for brain deformation under a variety of loading conditions.

4.1 Introduction

FE models of the human brain and head are powerful tools for studying brain injury and have been increasingly used over the past few decades (Gabler et al., 2016; Giordano and Kleiven, 2014a; Ji et al., 2015; Sahoo et al., 2016; Sanchez et al., 2018; Takhounts et al., 2008). Although these computational models can accurately capture macroscopic brain anatomy for the general population, the sophisticated material properties of the brain tissue (Zhao et al., 2018) and various numerical modeling techniques (Giudice et al., 2018) may result in considerable variability in the performances and injury prediction. Therefore, the biofidelity of these models needs to be evaluated with experimental data before applying them in the TBI studies.

Early FE models were evaluated with impact-induced cadaver intracranial pressure (Nahum et al., 1977; Trosseille et al., 1992). Later analysis has revealed that this type of evaluation was insufficient and probably unnecessary (Zhao et al., 2015). Due to the nearly incompressible nature of brain tissue, the intracranial pressure responses were essentially hydrostatic for most blunt impacts relevant to real-world events (with a duration longer than 2 ms) and not affected by

other assigned material properties in the computational models. Therefore, efforts shifted towards studying brain deformation (or relative motion between the brain and skull) when the head was in motion. In-plane brain motion was measured using high-speed biplanar X-ray and neutral density targets (NDTs) for 17 human cadaver subjects (Hardy et al., 2007, 2001) while the re-pressurized head and neck complexes were subjected to frontal and occipital impacts. For decades, this set of two-dimensional brain displacement data was widely used for the development and validation of human brain FE models, although they were not "totally suited" or "designed" for model evaluation (Yang et al., 2006). Previous validation studies have demonstrated that even the state-of-the-art brain FE models performed poorly to reproduce the experimental NDT measurements (Giordano and Kleiven, 2016; Miller et al., 2017). Recently, Alshareef et al. (2018) measured the 3-D in-situ brain deformation (displacement) under rotational loading of the head utilizing sonomicrometry. These tests were conducted in a well-controlled pure rotational boundary condition with high repeatability to obtain validation targets for brain FE models, which provides significant advantages over previous experiments and enable comprehensive evaluation for the computational models. Established validation protocols (Giordano and Kleiven, 2016; Miller et al., 2017) to assess the biofidelity of FE models should also be re-investigated to compare with the new 3-D brain deformation data.

Given that brain FE models usually utilize strain measures such as MPS and CSDM to estimate brain injury (Gabler et al., 2016; Takhounts et al., 2013), evaluation against experimentally observed tissue strains in the whole brain are much-needed. However, the resolution of the neural targets implanted in the cadaver brain was too sparse to provide strain data with good quality (Zhou et al., 2018). To date, well-characterized strain response of the brain was only available at low-severity impacts measured using tagged MRI for human volunteers (Chan et

al., 2018; Feng et al., 2010; Knutsen et al., 2014; Sabet et al., 2008). Nevertheless, FE models should be able to predict biomechanical responses under a wide range of loading conditions; *in vivo* human data measured at non-injurious impacts can be used in conjunction with cadaveric *in situ* data to evaluate computational models.

The objective of this study was two-fold. The first goal is to evaluate the baseline model and the axon-based model using the most recent biomechanical brain deformation data under a wide range of loading conditions. Second, we further investigated the questions inherent in model evaluation studies, including effects of brain sizes, brain shapes, and choices of receiver locations on evaluation results, the biofidelity for specific brain regions, and suitable evaluation protocol in utilizing newly collected experimental data. The findings would guide the continual development of FE models and the future direction of collecting experimental data for model evaluation, and thus would facilitate developing the next generation of brain computational models.

4.2 Methods

4.2.1 Nodal Displacement Evaluation

FE Models were first evaluated with *in situ* brain displacement of six postmortem human surrogates under rotational loading (Alshareef et al., 2018). Each specimen was implanted with 24 neutrally-dense sonomicrometry crystals to track motion in the whole brain. Each specimen was tested at least 12 times with four different combinations of pulse magnitude and duration in 3 different rotational directions. The experimental conditions and specimen information are summarized in Table 4-1.

Table 4-1. Experimental conditions and specimen information.

Subject	**846**	**896**	**900**	**902**	**903**	**904**
Sex	Male	Female	Female	Female	Female	Male
Age	53	57	66	61	80	67
Receiver Location	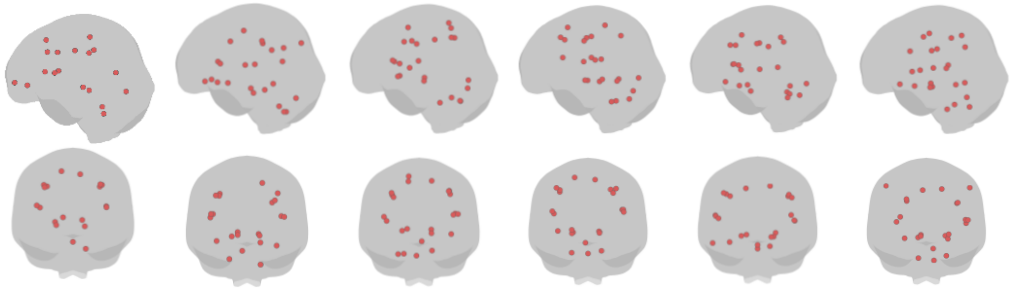					
Brain Mass (kg)	1.265	1.205	1.340	1.295	1.110	1.490
Brain Volume (cm^3)*	1442	1435	1558	1481	1298	1692
Test Matrix	12 test conditions, consisting of three directions (X, coronal; Y, sagittal; Z, axial) and four pulses characterizing using peak angular velocity and durations (20 rad/s and 30 ms, 20 rad/s and 60 ms, 40 rad/s and 30 ms, 40 rad/s 60 ms). These test conditions were hereafter referred to as 'X:20-60', 'X:20-30', 'X:40-60', 'X:40-30', 'Y:20-60', 'Y:20-30', 'Y:40-60', 'Y:40-30', 'Z:20-60', 'Z:20-30', 'Z:40-60', 'Z:40-30'.					

* Intracranial volume calculated based on CT.

For each specimen, subject-specific brain FE models were respectively derived from the standard baseline model, and the axon-based model (representing the 50^{TH} percentile male) based on CT scans using the same morphing technique described in Chapter 3 (Park et al., 2017). The subject-specific brain FE models would match the external geometry of the brain with the experimental specimen (Figure 4-1). The nodal representation of the corresponding crystal receiver in the subject-specific brain FE models was chosen by finding the nearest node.

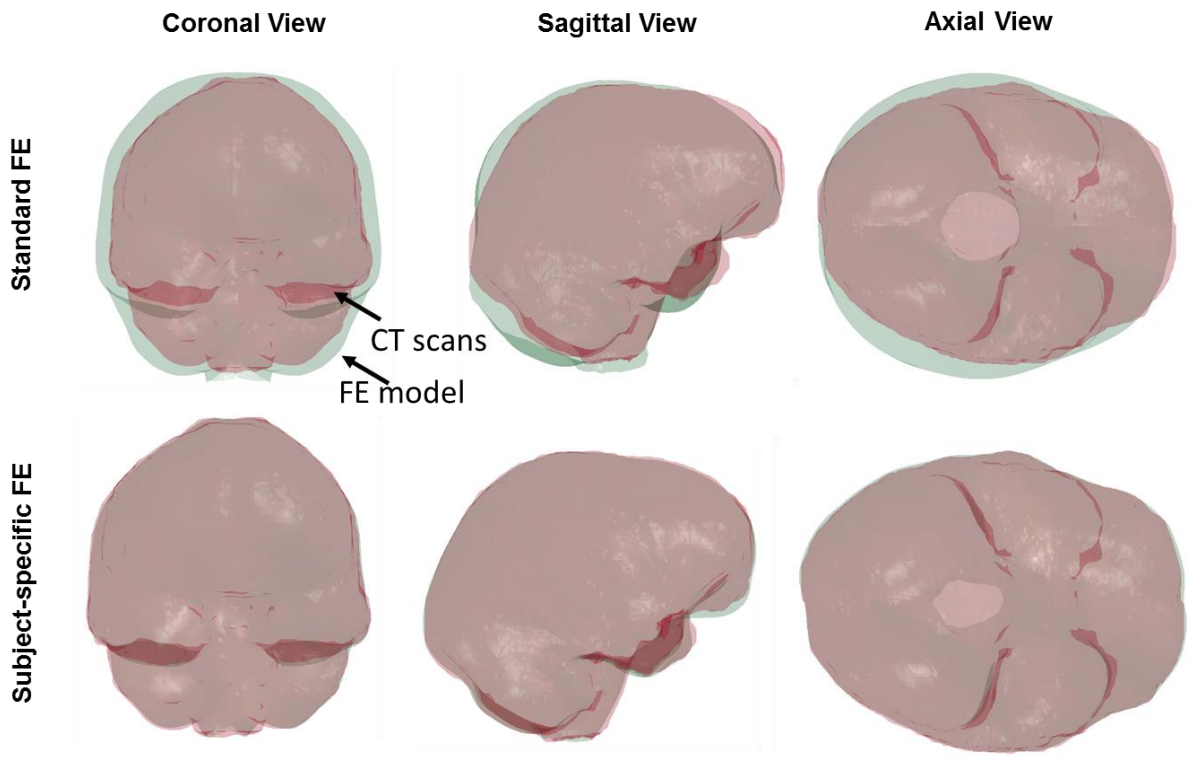

Figure 4-1. Subject-specific brain FE models for evaluation (subject 903).

4.2.2 Objective Rating System

CORA (CORrelation Analysis) objective rating system (Gehre et al., 2009) was previously recommended (Giordano and Kleiven, 2016; Miller et al., 2017) as a quantitative method to compare the predicted 2-D displacement-time histories to the experimental measurements. In this study, the predicted displacement-time histories of the relevant nodes were compared with the experimental measurements in three Cartesian components for each evaluation case. The *in situ* tests performed were uniaxial rotation with primary deformation in a certain plane, while CORA was unable to differentiate the differences in the magnitudes of the three components. Therefore, a weighted averaging was applied to obtain a single representative objective rating for each 3-D signal (Davis et al., 2016). The weighted CORA (WCORA) score was calculated by weighting the component CORA scores ($CORA_{x,y,z}$) by the peak-to-peak displacement values of motion in the three axes (d_x, d_y, d_z) from the same signal as per Equation [4-1]. For each validation case, an

overall score was computed by averaging the individual signal scores (mWCORA). However, it may be necessary to discriminate between signals of varying magnitude to provide a clearer picture of model behavior. This is particularly important for signals of low magnitude which can register artificially low scores. So, a second overall score (wWCORA) for each case was provided, per Equation [4-2] , by weighting the individual signals with peak-to-peak displacement (pp) defined as the maximum point-to-point displacement during the trajectory of each receiver.

$$WCORA = \frac{d_x \times CORA_x + d_y \times CORA_y + d_z \times CORA_z}{d_x + d_y + d_z} \quad [4\text{-}1]$$

$$wWCORA = \frac{\sum_{i=1}^{n}(WCORA_i \times pp_i)}{\sum_{i=1}^{n}(pp_i)}, \quad n\text{: number of receivers} \quad [4\text{-}2]$$

4.2.3 Effect of Brain Anthropometry

In addition to the subject-specific evaluation analysis, different evaluation methods were explored. Given that the sizes of the cadaver brain in these experiments (Table 4-1) were quite different from one another and from the FE model representing the 50th percentile male (volume:1569 cm^3), it was motivation to investigate the effect of brain size and shape on brain deformations. Historically, cadaver head (not brain) width and length dimensions are the only anthropometric measurements provided from the legacy experimental study (Hardy et al., 2007, 2001); the sizes of the brain were often unknown, and corresponding NDT locations in FE models were difficult to determine. Based on previous evaluation studies, one method would utilize the absolute coordinates of the NDT position provided in the experimental study in reference to the center of gravity (CG) of each cadaver head to identify the corresponding node in the standard brain FE model (referred to as the 'absolute' method). Another method would use the relative coordinates based on the maximum length (x), width (y), and height (z) of the head to identify the corresponding node (referred to as the 'relative' method). The results using those alternative

evaluation methods were compared to the standard morphing method. The analysis was performed using the original axon-based model for the representative case (subject 903). The representative specimen was chosen because her anthropometric measurements had the most substantial differences when compared to that of the brain FE model (Figure 4-1).

4.2.4 Strain Evaluation

In addition to the nodal displacement evaluation, the strain responses of FE Models were further evaluated with human brain deformation during mild angular acceleration (approximately 200 rad/s^2) measured *in vivo* by tagged magnetic resonance imaging (Chan et al., 2018). The multislice in-plane Lagrangian strain fields were measured for 34 healthy human volunteers under axial rotation (Figure 4-2). The resolution of the strain fields was based on 1.5 by 1.5 mm^2 voxel with 8 mm thick slices. Head kinematics and strain maps were provided for a representative subject which was chosen based on the criterion that the area fraction at the 3% threshold of the peak strain was closest to the mean value across all subjects. FE simulation was performed for both the baseline model and axon-based model to compare with the representative subject. The maximum Lagrangian shear strain maps were visually evaluated, and cumulative strain results were compared with experimental results using the same 3% threshold.

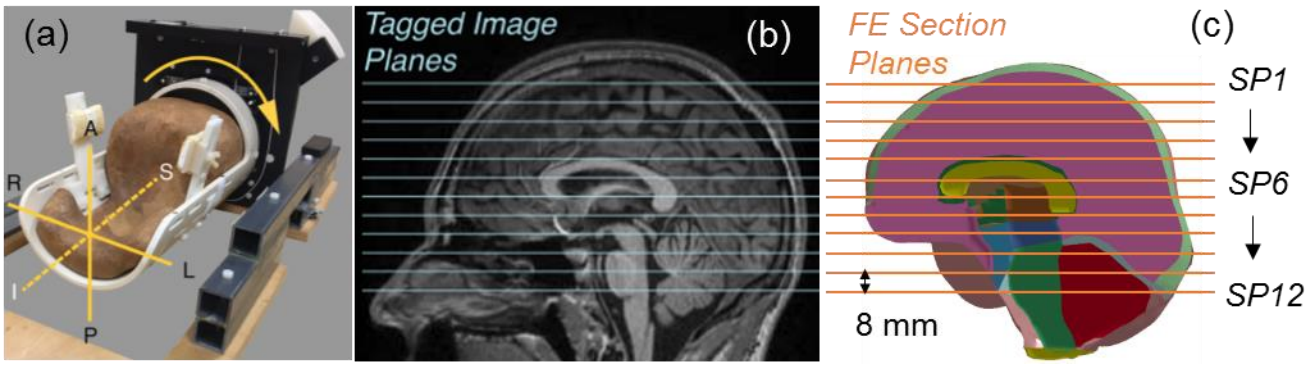

Figure 4-2. In vivo test conditions and data acquisitions. (a) Head axial rotation device showing the rotation direction (arrow) for tagged MRI acquisitions (Chan et al., 2018); (b) T1-weighted image showing axial tagged image planes of 8 mm thickness; (c) FE section planes to match the image planes.

4.3 Results

4.3.1 Subject-Specific Displacement Evaluation

Exemplar triaxial nodal displacements for the baseline model and axon-based model are shown in Figure 4-3, and are compared to the experimental displacements for corresponding crystal receivers. Figure 4-4 compares the biofidelity of the baseline model and the axon-based model per CORA scores. Overall, the axon-based model reported a higher mWCORA score (0.590 $\pm$ 0.048) for all the subjects than the baseline model (0.534 $\pm$ 0.049). The wWCORA scores were slightly higher than the mWCORA scores by 0.032 $\pm$ 0.022, as given in Table A1 (Appendix A), but captured similar discrepancies between the performance of these two FE models.

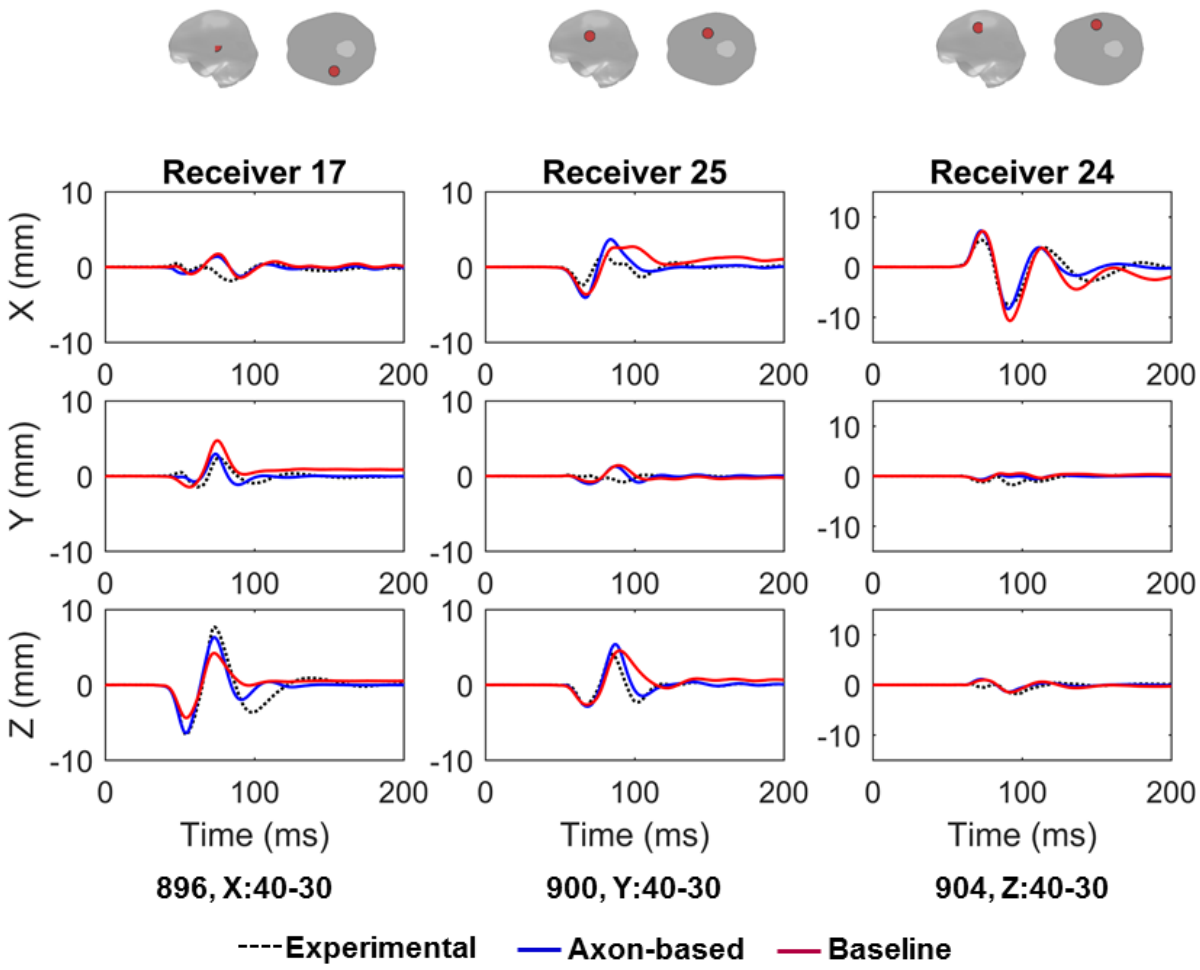

Figure 4-3. Example relative brain-skull displacements comparisons.

4.3.2 Different Displacement Evaluation Methods

Figure 4-5 shows different WCORA scores and different nodal displacement for example receiver locations by reason of different evaluation methods. Nodal displacements calculated using different evaluation methods were inconsistent. It was difficult to ascertain which method was more 'biofidelic' considering that they had similar mWCORA scores.

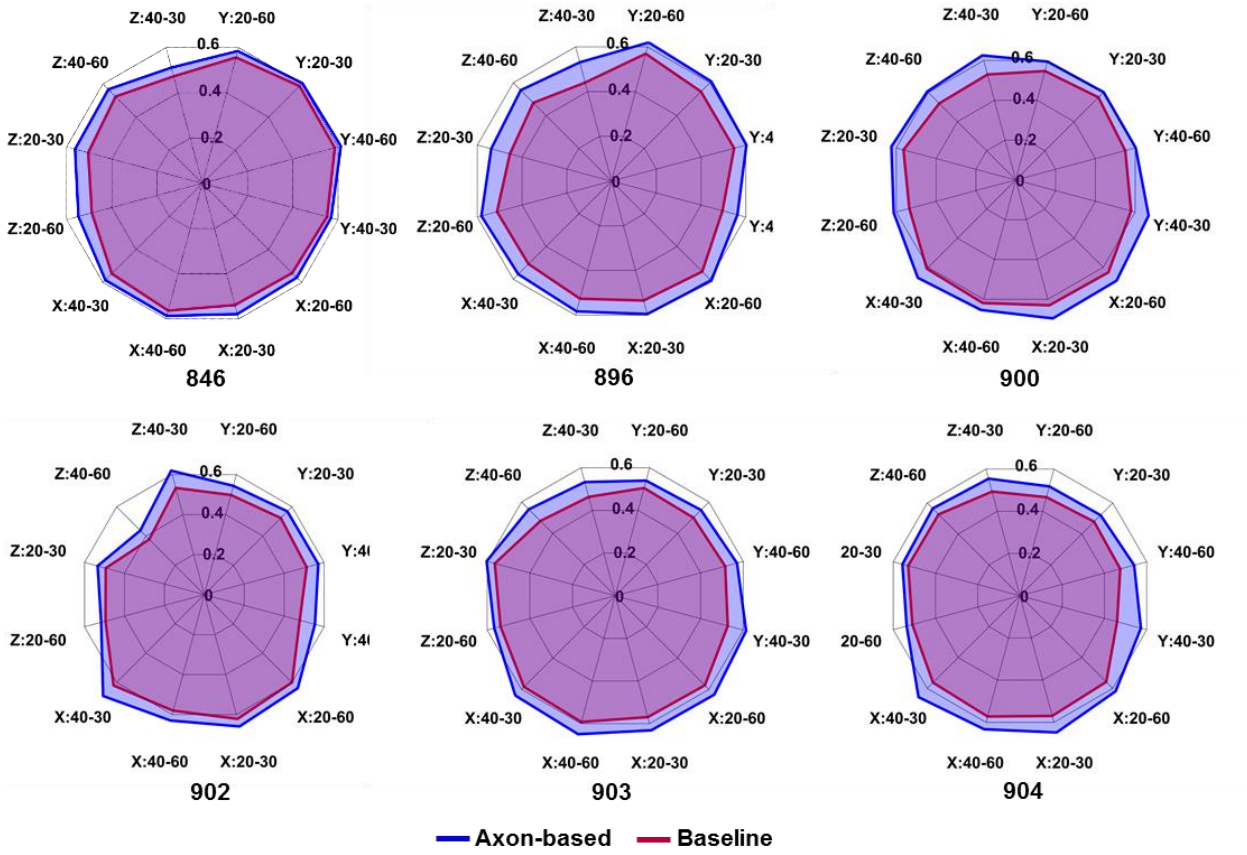

Figure 4-4. Performance of the axon-based and baseline models quantified by mWCORA scores.

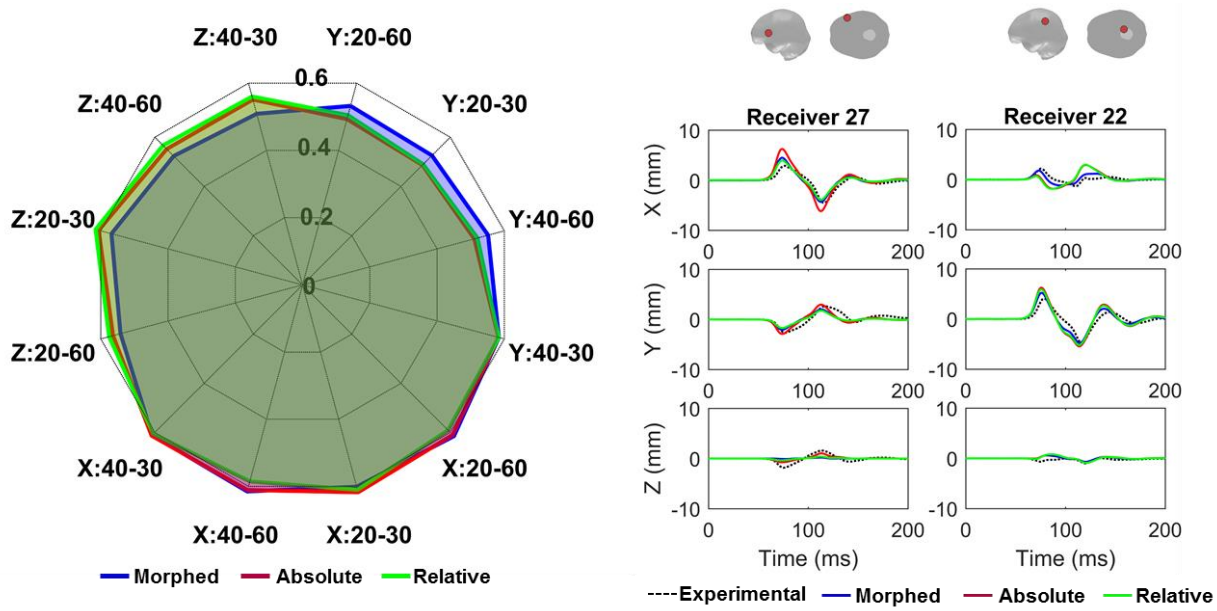

Figure 4-5. Effect of different methods on nodal displacement evaluation for specimen 903; mWCORA scores (left) and example nodal displacement curves for Z:40-60 (right).

4.3.3 Strain Evaluation

For low-severity impact, the two FE models produced similar patterns of shear strains. Figure 4-6 compares the estimated shear strain patterns with those measured by tagged MRI in the experiment at peak deformation. Similar patterns and magnitudes of shear strains were observed for the cerebrum region between the simulation and experiments, and the cortical gray matter consistently experienced the highest shear strains. The inferior region of the brain (cerebellum and brainstem) showed stiffer responses compared with the *in vivo* human subject, but the magnitude of tissue deformation was much smaller than those in the cerebrum.

The whole brain, cortical gray matter, and deep gray matter in both FE models experienced similar fractions of strain with the experimental measurements, while the white matter experienced a higher amount of deformation in both FE models (Figure 4-7). The inconsistency in the whiter matter strain was likely due to the lack of consideration of the subject-specific internal anatomy of the brain (e.g., the size of the ventricles). Considering that the noise inherent to the tagged imaging and image analysis methods (the precision of the strain measurement was estimated to be around 1% strain, Chan et al., 2018), the strain prediction from both the baseline and the axon-based model could be deemed as a good match to the experimental data. However, it was difficult to ascertain which model was more "biofidelic," despite some observed differences.

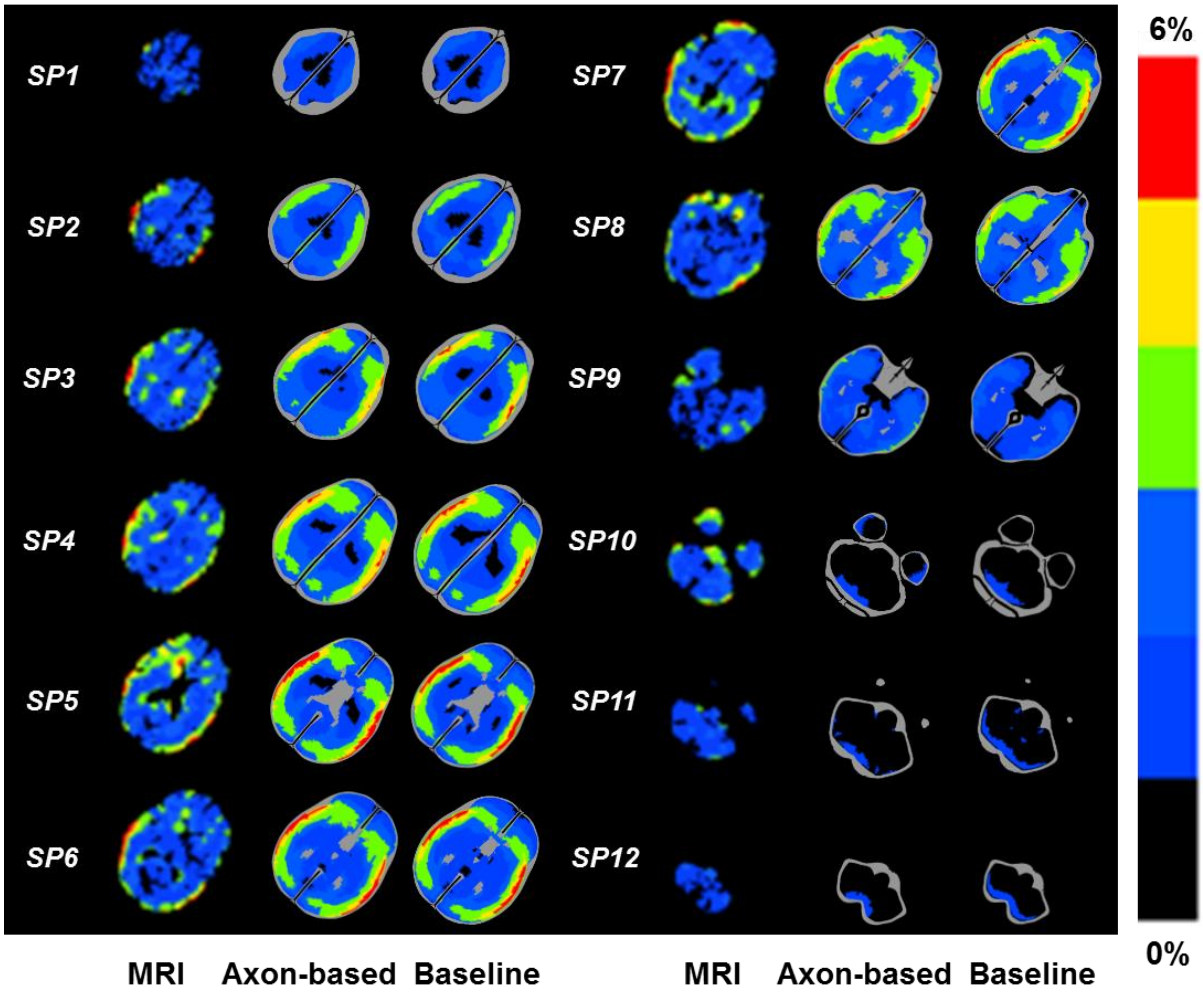

Figure 4-6. The peak experimentally measured in-plane Lagrangian shear strains (MRI) on axial planes in comparison with maximum Lagrangian shear strain estimated by using the baseline model and the axon-based model.

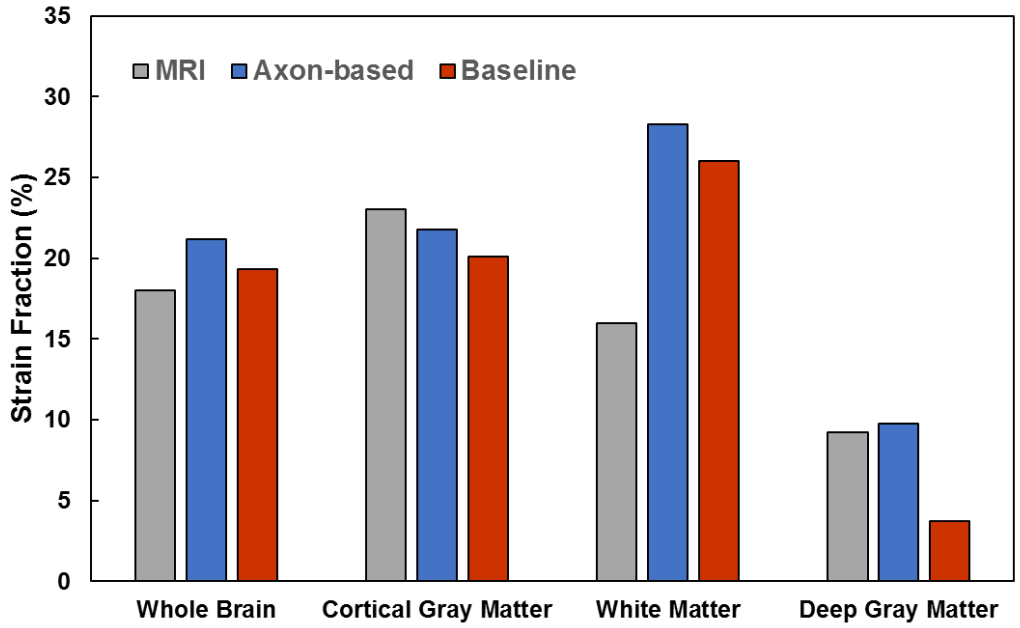

Figure 4-7. Comparison of strain fractions measured by MRI and FE simulations. Strain fraction was computed for a threshold of 3% absolute strain in the whole brain and tissue types of interest.

4.4 Discussion

A comprehensive evaluation study was performed on two state-of-the-art brain FE models. The simulation results were compared with experimental data, which contained a total 1652 nodal displacement curves of 139 receiver positions at high-severity impacts and 12 axial strain maps at low-severity impacts. Based on the evaluation results, the axon-based model consistently showed a better correlation with the experimental measurements than the baseline model between different specimens.

4.4.1 Experimental Dataset

The head kinematics of the evaluation data in this chapter were purely rotational with well-controlled boundary conditions, whereas previous validation/evaluation studies (Giordano and Kleiven, 2016; Miller et al., 2017; Zhao and Ji, 2018) utilized data from a series of impacts performed by Hardy et al. (2001, 2007) with resulting linear and rotational head kinematics. The

performance of FE models evaluated with Hardy's data was always inconsistent regarding different cases, in particular, different models performed better under different experimental conditions, with no single model consistently performing best, as illustrated in Figure 3-9 (Chapter 3). This inconsistency was likely due to the inconsistencies of the experimental data themselves. The neck was constrained in the Hardy studies while the head was impacted. A constrained boundary condition at the neck could potentially influence the deformation of the inferior regions of the brain caused by pulling through the cervical spine and spinal cord (Alshareef et al., 2018). This is evident as the NDTs markers in the inferior regions of the brain experienced unusually large displacement (Figure 4-8). However, this boundary condition is difficult to reconstruct without the correct modeling of the craniocervical junction and thus has never been considered in previous validation studies. In this evaluation study, the boundary condition of the head was straightforward and easy to reconstruct through simulation.

Another common limitation of existing evaluation studies was the lack of precise representation of the brain morphology of experimental subjects and the accurate location of the markers. As illustrated in Figure 4-5, this factor would contribute to the responses of individual markers/receivers, but systematically the subject-specific model didn't predict more biofidelic responses than the standard male 50th model per CORA. The benefit of the subject-specific model was not shown, likely due to the lack of consideration for other variabilities in the human brain such as the anatomy of the brain and the material properties. The morphing techniques adopted to generate the subject-specific model can only account for the external shape of the brain. Converting image voxels of the brain directly into hexahedral mesh elements (Miller et al., 2016) would potentially capture the internal anatomy of the individual brain, while the effect of detailed anatomy on biomechanical responses remains to be investigated.

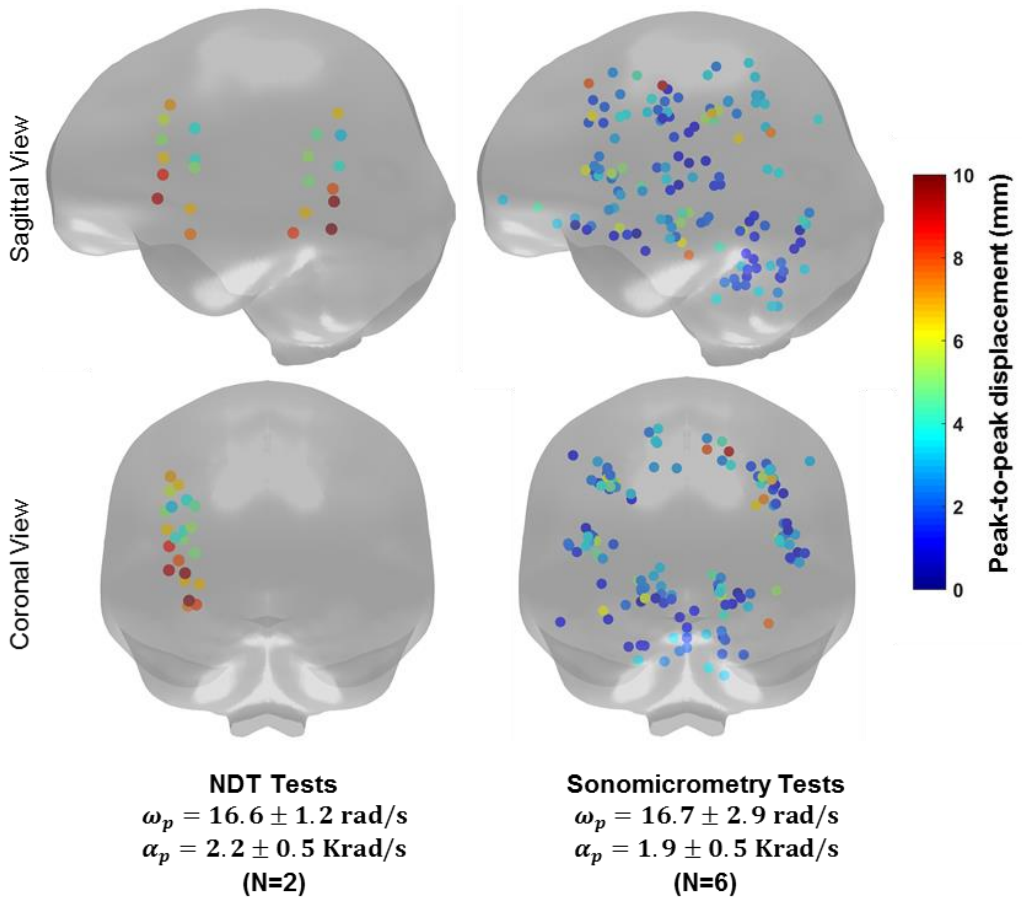

Figure 4-8. Comparison of the peak-to-peak deformation between NDT tests (Hardy et al., 2007, 2001) and sonomicrometry tests (Alshareef et al., 2018) under sagittal rotational motions at similar loading severity.

4.4.2 Regional Performance

Historically, NDTs were sparsely measured and did not have sufficient spatial resolution to evaluate the biofidelity of the model per region. The evaluation data collected in the recent study (Alshareef et al., 2018) enable us to investigate the regional performance of the FE models for the first time.

Both the *in vivo* test (Figure 4-6) and *in situ* tests (Figure 4-9 (a)) showed that there was a spatial dependence of brain deformation, with receivers in the inferior brain regions, including the cerebellum and brainstem, experiencing low deformations. Both FE models were able to capture this spatial pattern of deformation. Interestingly, the spatial distribution of the WCORA scores

indicated poor biofidelity in the inferior region of the brain, as illustrated in Figure 4-9 (b) using the axon-based model results, although not shown, a similar pattern was observed for the GHBMC model. Both the relative error (Figure 4-9 (c)) and absolute error (Figure 4-9 (d)) of the peak-to-peak displacement between the axon-based model and the *in situ* subjects did not reflect this trend. CORA, as a biofidelity rating metric, accounts for both the shape and phase of the signal in addition to the magnitudes, the lower CORA scores were likely caused by the differences in shape and phase of the displacement curves between simulation and experiment. At the current stage of TBI research, magnitudes (e.g., peak strain) are still the quantity of most concerned, and the regional differences in model biofidelity might be overemphasized by CORA.

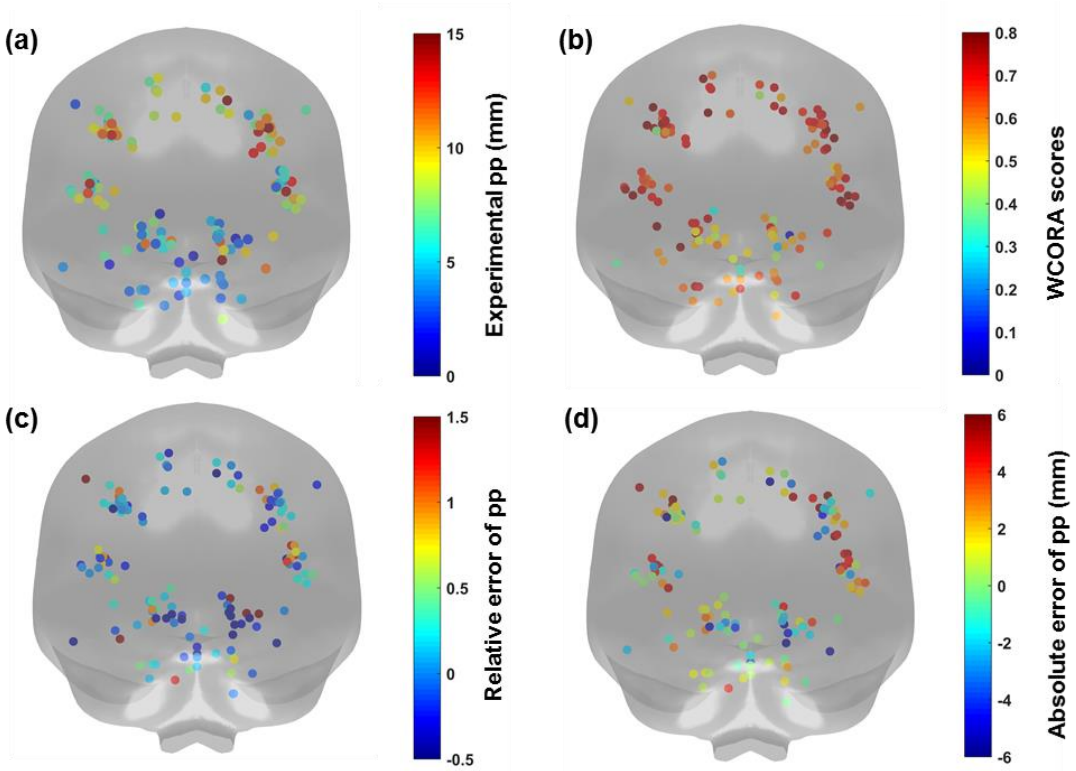

Figure 4-9. Spatial responses of the in situ experiment and the axon-based model under coronal rotation (40 rad/s,30 ms). (a) Experimental peak-to-peak displacement (pp); (b) WCORA scores per receiver for the axon-based model; (c) Relative error of peak-to-peak displacement (negative value means smaller deformation for the model); (d) Absolute error of peak-to-peak displacement.

Another uncertainty introduced into the biofidelity of the inferior region is the tentorium, whose mechanical properties were least understood in the brain along with other membranes. The falx and tentorium material properties for many existing FE models were derived from dura mater experimental tests (Galford and McElhaney, 1970) with an elastic modulus of 31.5 MPa. A recent study (Golman et al. 2013) reported a mean quasi-static modulus of 36 MPa under uniaxial tension tests with falx and tentorium specimens from post mortem human subjects, while the response was apparently not linear with dynamic modulus as high as 138 MPa on average. The thickness of the membrane would also affect its mechanical responses; a significant difference between the falx (0.45 mm) and tentorium (0.36) was found (Golman et al. 2013). Previous sensitivity studies have shown the importance of the tentorium, as well as other membranes, in affecting brain deformation (Hernandez et al., 2019; Ho et al., 2017; Lu et al., 2019). To improve the biofidelity of the brain FE model, the mechanical characterization and modeling of the membranes requires effort in the future.

4.4.3 Correlation between Displacement and Global Strain

The previous study suggested using strain responses, rather than displacement, to evaluate FE simulation results (Sullivan et al., 2015; Zhao and Ji, 2018). Without considering the quality of potential *in situ* strain data, the correlation between the maximum peak-to-peak displacement of the receiver locations and global strain measurement (maximum principal strain) is high (R^2=0.89), at least for simulation results. The relative lower correlation (Figure 4-10 (b)) between the experimental peak-to-peak displacement and MPS reflect the inherent biofidelity issue of the model (Figure 4-10 (c)). In this sense, the model evaluation study shows no preference for using strain responses or displacement responses. However, considering the low data quality of *in situ* experimental strain measurement (Zhou et al., 2018) and mesh-dependent strain output in current

brain FE models (Giudice et al., 2018), validation using nodal displacement-time histories instead of using experimental strain measurement is still a more robust approach for current FE models.

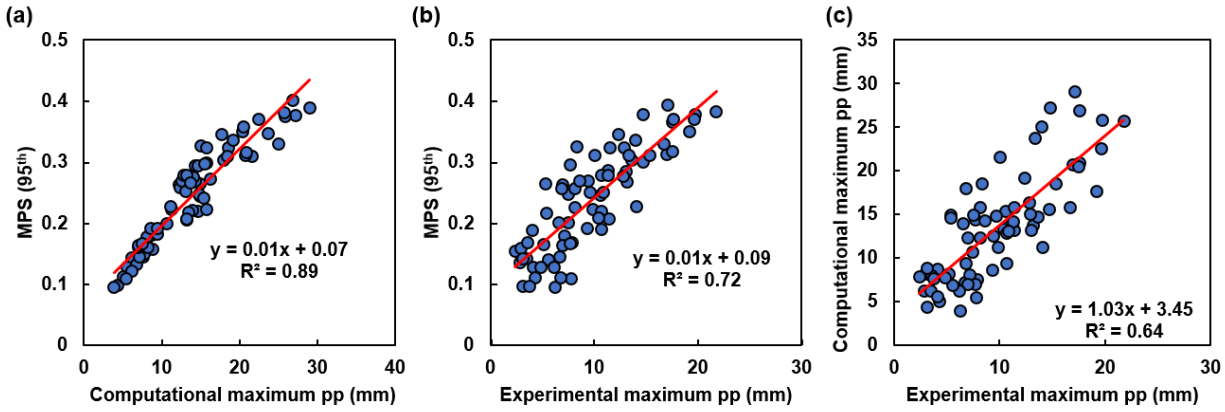

Figure 4-10. Correlation between the experiments and axon-based model simulations. (a) Correlation between computational maximum peak-to-peak displacement and MPS (95^{th}) predicted by the axon model in each loading case. (b) Correlation between experimental maximum peak-to-peak displacement and MPS (95^{th}) predicted by the axon model in each loading case. (c) Correlation of maximum peak-to-peak displacement between model prediction and experimental measurements in each loading cases.

4.4.4 Summary

In summary, the updated model demonstrated better biofidelity over the baseline model when simulating the latest human brain deformation data. These evaluations are a more demanding and much-needed verification process for the next generation of numerical models. Subject-specific assessment, with accurate geometry representation, did not improve the correlation between simulation and experiments. Future efforts should be focused on modeling precise internal anatomical details and enhancing the understanding of membranes, whose mechanical responses were rarely characterized, while expecting to have significant influences. The improved model will help advance the understanding of injury mechanisms and facilitate research in predicting and mitigating TBI.

CHAPTER 5 : NON-HUMAN PRIMATE FINITE ELEMENT MODELS

As a surrogate for humans, the most commonly used NHP models to study brain injury are the macaque (*Macaca mulatta*) and baboon (*Papio anubis*). As discussed in Chapter 2, the development of existing animal brain FE models is not as advanced as the existing human FE models, and only a few NHP FE models were available (Antona-Makoshi, 2016; Ng et al., 2017), which significantly hampers the application of animal data in the TBI study. To fill this gap and refine to a level commensurate with the state-of-the-art human brain FE models, the macaque and baboon FE models were developed and modified in a manner specifically intended to facilitate the study in this dissertation.

5.1 Introduction

To date, numerous human and animal brain injury models have been developed (Table 2-3 and Table 2-4). However, even human brain injury models "validated" against the same set of experiments produce (Hardy et al., 2007, 2001) predicted significantly discordant tissue-level responses under identical impact conditions (Miller et al., 2017). The technical gap between animal brain FE models and human models are even wider because of the paucity of NHP biomechanical data. The model inconsistency precludes effective comparisons among the simulation results for different models and brings uncertainties when applying animal-based findings to humans.

A critical contributor to such model inconsistency is the various numerical methods used by different developers, particularly, the choice of FE solver, FE mesh type, element size, element formulation, and hourglass control formulation. Order-of-magnitude differences in brain response would result from changing the characteristics of the numerical method, of which mesh type and mesh size were the most influential factor (Giudice et al., 2018). For modeling brain tissue, which

is nearly incompressible while can sustain large deformation, hexahedral elements are the commonly preferred mesh type (Table 2-3 and Table 2-4) because of their stability and capacity to compute accurate solutions. The desired mesh size, however, was not known and should be determined according to mesh convergence behavior. Mesh convergence studies (Giudice et al., 2018; Panzer et al., 2013; Zhao and Ji, 2019) of brain FE models were rarely performed or reported, notably lacking in terms of strain, which is most relevant to brain injury. Giudice et al. (2018) showed that a mesh resolution smaller than 1 mm was necessary to get within 10% of error for global MPS, while Zhao and Ji (2019) demonstrated that convergence on global MPS was approached using an average brain element size of 1.8 mm (similar mesh resolution to GHBMC). The desired mesh sizes for convergence might vary depending on other numerical characteristics, material models and loading conditions. Nevertheless, very small mesh size was required for human brain models to converge to a mesh-size independent strain value for injurious impacts, which is not feasible given the computational cost necessary.

Another important factor to the model response is the material model. Due to the complex nature of brain tissue, there is no consensus on what type of material constitutive model to adopt for characterizing brain tissue, (de Rooij and Kuhl, 2016) or what material coefficients to use for a given material model. Shear moduli reported in the literature vary by order of magnitude (Chatelin et al., 2010; Panzer, 2012), partially due to the tissue's viscoelastic behavior and the broad range of loading conditions in the literature. These variations in measured brain material properties could cause substantial disparities in predicted brain strains (Zhao et al., 2018).

The objective of this chapter is to improve the NHP brain model to a level corresponding to the state-of-the-art human brain FE models. Numerical methods and material model were investigated and determined based on the best knowledge. Mesoscale anatomical details (axonal

tractography) featured with embedded 1-D elements were incorporated into the model to improve the biofidelity and facilitate the continual research on tissue-level injury metrics.

5.2 Macaque Model

A previously developed rhesus macaque (*Macaca mulatta*) brain FE model was extensively modified to harmonize with the discretization method (e.g., mesh type, number of elements), anatomical features (axonal tract information), and brain tissue constitutive models used in the human brain model, as detailed in the following subsections.

5.2.1 Baseline Model

The baseline monkey brain model was extracted from a model of the head and neck complex, which was previously developed (Antona-Makoshi, 2016; Antona-Makoshi et al., 2013, 2012) by combining a rhesus monkey brain digital atlas in stereotactic coordinates, and an original set of CT scans and MRI from a Japanese macaque subject (*Macaca fuscata*). The brain model has 21,750 hexahedral elements of approximately 3 mm in total and includes macroscopic anatomical representation of the cerebrum, cerebellum, brainstem, corpus callosum, CSF, and membranes (falx, tentorium, pia, dura). The brain tissue was only calibrated with experimental data of compressive relaxation (Galford and McElhaney, 1970). The original model was generated based on a rhesus macaque and could also be applied to other macaque species (including *Macaque Fascicularis,* and *Macaque Fuscata*), because the brains of these species were sufficiently similar in anatomy and morphology to justify using the same brain template (Bowden and Dubach, 2000).

5.2.2 Mesh Consideration

Mesh size is an essential consideration in all FE applications and is intrinsically related to the accuracy of the FE solution in several ways. Therefore, mesh size should be an important

consideration when comparing results from different brain FE models. Ideally, FE simulations of two similar problems should give the same solutions if mesh size is 'equivalent'. However, the vast differences in brain size and external loading conditions between human and NHP brain models raise new questions. How should the mesh size of those models be compared? In other words, will the human FE model and NHP FE model with the same mesh size provide the same results? This was investigated using the sphere model representing a simplified skull-brain model.

Three sphere models discretized with hexahedral elements surrounded by a rigid outer shell were created. The identical solid material for all three models was based on elastic, homogeneous, isotropic material with reasonable properties ($\rho = 1.04\ \mathrm{gm/cm^3}$, $\mathrm{G} = 1\ \mathrm{kPa}$, $\upsilon \approx 0.5$) to mimic brain tissue responses under certain loading rate. The models were subjected to uniaxial rotational motion with ideally sinusoid angular acceleration at the outer shell. The magnitudes of the loadings for each model were determined per dimensional analysis. The standard under integrated formulations were used for all elements. All simulations were conducted with the same viscous hourglass control (IHQ = 3, in LS Dyna). Information regarding the dimensions, loading conditions, element count, and quality are found in Figure 5-1.

The MPS responses were illustrated in Figure 5-2. MPS distributions of the spheres with similar mesh density (a and c) are substantially different, while the spheres with the same number of elements (a and b) give equal strain distributions. Consequently, to reduce the influence of element size on the solutions of FE simulations, the human FE model and the NHP FE models should have a similar number of elements. The mesh-independent solutions also corroborate the difficulties of mesh convergence in modeling head impact.

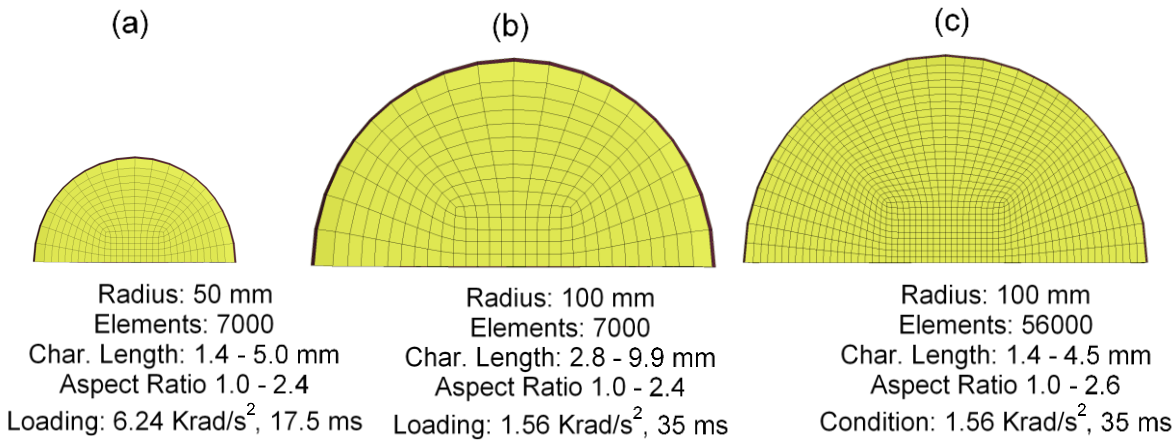

Figure 5-1. Mesh design and loading conditions for three sphere models.

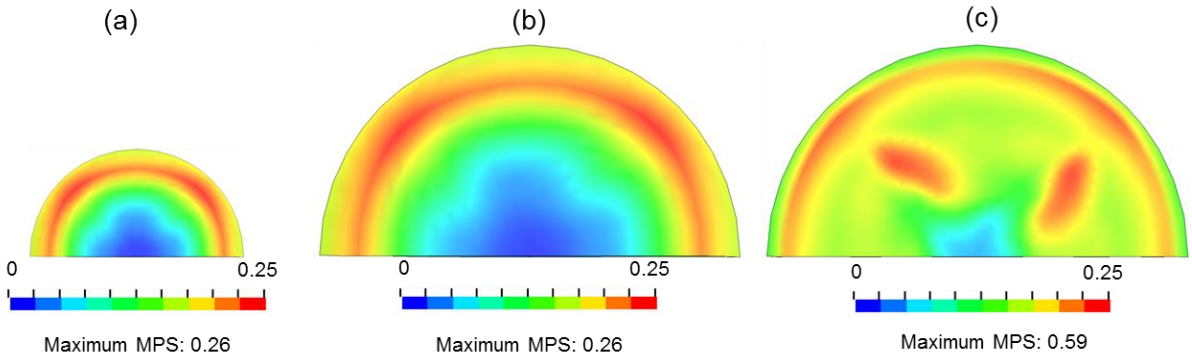

Figure 5-2. Maximum principal strain distributions at the center cross-section planes along the rotation direction for these three sphere models (symmetric to the center point).

5.2.3 Modeling Axonal Tractography

The same methodology developed in Chapter 3 was used to incorporate axonal fiber tract networks explicitly as 1-D cable elements into the macaque FE model, as highlighted in Figure 5-3. The axonal fiber tractography for the rhesus macaque brain was derived from a group-averaged diffusion tensor imaging (DTI) brain template, UWRMAC-DTI271. (Adluru et al., 2012). The template was generated from 271 rhesus monkeys, collected as part of a unique brain imaging genetics study. It is the largest number of animals ever used to create a computational brain template, which enables the generation of a template that has high image quality and accounts for variability in the species. Deterministic tractography was executed in an open-source diffusion

MRI toolkit (Camino) based on the FACT algorithm (Mori et al., 1999). The construction of the fibers was stopped either in correspondence of voxels with fractional anisotropy lower than 0.1 or when the curve direction changed more than 60 degrees in 1 mm.

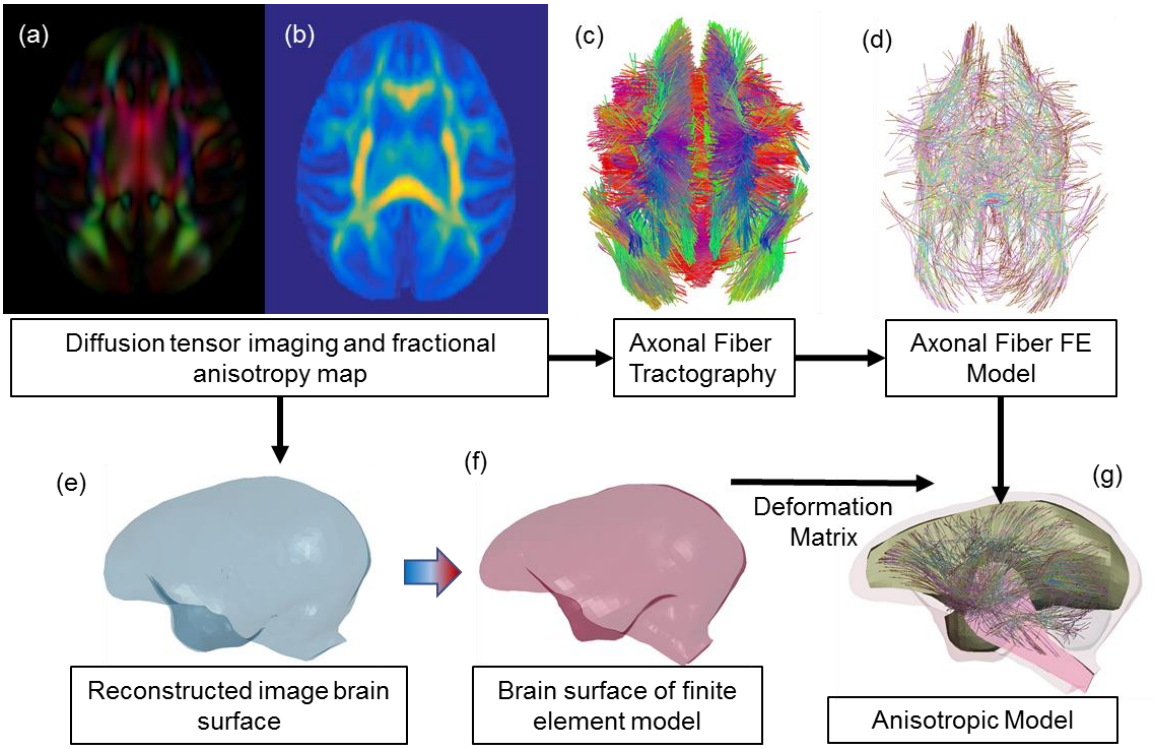

Figure 5-3. Modeling axonal tractography in non-human primate finite element model. (a) Diffusion tensor imaging; (b) Fractional anisotropy map; (c) Reconstructed axonal tractography; (d) Axonal tracts in 1-D cable elements; (e) Reconstructed 3-D brain surface of atlas brain; (f) Dura surface of the brain finite element model; (g) Finite element model embedded with axonal tracts.

5.2.4 Material Model

Mechanical characterization of NHP brain tissue models requires the development of constitutive laws calibrated with adequate experimental data to accurately relate tissue deformation to tissue stress. However, relevant experimental data is very limited in the literature. A brief overview of existing NHP tissue is summarized in this section. The emphasis is on comparing the properties of human and NHP brain tissue.

Estes and McElhaney (1970) found the response of the rhesus monkey was slightly stiffer than the responses of human brain tissue at comparable compression strain rates of 0.08, 0.8, 8,

and 40 s^{-1}. The significance of these differences is minor when the amount of variation for each type of tissue is considered (Figure 5-4). Dynamic characterization of both human and rhesus monkey brain was also investigated by experimental tests, as summarized in Table 5-1. Galford and McElhaney (1970) have reported on the creep, relaxation and free vibration characteristics of human and rhesus monkey brain. Significant differences have only been found for creep compliance curves for the human and rhesus monkey brain, but the discrepancy may be caused by the fact that the human brain specimens were tested at a significantly later time after death. The viscosity and bulk modulii of the human and rhesus monkey brain were later investigated by McElhaney et al. (1973), and no significant differences were found between the human and rhesus monkey brain. The dynamic shear properties of the human brain *in vitro* and of rhesus monkey brain, both *in vivo* and *in vitro*, were determined by Fallenstein et al. (1969) and Wang and Wineman (1972a, 1972b), but a direct comparison between human and rhesus monkey was not available because of the differences in loading conditions.

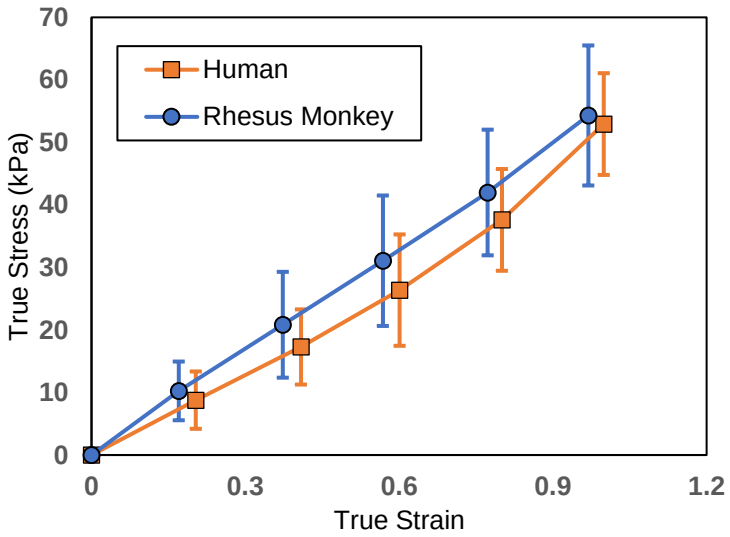

Figure 5-4. Compressive stress-strain relations for human and rhesus monkey brain tissue at a strain rate of 40 /s.

Table 5-1. Summary of mechanical properties of human and rhesus monkey brain tissue in the literature.

Test	Mechanical Properties	Human	Rhesus Monkey	Findings	Reference
Creep	Creep compliance $\mathrm{J(t)} = C_1 + C_2 \ln(t)$	$C_1 = 2.4$ kPa $C_2 = 0.18$ kPa	$C_1 = 2.9$ kPa $C_2 = 0.18$ kPa	Significant difference	(Galford and McElhaney, 1970)
Relaxation	Instantaneous modulus	$E_0 = 6.6$ kPa	$E_0 = 10.3$ kPa	No significant difference	(Galford and McElhaney, 1970)
Free vibration	Dynamic modulus $E^* = E_1 + iE_2$	$E_1 = 66.7$ kPa E_2 =26.2 kPa $\omega_f = 34$ Hz	$E_1 = 91.0$ kPa E_2 =53.8 kPa $\omega_f = 34$ Hz	Monkey brain is slightly stiffer and more viscous than the human brain	(Galford and McElhaney, 1970)
Capillary rheometer	Viscosity	4×10^{-3} Pa · s	5×10^{-3} Pa · s	No significant differences	(McElhaney et al., 1973)
Capillary rheometer	Kinematic viscosity	43 Pa · s	51 Pa · s		(McElhaney et al., 1973)
Bulk modulus	Bulk modulus	2.1 GPa	2.07 GPa		(McElhaney et al., 1973)

According to the above survey, the same hyper-viscoelastic constitutive model and brain material properties used in human brain modeling were applied, assuming the mechanical properties of primate and human brain tissue are similar.

5.3 Baboon Model

The newly improved macaque brain model was morphed to generate the baboon (*Papio anubis*) brain model using a morphing technique developed in Park et al. (2018) since brain anatomy is similar across these two species (Figure 5-5 (a)). First, the surface of the macaque brain was aligned and scaled to the target reconstructed surface of a group-averaged baboon brain medical image template (Love et al., 2016) using iterative closest point approximation (Besl and McKay 1992). Next, the macaque surface nodes were used as landmarks to map the macaque model to the baboon surface using Burr's elastic iterative registration method (Bryan et al. 2010) to match the external geometry of the two surfaces (Figure 5-5 (b)). The same transformation in this step was then applied to the macaque brain FE model, a thin-plate spline method with a radial basis function (Rohr et al. 2001) was used to interpolate and smooth the FE model to match the

geometry of the baboon brain. The results of the morphing are shown in Figure 5-5 (c), and the baboon brain FE model derived from the macaque brain model was able to represent the morphology of the template baboon brain sufficiently.

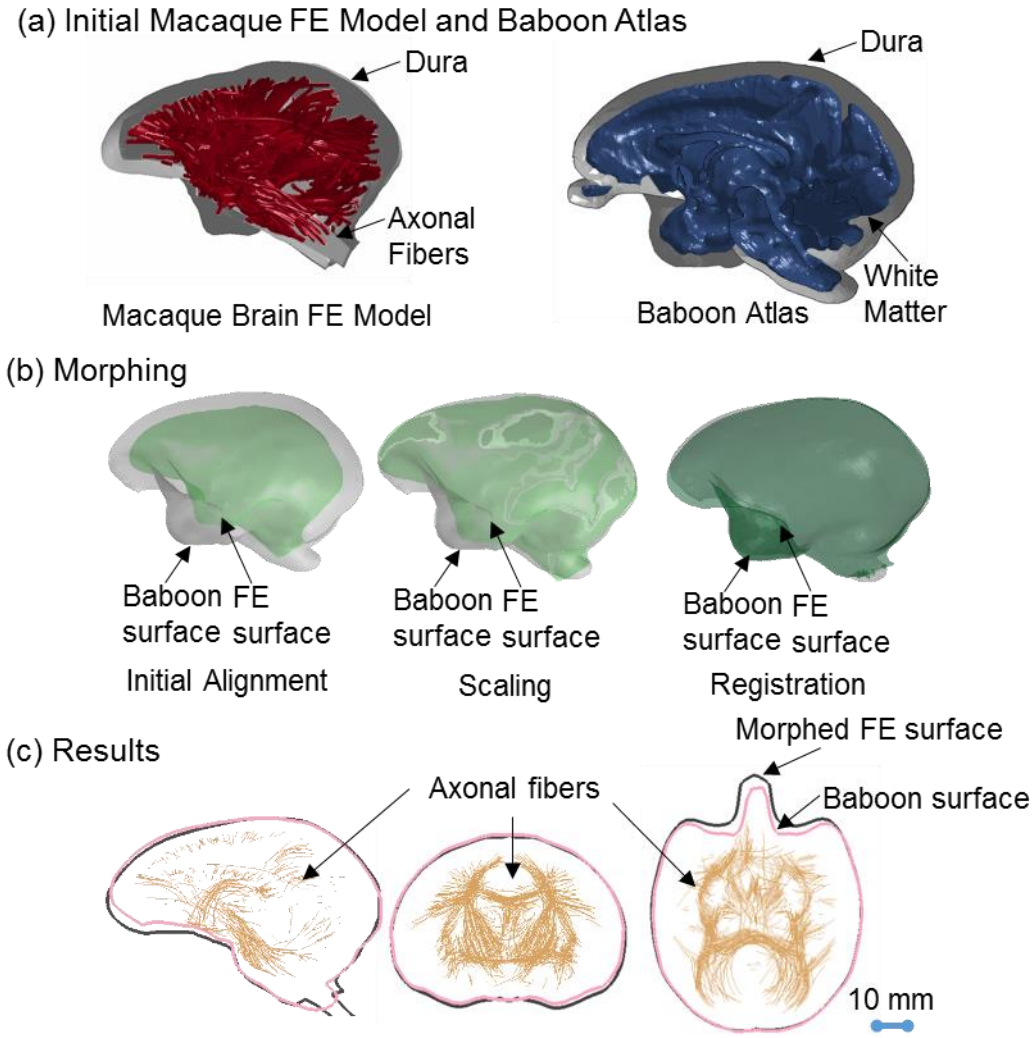

Figure 5-5. Morphing process and results. (a) An initial comparison between the macaque FE brain and the baboon atlas; (b) The morphing procedure; (c) Comparison between the morphed FE brain and the baboon atlas.

5.4 Brain Injury Simulation

To demonstrate the ability of the model and numerical stability, the newly developed baboon model was utilized to simulate experimental uniaxial coronal, sagittal and axial rotation. The loading pulse to the brain model was based on one of the cases initially performed by

(Gennarelli et al., 1982) and documented in Mendis (1992), as shown in Figure 5-6. The loading pulse caused severe disability for a baboon subject (brain mass: 160g) with prolonged traumatic coma (> 6 hours) and neuropathological evidence of DAI.

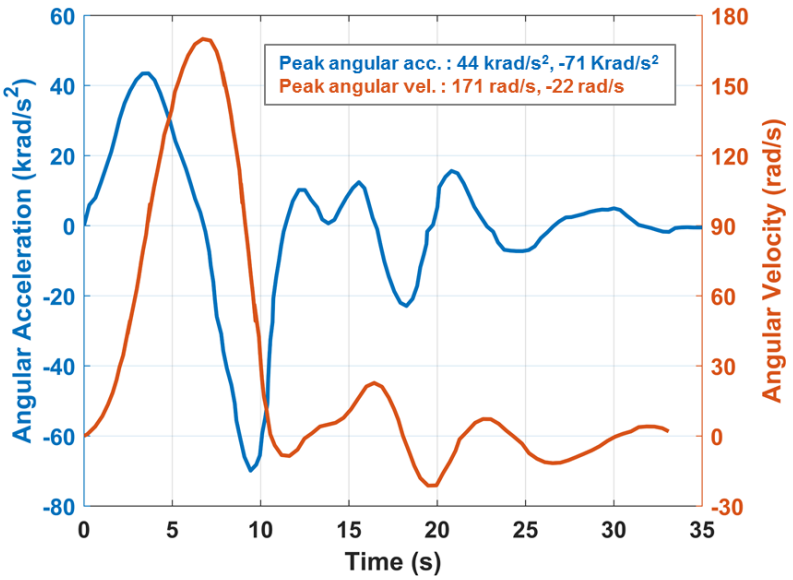

Figure 5-6. Loading pulse of the brain injury simulation, original case ID was B010 in Mendis (1992).

5.5 Results

5.5.1 Summary of Models

As illustrated in Figure 5-7, the newly developed brain FE models in this dissertation were summarized and compared with the axon-based human model. Three models were commensurate with each other in terms of macroscale and mesoscale anatomical details, the number of elements (5% difference), and mesh quality.

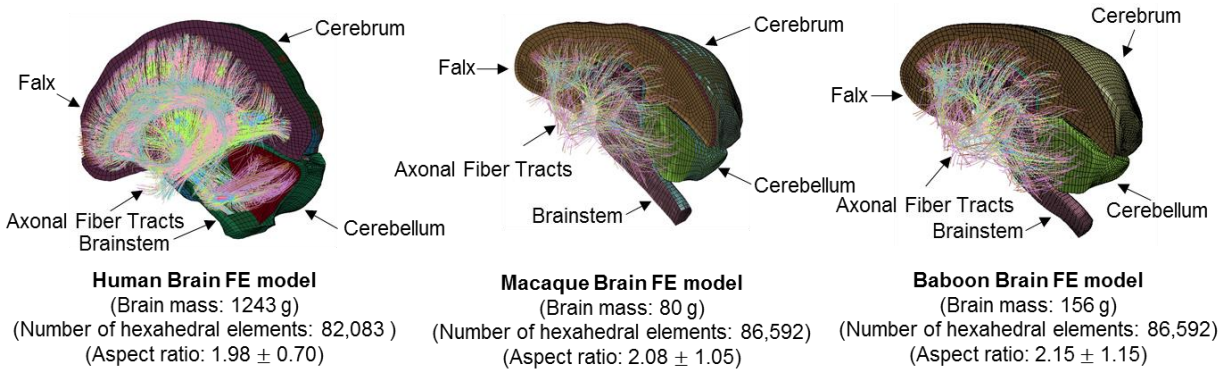

Figure 5-7. Brain FE models developed in this dissertation. They were modeled with similar numbers of hexahedral elements, mesoscopic details (axonal tracts), and same hyper-viscoelastic constitutive model.

5.5.2 Results of Simulations

Figure 5-8 shows the strain distributions in a certain plane for the baboon brain injury simulation at each rotation direction. The strain metrics, including MPS, MAS, and CSDM for interested regions were summarized in Figure 5-9. Although no experimental data were available to verify the absolute value of these metrics, the influence of the direction of head motion on regional responses tells an interesting story. The sagittal rotation induced a large amount of strain at parietal lobe on the cortex of the brain (not visible in the cross-section view) without the widespread deformation in the deep brain region. While the axial rotation induced a large amount of strain in deep gray or white matter region. In addition to large deformation in the central brain regions, the coronal rotation produced higher strain in the brainstem and cerebellum than the other head motion did.

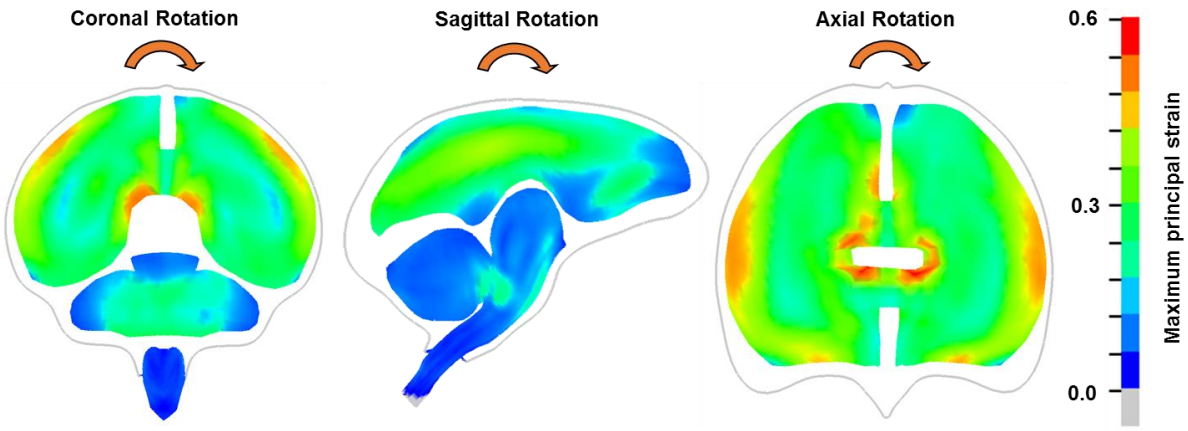

Figure 5-8. Maximum principal strain (MPS) distributions for the simulation of one NHP test to investigate the direction-dependent responses. For sagittal rotation, the plane with a maximum deformation response is not shown.

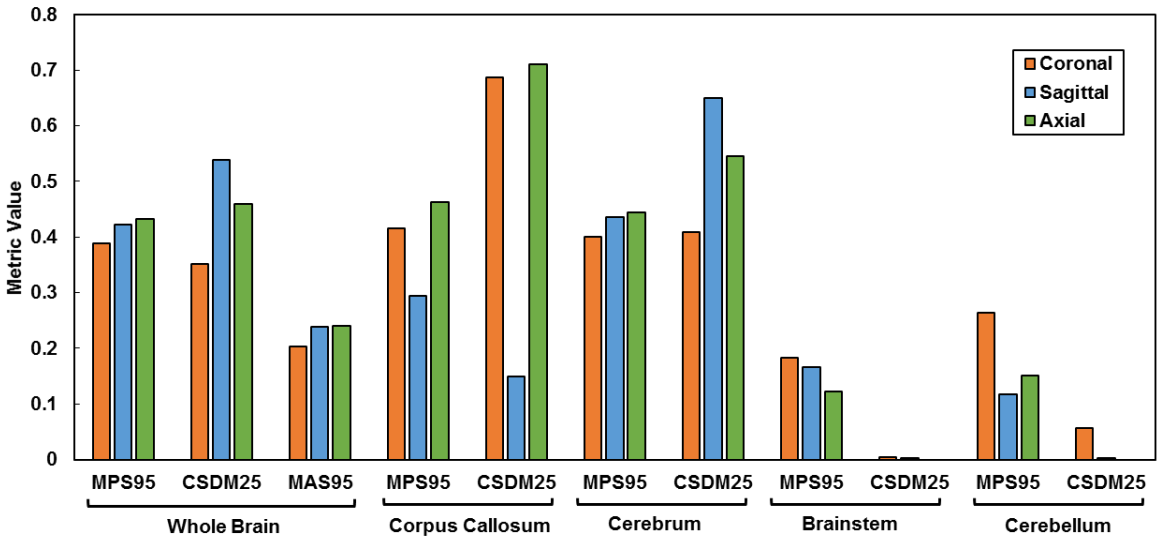

Figure 5-9. Comparison of the strain measurements between head rotational motions in each region of the brain.

5.6 Discussion

This chapter focused on developing NHP computational tools to facilitate the study in this dissertation. The macaque and baboon FE models were developed and modified in a manner to specifically harmonize with the state-of-the-art human brain FE models.

The most significant limitation of these NHP models is the absence of evaluation or validation due to the lack of biomechanical data. These basic constituents govern the response of

a computational brain model: model geometry, boundary conditions, numerical methods, and tissue material properties. Great efforts were made to reduce the influences of differences in numerical implementations (Giudice et al., 2018) and constitutive models (Zhao et al., 2018), and ensure the biofidelity of FE models without the demanding biomechanical data.

FE model simulation accuracy depends on mesh size, and in general, a more refined mesh (smaller mesh size) leads to a more accurate representation of the physics of the problem. A recent study (Giudice et al. 2018) showed that the human brain FE model results did not converge to a mesh-size independent value by a mesh resolution of 1 mm. There are currently no FE human brain models with element sizes smaller than 1 mm (Table 2-3). Conversely, mesh size should also be considered when comparing results from different models, especially when converged results cannot be reached. The existing NHP models and human models differ in terms of size and mass, and the loading conditions of NHP relevant to injury were also different from those of human. Mesh size, in a way, is also dimensional. Simple scaling arguments indicate that a similar number of elements (without large disparity in other numeric methods) should be maintained between NHP and human models to produce comparable strain and deformation results.

Utilizing the loading pulse of experimental baboon tests, the newly developed baboon model was applied to simulate uniaxial head rotation at three anatomical directions. Direction-dependent strain responses were observed for the different interested regions. In the central brain region, the higher strain was found in coronal and axial plane acceleration, while sagittal plane acceleration produces less deformation in the deep brain region. This corroborates the findings by Gennarelli et al. (1987), who assessed the influence of the direction of head motion on the amount and distribution of demonstrable axonal damage within the brain for comparable acceleration levels, and reported 56% (5/9) sagittal rotation had no evidence of axonal damage, 90% (9/10)

axial head rotation had evidence of corpus callosum/central brain axonal damage, whereas 89% (8/9) coronal rotation had axonal injury in the brainstem as well as in the central brain. Geometric constraints of the internal structure, such as falx, were believed to be responsible for these differences (Margulies, 1987; Mendis, 1992). All the subjects were injured in Gennarelli et al. (1987), so it is difficult to conclude which direction is more susceptible to injury. Another experimental head injury study with lateral impact using monkeys found tolerance to lateral head impacts was higher than sagittal impact tolerance (Sakai et al., 1982). In accordance with Sakai et al.'s findings, the injury simulation in this study did report lower global MPS, MAS, and CSDM for the coronal rotation.

In summary, two NHP brain FE models were developed in this chapter, considering the best knowledge of material properties and suitable numerical methods. Mesoscale axonal tractography was incorporated into these models to improve their capabilities of investigating novel tissue-level injury metrics. The newly developed model was used to study the direction-depend tissue responses and correlate well with the experimental injury findings. Experiments to characterize brain deformation for the animal were, in general, demanding, for model evaluation and for enhancing the understanding of the link between deformation and clinic outcomes.

CHAPTER 6 : INVESTIGATION OF CROSS-SPECIES SCALING METHODS

Scaling methods are typically used to correlate animal exposure data to humans, specifically to find the equivalent biomechanical impact conditions that result in similar tissue-level mechanical responses for different species, but the existing scaling methods have not been validated and fail to account for the anatomical and morphological complexity of the brains for different species. In this chapter, the relationship between head impact condition and brain tissue deformation was investigated using advanced computational models developed in previous chapters. The objective was to evaluate existing scaling methods in predicting similar biomechanical responses in the different species and to improve how animal data is scaled to humans. The traditional mass-based scaling method, inertia-based scaling, an optimization-based method, and a novel frequency-based scaling method were investigated using finite element models of brains. The performances of scaling methods were then assessed by comparing the brain strain results of different species using both idealized and real-world head impact pulses. The findings of this study enable better interpretation of mechanical-trauma responses obtained from animal data to the human, thus effectively advancing the development of human injury criteria and eventually mitigating the cost and burden of TBI.

6.1 Introduction

Despite decades of research conducted to understand the mechanisms of TBI in the human brain, there are still no universally accepted biomechanical brain injury criteria or thresholds, due in part to the uncertainty in scaling methods between animal models and humans. Animal models are valuable surrogates for humans and are critical for advancing the field's knowledge of TBI (Abel et al., 1978; Gennarelli et al., 1982; Olszko et al., 2018; Ommaya and Hirsch, 1971; Ono et al., 1980). They allow for the rigorous investigation of the biomechanical thresholds and the

pathophysiological mechanisms of TBI using controlled and highly efficient protocols (Shultz et al., 2017). However, the mechanical response associated with trauma characterized in these animal studies is difficult to translate to humans considering the differences in brain morphology and physiology across species (Panzer et al., 2014). Motivated by the goal of developing more effective helmets and automotive countermeasures for TBI, animal data has been used to help inform kinematic-based injury criteria, which predict brain injury using the kinematic responses of the head during impact (Takhounts et al., 2013). To accurately correlate animal data to human data, the equivalent human head impact kinematics that result in similar brain deformation to that of animals need to be determined, assuming comparable tissue deformation responses result in the comparable clinical outcome (Antona-Makoshi, 2016; Panzer et al., 2014).

To relate the mechanical trauma impact conditions in animal models to humans, it is imperative to establish a physics-based link between the intensity of the external loadings and the intensity of the internal tissue-level responses (e.g., brain deformation) across species. This physics-based link can be based on cadaveric models, physical models, or finite element models (FE). For example, Margulies et al. (1990) previously used physical skull models of different species filled with viscoelastic gel to provide a unique insight into the relationship between the kinematics of head motion and the associated deformation in heads of various morphologies. Considering the difficulty in measuring deformation with high spatial resolution under a broad range of loading conditions, brain FE models are a suitable research tool to allow strain field measurements with the desired temporal and spatial fidelity (Gabler et al., 2018c; Jean et al., 2014).

While a link between human and animal loading conditions can be established using FE simulations, computational simulations of animal tests are not always available since kinematics time history was not well documented for legacy animal data (Abel et al., 1978; Gennarelli et al.,

1982; Olszko et al., 2018; Ommaya and Hirsch, 1971; Ono et al., 1980) and corresponding animal FE models usually are not as advanced as existing human FE models (Antona-Makoshi, 2016). Analytical relationships between human and animal data, through kinematic scaling methods, provide a more accessible and generalized solution. Historically, the first scaling method for TBI was developed based on brain mass to scale NHP experimental data to develop human concussion thresholds (Ommaya et al., 1967). According to the mass scaling model, the level of rotational acceleration required to produce injury in brains with different sizes is inversely proportional to the 2/3 power of the ratio of the brain masses (hereafter referred to as 'mass scaling'). The method assumes the mechanical responses of the brain to be elastic, homogeneous, isotropic, and more importantly, geometrically similar across species. However, it is well known that the mechanical responses of brain tissue are nonlinear, viscoelastic, heterogeneous and anisotropic (Chatelin et al., 2010). Despite its limitations, the mass scaling method is widely used to relate the results of head rotation experiments on animals to humans (Browne et al., 2011; Cullen et al., 2016; Eppinger et al., 1999; Takhounts et al., 2013).

To my knowledge, few studies have attempted to address the challenges of scaling animal TBI data to humans using alternative scaling formulations. Margulies and Thibault (1989) developed an analytical model and an empirical scaling relationship between the NHP and human based on a cylindrical model. They found that the head angular acceleration was inversely proportional to the brain mass, but the power of this relationship was dependent on the frequency of the loading conditions, this dependence hampered the general application of this method as the frequency of real-world loadings is unusual unknown. Ibrahim et al. (2010) proposed that the scaling relationship between infant and juvenile piglets must include differences in brain mass, material properties, and tissue vulnerability (strain threshold required to produce injury in the

tissue). Scaling methods developed for blast-induced TBI are available in the literature (Jean et al., 2014; Panzer et al., 2014; Wood et al., 2018), but these are derived based on a different injury mechanism than blunt trauma. Consequently, these scaling procedures have not been evaluated or validated considering the differences across species in material characteristics of brain tissue and complex brain morphologies.

The objectives of this study were to investigate and evaluate scaling methods for TBI using finite element (FE) models of brains from multiple primate species (human, macaque, and baboon). Four scaling methods, the traditional mass-based scaling method, inertia-based scaling, an optimization-based method, and a novel frequency-based scaling method, were assessed using the strain response surfaces, which were generated from a parametric study based-on idealized kinematics pulse over a range of uniaxial rotational impact conditions for different brain FE models. The proposed scaling method was further explored and evaluated under three-dimensional real-world head impact scenarios to ensure that the scaling method is effective and generally applicable.

6.2 Methods

6.2.1 Brain FE Models

Three FE models representing human, macaque and baboon brains detailed in previous Chapters were used (Figure 5-7). As mentioned, they were developed or modified to harmonize the numerical methods, anatomical features (axonal tractography), and constitutive models to reduce the influences of differences from numerical implementations and constitutive models.

6.2.2 Parametric Study: Strain Response Surfaces Generation

A series of idealized rotational pulses were applied to the FE models about each anatomical axis of the head to study the relationship between head kinematics and maximum brain deformation, in a manner similar to Gabler et al., (2018). Consistent head anatomical coordinate systems were defined for the three FE models. The x-axis was defined along the intersection of the Frankfort and mid-sagittal planes in the posterior-to-anterior direction (corresponding to coronal rotation). The y-axis was defined along the line joining the two superior edges of the auditory meatus in the left-to-right direction (corresponding to sagittal rotation). The z-axis laid in the mid-sagittal plane perpendicular to the Frankfort plane and in the superior-to-inferior direction (corresponding to axial rotation). Rotations were applied in positive directions. Translational kinematics were not investigated in this study since previous work has shown a weak correlation between linear acceleration and brain strain (Gabler et al., 2016). A sinusoidal pulse shape was chosen for this parametric study, and each loading case was uniquely defined by two kinematic parameters: angular velocity (ω_0) and angular acceleration (α_0) (Figure 6-1). The ranges of acceleration and velocity magnitudes for each species were informed by existing experimental data (Mendis, 1992; Ommaya and Hirsch, 1971; Sanchez et al., 2018) (Figure 6-2).

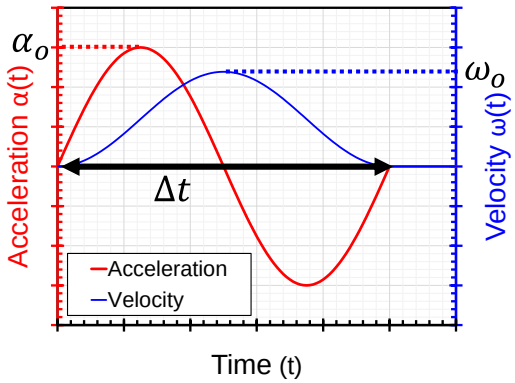

Figure 6-1. Sinusoidal loading pulses for simulations in the parametric study.

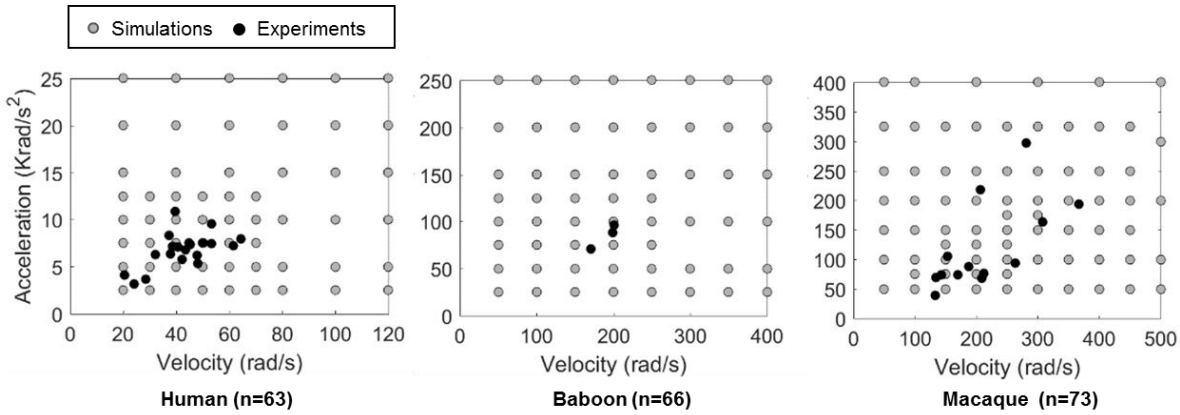

Figure 6-2. Design space for simulations.

6.2.3 Data Analysis

All FE simulations were performed using LS-Dyna (v971 R9.2.0, double precision; LSTC, Livermore, CA). The rotational head kinematics were applied to the rigid dura through the head center of gravity. The tissue deformation was quantified using strain-based metrics: MPS and MAS. MPS and MAS are respectively defined as the maximum value of the maximum principal strain occurring in all solid elements of the brain model and the maximum axial strain occurring in all axonal fiber elements of the brain, over the entire time history of the impact event. The 95th percentile peak MPS and MAS response (ranked by element) were used to avoid potential non-physical deformation measurements that may have been related with the 100th percentile value (Panzer et al., 2012). Relationships between the strain metrics (MPS and MAS) and applied head kinematics were depicted in angular acceleration-angular velocity space using deformation-based response surfaces (contour plots) (Gabler et al. 2018).

6.2.4 Scaling Methods

Four scaling methods were investigated to determine the equivalent kinematics for different species based on the brain deformation response surfaces. Depending on the mechanism of TBI, the equivalent kinematics can be defined as loading conditions resulting in the same maximum brain strain of the whole brain (MPS), or the same maximum tensile strain of the white

matter tracts (MAS). MAS was investigated because the axonal strain is the critical mechanism of TBI (Meaney and Smith, 2011).

First, the traditional mass scaling method (Eppinger et al., 1999; Ommaya et al., 1967) was applied to the head kinematics based on the brain mass for each species in the following manner:

$$\text{Angular velocity: } \omega_h = \lambda_{\omega,mass}\omega_a = (\frac{m_a}{m_h})^{1/3}\omega_a \quad \textit{[6-1]}$$

$$\text{Angular acceleration: } \alpha_h = \lambda_{\alpha,mass}\alpha_a = (\frac{m_a}{m_h})^{2/3}\alpha_a \quad \textit{[6-2]}$$

$$\text{Time: } t_h = \lambda_{t,mass}t_a = (\frac{m_a}{m_h})^{-1/3}t_a \quad \textit{[6-3]}$$

In which m are the brain masses, ω are the angular velocities, and α are the angular accelerations with subscripts h and a denote the human and animal respectively. The mass scaling method is not directionally dependent, so the same set of scaling factors ($\lambda_{\omega,mass}$ and $\lambda_{\alpha,mass}$) were employed for rotational kinematics in all three anatomical directions (coronal, sagittal, and axial).

Secondly, considering that the inclusion of cerebral moments of inertia in rotational head injury metrics might improve prediction of diffuse axonal injury for piglets (Atlan et al., 2018), the second method was to utilize the brain moment of inertia for each species instead of brain mass to scale the head kinematics, as formulated in Equation [6-4] – [6-6], following the principles of dimensional analysis.

$$\text{Angular velocity: } \omega_h = \lambda_{\omega,inertia}\omega_a = (\frac{I_a}{I_h})^{1/5}\omega_a \quad \textit{[6-4]}$$

$$\text{Angular acceleration: } \alpha_h = \lambda_{\alpha,inertia}\alpha_a = (\frac{I_a}{I_h})^{2/5}\alpha_a \quad \textit{[6-5]}$$

$$\text{Time: } t_h = \lambda_{t,inertia}t_a = (\frac{I_a}{I_h})^{-1/5}t_a \quad \textit{[6-6]}$$

The third scaling method was inspired by previous studies that showed that simple mechanical models could be used to predict the relationship between rotational head motion and brain deformation (Gabler et al., 2018c). Single-degree-of-freedom (sDOF) mechanical systems with base excitation were developed for characterizing both the animal brain responses and the human brain responses. For each loading direction, 5 parameters were identified to fit the sDOF model to the MPS or MAS responses of each brain model: the natural frequencies of the three species (f_i) and the two common dimensionless parameters: damping ratio (ζ) and strain regressor coefficient (β). An optimized set of coefficients (f_i, ζ and β) were determined independently for each anatomical direction using a nonlinear, least-squares solver (lsqcurvefit; Matlab) to minimize the sum-squared error (SSE) between FE-measured and sDOF-predicted MPS (or MAS). It can be shown (details in Appendix B) that the response of a pair of sDOF systems (equal in ζ and β), with different natural frequencies, can be scaled based on the ratio of natural frequency in the following manner (Equation [6-7] – [6-9]). This scaling method is hereafter referred to as 'frequency scaling', and it considers directional dependence since there are independent scale factors for each loading direction. Furthermore, this scaling method indicates that a brain with higher natural frequency (often smaller brains) will require higher angular velocity and acceleration than a brain with a lower natural frequency (often larger brains) for the equivalent biomechanical responses.

$$\text{Angular velocity: } \omega_h = \lambda_{\omega,freq}\omega_a = \frac{f_h}{f_a}\omega_a \qquad \textit{[6-7]}$$

$$\text{Angular acceleration: } \alpha_h = \lambda_{\alpha,freq}\alpha_a = (\frac{f_h}{f_a})^2\alpha_a \qquad \textit{[6-8]}$$

$$\text{Time: } t_h = \lambda_{t,freq}t_a = \frac{f_a}{f_h}t_a \qquad \textit{[6-9]}$$

The last scaling method used in this study was not based on physics-based dimensional analysis but was based on determining an optimal set of scaling factors for angular velocity and

angular accelerations ($\lambda_{\omega,opt}$ and $\lambda_{\alpha,opt}$), using an unconstrained optimization solver (fminsearch; Matlab). The optimal set of scaling factors, for each loading direction, resulted in minimum SSE between the scaled animal responses surfaces and the target human responses surfaces. This scaling method was referred to as 'optimal scaling', and was used as a reference for the best possible scaled responses for the dataset generated in this study because it was not constrained by physics principles.

6.2.5 Extension to Three-Dimensional Time-Histories

While only single, uniaxial pulses with a sinusoidal shape were considered in the above parametric study to develop the frequency-based and optimal scaling methods, real-world impacts often result in complex, three-dimensional, and multi-impact head motions. The scaling factors obtained from the frequency scaling method are directionally dependent (e.g. $\lambda_{\omega,x,freq} \neq \lambda_{\omega,y,freq} \neq \lambda_{\omega,z,freq}$), which raised new challenges when they were applied to three-dimensional data.

Three methods were further investigated to employ direction-dependent scaling factors to three-dimensional (3D) rotational data. Taking 3D angular velocity time histories as an example, these methods were detailed as follows (these methods can be seamlessly applied to angular acceleration).

First, the scaling factors derived from different uniaxial loadings ($\lambda_{\omega,i}$ and $\lambda_{t,i}$, $i = x, y, z$) were respectively applied to scale the corresponding Cartesian components ($\omega_{a,i}$ and $t_{a,i}$) of the complex time-history pulses of rotational kinematics (Equation [6-10] – [6-11]) (referred to as 'triaxial method').

Angular velocity: $\omega_{h,i} = \lambda_{\omega,i}\omega_{a,i}$, $i = x, y, z.$ *[6-10]*

Time: $t_{h,i} = \frac{t_{a,i}}{\lambda_{\omega,i}} = \lambda_{t,i}t_{a,i}$, $i = x, y, z.$ *[6-11]*

Secondly, an average scaling factor of the uniaxial scaling factors ($\lambda_{\omega,m} = \frac{\lambda_{\omega,x}+\lambda_{\omega,y}+\lambda_{\omega,z}}{3}$) was found and applied to uniformly scale the Cartesian components of the complex time-history pulses of rotational kinematics (referred to as the 'average method').

Angular velocity: $\omega_{h,i} = \lambda_{\omega,m}\omega_{a,i}$, $i = x, y, z.$ *[6-12]*

Time: $t_{h,i} = \frac{t_{a,i}}{\lambda_{\omega,m}} = \lambda_{t,m}t_{a,i}$, $i = x, y, z.$ *[6-13]*

Lastly, the time-dependent scaling factor ($\lambda_{\omega,r}(t)$) was applied to uniformly scale the Cartesian components of the rotational kinematics in the following manner (Equation [6-14], [6-15]). At any point in time, the scaling factor $\lambda_{\omega,r}$ was determined by the input angular velocity (ω_i, $i = x, y, z$), and the direction-dependent scaling factors ($\lambda_{\omega,i}$), given by the following expression (Equation [6-16]). The equation is similar to the standard equation of the ellipsoid in the Cartesian coordinates, thus referred to as 'ellipsoidal method' (Figure 6-4).

Angular velocity: $\omega_{h,i}(t_h) = \lambda_{\omega,r}(t_a) \cdot \omega_{a,i}(t_a)$, $i = x, y, z.$ *[6-14]*

Time: $t_h = \int_0^{t_a}(\Delta t_a/\lambda_{\omega,r}(\tau))d\tau = \int_0^{t_a}(\Delta t_a \cdot \lambda_{t,r}(\tau))d\tau$

$\lambda_{t,r}(\tau) = 1/\lambda_{\omega,r}(\tau)$, Δt_a is the time step of the kinematics data. *[6-15]*

$$(\frac{\lambda_{\omega,r}\omega_x}{\lambda_{\omega,x}})^2 + (\frac{\lambda_{\omega,r}\omega_y}{\lambda_{\omega,y}})^2 + (\frac{\lambda_{\omega,r}\omega_z}{\lambda_{\omega,z}})^2 = 1 \quad \textit{[6-16]}$$

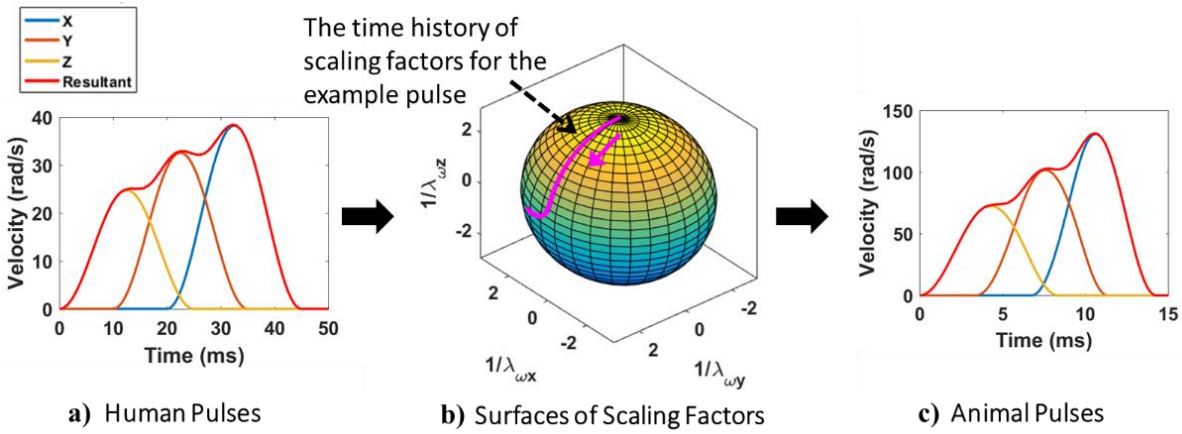

a) An example of human loading pulses which only have axial (z) angular velocity before 10 ms and coronal angular velocity after 35 ms. b) The time history of scaling factors for this example on the assumed ellipsoidal surfaces. Corresponding to the pulses, for the first 10 ms, the scaling factor is equal to the scaling factor for uniaxial axial rotation (north pole), then the curve of the scaling factor moves to the south and then the west, and near the end the scaling factor is equal to the scaling factor for uniaxial coronal rotation. c) Scaled loading pulses.

Figure 6-3. Schematic diagram to apply frequency scaling in 3D scenarios using the ellipsoidal method.

6.2.6 Application Assessment

The four scaling methods were first applied directly to scale the animal response surfaces and compared with the human response surfaces to assess the goodness of fit (for frequency and optimal scaling) and accuracy of prediction (for mass-based and inertia-based scaling). Simple linear regression using ordinary least squares was used to quantify the accuracy between the scaled animal strain response surfaces and the human strain response surfaces.

The applicability of newly proposed frequency scaling, which had scaling factors based on the anatomical direction of loadings, were further assessed in correlating human real-world head impact conditions to the equivelent macaque condtitions using a combination of 14 football reconstructions, sled, crash, and pendulum tests (Gabler et al., 2016; Sanchez et al., 2018). The range and distribution of component peak kinematic values of those tests are illustrated in Figure 6-4. The mass scaling method was also assessed for 3D application as a reference method. This

scaling study focused on scaling rotational kinematics. Linear kinematics were expected to induce negotiable strain in the brain (Gabler et al., 2016), and were scaled based on mass (Eppinger et al., 1999) in any situations no matter what scaling methods were used for rotational motion. These pulses were first applied to the human model to predict target strain responses. Then, simulations using the macaque model were conducted for the equivalent loading scenarios defined separately based on the frequency scaling or the mass scaling method. The 95th percentile peak MPS outputs for human and macaque were compared and qualified using linear regression analysis.

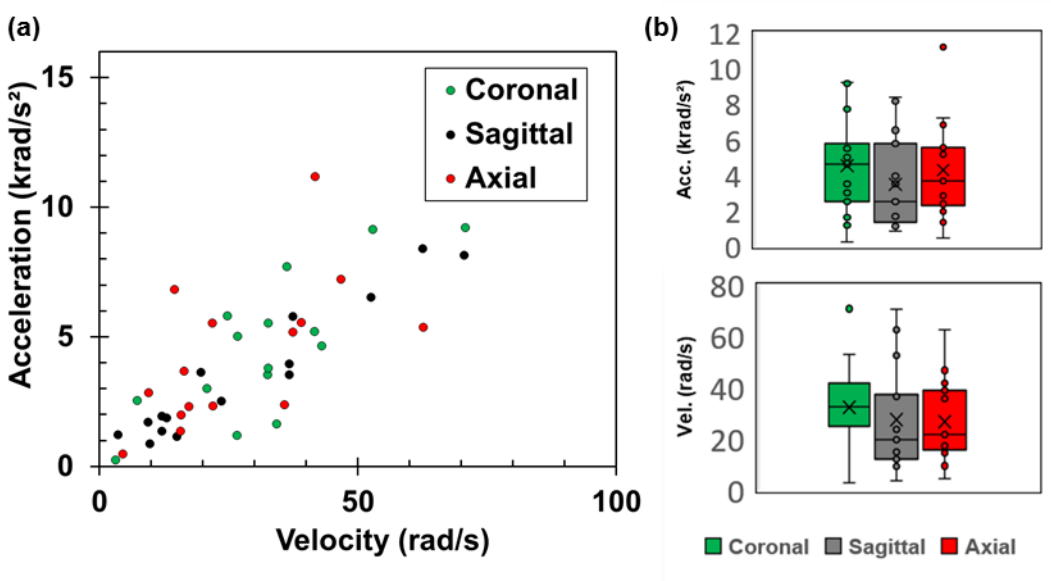

Figure 6-4. Realistic loading pulses from experimental data. (a) Scatter plots to show the distribution of component peak angular velocities and component peak angular accelerations for coronal, sagittal, and axial directions. (b) Box plots to show the minimum, first quartile, median, third quartile, and the maximum value of the same dataset.

6.3 Results

6.3.1 MPS/MAS Response Contours

A total 18 of MPS/MAS response surfaces of uniaxial rotations (Figure 6-5 and Figure 6-6) for three anatomical directions (coronal, sagittal, axial) and three species (human, macaque, baboon) were generated in this study. Each response surface shows the contour lines representing constant levels of MPS/MAS for the applied peak loading angular velocities and angular accelerations.

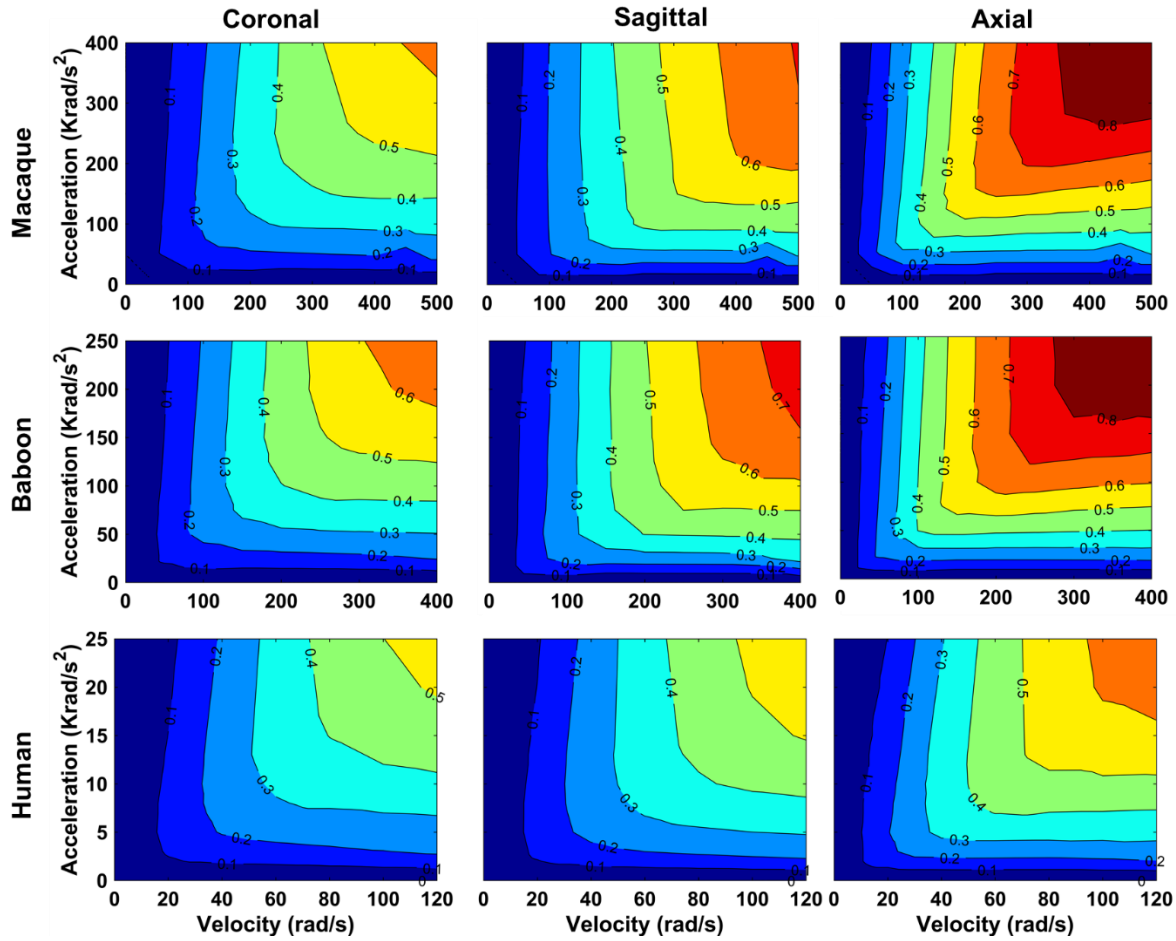

Figure 6-5. MPS (95th) response surfaces of uniaxial rotations for the human, baboon, and macaque.

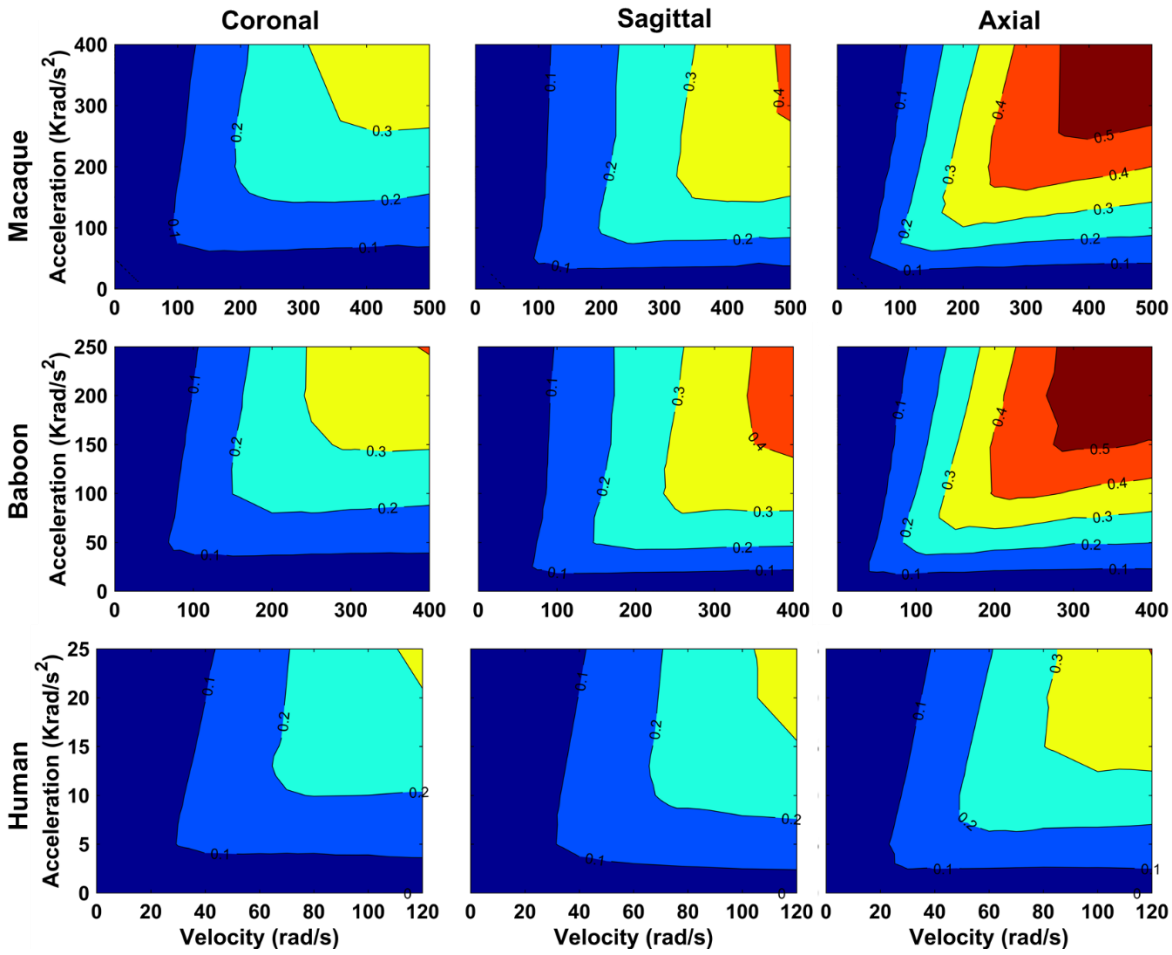

Figure 6-6. MAS (95th) response surfaces of uniaxial rotations for the human, baboon, and macaque.

6.3.2 Scaling Factors

The inertia, mass, and natural frequency information for the three brain models are provided in Table 6-1, the directionally dependent natural frequencies were estimated by fitting the FE response surfaces with the sDOF models. Other resulting parameters (β, ζ) of the sDOF models and the goodness of fit were included in Appendix B. The sDOF models fit the MPS and MAS responses well for the coronal and sagittal rotations (R2 > 0.950) but had slightly lower correlations for the axial rotations (R2 ≈ 0.9).

Table 6-1. Inertia, mass, and natural frequency information for the brain models of three primate species.

Parameters		Macaque	Baboon	Human
Mass (g)		80	156	1243
Moment of Inertia (Kg.mm^2)	I_x	25.3	73.8	2715.2
	I_y	32.2	96.0	2489.7
	I_z	20.8	66.9	2039.7
Natural Frequency (MPS) (Hz)	f_x	194.1	148.0	56.6
	f_y	155.2	116.3	49.8
	f_z	219.2	167.2	74.9
Natural Frequency (MAS) (Hz)	f_x	213.9	162.9	62.4
	f_y	131.4	100.0	41.9
	f_z	194.7	149.4	68.6

Table 6-2 summarizes the scaling factors obtained using the four scaling methods. For both angular velocity and angular acceleration, the frequency-based scaling factors and optimal scaling factors are similar, with an average difference of 8% ± 7%. Conversely, the mass-based scaling factors are significantly different from the optimal scaling factors with an average difference as significant as 24% ±14%. The inertia-based scaling factors, while direction-dependent, are similar to the mass-based scaling factors, with the largest difference being less than 9%.

Table 6-2. Animal-human scaling factors under uniaxial rotations.

Species	Methods	Parameters	MPS (95th)			MAS (95th)		
			X	Y	Z	X	Y	Z
Macaque	Mass	$1/\lambda_\omega$	2.495					
		$1/\lambda_\alpha$	6.227					
	Inertia	$1/\lambda_\omega$	2.547	2.386	2.501	2.547	2.386	2.501
		$1/\lambda_\alpha$	6.487	5.692	6.255	6.487	5.692	6.255
	Freq.	$1/\lambda_\omega$	3.425	3.117	2.929	3.428	3.134	2.837
		$1/\lambda_\alpha$	11.732	9.714	8.580	11.753	9.819	8.048
	Optimal	$1/\lambda_\omega$	3.124	3.065	2.464	3.0232	3.012	2.299
		$1/\lambda_\alpha$	11.920	10.025	10.870	10.129	9.990	9.845
Baboon	Mass	$1/\lambda_\omega$	1.997					
		$1/\lambda_\alpha$	3.989					
	Inertia	$1/\lambda_\omega$	2.057	1.918	1.981	2.057	1.918	1.981
		$1/\lambda_\alpha$	4.230	3.677	3.924	4.230	3.677	3.924
	Freq.	$1/\lambda_\omega$	2.613	2.338	2.233	2.610	2.385	2.177
		$1/\lambda_\alpha$	6.826	5.469	4.986	6.813	5.691	4.740
	Optimal	$1/\lambda_\omega$	2.519	2.260	2.258	2.435	2.249	2.054
		$1/\lambda_\alpha$	7.203	5.337	5.409	7.406	5.569	4.763

6.3.3 Assessment of Scaling for Uniaxial Motions

As an example, the comparison between the scaled baboon response surfaces and human response surfaces is illustrated in Figure 6-7 and Figure 6-8 for the sagittal rotation direction. All the scaled animal response surfaces are reported in Appendix B. For the frequency scaling, the scaling factors obtained based on MAS were similar to the scaling factors obtained based on MPS (difference < 6%). Therefore, only the results using MPS-based scaling factors were assessed in the following analysis.

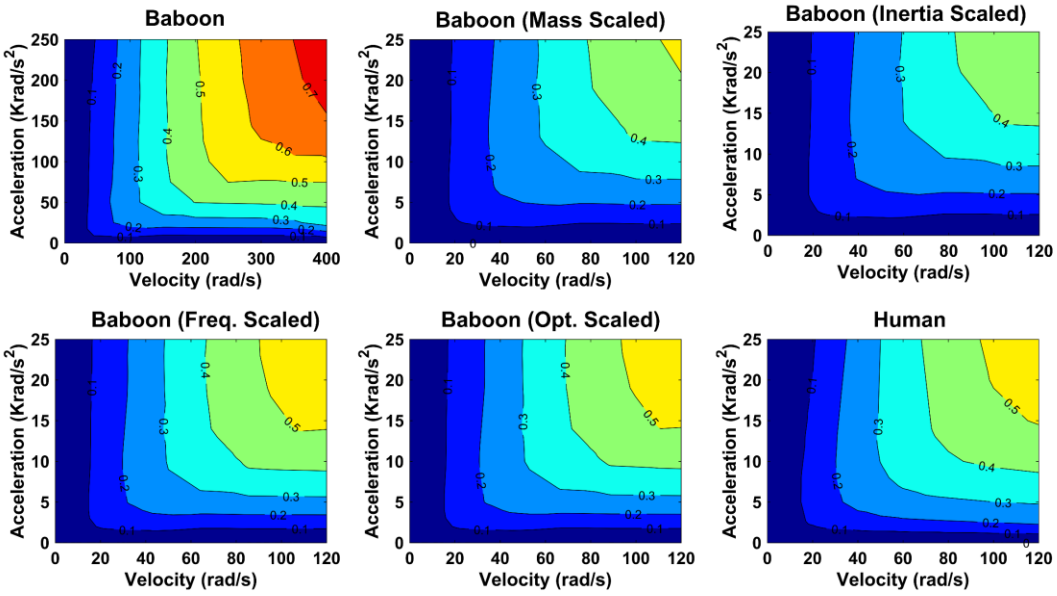

Figure 6-7. Exemplary scaled baboon MPS (95th) response surfaces under uniaxial sagittal rotations.

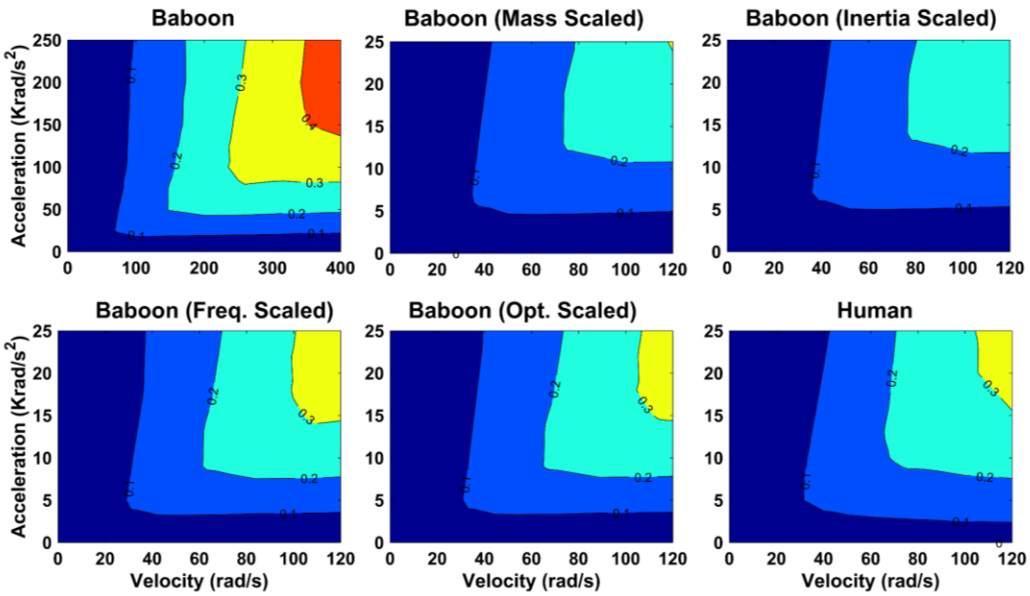

Figure 6-8. Exemplary scaled baboon MAS (95th) response surfaces under uniaxial sagittal rotations.

Using linear regression analysis, substantial differences between the mass-scaled animal responses and human responses (slopes: 0.680 to 0.844, and R^2: 0.838 to 0.952), and between animal responses and human responses (slopes: 0.697 to 0.847, and R^2: 0.838 to 0.943) were found, compared with frequency-scaled animal responses (slopes: 0.987 to 1.012, and R^2 : 0.896 to 0.985) and optimal-scaled animal responses (slopes: 0.946 to 1.007, and R^2 : 0.964 to 0.991), as shown in Figure 6-9. Performances of frequency scaling and optimal scaling were similar for coronal and sagittal rotations, while the optimal-scaled animal responses correlated better with human responses, compared to frequency scaling (R^2 : 0.962 versus 0.896).

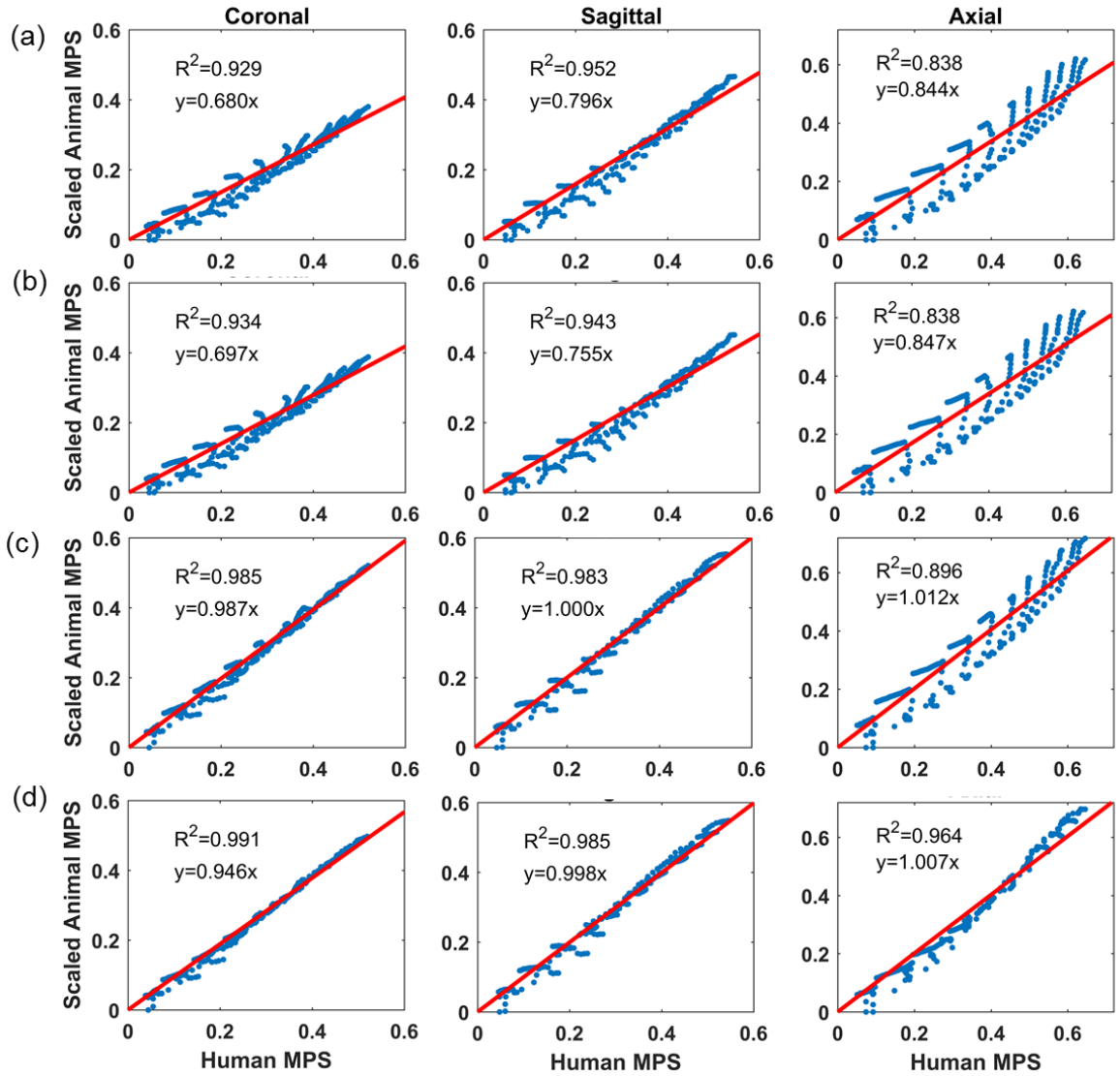

Figure 6-9. Scatter plots showing correlations between MPS (95th) from human responses and scaled macaque responses using (a) mass scaling, (b) inertia scaling, (c) frequency scaling, and (d) optimal scaling.

6.3.4 Application in Real-World Impact Scenarios

The assessment using 14 real-world head impacts also revealed better correlations between frequency-scaled animal strain results and human strain results (slopes: 0.914-0.966, and R^2: 0.928-0.946) when compared to mass-scaled animal results (slopes: 0.707, and R^2 : 0.768) (Figure 6-10). Amongst the three methods for 3D extension based on frequency scaling, the averaging

method (Figure 6-10 (c)) and ellipsoidal method (Figure 6-10 (d)) demonstrated similar performance, which were marginally better than the triaxial method (Figure 6-10 (b)).

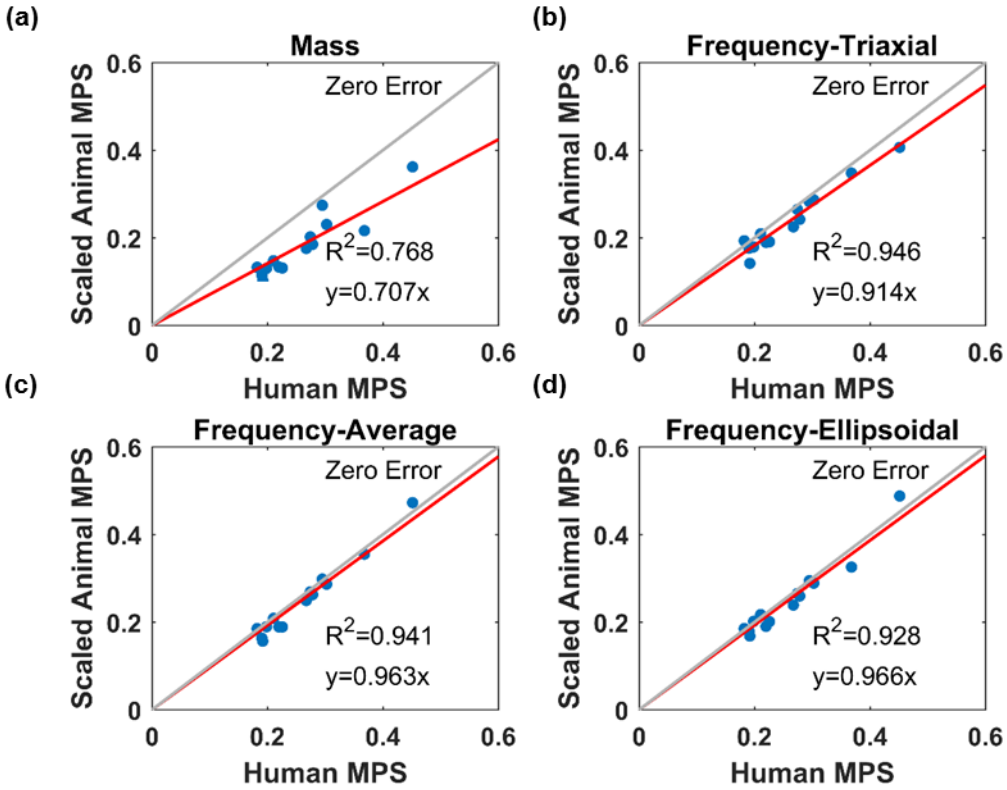

Figure 6-10. Scatter plots showing correlations between MPS (95th) from human responses and scaled macaque responses using (a) mass scaling, (b) triaxial frequency scaling, (c) average frequency scaling, and (d) ellipsoidal frequency scaling.

6.4 Discussion

Animal studies have resulted in meaningful advances in the understanding of TBI. However, the applicability of animal brain injury results to humans remains uncertain due to the limitations that exist in traditional scaling methods. Here, we used advanced computational models to help derive and evaluate cross-species scaling laws for brain trauma. The tissue deformation response surfaces of three species (human, baboon, macaque), represented by MPS or MAS, was correlated with head kinematics for a broad range of external loading conditions. Traditional mass-based scaling was not able to capture similar brain tissue response to equivalent rotational

kinematic inputs across species. In this study, we showed that the mechanical trauma relationship of animals could be scaled according to a novel frequency method derived from fitting sDOF mechanical models to FE model results.

6.4.1 Comments on Response Surfaces

Contour surface response patterns observed in the mechanical models showed a remarkable similarity to a previous simulation study (Gabler et al., 2018) and an experimentally derived rotational brain injury tolerance proposed in the literature (Margulies and Thibault, 1992). Surface response patterns across different brains were also similar, which indicated that they could be accurately modeled using the same damping ratio (ζ) and regressor (β). The biggest differences between the animal contours and human contours were observed in axial rotation, which yielded difficulties in scaling the responses for that direction. Although the parametric study was conducted using positive rotation pulses, response surfaces under coronal and axial rotations in negative directions were expected to be identical due to the geometric symmetry of the brain models. As shown in Gabler et al. (2018), the strain response in the sagittal rotation was also independent of the negative or position direction, although geometric symmetry did not hold. The response surfaces also suggest that both the NHP and human tolerance to rotational acceleration was, in general, lower in the axial plane than in the sagittal and coronal. This is consistent with a recent experimental study by Alshareef et al. (2018), where the maximum peak-to-peak brain deformation observed in coronal, sagittal, and axial dynamic rotations were 11, 12, and 23 mm respectively.

6.4.2 Physical Meaning of Frequency Scaling

For the uniaxial study, in the scenario with the largest discrepancy of scaling factors between mass scaling and frequency scaling (coronal), the equivalent angular velocity and angular

acceleration scaled by mass scaling from NHP data were 27% and 47% larger, respectively, than those of the frequency scaling method. Although there is no direct experimental data to verify these results, the current findings agree with previous analytical results (Margulies, 1987). As shown in Figure 6-11, the frequency-scaled tolerance of the baboon matches well with the human threshold reported by Margulies (1987), in which they used physical models as an empirical scaling technique to find the load associated with the same critical strains. In stark contrast to the proposed frequency method, the threshold scaled using mass scaling laws underestimates the brain vulnerability for a human. Relevant experimental studies are required to provide insight into these scaling relationships.

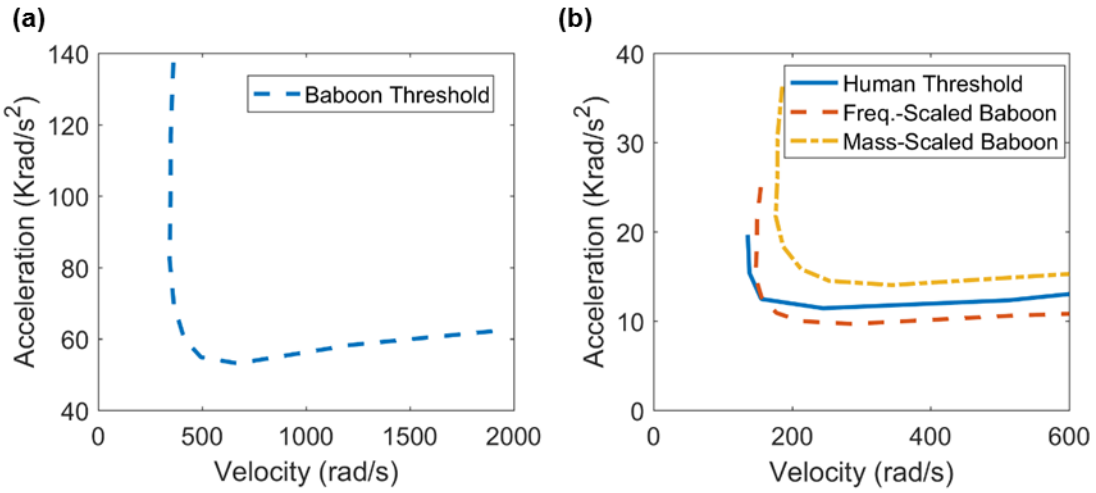

Note that the velocity for the tolerances derived by Margulies (1987) was very high, this might be due to the incorrectly assumed recording frequency for those animal data as found by Mendis (1992), refer to Margulies and Thibault (1992) for comparison with the corrected tolerance. This will not affect the scaling techniques.

Figure 6-11. Comparisons of DAI tolerances for human using different scaling methods. (a) The unscaled baboon tolerance adapted from Margulies (1987); (b) Scaled baboon tolerances using frequency (the dashed line) and mass scaling (the dash-dotted line) respectively, compared with human tolerance (the solid blue line) derived by Margulies (1987).

Both the optimal scaling method and frequency scaling method yielded a good fit of the strain results, especially for the sagittal and coronal rotations. The differences between the frequency-based scaling factors and optimal scaling factors were within 10%. The advantage of the frequency scaling method over the optimal scaling is its robustness, which was demonstrated by fitting the model using randomly sampled subsets of the dataset (details in the Appendix B). In that situation, the variation of scaling factors using the frequency method was much smaller than those using optimization. The optimal scaling method is a numerical fit and only captures the phenomena in the range of the fitted data and not the underlying deformation-based physics of the injury. It tends to lead to nonsensical predictions when extrapolated beyond the range of fitted data and a more significant error when the sample size is not large enough. Also, the optimal scaling factors were not applicable in situations when scaling time-history data is required, because the scaling factors of physical quantities are not compatible with each other (e.g., $\lambda_\alpha \neq (\lambda_\omega)^2$, so λ_t cannot be derived from λ_α and λ_ω based on dimensional analysis). An alternative method for the optimal scaling was to perform the optimization with physical constraints ($\lambda_\alpha = (\lambda_\omega)^2$). In that case, the optimal scaling factors were similar to the frequency-scaling factors, even for the axial rotation conditions (within 5%), suggesting that the frequency scaling approach approximately represented the best fit obtainable from physically-bounded (linear) scaling laws.

Previous animal-to-human scaling laws for TBI on the brain have been derived using mass scaling techniques (Eppinger et al. 1999). These are limited since they do not consider the physical mechanisms that determine brain response to impact, the nonlinear and viscoelastic material properties of the brain tissue, and significant morphological and anatomical differences. The proposed frequency scaling method can address some of these limitations through the analogy between the simple mechanical systems and the relationship between head kinematics and

intracranial deformation observed in FE simulations. In the sDOF system, the deformation resulting from loading is governed by the natural frequency ($\omega_n = \sqrt{k/m}$) which contains parameters such as length, stiffness, and mass. The effects of different material parameters (e.g., the constitutive model) and structural parameters (e.g., the morphology of the brain) of various brains were taken into account by the parameter fitting (e.g., stiffness and damping) of the sDOF model.

Although the natural frequency of brains was estimated computationally in this study, the skull-brain dynamics will be better understood through experiments in the future. The findings of existing experimental studies on the modal behavior of the brain were not conclusive, the reported natural frequency for the human brain ranges from 15 Hz to 50 Hz at low-severity impacts (Laksari et al., 2015; Zou et al., 2007). The analysis performed here may facilitate future investigations along this line of research.

6.4.3 Application of Frequency Scaling for Three-Dimensional Kinematics

The assessment for application in human real-world head impact conditions suggested that the scaling factors, although obtained using simulations under only single, uniaxial pulses with a sinusoidal shape, could be applied to complex, multi-directional loading conditions. This finding agrees with previous work, in which the global strain-based responses were reasonably insensitive to pulse shape (Gabler et al. 2018). However, as noted by Yoganandan et al. (2008), regional strain response in the brain could be dependent on the profile of the acceleration-deceleration pulse.

As shown in Table 6-2, the scaling factors obtained from frequency scaling methods were directionally dependent, which introduced new challenges when applied to three-dimensional data. For the three application methods investigated in this study, differences in performance were not

significant. This was likely due to the small differences in uniaxial scaling factors. The triaxial method was unable to preserve the time-history of angle (e.g., $t_{ax} \neq t_{ay} \neq t_{az}$) and the features of the rotational angle, since the time scaling factors for different Cartesian components were different, and the relative phases between x, y, and z changed after scaling. The averaging method was able to preserve the angle but was not compatible with the uniaxial scaling factors, thus this method was expected to compromise the accuracy for uniaxial loadings or loadings dominated by uniaxial rotations. The ellipsoidal method was the only method amongst them able to approximately preserve the angle and overall motion, while still remain compatible with the direction-dependent scaling factors of uniaxial loading.

6.4.4 Limitations

A critical assumption in this study was that comparable strain metrics result in an equal clinical outcome. As proof of concept, the current study was performed using two non-human primate species. The human brain is 'a scaled-up primate brain' in its cellular composition (Azevedo et al., 2009), but the interspecies differences in structural pathology, pathophysiology, and behavioral pathology are still unknown. Furthermore, whether this assumption applies to other animal species used as human surrogates (e.g., rodents, ferrets, pigs; Shultz et al. 2017) requires further investigation. It is possible that this assumption is not appropriate for rodents as several studies have noted the limited similarity to humans in genomic and proteomic responses, injury time course, and grey and white matter distribution (Duhaime, 2006; Seok et al., 2013).

A limitation of this study was the absence of validation data for the intracranial deformation response of the NHP brain models, due to the lack of experimental data. The current study assumed similarity in material properties between primate and human brains and the brain tissue material properties of the NHP models were not thoroughly investigated. Although existing experimental

data on the mechanical properties of primate brain tissue exists, previous studies have indicated mechanical similarity between human and NHP brain material properties (Estes and McElhaney, 1970; Galford and McElhaney, 1970). However, contradictory findings have also been reported, probably because the human brain specimens were tested at a significantly later time after death than the NHP (Galford and McElhaney 1970). Brain deformation response was also sensitive to numerical implementation (Giudice et al. 2018). Therefore, a similar number of elements (Figure 5-1) and mesh type were adopted across different brain models to mitigate the possible effects of mesh architecture. Although similar white matter patterns were observed between the macaque and baboon (Figure 5-5 (a)), it is possible that errors in MAS were introduced by morphing the macaque axonal tracts networks to represent the baboon. A tractography atlas of the baboon brain is not currently available in the literature, but it was expected that the anisotropic effects on the MPS would be minimal (Wu et al. 2019).

Furthermore, only global measures of brain strain were used to quantify the tissue deformation. Additional work is needed to determine whether metrics based on regional tissue strain improve the prediction of these brain injury types. Additionally, metrics such as strain rate, and the product of strain and strain rate may improve correlation with brain injury, but there is a lack of supporting experimental data to include the effects of strain rates on injury vulnerability (Cater et al., 2006). Using dimensional metrics (e.g., strain rate) as tissue-level injury metrics would also introduce new challenges for interpreting tissue-level metrics across species.

6.4.5 Summary

In conclusion, rotation-induced brain strain does not scale solely with brain mass across species. Instead, an appropriate scaling variable must consider the mass of the brain, as well as viscoelastic properties of brain tissue and the morphological features. Therefore, a novel frequency

scaling method was proposed based on the analogy between the FE results and a simple mechanical system. This scaling method enables the interpretation of mechanical-trauma responses obtained from animal data to the human, thus effectively allowing the development of human injury criteria and injury risk functions based on a plethora of animal tests available in the literature. This is a critical step in the design and development of effective countermeasures and the understanding of TBI. In Chapter 8, the scaling method developed in this chapter was utilized to develop tissue-level injury risk and scale kinematics-based metrics.

CHAPTER 7 : BRAIN INJURY DATA AGGREGATION

In vivo biomechanical data with known head kinematics and clinic outcomes are vital to an improved understanding of TBI mechanism. Beginning in the 1960s, many experimental studies have been performed to investigate brain injury. This chapter started with a critical review of existing injury data in the literature. The pros and cons for each experimental work were discussed in an attempt to find the proper dataset for the development of injury risk functions. Finally, a selected database of *in vivo* biomechanical brain injury data was collected for this dissertation and details are provided in this chapter.

7.1 Literature Review on Brain Injury Data

Brain injury data can be divided roughly into three main categories: sub-injurious experiments with volunteers, reconstruction or measurement of real-world events, and experiments with animals. A variety of TBIs were produced in these tests, including concussion, contusion, diffuse axonal injury (DAI), intracerebral hemorrhage (ICH), subarachnoid hemorrhage (SAH), subdural hemorrhage (SDH), epidural hemorrhage (EDH), and brainstem injury. Legacy volunteers and non-human primate biomechanical data were extremely valuable and were unlikely to be repeated, which calls for a combination of novel research methodologies with experimental data obtained in the past.

7.1.1 Volunteer Data

A large number of sub-injurious sled tests with young male military volunteers were performed at the US Naval Biodynamic Laboratory (NBDL) between 1968 and 1978 (Ewing and Thomas, 1972). The volunteers were restrained in a seated posture on a sled buck that could be mounted in different orientations (front-facing rearward, oblique, and pure lateral acceleration)

with respect to the direction of sled motion. 355 cases of these experiments conducted on 22 volunteers with frontal, oblique and pure lateral sled configurations have been recently re-evaluated and applied to examine the predictive capability of several existing head and brain injury risk functions (Sanchez et al., 2017). While such data and approaches have been proven invaluable for evaluating the ability of injury risk functions to predict non-injury response correctly, the sub-injurious data cannot achieve the severities necessary for comprehensive validation of injury risk functions or the development of new injury risk functions.

7.1.2 Real-world Data

Injury risk functions can be developed based on data from real-world events in which the participants are at risk of suffering brain injuries. For example, sensors worn by athletes have been used (Duma et al., 2005; King et al., 2015, 2016) to capture head kinematics during both concussive and sub-concussive hits, and the acquired data have been used to propose concussion injury risk functions (Rowson et al., 2012a). Unlike the volunteer data, which were directly measured with sensors tightly-coupled to the head in a laboratory setting, the limitation associated with the data acquisition led to questionable fidelity (O'Connor et al., 2017). For example, the accuracy of the head kinematics depends on a good helmet fit if helmeted devices were used (Joodaki et al., 2019). The kinematics of the hits sustained by professional football players have also been reconstructed experimentally (Pellman et al., 2003) and evaluated using video analysis (Sanchez et al., 2018). Questions exist in the fidelity of the indirectly measured kinematics through laboratory reconstruction, partially due to concerns within the biofidelity of the Hybrid III anthropometric test devices. The main limitation of football data is that it provides information on injuries representative only of the mild forms of brain injuries.

Data from motorsports accidents (Mellor, 2000; Somers et al., 2011; Weerappuli et al., 2002), motorcycle accident (COST, 2001), and pedestrian accidents (Deck and Willinger, 2008; Longhitano et al., 2005; Munsch et al., 2009; Peng et al., 2013) have also been reconstructed, usually through simulation, and used to develop injury criteria (Deck and Willinger, 2008; Laituri et al., 2016; Sahoo et al., 2016). The main limitation of these data is the questionable fidelity of the head kinematics, as the crash scenarios were complex, and the data were extrapolated from limited boundary information (e.g., the three-dimensional crash pulse of the vehicle from electronic data recorders).

7.1.3 Non-Human Primate Data

Five series of experiments performed by different groups from the 1960s to the 1980s using a large number of NHP specimens are summarized in Table 7-1. A more detailed discussion of these experiments is provided as follows with the intention of understanding the inherent limitations and ensuring their appropriate utilization in TBI studies.

Table 7-1. Summary of experiments on NHP to study TBI

Group	NIH	Penn	JARI	UMTRI	NBDL
Species	S, R, C	S, R, B	J, R, L, B	R, L	R
Ref.	(Letcher et al., 1973; Ommaya et al., 1973, 1967; Ommaya and Gennarelli, 1974)	(Gennarelli et al., 1982; Thibault and Gennarelli, 1990)	(Kanda et al., 1981; Kikuchi, 1982; Ono et al., 1980; Sakai et al., 1982; Sekino et al., 1981)	(Nusholtz et al., 1986; Stalnaker et al., 1973)	(Olszko et al., 2018)
Types	Sled, impactor, inertial loading	Non-impact rotation	Padded impactor	Padded and rigid impactor	Sled
Typical injuries	Concussion	DAI SDH	SDH, contusion, SAH, brainstem	Brainstem, fracture, hematoma, concussion	Brainstem
Head motion source	High-rate film	Sensor	Sensors mounted to the skull	Sensors mounted to the skull	High-rate film/sensor

S: squirrel monkey (*Saimiri sciureus*), R: rhesus macaque (*Macaca mulatta*), C: Chimpanzee (*Pan satryrus*), Baboon (*Papio nubis*), J: Japanese macaque (*Macaca fuscata*), L: Long-tailed macaque/crab-eating macaque/cynomolgus (*Macaca fascicularis*).

The first large series of experiments were performed by the US National Institutes of Health (NIH) on three non-human primate species (squirrel monkey, rhesus monkey, and

chimpanzee) to define tolerance thresholds for the onset of cerebral concussion. The injury was either produced by direct impact to the occipital zone of the head or caused by impact to the sled carrying the seated animal. The head kinematics were calculated from the analysis of high-speed movies and only peak angular kinematics were reported. Recognizing the complexity of injuries produced in the impactor and sled tests, squirrel monkeys were tested with controlled inertial loading, the isolated effects of translation and rotation on injuries were first evaluated by eliminating the effects of hard contact. While focal SDH and SAH were observed in the translated group, only the animals in the rotated group exhibited neurological evidence of cerebral concussion defined as the sudden onset of unconsciousness (Ommaya and Gennarelli, 1974). This finding motivated the following-up research on rotation-induced TBI.

Under the auspice of the US NIH, the second large series of experiments were conducted at the University of Pennsylvania (Penn). Three different test devices were successively utilized to deliver controlled non-impact biphasic rotational accelerations-decelerations to the head of more than one hundred specimens of different NHP species. Tests involved sagittal, lateral, oblique and axial acceleration. The experiments predominantly produced cerebral concussion, SDH, and DAI injury. Although the head motion was controlled, questions exist as to the accuracy of the recorded time-history kinematics. Subsequent inspection revealed that the original time scale of the angular acceleration curves was incorrectly documented, which resulted in the extremely high angular velocities seen in the literature (Gennarelli et al., 1987; Margulies and Thibault, 1992). The acceleration traces could be corrected to yield reasonable angular velocity and displacement (Mendis, 1992). The subjects were sacrificed hours to days after the test was completed, which hampers the understanding of the acute pathophysiological response after TBI.

The third large series of experiments were conducted at the Japan Automobile Research Institute (JARI) under the auspice of the Japanese government. Three different apparatus and a variety of loading conditions were utilized to deliver a total of 193 head impacts to the frontal, lateral or occipital part of the head of 89 specimens (mostly macaques). The experiments produced a wide range of brain injuries ranging from concussion-like symptoms, contusion, SAH, SDH and brainstem injuries. A subset of the JARI data comprised of mild head padded impacts has been re-analyzed to investigate concussive injury mechanisms utilizing simulations of the impacts with a head-neck macaque FE model (Antona-Makoshi et al., 2013). Most of the subjects were repeatedly impacted several times before autopsy which resulted in the ambiguities of the injury diagnosis.

The fourth large series of experiments was conducted by the University of Michigan Transportation Research Institute (UMTRI) using a pneumatic impacting device to deliver padded and rigid impacts on the heads of two different species of macaque. The tests performed by Nusholtz et al. (1986) produced predominately brainstem and spinal cord injuries, while the tests conducted by Stalnaker et al. (1973) led to a large variation of injury types including concussion, skull fracture, contusion, and hematoma. Both the JARI and UMTRI experiments measured 3-D head kinematics by accelerometers mounted to the skull. This invasive method would potentially provide more accurate head motion, but it precluded precise injury diagnosis. A subset of this data series (Stalnaker et al., 1973) have been scaled to humans and applied to develop the BrIC injury risk curves for AIS4+ injuries (Takhounts et al., 2013).

The fifth large series of experiments were conducted by the NBDL between 1973 and 1989 and has been recently processed and reported (Olszko et al., 2018). A total of 240 sled test were performed with 94 macaque specimens. The specimens were seated with the whole body below the neck restrained to a buck mounted on the sled and subjected to high accelerations in the frontal

or the rear directions. The existing analysis on these NBDL experiments was conducted using sled accelerations, while head kinematics data (measured during the experiments) have yet to be analyzed and made accessible to the scientific community. Predominantly, brainstem injuries due to cranio-vertebral junction dislocations were reported due to the torso of each NHP being fully restrained during the sled impact, which makes this data representative of only the upper-end tolerance limits for NHP brain injury.

7.1.4 Other Animal Data

Other animal models for studying TBI found in the literature include rodents, ferrets, pigs, and sheep, as surveyed and reviewed in Johnson et al. (2015) and Xiong et al. (2013). However, the efforts have focused on modeling cerebral contusion. Few clinically relevant models of diffuse injury have been developed. As a continuation of the TBI research on NHP, a porcine model of rotational acceleration brain injury has been developed by Penn (Browne et al., 2011; Cullen et al., 2016; Meaney et al., 1995) and other groups (Fievisohn, 2015) using young or adult miniature swine. Recently, an animal model called CHIMERA (Closed-Head Impact Model of Engineered Rotational Acceleration) was developed to primarily produce DAI using mice, rats or ferrets (Namjoshi et al., 2017; Sauerbeck et al., 2018). Although these animal models of TBI can provide insight and guidance to studies of human TBI, ultimately, the findings from animal model studies must be translated to make preventing human TBI possible. This translational challenge requires significant efforts and collaboration in the future.

7.2 Assembled Database

7.2.1 Data Summary

In this work, a comprehensive injury dataset (including sub-injurious cases) was collected to evaluate injury metrics and develop injury risk functions. The injury dataset consists of sub-

injurious volunteer tests, laboratory reconstruction data of professional football, and NHP tests (Figure 7-1). For each head impact scenario in the primary database (Table 7-2), six-degree-of-freedom (6DOF) time-history head kinematic data is either experimentally reconstructed from real-world impacts (football), or directly measured from sensors attached to the head (human volunteer tests and animal tests). The gross clinic outcome from the impact was well documented based on diagnosis or pathology. The secondary database (Table 7-2), in which only peak magnitudes of the kinematics were available, was less effective in estimating brain injury tolerance but might be useful for evaluating developed injury tolerance.

Table 7-2. Summary of injury data collected for this dissertation

	Data Source (Reference)	Sample Size (n=300)	Surrogate	Impact Category (Direction)	Severity (Sample Size)
Primary	NBDL volunteer (Ewing et al.1972)	50	Human (male)	Sled (oblique, lateral & frontal)	Sub-injurious (50)
	Pellman football reconstruction (Pellman et al. 2004, Sanchez et al. 2018)	53	HYBRID III, 50TH	Real-world impact (complex)	Sub-injurious (33), mild (20)
	McCarthy football reconstruction (Internal*)	36	HYBRID III, 50TH	Real-world impact (complex)	Sub-injurious (17), mild (19)
	Penn non-impact rotational tests (Thibault & Gennarelli. 1990)	56	Baboon	Rotation (axial & coronal)	Severe (56)
	UMTRI blunt Impact (Stalnaker et al. 1977)	17	Macaque	Impactor tests (lateral and occipital)	Sub-injurious (4), mild (8), Severe (5)
	JARI blunt Impact (Kikuchi et al. 1982)	5	Macaque	Impactor tests (lateral)	Sub-injurious (5)
Secondary	NIH whiplash (Ommaya, 1971)	38	Macaque	Sled (rear)	Sub-injurious (22), mild (16)
	NIH blunt Impact (Ommaya, 1971)	45	Macaque	Impactor tests (occipital)	Sub-injurious (28), mild (17)

*Funk et al., 2019. Personal Communication.

Figure 7-1. Examples of biomechanical injury data included in this dissertation.

7.2.2 Injury Diagnosis and Classification

To determine and to quantify individual injuries, the degrees of injury severity in the dataset are classified as 'no injury,' 'mild TBI,' and 'severe TBI.' A concussion is considered as a mild TBI (mTBI), while severe TBI (sTBI) includes DAI and ICH. The diagnosis of concussion for individual human data is from the data sources (Pellman et al., 2003; Ewing et al., 1972). The injury severity of the animal data is classified by considering both the documented symptoms and the pathology results, as shown in Table 6-3, in which corresponding injury severities in terms of the Abbreviated Injury Scale (AIS) coding system is also summarized. The AIS, widely accepted as a gold standard for traumatic injury classification and severity scaling, classifies individual injuries on a 6-point scale (1=minor and 6=maximal) (Gennarelli and Wodzin, 2006), but the injury report for the legacy data in the current dataset was not sufficient so that the injuries can be measured using a 6-levels classification system.

Typical focal injuries (e.g., contusion, SDH, and EDH) and brainstem/spinal cord injuries are not included, and cases with those injuries were discarded because the current FE models were not suitable for predicting those types of injuries. The procedure for injury classification adopted in this dissertation is illustrated in Figure 7-2.

Table 7-3. Injury classification system for animal data used in this study.

Severity Level*	Injuries	Symptoms**	Pathology	AIS98	AIS2005
No Injury	-	-	-	0	0
Mild TBI	Concussion	Coma, other symptoms	-	2-3	1-3
Severe TBI	DAI, ICH	Coma	Axonal damage, hematoma	4-5	4-5

*Note: The is different from the AIS system. The AIS classifies individual injuries as follows: AIS 1 – Minor, AIS 2 – Moderate, AIS 3 – Serious, AIS 4 – Severe, AIS 5 – Critical, AIS 6 – Maximal (currently untreatable).

**Coma is the necessary symptom for severe TBI, while not necessary for mild TBI.

*** Critical revisions were made for AIS in 1998 (AIS98) and 2005 (AIS2005).

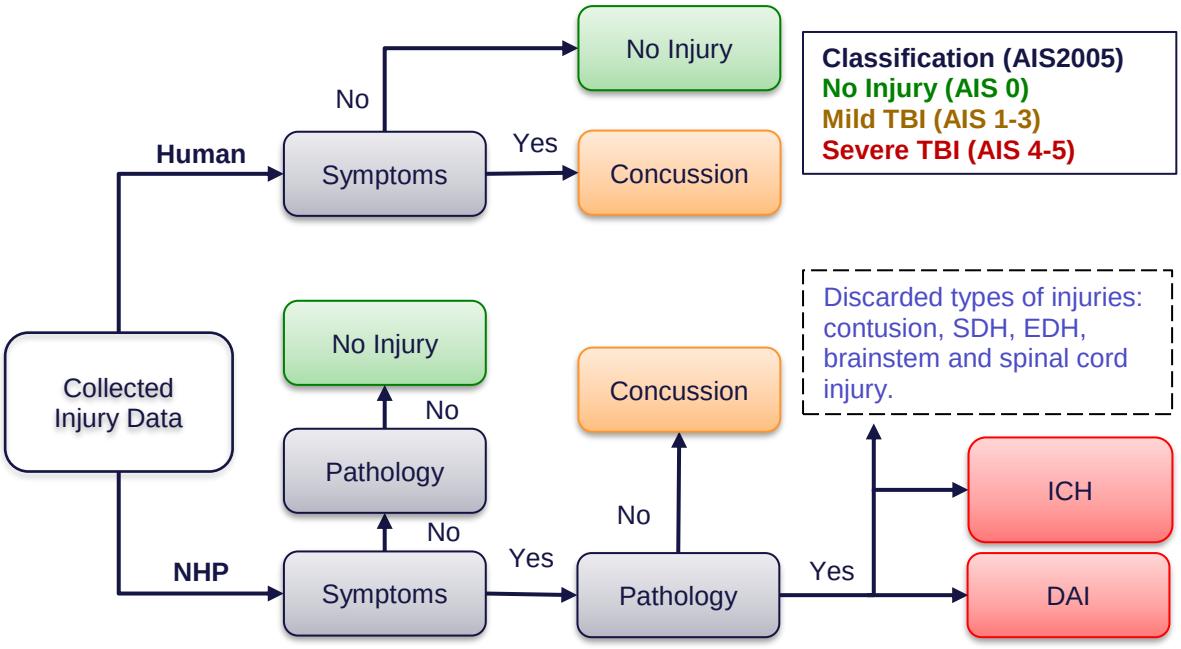

Figure 7-2. Schematic diagram of injury classification.

7.2.3 Head Kinematics

Head kinematics of human cases were previously processed in a standardized manner (Sanchez et al., 2018, 2017), and newly collected data were prepared by following the same procedure. Head kinematic data of animal tests was digitalized from referred publications or internal test reports. The kinematics traces were processed to account for certain notable errors

incurred during recording and revealed in the literature (Mendis, 1992). After correction, all the included NHP kinematics traces yielded reasonable head motion, which corroborates the documented information (e.g., films and photos) and physical constraints of the test device.

The resultant head peak rotational kinematics sustained by the subjects in the compiled database covers a broad range of acceleration and velocity magnitudes for both the human (64.5 – 12,475.0 rad/s^2, 3.3 – 63.8 rad/s) and the NHP (1,566.0 – 476,765.1 rad/s^2, 31.0 – 594.0 rad/s), as illustrated in Figure 7-3. Unlike the controlled animal tests, in which the tests were designed and performed under certain dominant direction. The human data, in particular, the football reconstruction data has more complex head kinematics. The distribution of direction-dependent rotational kinematics for the human data is shown in Figure 7-4. The football reconstruction data from two separate sources had a similar distribution of kinematics and clearly high-level rotational motion in the coronal direction.

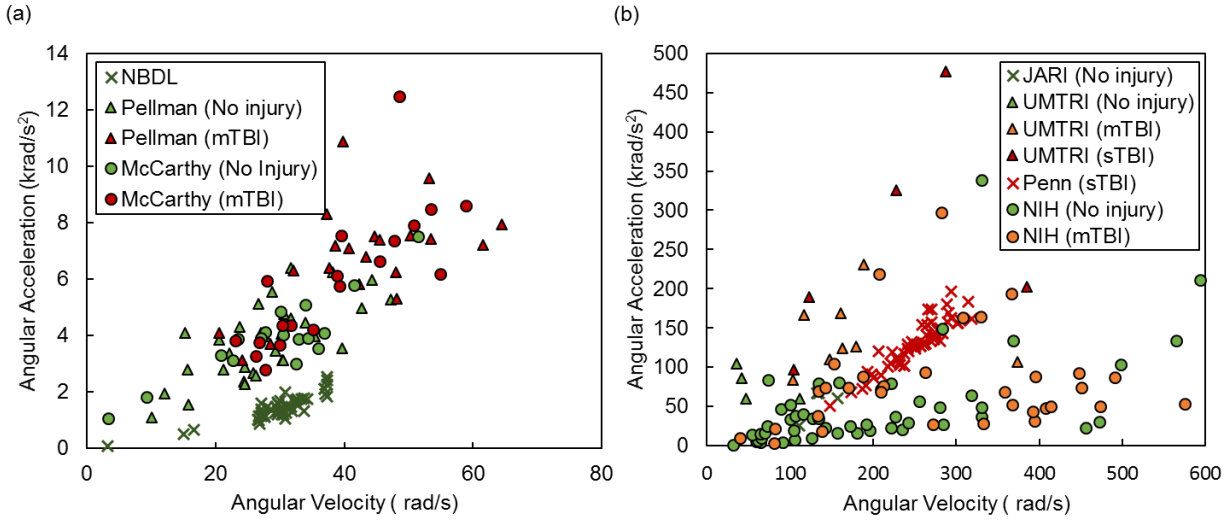

Figure 7-3. Resultant peak angular velocities and peak angular accelerations in the compiled human (left) and NHP (right) database.

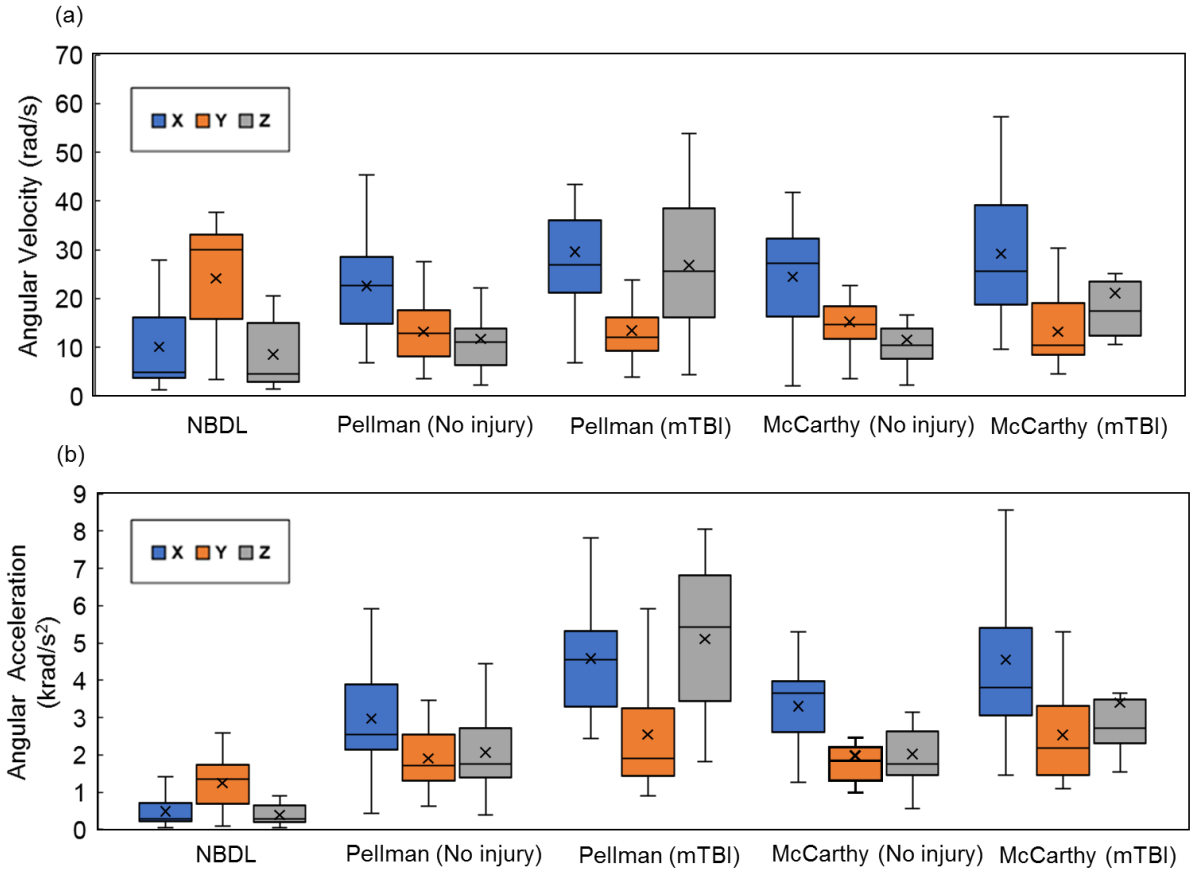

Figure 7-4. Directional distribution of angular velocities (a) and peak angular accelerations (b) in the compiled human database.

7.2.4 Data Integration

In this dissertation, the underlying assumption is that tissue-level responses can be aggregated together independent of loading conditions and (primate) species. Using the advanced FE models developed in Chapters 3 – 5 and by applying the head kinematics directly to the rigid dura through the center of gravity of the head, tissue-level metrics were predicted for each test. As an example, the distributions of MPS (95^{th}) in the primary database categorized by their injury severities and sources are shown in Figure 7-5. In average, the three sets of mTBI cases from different sources had similar MPS values ($p= 0.463$), when comparing different groups using one-way analysis of variance (ANOVA). This similarity partially confirms the validity of the underlying assumption.

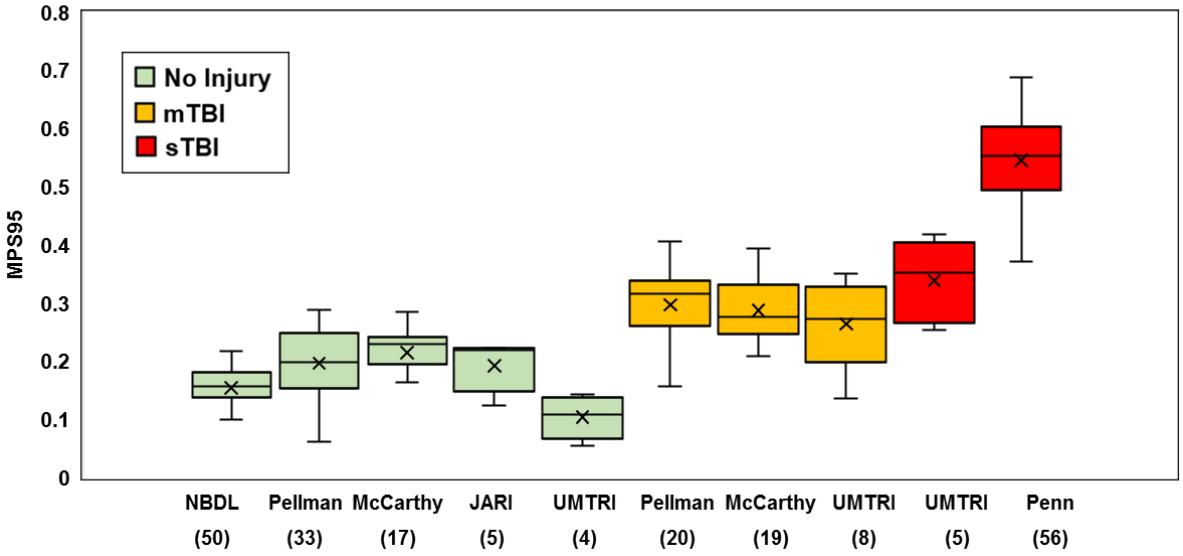

Figure 7-5. Distributions of maximum principal strain in the primary database.

7.3 Summary

In this chapter, sixty years of brain injury investigations using *in vivo* model were taken together. The main observation is the huge disparities in relation to test protocols, loading conditions, and the resulting types of injuries. Thus, when selecting the existing experimental results to study specific types of brain injuries, it has to be oriented towards the objectives. A dataset of 300 cases, with a diverse spectrum of clinical outcomes spanning from no injury to severe diffuse injuries, was collected and prepared for simulation. Despite the seeming huge disparities in head kinematics, injury data from different sources from the tissue-level perspective seem to corroborate with each other. Integration of this dataset and utility of this dataset in understanding injury tolerance was explored in the next chapter.

CHAPTER 8 : EVALUATION OF INJURY METRICS AND DEVELOPMENT OF INJURY RISK FUNCTIONS

In this chapter, tissue-level responses predicted by the newly developed computational models were analyzed for their correlation with injury outcomes using the database established in Chapter 7. The efficacy of existing tissue-level injury metrics for predicting brain injury were evaluated through statistical analysis. To delineate actual injury causation and establish a meaningful injury metric, the uncertainty of model/metric selection linked with small sample sizes as well as the frequently misunderstood statistical ideas were discussed before arriving a tentative conclusion based on the state of knowledge of injury mechanism. New brain injury tolerance levels in the form of injury risk functions were established using a subset of the compiled database and validated for efficiency through the independent dataset.

8.1 Introduction

Numerous brain injury tolerance curves and injury risk functions (IRFs) have been proposed over the years (Gurdjian et al., 1966; Ono et al., 1980; Rowson et al., 2012a; Rowson and Duma, 2013b; Takhounts et al., 2013). However, the efficacy of these brain IRFs depends on the capability of the associated injury metrics to predict brain injury. Historically, these injury metrics have been derived using a mathematical combination of either the external head kinematics (kinematics-based metrics) or measurements of internal responses at the tissue-level, such as stress or strain (tissue-level metrics) from FE models. The earliest kinematics-based metrics were based on the linear acceleration of the head (Elliot J Pellman et al., 2003; Versace, 1971), but recent injury criteria have shifted towards using rotational head kinematics (Gabler et al., 2018a, 2018b; Rowson et al., 2012a; Takhounts et al., 2013) or a combination of linear and rotational kinematics

(Rowson and Duma, 2013b). This is due to the recognition that rotational head kinematics are the primary cause for brain deformation given the incompressibility of brain tissue (Holbourn, 1943). However, because of the limited quantity of injury data, many of these kinematics-based metrics (Gabler et al., 2018b, 2018a; Takhounts et al., 2013) were developed with the underlying assumption that the corresponding tissue-level responses (strain in particular) are accurate predictors of brain injury (Gabler et al., 2016).

Many tissue-level metrics have been derived from finite element (FE) simulations of reconstructed real-world events. Most notable candidates are the maximum principal strain (Takhounts et al., 2013), tract-oriented strain (Giordano and Kleiven, 2014a), Von Mises Stress (Kleiven, 2007), strain rate (Sullivan et al., 2015), and pressure (Zhang et al., 2004). However, the accuracy of these tissue-level metrics has yet to be determined with reliable experimental TBI data.

Recently, Sanchez et al. (2018) evaluated fourteen existing head and brain IRFs with respect to laboratory-controlled human volunteer response data (Sanchez et al. 2018) and found that several injury risk curves substantially overpredicted the likelihood of mTBI. Given the various brain injury metrics and IRFs that have been proposed, it is not always clear which metric (s) should be used to characterize human brain injury tolerance, and there is no consensus on human brain injury tolerance. The objective of this study was to estimate human tolerances of mTBI and sTBI based on comprehensive statistical analysis. The capability of existing tissue-level and kinematics-based brain injury metrics was first assessed for predicting TBI. Based on their correlation with injury, a set of favorable tissue-level metrics were used to develop injury risk functions for mTBI and sTBI.

8.2 Method

8.2.1 Injury Data

The injury database collected and used in this study was introduced in Chapter 7. The primary dataset (including NBDL volunteer data, Pellman and McCarthy football reconstruction data, UMTRI, UPenn, and JARI NHP data, n=217) was used to evaluate injury metrics. Most of the data in the primary dataset were used as a training set (n=181) to build IRFs. The McCarthy football reconstruction data in the primary dataset (n=36) and the secondary dataset (n=83) were used as an independent test set left aside for evaluation purposes, as those data have never been used in developing injury risk functions.

8.2.2 Injury Metrics Evaluation

A range of tissue-level strain injury metrics (Table 8-1) widely used in the literature was assessed using the injury data. These metrics included the most widely used tissue-level injury metrics proposed in the literature and can be categorized into dimensionless metrics and dimensional metrics. For all the tissue-level injury metrics using peak values (all metrics except for CSDM25 and CSDM15), the 95th percentile values were used to avoid any numerical instabilities (Panzer et al., 2012). These tissue-level metrics were derived by simulating the head impacts in each of the experiments included in the database using the computational models developed in Chapters 3 – 5.

In addition to the tissue-level metrics, a battery of kinematics-based injury metrics commonly used for predicting human brain injury in the literature was assessed, as summarized in Table 8-2. The assessed metrics included head kinematic metrics: peak resultant linear acceleration (a_{max}), peak resultant angular velocity (ω_{max}), and peak resultant angular acceleration (α_{max}); the most frequently used metrics: Head Injury Criterion (HIC), Combined Probability of

Concussion (CP), Brain Injury Criteria (BrIC), and the most recently proposed metrics: Convolution of Impulse Response for Brain Injury Criterion (CIBIC), Universal Brain Injury Criteria (UBrIC), and Diffuse Axonal Multi-Axial General Evaluation (DAMAGE). The constraints and critical values for these injury metrics were adapted from the corresponding studies. A brief description of each metric is provided in Appendix D.

Table 8-1. Tissue-level injury metrics assessed in this study.

Metrics	Description	References	Dimensional
MPS95	maximum principal strain	Gabler et al., (2016)	No
CSDM25	cumulative strain damage measure (25%)	Takhounts et al., (2013)	
CSDM15	cumulative strain damage measure (15%)	Sahoo et al., (2016)	
MAS95	axonal strain	Giordano and Klevien, 2014b	
PRS95	absolute pressure	Zhang et al., (2004)	Yes
VMS95	Von Mises stress	Kleiven, (2007)	
MPSSR95	the strain rate of the maximum principal strain	Kleiven, (2007)	
MPS×SR95	the product of MPSSR and MPS	Kleiven, (2007)	
MASSR95	the strain rate of the maximum axonal strain	Sullivan et al., (2015)	
MAS×SR95	the product of MASSR and MAS	Sullivan et al., (2015)	

Table 8-2. Kinematics-based injury metrics assessed in this study.

Metrics	Underlying Kinematics	References	IRCs*
$\mathbf{a_{max}}$	LA	Pellman et al., (2003)	Yes
$\boldsymbol{\omega_{max}}$	AV	Rowson et al., (2012)	
$\boldsymbol{\alpha_{max}}$	AA	Rowson et al., (2012)	
HIC	LA[d]	NHTSA, (1995)	
CP	LA, AA	Rowson and Duma, (2013)	
BrIC	AV[c]	Takhounts et al., (2013)	
CIBIC	AA [c,d]	Takahashi and Yanaoka,(2017)	No
UBrIC(M),(C)**	AV [c] ,AA [c]	Gabler et al., (2018a)	
DAMAGE	AV [c,d] ,AA [c,d]	Gabler et al., (2019)	

LA: linear acceleration; AV: Angular velocity; AA: Angular acceleration; c: Indicates that the metric is directionally dependent. d: Indicates that the metric requires time history information.
*Indicates whether IRCs were available, for details on these IRCs, please refer to the appendix E.
** M: MPS-based UBrIC, C: CSDM-based UBrIC.

Since the injury metrics investigated here includes both dimensional and dimensionless metrics, the evaluation processes were two-fold:

First, the evaluation was performed separately for human data and animal data to reduce the influence of size and mass. The human data were used to evaluate the capability of the metrics to distinguish between no injury and mTBI, while the animal data were used to evaluate the capability of the metrics to distinguish between mTBI and sTBI. Kinematics-based metrics were not evaluated with animal data, except for ω_{max} and α_{max}, as most of them are designed only for predicting human brain injury with specific critical values. Most of the animal data in the database also lack translational motion and thus were unable to access the metrics associated with linear acceleration (e.g., a_{max} and CP).

Second, both dimensional and dimensionless tissue-level metrics were accessed using all the data in the primary database, as integrating data for different tissue metrics requires a fundamental understanding and consideration of the biomechanical principles, as detailed in the following section.

8.2.3 Data Integration Strategy

The central idea of integrating injury data across species based on an underlying assumption that tissue damage (and microscale damage) is the causation of TBI, and the threshold of tissue damage should be not affected by the brain size but can be affected by loading conditions (e.g., strain rate effect). In other words, tissue-level metrics derived from brain FE models of different species should be combined without scaling. However, basic kinematics-based metrics should be scaled to obtain a similar tissue-level response, and ω_{max} and α_{max} were scaled based on frequency scaling (Chapter 6) using individual brain mass. Kinematics-based metrics, including BrIC, CIBIC, UBrIC, and DAMAGE, were designed to predict strain responses. Theoretically, they were dimensionless. But a large disparity in the metric values was observed between animal and human as a result of the differences between the underlying human FE models and the models

used here (both human and animal brain models). Those metrics were not directly scaled, but the underlying kinematics (ω and α) were scaled using frequency scaling, and the scaled kinematics were used to calculate the injury metrics.

Assuming the tissue-level metrics were also not the causation of TBI, some tissue-level metrics can be scaled based on the principles of dimensional analysis. Dimensionless tissue-level metrics, including MPS, MAS, CSDM15/25, can still be directly compared with each without the influence of size or loading conditions. So those data for different species could be directly combined. The pressure response mechanism and the dimensional relationship was derived analogously to the well-established hydrostatic pressure (Zhao et al., 2015). Brain pressure responses are uniquely determined by linear acceleration (a, magnitude and directionality), brain mass (m) and the effective brain-skull contact area (A) effected by brain shape ($\lambda_{PRS} = \frac{\lambda_m}{\lambda_A}\lambda_a$). The ratio of the pressure of different sizes is close to 1 (thus pressure does not need scaling between species) , this is similar to the findings in the literature (Panzer et al., 2014). Strain rate associated metrics, including MPSSR, MPS×SR, MASSR, MAS×SR are driven by the loading conditions, consequently, those metrics from animal tests could be scaled based on dimensional analysis. Frequency scaling using individual brain mass information was used to compare and combine with those resulting from the human cases. VMS has the same units as that of pressure and does not need scaling if the material follows the linear stress-strain behavior. However, VMS is strain rate dependent due to the viscoelastic behavior of brain tissue, no existing scaling technique was able to account for the effect of strain rate according to my knowledge. The VMS results of the animal results were scaled to match with the human results through phenomenological relationship to alleviate the effect of loading rate (Figure 8-1). Taken together, both the unscaled and scaled values of the tissue-level metrics were considered in the metric selection process.

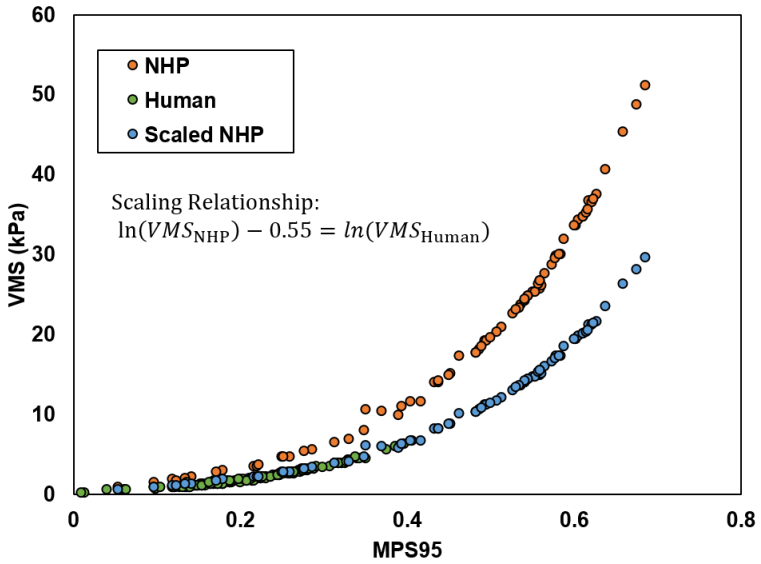

Figure 8-1. Comparison between the VMS results of the human and animal simulation.

8.2.4 Metrics Selection

To evaluate injury metrics, logistic regression (Equation [8-1]) was employed to correlate binary injury data (injury/no injury or mTBI/sTBI) with continuous metrics (x). Stukel tests (Stukel, 1988) were performed to determine whether or not the relationship between the clinical outcome and the injury metrics were statistically significant. The Stukel test evaluated whether a generalized logistic model is a better fit to the data than a standard logistic model. Two additional parameters (z_a and z_b) were added in the generalized logistic model to allow the tails of the logistic regression model to be either heavier or lighter than the standard logistic regression model. This significance test determines whether the two parameters in the modified generalized logistic model are equal to zero. If $z_a = 0$ and $z_b = 0$ (P > 0.1), the generalized logistic model of interest is not a significantly better fit to the data, while the standard logistic model based on the associated metric is regarded as a good fit to the data.

$$P_{inj} = \frac{e^{a+bx}}{1 + e^{a+bx}} \qquad [8\text{-}1]$$

For model/metric selection, Akaike information criterion (AIC) (Akaike, 1974) has been widely used (Petitjean et al., 2012; Yoganandan et al., 2016). It has been shown that choosing a model that has the lowest AIC value is asymptotically equivalent to choosing the model with the lowest expected information loss (Wagenmakers and Farrell, 2004). The AIC is defined as

$$AIC = -2\log(L) + 2V \qquad [8\text{-}2]$$

Where L is the maximum likelihood for the candidate model, V is the number of independent variables (Note that V= 1 in this study). However, it was difficult to intuit how much statistical importance should be given to a difference in the AIC values. Selecting a single model may lead to a false sense of confidence, especially when the sample size is small. The weight of evidence in favor of the good models was evaluated using Akaike weights (Equation [8-3]). The rule of thumb (Posada and Buckley, 2004) was that a 95% confidence set of models could be established for the best model by summing the Akaike weights from largest to smallest until the sum is just 0.95 (Akaike weights for all models combined should add up to 1).

$$w_i(AIC) = \frac{\exp(-0.5\Delta_i(AIC))}{\sum_{i=1}^{K}\exp(-0.5\Delta_i(AIC))} \qquad [8\text{-}3]$$

$$\Delta_i(AIC) = AIC_i - \min AIC \qquad [8\text{-}4]$$

8.2.5 Development of Tissue-Level Injury Risk Functions

Tissue-level IRFs for mild TBI and severe TBI were developed using a combination of human and NHP data from the primary database. The development of IRFs was guided by the International Organization for Standardization (ISO) procedure (ISO/TS 18506:2014) to construct IRFs for the evaluation of road user protection in crash tests (Petitjean and Trosseille, 2011). IRFs were also developed using survival analysis if applicable, assuming a Weibull distribution per Equation [8-5]. A Weibull distribution was selected to ensure zero risks of injury given zero

stimuli. All the statistical analysis mentioned above was conducted using the R-studio software, version 1.1.456 (R Studio, Inc.)

$$P_{inj} = 1 - e^{\left(-e^{\left(\frac{1}{b}*\ln(x)-\frac{a}{b}\right)}\right)} \quad [8\text{-}5]$$

Where a and b are coefficients corresponding to the scale (1/b) and shape (e^a) parameters in the Weibull distribution.

8.2.6 First-Step Evaluation using Sub-Injurious Data.

In addition to the above analysis, the accuracy of each generated risk function was evaluated by comparing the expected number of injuries predicted by injury risk functions relative to the true diagnosis of the NBDL volunteer data (Sanchez et al., 2017). For each of these volunteers, the most severe sled run (based on injury risk) was identified for each of 16 volunteers (subject-specific identifiers were only available for 16 subjects out of 22). For each risk function, the highest injury probability measurements for each of the 16 volunteers were collected and summed to obtain the expected number of injuries (Sanchez et al., 2017).

8.2.7 Evaluation of Injury Risk Functions using Independent Experimental Data

Both the McCarthy football reconstruction data and the NIH NHP data have never been used to develop injury risk functions, which makes them an ideal test set to evaluate the proposed IRCs. The predicted injury probability based on the newly developed mTBI IRFs and some of the existing IRFs (NHTSA, 1995; Rowson et al., 2012a; Rowson and Duma, 2013b; Takhounts et al., 2013) were compared with the real injury results. All risk functions based on the HIC, ω_{max}, α_{max}, and CP were from the literature (Table A7 in Appendix E) unless indicated otherwise.

The receiver operating characteristic curves (ROC) curve was used to assess how well the metric discriminates, or separates individuals with or without injury, while the predictive

capability of the IRFs was evaluated by comparing the expected values with the true number of injuries. ROC curves are frequently summarized in a single value, the area under the ROC curve (AUC). A major advantage of ROC curves is that they depict the performance of the classifiers over the complete range of threshold values. As the ROC curve is threshold-independent, so is the resulting AUC. In other words, shifting or scaling the risk function along the predictor axis would not change the AUC values. Predicted risk probabilities are important for IRFs; therefore, the expected values were used in conjunction with AUC to evaluate the performance of the IRFs.

While it was straightforward to use the McCarthy football cases to evaluate IRFs, calculating the risk of cases in the secondary database (NIH data, Ommaya, 1971) requires further approximation because of the lack of the time-history head kinematics data required for simulation. In those experiments, mTBI was produced either by direct impact to the occipital zone of the head or by experimental whiplash sled tests; thus, the primary rotational motion was assumed to be in the sagittal plane. Since the global strain-based responses were reasonably insensitive to pulse shape (Gabler et al., 2018c), the MPS values of those tests were estimated using the uniaxial sagittal response surface generated from Chapter 6 (Figure 6-5). For metrics that do not require the full time-history head kinematics (e.g., BrIC), metric values were scaled to humans using the frequency scaling.

8.3 Results

8.3.1 Metrics Evaluation Using Separate Dataset

As shown in Table 8-3, significance test results clearly show that metrics associated with pressure and linear acceleration (PRS95, a_{max}, HIC) result in a poor fit to the data using logistic regression. In general, strain metrics (MPS95, MAS95) were deemed a good predictor of both mTBI and sTBI based on the current dataset. The correlation between CSDM and injury depended

on the choice of critical strain threshold and injury severity. The current analysis was unable to delineate the effect of strain rate as metrics associated with strain rate (MPSSR95, MPS×SR95, MASSR95, MAS×SR95) correlated well with human injury data when the range of strain rate was small (0.5 – 65 1/s) but did not represent NHP data when the range of strain rate was large (29 – 447 1/s). MPS95 and VMS95 were the only two metrics that fall within the 95% confidence set of selected models for both human and NHP data. No evidence in the current database showed that the global axonal strain (MAS95) correlates better with injury than the global principal strain (MPS95).

Table 8-3. Significance tests for logistic regression models using different injury metrics.

Metrics	Category	Human Data (No Injurys:139, TBI:39)					NHP Data (mTBI:17, sTBI:61)				
		Stukel (P*)			AIC	Weight**	Stukel (P)			AIC	Weights
		z_a	z_b	z_a&z_b			z_a	z_b	z_a&z_b		
MPS95	Tissue	0.72	0.95	0.87	92.2	4.8%	0.42	0.86	0.72	20.4	16.7%
CSDM25		0.41	0.03	0.07	102.2	0.0%	0.78	0.76	0.92	19.7	23.2%
CSDM15		0.52	0.63	0.81	95.2	1.1%	0.04	0.12	0.03	24.5	2.1%
MAS95		0.63	0.98	0.80	94.2	1.8%	0.58	0.73	0.81	22.9	4.7%
PRS95		0.02	0.01	0.03	128.1	0.0%	0.20	0.31	0.26	76.8	0.0%
VMS95		0.72	0.30	0.52	90.2	13.6%	0.47	0.92	0.77	18.1	52.4%
MPSSR95		0.85	0.38	0.60	89.4	20.2%	0.16	0.31	0.22	39.3	0.0%
MPS×SR95		0.53	0.19	0.42	91.6	6.6%	0.61	0.33	0.55	26.4	0.9%
MASSR95		0.54	0.79	0.51	88.6	29.2%	0.03	0.25	0.05	56.2	0.0%
MAS×SR95		0.99	0.37	0.42	90.5	11.5%	0.14	0.05	0.05	39.3	0.0%
a_{max}	Kinematics	0.92	0.16	0.37	109.0	0.0%	--	--	--	--	--
ω_{max}		0.43	0.09	0.17	128.3	0.0%	0.00	0.90	0.00	46.8	0.0%
α_{max}		0.61	0.51	0.71	91.0	9.1%	0.00	0.46	0.00	76.0	0.0%
HIC		0.07	0.01	0.01	108.2	0.0%	--	--	--	--	--
CP		0.73	0.43	0.69	94.7	1.4%	--	--	--	--	--
BrIC		0.63	0.09	0.22	117.6	0.0%	--	--	--	--	--
CIBIC		0.56	0.44	0.62	100.0	0.1%	--	--	--	--	--
UBrIC(M)		0.49	0.89	0.78	109.2	0.0%	--	--	--	--	--
UBrIC(C)		0.24	0.39	0.34	107.0	0.0%	--	--	--	--	--
DAMAGE		0.91	0.66	0.90	97.0	0.4%	--	--	--	--	--

*A low power score (P<0.2) indicate a poor fit to the data.
** Blue highlights indicate the 95% confidence set of models.

Figure 8-2 illustrates the Δ(AIC) values of various injury metrics using different datasets. The fact that different data sets suggest the use of different metrics leads us to the issue of model

selection uncertainty inherent in the statistical analysis on a small dataset. So, it was more reasonable to select a set of favorable metrics instead of a single metric.

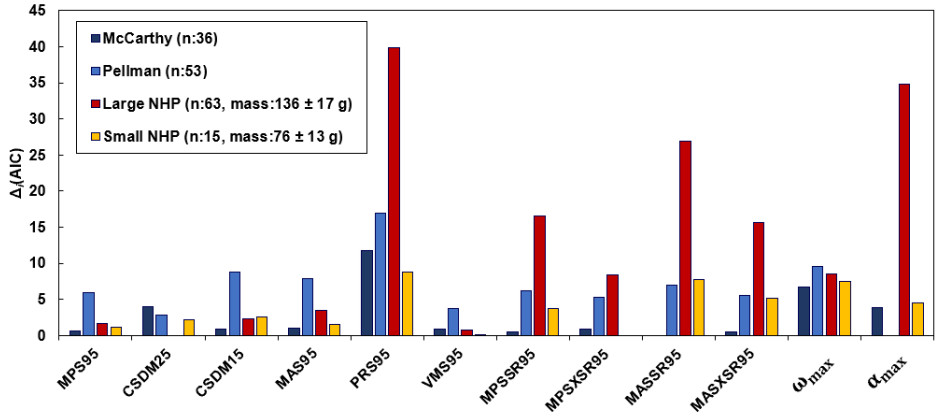

Figure 8-2. Δ(AIC) values of various injury metrics using different datasets.

8.3.2 Metrics Evaluation Using an Integrated Database

Injury metrics were further evaluated using the integrated database. The results of the significance test are summarized in Table 8-4, indicating the following metrics resulting in a good fit of the data: MPS95, MAS95, VMS95 (scaled), MPS×SR95 (scaled). None of the kinematics-based metrics fit the integrated database well. Note that the values of the dimensional metrics in the animal data were usually higher than those in human data because of the size effect, and most of the animal subjects coincidentally sustained more severe injuries. So multiple models/metrics had perfect or quasi-perfect separation.

Table 8-4. Significance tests for different models using the compiled dataset.

Metrics	Scaling Method	mTBI					sTBI				
		Stukel (P*)			AIC	Weight	Stukel (P)			AIC	Weights
		z_a	z_b	z_a&z_b			z_a	z_b	z_a&z_b		
MPS95	Unscaled	0.60	0.40	0.61	114.2	0.49%	0.37	0.23	0.32	45.5	0.00%
CSDM25		0.11	0.01	0.01	123.3	0.01%	0.21	0.53	0.37	46.2	0.00%
CSDM15		0.11	0.12	0.08	131.6	0.00%	0.10	0.00	0.00	81.7	0.00%
MAS95		0.49	0.35	0.51	115.6	0.24%	0.47	0.83	0.75	43.8	0.00%
PRS95		0.01	0.00	0.00	187.9	0.00%	0.00	0.00	0.00	96.3	0.00%
VMS95		0.89	0.15	0.35	108.2*	9.76%	0.52	0.98	0.81	22.3*	96.00%
MPSSR95		0.06	0.00	0.00	163.5	0.00%	0.05	0.22	0.07	40.4	0.01%
MPS×SR95		0.00	0.00	0.00	135.3*	0.00%	0.14	0.07	0.07	28.7	3.91%
MASSR95		0.10	0.00	0.00	169.6	0.00%	0.00	0.00	0.00	61.9	0.00%
MAS×SR95		0.00	0.00	0.00	144.0*	0.00%	0.00	0.00	0.00	46.2	0.00%
VMS95	Scaled	0.71	0.53	0.77	108.1*	10.26%	0.63	0.59	0.77	39.4*	0.02%
MPSSR95	Frequency Scaled	0.91	0.30	0.58	105.9	30.84%	0.10	0.44	0.19	45.8	0.00%
MPS×SR95		0.87	0.40	0.69	107.7*	12.54%	0.75	0.59	0.82	37.3	0.05%
MASSR95		0.77	0.45	0.72	111.6	1.78%	0.01	0.05	0.01	66.5	0.00%
MAS×SR95		0.74	0.54	0.78	105.7*	34.08%	0.17	0.04	0.04	49.8	0.00%
ω_{max}	Frequency Scaled	0.45	0.11	0.21	158.8	0.00%	0.08	0.26	0.11	54.9	0.00%
α_{max}		0.01	0.00	0.00	135.7	0.00%	0.00	0.04	0.00	64.9	0.00%
BrIC		0.43	0.18	0.30	151.2	0.00%	0.07	0.40	0.14	73.4	0.00%
CIBIC		0.87	0.62	0.87	137.4	0.00%	0.45	0.11	0.20	49.5	0.00%
UBrIC(M)		1.00	0.93	1.00	144.0	0.00%	0.24	0.11	0.14	66.0	0.00%
UBrIC(C)		0.64	0.46	0.68	138.5	0.00%	0.30	0.14	0.20	55.7	0.00%
DAMAGE		0.64	0.97	0.89	131.4	0.00%	0.38	0.06	0.11	42.9	0.00%

*Perfect or quasi-perfect separation.

Since both the animal and human data have several mild injury cases, to see if a metric is actually a reflection of injury, the values of the metrics from the human and animal mTBI groups were compared and analyzed for differences using an independent t-test, as shown in Figure 8-3. The averages of animal metrics were significantly different from that of the human metrics, except for those of strain-based tissue-level metrics (MPS95, MAS95, CSDM15, and CSDM25) and VMS95. Significant discrepancy indicates the violation of the fundamental assumption that tissue-level metrics were equivalent. Interpretation of the results based on the scaled tissue-level variable values was manifold and dependent on the scaling approaches. A rational basis for scaling tissue-level metrics is still lacking from the biomechanical perspective. So, the AIC values from scaled tissue-level metrics were not used to select the models.

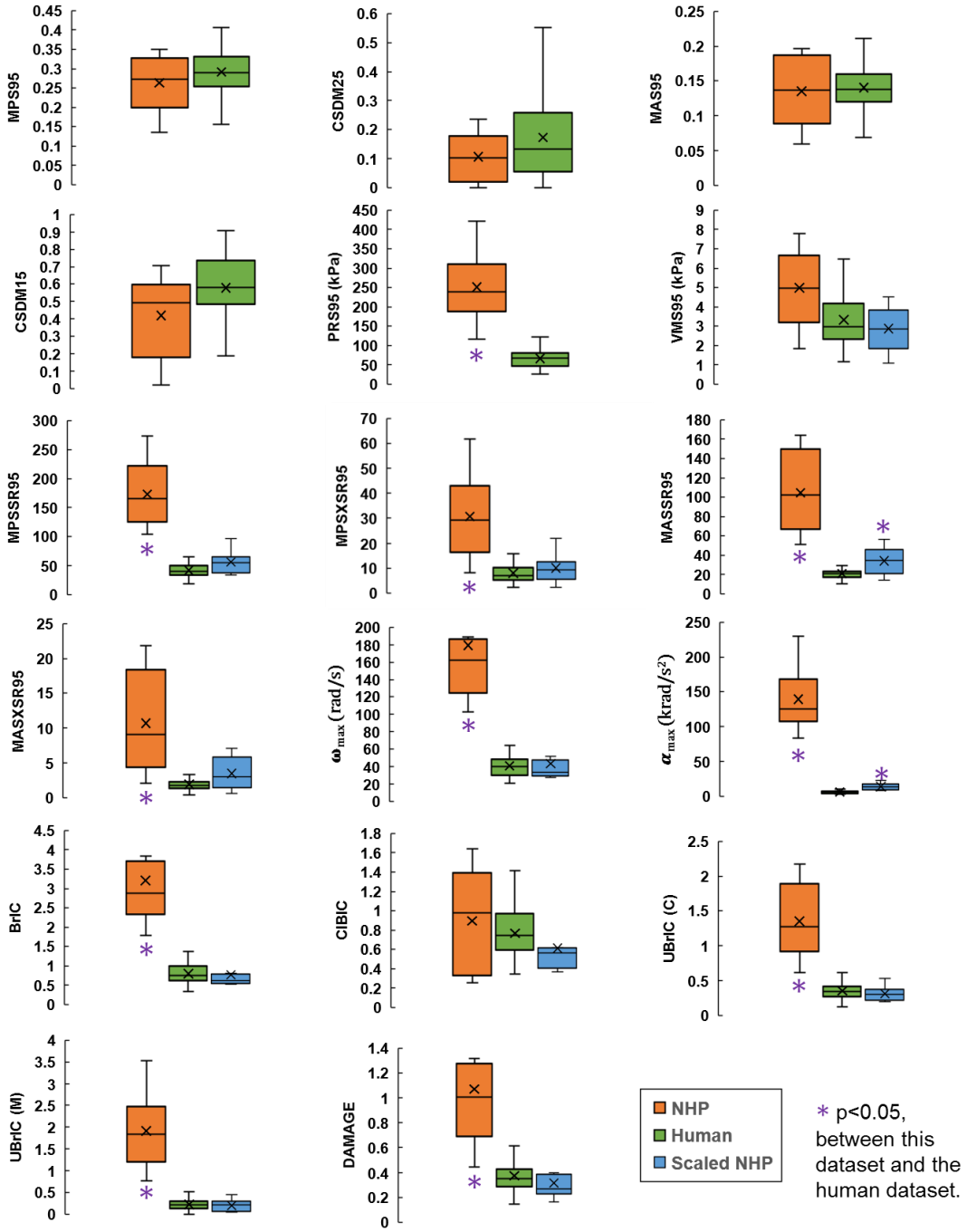

Figure 8-3. Distribution of metric values for mild brain injury cases in the human and animal dataset.

8.3.3 Injury Risk Curves

Based on the above analysis, a set of tissue-level metrics, including MPS95, MAS95, and VMS95 (unscaled) were selected to develop IRFs assuming Weibull distribution in the survival analysis. As illustrated in Figure 8-4, two alternative distributions, log-logistic distribution, and log-normal distribution were considered and plotted with nonparametric maximum likelihood estimation (NPMLE). Regardless of the form of the injury risk function, the underlying data samples used to develop the injury risk function have a profound effect on the final fit.

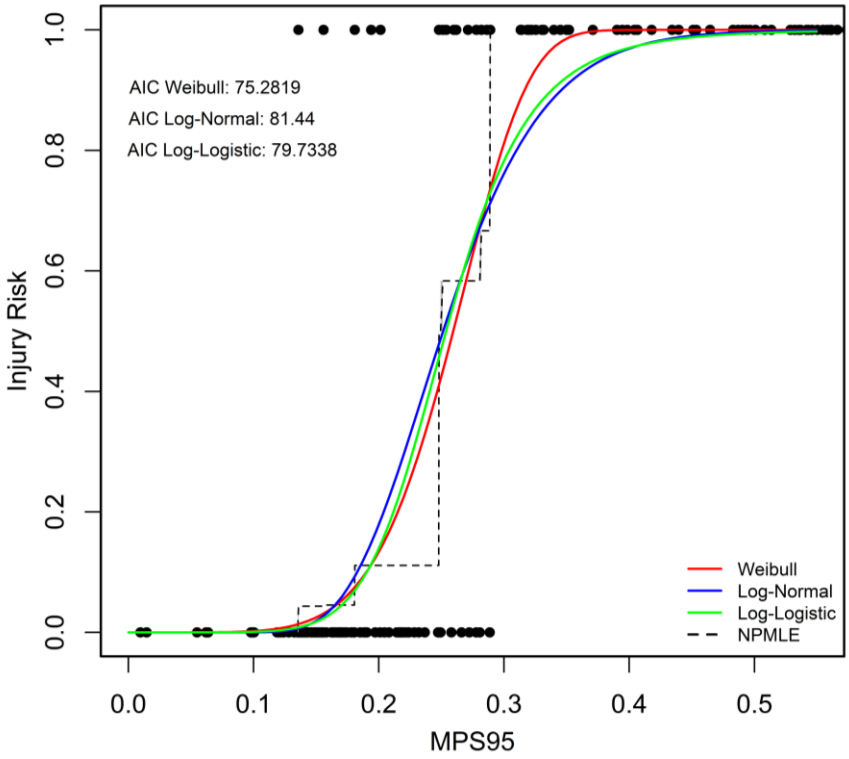

Figure 8-4. Comparison of risk curves based on different distribution assumption.

Figure 8-5 shows exemplary mTBI IRF based on MPS95 using survival analysis and data integration method 3. The influential cases were identified using the dfbeta statistics, but these cases did not significantly change the IRF. These cases were kept in the construction of the IRF (Figure 8-5 (b)). The distribution assumption was checked graphically using a Q-Q plot ("Q" stands for quantile). The percentiles of the distribution are plotted against the corresponding percentiles

of the biomechanical sample. The points seem to fall about a straight line; thus the chosen distribution is appropriate (Figure 8-5 (c)). Another way is to graphically plot the cumulative risk calculated with the survival analysis with a given distribution against the cumulative risk calculated with an NPMLE. The cumulative risks lie close to one another, indicating that the chosen distribution is appropriate (Figure 8-5 (d)). These analyses were performed for all IRFs, and detailed results are provided in Appendix E.

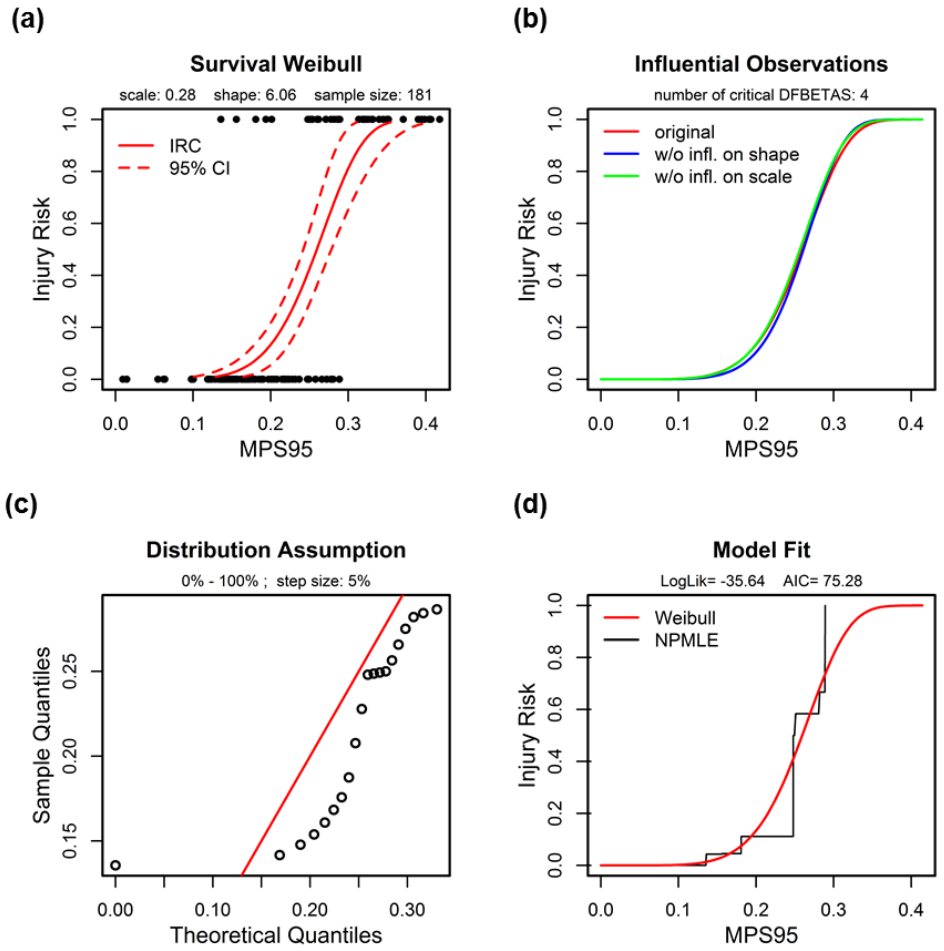

Figure 8-5. Mild brain injury risk curves based on MPS95. (a) Injury risk curves and 95% confidence interval; (b) Effects of overly influential observations; (c) Q-Q plot to check distribution assumption; (d) Model fit verified with non-parametric method (NPMLE).

8.3.4 Evaluation of Injury Risk Functions Using Sub-Injurious Data

Using responses of the sub-injurious volunteer tests, the MPS95 and MAS95 predict a similar number of mTBI injuries (1.407 and 1.234 respectively), while VMS95 estimates a smaller number of mTBI injuries (0.571). All these predictions were reasonable and consistent with the diagnosis in the volunteer data.

8.3.5 Evaluation of Injury Risk Functions Using Independent Data

The newly developed IRFs were evaluated with the pre-reserved independent data, and their performances were compared with the performance of existing IRFs (HIC, ω_{max}, α_{max}, and CP) from the literature (NHTSA, 1995; Rowson et al., 2012a; Rowson and Duma, 2013b; Takhounts et al., 2013). MAS95 results are not shown as they are almost identical to those of the MPS95. ROC curves were drawn using the injury risk probabilities from each injury risk function (Figure 8-6). The AUC of each predictor was also computed for all ROC curves to compare the predictive capability of the different injury risk functions. As expected, all injury risk probabilities were statistically better than random guessing. Both the VMS and MPS injury risk functions showed better performance than existing risk functions considering both the AUC (Figure 8-6) and expected values (Figure 8-7).

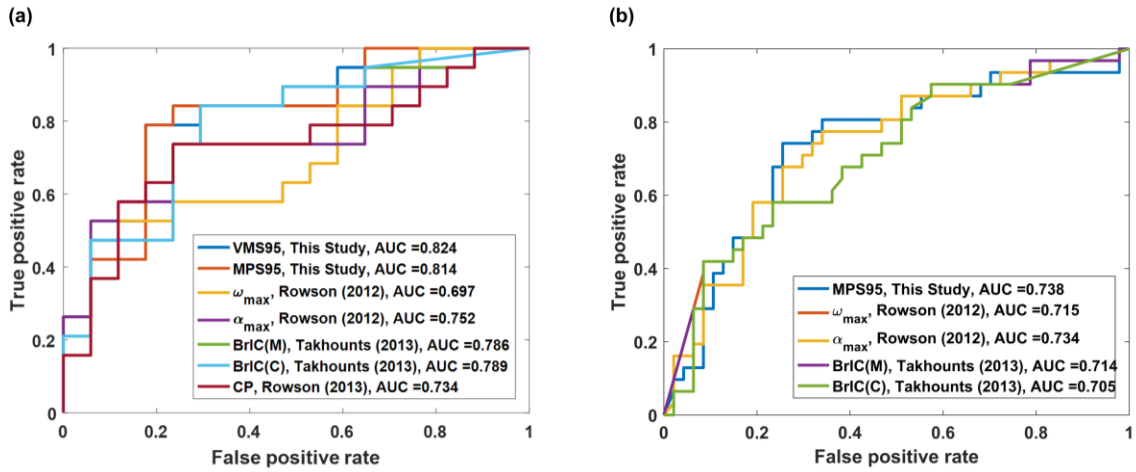

Figure 8-6. ROC curves and their respective area under the curves (AUC) using various injury risk metrics for the McCarthy football data (a) and NIH NHP data (b).

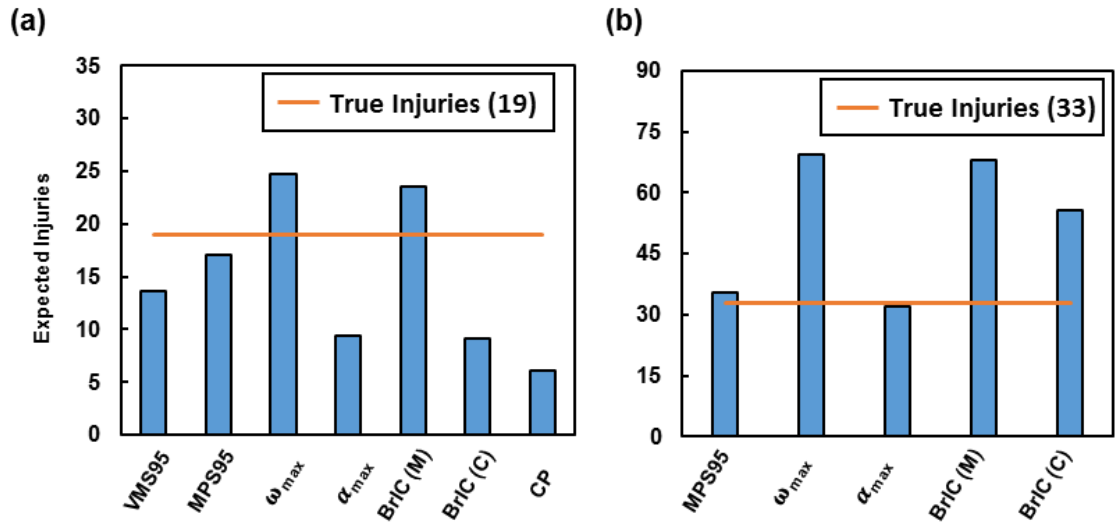

Figure 8-7. Expected number of mild brain injuries predicted using each of the injury risk functions for the McCarthy (a) and NIH dataset (b).

8.4 Discussion

A variety of *in vivo* injury data collected in the past sixty years was taken together to assess the correlation between various injury metrics and injury outcomes. Based on the analysis, tissue-level metrics including VMS95, MPS95, and MAS95 were selected to develop the human risk functions of mTBI and sTBI. Better predictability was found by using the newly developed IRFs compared with existing IRFs when evaluated with independent injury data. The findings of this analysis partially confirm the popular hypothesis that deformation is the causation of brain injury.

8.4.1 Comments on Statistic Analysis

Logistical regression was used to assess the correlation between various injury metrics and clinical outcomes. The results indicated that most of the assessed injury metrics strongly correlated with injuries. However, the current injury dataset utilized in this study was unable to determine which metric was the best predictor of injury. Although AIC analysis lends some favor to VMS over MPS, these two quantities are strongly related (Figure 8-1), in a nearly homogeneous range of loading conditions, switching from VMS to MPS is simply a nonlinear rescaling of the predictor axis. From this point of view, the choice between these potential predictors is equivalent to a choice of the functional form for the statistical model. Because statistical methods offer little help with the choice of model, they cannot be expected to adequately choose between strongly related predictors (McMurry and Poplin, 2015). It has been demonstrated that with small sample sizes the AIC cannot reliably select the best model (McMurry and Poplin, 2015). But the difficulties associated with these small sample troubles are not a shortcoming of the AIC. Other model fit metrics can be expected to have the same trouble. Hosmer et al. (1997) demonstrated that none of the overall goodness-of-fit tests were especially powerful for small to moderate sample sizes $n < 500$. Even if the sample size was 500, the power of the Stukel score test, which was the highest among all tests considered, was considered as 'moderate'. Thus, the choice of injury metric should have a strong biomechanical basis in addition to an overall goodness-of-fit.

8.4.2 Injury Mechanism

From a biomechanical perspective, an injury was assumed to be related to tissue damage/failure, probably at a micro scale. Because the brain is a viscoelastic biological tissue (Chatelin et al., 2010), it was reasonable to hypothesize that its injury/failure response was dependent on both the magnitude and rate of applied strain. Strain rate and the product of the strain

and strain rate were proposed as injury metrics (Sullivan et al., 2015). These metrics certainly overemphasized the effect of strain rate. Some *in vitro* experiments of brain tissue found strain rate effect was insignificant (Cater et al., 2006) for the death or swelling of the cell, and other studies found that the strain rate did not affect the cellular response until a certain strain level (10%) was reached (Elkin and Morrison, 2007; Morrison et al., 2003; Nakadate et al., 2017). While these metrics might correlate well with the injury in a relatively homogeneous loading range when strain rate effect is small, the metrics values between species suggested they are not the tissue-level causation of the injury, as these metrics varied by orders of magnitude for brains from different species that sustained an injury of similar severity. The merit of stress form is the inclusion of both strain and strain rate effect in a way compatible with the biomechanics of the tissue. Whether failure criteria should be expressed in terms of stresses or in terms of strains is probably the longest standing issue in mechanics. While in biomechanics, the preferred criterion in the literature is strain (Gabler et al., 2018a; Giordano et al., 2014; Sahoo et al., 2016), probably because strain was more accessible from direct measurement in experimental tests while stress was derived from strain and influenced by pre-stress. For stress-based criteria, a commonly used form is that of the Von Mises criterion, which was also used in predicting brain damage (Afshari et al., 2017; De et al., 2007; Ueno et al., 1995). But the Von Mises criterion is widely believed to be applicable only to ductile metal, and it is in serious error for predicting biological tissue damage (Korenczuk et al., 2017). The performance of maximum shear stress and maximum principal deviatoric stress was expected to be similar to that of VMS in predicting brain injury because of the linear correlation between them and VMS in the current injury data ($R^2 > 0.999$). The current study was unable to delineate whether or not the marginally better correlation with injury implies that stress is the mechanism. More experimental evidence is required to answer this question.

One significant finding of this work was that the performance of axonal strain in predicting injury was nearly equivalent to the performance of the principal strain of the ground substances. Tract-oriented strain (Sullivan et al., 2015) or axonal strain (Giordano and Kleiven, 2014a; Sahoo et al., 2016) have been suggested to be a better predictor of injury. Despite the uncertainty introduced by statistical analysis using small dataset, other reasons would also lead to this inconsistency. As discussed in Chapter 2, the traditional method for incorporating the tractography information oversimplified the complex fiber network in the brain, and the strain measurement at the fiber direction was a tedious and error-prone process. The underlying fiber architecture is so complex and broadly distributed that the macroscale properties of brain tissue appear to be isotropic (Budday et al., 2017, 2015). In addition to the disparities in the biofidelity of the based FE models, the current analysis was also based on the injury data with better fidelity. The analysis in the aforementioned studies was using computational reconstruction of field incidence where limited information about head kinematics was known (Chapter 7).

It should also be noted that the use of a stress or strain criterion is dependent upon the objectives of a given study. Considering that almost all the existing kinematics-based injury metrics were developed based on their correlation with the principal strain responses, the principal strain would still be the popular choice by balancing the simplicity and performance until new experimental data and evidence are present to prove otherwise.

8.4.3 Comments on Kinematic-Based Metrics

Kinematics-based metrics have been evaluated for predicting injury in the literature. While the formulation of the metrics can be diverse, the performance was mainly determined by the basic underlying kinematics (a, α, ω). Consistent with the current findings, linear acceleration (a) alone was generally not recommended as the best predictor of brain injury (Gabler et al., 2016; Ommaya

and Gennarelli, 1974; Takhounts et al., 2013). In the literature, maximum resultant angular acceleration (α_{max}) was found among the best kinematic-based predictors of injury using head impact data from automotive crashes (Laituri et al., 2016), football, boxing, and martial arts (Hernandez et al., 2015). This finding was consistent with our analysis of human data, but contradicts the analysis of animal data. Some metrics may perform better for specific types of data. A possible explanation is the resonance behavior of brain tissue. Using the mechanical models, Gabler et al. (2018) demonstrated that maximum brain deformation magnitude was governed by the frequency of the input pulse relative to the natural frequency of the brain. When the frequency of head kinematics was lower than the natural frequency, deformation was mainly driven by angular acceleration, but when the frequency of head kinematics was lower than the natural frequency, deformation was mainly driven by angular velocity.

Figure 8-8 illustrates the distribution of the head kinematics relative to the FE-derived natural frequency. Most of the human cases were lower than the natural frequency of the brain, while the animal data was more broadly distributed. This finding may suggest the preference of using certain kinematics as injury predictor in certain applications. For example, the leading candidate, BrIC (depends solely on angular velocity), for the US New Car Assessment Program (USNCAP), might not be the appropriate metric as the nature of crash-relative events was a low-frequency impact. It is also worth pointing out that the frequency of the football data was previously found to be higher than the FE-derived natural frequency based on the GHBMC model (f_n: 22 – 28 Hz) (Gabler et al., 2018c), but the GHBMC model had an erroneous time constant and lower dynamic stiffness than the experimental measurements (Figure 3-7 in Chapter 3). The resonance behavior of the brain in the skull was rarely studied through experiment, and the

calculated natural frequency ranges from less than 20 Hz (Laksari et al., 2015) to more than 50 Hz (Zou et al., 2007) during low-severity impacts.

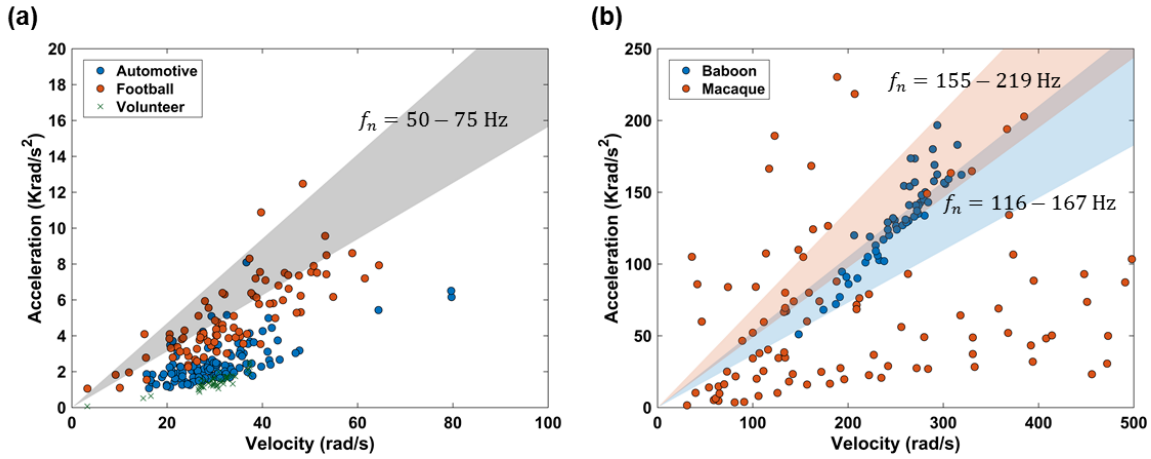

Figure 8-8. Distribution of resultant head kinematics with respect to FE-derived natural frequencies (shaded corridors) of the brain for human (a) and NHP (b).

8.4.4 Comparison of IRFs

Although tissue-level IRFs are also available in the literature (Sahoo et al., 2016; Takhounts et al., 2013), they cannot be directly compared with the current study. This was because the strain and stress results in different FE models are not equivalent (Giudice et al., 2018) due to disparities inherent in the FE models from different groups. Most previous studies have proposed IRFs based on a single kinematics-based measure, such as linear acceleration (a_{max}), angular velocity (ω_{max}, BrIC), and angular acceleration (α_{max}). As discussed above, these are unlikely to fully characterize the human tolerance under a broader range of loading conditions. Consequently, direct comparisons between the tissue-level IRFs developed in this study with those previously established in the literature was difficult and might not be appropriate.

To transfer the tissue-level metrics to the kinematics-based frame, the human brain response surfaces of uniaxial rotation (Figure 6-5 in Chapter 6) were utilized to identify the thresholds of angular kinematics that produced the MPS95 values for the 50% risk of mTBI (0.26)

and sTBI (0.37). Those thresholds were shown in Figure 8-9, along with the tolerances of 50% risk found in the literature (Löwenhielm, 1975; Margulies and Thibault, 1992; Ommaya and Hirsch, 1971; Patton et al., 2012; Elliot J Pellman et al., 2003; Rowson et al., 2012a).

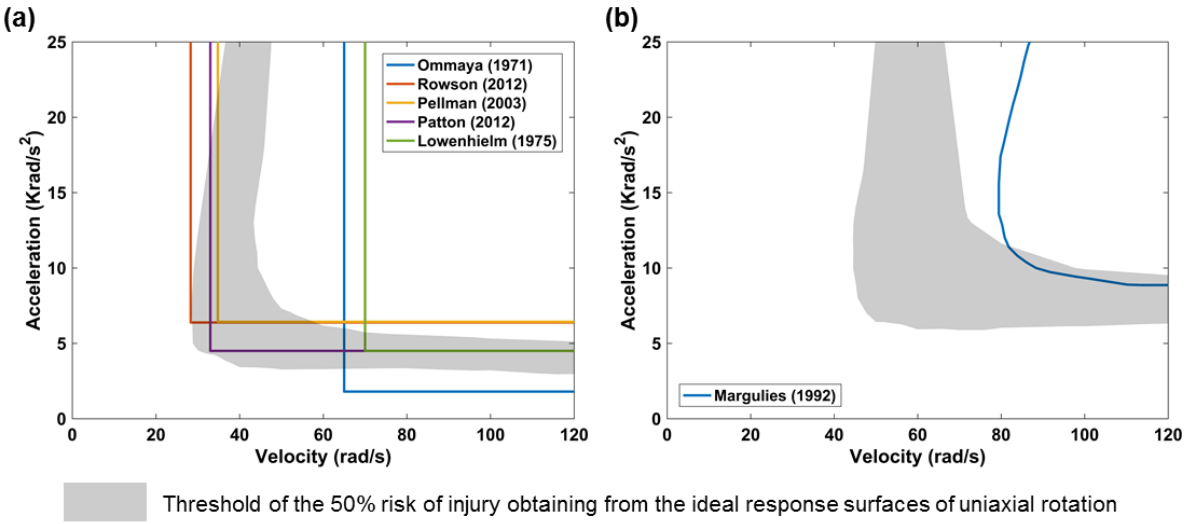

Figure 8-9. Comparison between developed IRFs and proposed mTBI (a) and sTBI (b) tolerances in the literature.

Although the thresholds were based on ideal sinusoidal pulses, the global strain responses were fairly independent of the shape of the loading curves (Figure A21 in Appendix E). Most of the recent injury tolerances, as expected, were reasonably consistent with the current thresholds. Note that some of the data used to develop the tissue-level injury risk functions were previously used to develop these kinematics-based tolerances (Margulies and Thibault, 1992; Elliot J Pellman et al., 2003), although some corrections were made recently (Sanchez et al., 2018).

8.4.5 Different Methods of Utilizing Animal Data

Multiple methods of obtaining animal tissue responses and their effects on the development of injury risk functions were investigated, as given in Figure 8-10. The first two methods were scaling the head kinematics of the NHP data by mass scaling (Method 1, Takhounts et al., 2013) or frequency scaling (Method 2, Chapter 6) to humans and applying the scaled kinematics to

human brain FE models to predict corresponding tissue metrics. The primary method used in this chapter to obtain the tissue-level metrics for the animal tests was through computational reconstruction of the NHP tests using the NHP brain model (Method 3).

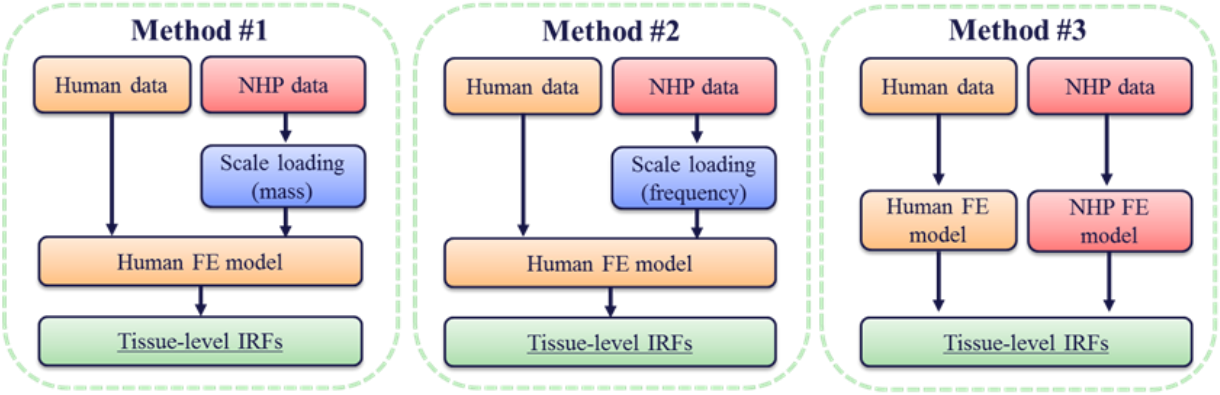

Figure 8-10. Several methods investigated for the development of tissue-level injury risk functions.

The last two methods (frequency scaling and NHP FE models) resulted in very consistent MPS95 IRFs (Figure 8-11). Note that the mTBI IRFs did not vary much when different methods were used because the mTBI IRFs were mainly determined by the human injury data. Large discrepancies between method 1 (mass scaling) and the other two methods were observed for the sTBI IRFs (50% probability of injury: 0.444 vs. 0.384 and 0.397). This finding demonstrated frequency scaling is a reasonable method to develop strain-based tissue-level injury risk functions based on the human FE model, while traditional mass scaling method would result in a large error.

Previously, for the lack of integration method and injury data to characterize the full spectrum of injury severity, only IRF for severe injury can be developed based on animal data. The risk curves for HIC (NHTSA, 1995) were used to derive IRFs of other injury severity level (Takhounts et al. 2013), based on the assumption that severity ratios of the metric (e.g., BrIC) would be similar to those derived for HIC (NHTSA, 1995) at a 50% probability of injury. Figure 8-12 shows the mTBI IRF scaled from the sTBI IRF based the HIC scaling relationships, the scaled mTBI IRF was more conservative compared with the IRF developed based on the integrated injury

data, which indicates that the assumption was not fulfilled and highlights the demand for data integration to develop IRFs for a spectrum of injury severity.

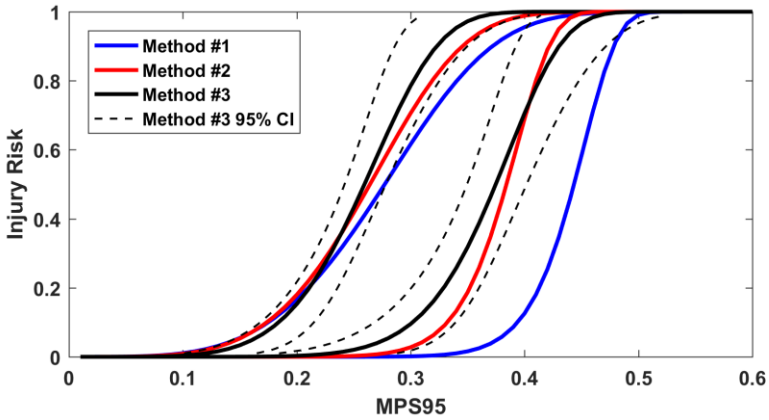

Figure 8-11. Mild and severe brain injury risk curves based on MPS95 using three different methods.

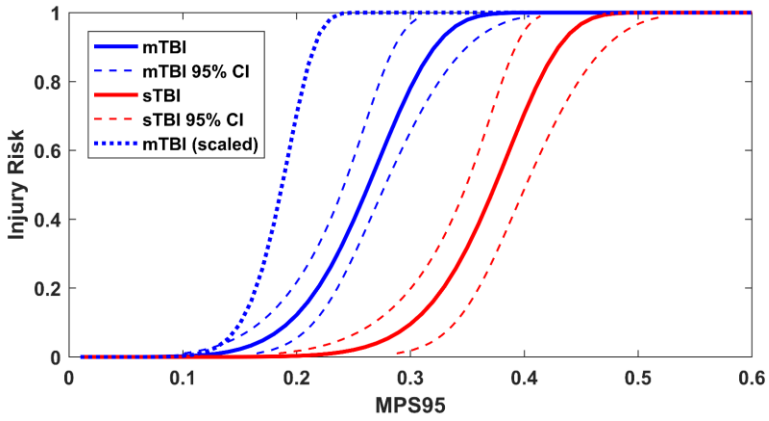

Figure 8-12. Mild brain injury risk curves scaled (the dotted blue line) from severe brain injury risk curves (the solid red line) based on the HIC (NHTSA, 1995) at a 50% probability of injury.

8.4.6 Bias and Limitation in the Dataset

There were several limitations related to diagnosing injury in the subjects included in the database. Historically, the clinical and theoretical definitions of mTBI have varied (Petchprapai et al. 2007), and these subsequent revisions may have introduced changes in coding the severity of equivalent traumatic brain injuries. The volunteer and NHP tests were conducted when the concussion was defined by a loss of consciousness, and the definition of concussion has changed since then. Modern definitions have a wider range of symptoms and do not require the loss of

consciousness. The medical reports for the human volunteers indicated that symptoms were mild and transient. However, little effort was made at the time of the tests to distinguish symptoms as being a musculoskeletal or a neurological issue (Sanchez et al., 2017). The diagnoses for the professional football players were more consistent with the contemporary definition of concussion, were established after play and verified with follow-up medical testing and treatment of the players. However, there were still some variations in symptoms compared with current concussion diagnosis techniques (Pellman et al., 2004). Although the injuries produced in the animal models were expected to be more accurate based on pathology and autopsy, the invasive methods adopted to measure head kinematics brought up ambiguities in injury diagnosis. Cognitive dysfunction in the animal was also difficult to detect, and the diagnosis of mild TBI or no injury could be erroneous. Fortunately, the mTBI IRFs developed in this study were dominated by human data. The error introduced by the uncertainty due to the mTBI diagnosis in the animal data was negligible for the IRF development but could affect the inference drawn from the mTBI overlap between the animal and human tissue-level metrics (including MPS95, MAS95, CSDM15, CSDM25, VMS95). Uncertainty was also introduced to this inference by the small sample size (NHP: 8, human: 39), future studies to acquire mTBI injury data from both human and animal subjects would improve the finding made in this work.

As recognized previously (Sanchez et al., 2017; Sanchez et al., 2018), selection bias was also a concern with the current dataset. The human subjects used in this analysis were military personnel (NBDL) and professional football players and are not necessarily representative of the general population. Furthermore, the hits collected for the football reconstruction are not representative of the head impact exposure during professional football games. This overrepresentation of concussive events may result in IRFs that over-predict the risk of injury in

the football game (Broglio et al., 2010; Funk et al., 2007, 2012). It is important to keep in mind that the goal of this study was to estimate the human biomechanical tolerance for mTBI and improve head protection, regardless of the application. The selection bias towards significant head impacts was not expected to have a significant effect on the estimation of human tolerance but ensuring the appropriateness of the IRFs to evaluate the real injury risk for certain applications is critical. Evaluating IRFs with real-world crash data would provide more insights into the efficiency of developed IRFs and associated injury metrics.

Only global measures of brain tissue-level metrics were considered in this study since there is currently a lack of experimental datasets (pathology data) to develop a regional-specific tolerance for the brain. The proposed tissue-level IRFs for this dissertation were intended for diffuse-type injuries, which are the most common brain injury types sustained in automotive and sport-related head impact environments (Takahashi and Yanaoka, 2017; Antona-Makoshi et al., 2018). However, it is essential to acknowledge the existence of other brain injury mechanisms for other types of injury, such as contusion, brainstem injury. Because of the lack of biomechanical data to characterize the brain-skull interface and craniocervical junction, the current FE models are not suitable for predicting those types of injuries.

8.4.7 Summary

In this study, a database of brain injury was used to evaluate a variety of injury metrics and to estimate human tolerance to TBI. The correlation between TBI and most of the assessed injury metrics were statistically significant, but the choices of injury metrics were inconclusive and limited by a small dataset. Future efforts should be focused on collecting more brain injury data. Human brain tolerances for TBI were estimated and presented in the form of injury risk functions

based on various injury tissue-level metrics: MPS95, MAS95, and VMS95. The core findings and results from the current investigation include:

1. Consistent with the deformation-based injury mechanism, a strong correlation between strain or stress with the injury was found. For similar injury severity, principal strain and Von Mises stress obtained from the brain of different species were comparable, indicating they are good tissue-level predictors (or even the causation) of brain injury.
2. Axonal deformation, which might still be the microscale injury mechanism, did not show better predictability of brain injury than the tissue deformation (principal strain), which indicates the tissue strain without taking the heterogeneities at the cellular level into account is sufficient for the current application.
3. The inclusion of the strain rate effect on tissue-level injury metric marginally improved the goodness of fit of the model to the human data, but existing metrics associated with strain rate (MPSSR, MPS× SR95, MASSR, MAS×SR95) might not be a good formulation of coupling strain rate effect, as they were incompatible for the brains of different sizes.
4. Although the choice of tissue-level metric is only tentative, the associated IRFs developed in this study do show better efficiency for predicting injury using independent test dataset.
5. The most significant contribution of this work is presenting an overarching framework for the development of IRF using interspecies data integration. The frequency scaling developed in Chapter 6 was also demonstrated to be a practical approach for developing IRFs with sufficient accuracy when advanced animal FE models were inaccessible.

These newly developed risk functions characterize the biomechanical tolerance for TBI; their application in real-world seniors is further pursued in Chapter 9.

CHAPTER 9 : EVALUATION OF THE FIELD RELEVANCE OF INJURY RISK FUNCTIONS

Injury risk functions of TBI developed using biomechanical data are the cornerstone of the design and development of effective countermeasures and safety testing standards. While the risk functions represent the tolerance of the human brain to the specific injury regardless of the scenarios for application, automotive or sports, they were commonly evaluated by comparing the predicted injury risk with real-world epidemiological injury data. To ensure the proper usage of the risk functions, the newly proposed tissue-level injury risk functions were applied to automotive safety and evaluated with real-world accident analysis.

9.1 Introduction

Historically, existing brain injury criteria and tolerances, such as the HIC (Versace, 1971) and SI (Gadd, 1966), have been valuable in reducing field injury incidence, notwithstanding that they deviated from what is now thought to be the causation of injury. Shortly after the implementation of the standards, that adopted those criteria, the fatality rates of motor vehicle occupants and football athletes were reduced by 81% (Kahane, 2015) and 74% (Mertz et al., 1996) respectively. Whenever a new metrics or risk function was proposed, its field relevance was a topic of interest.

Studies have assessed IRFs by comparing the predicted injury risk to real-world injury rates obtained from sports epidemiology studies (Funk et al., 2012) and motor vehicle accident databases such as the National Automotive Sampling System (NASS-CDS) (Laituri et al., 2015; Mueller et al., 2015). Results from these epidemiological studies did not correlate well with predicted injury probabilities. The critical missing link between the biomechanical tolerances and

the true injury risk probabilities is the unbiased exposure data. Alternative IRFs were developed or corrected using unbiased real-world data (Funk et al., 2007; Laituri et al., 2016), and these injury risk functions were more aggressive (lower risk for the same predictor value) than the IRFs derived from biomechanical data. Questions exist about not only the validity of the criterion and associated IRF but also concerning the limited information and the crude approximation about real-world impacts.

A myriad of innovative wearable devices in the field of sports biomechanics was introduced to measure real-time head kinematics of players; notable applications included an instrumented helmet (Rowson et al., 2009), mouthguard (King et al., 2015), and ear patches (King et al., 2016). Data collected from these types of systems would have the potential to provide estimates of player exposure and eventually close the gap between biomechanical tolerance and real-world injury risk in the future, but the currently available devices still have limited utility due to the low fidelity of the data (Joodaki et al., 2019; O'Connor et al., 2017).

The automotive crash is probably a more complex real-world scenario; real-time head kinematics were not accessible and generally predicted through laboratory or computational reconstruction of the field crash event. The most notable dataset of this kind was the crash tests conducted by NHTSA and the Insurance Institute for Highway Safety (IIHS) using Anthropomorphic Test Devices (ATD). The fidelity of the ATD used to measure the head motion in the crash tests is one of the lingering uncertainties that would result in a discrepancy between crash tests and real-world crashes. For example, the widely used Hybrid III ATD had limited biofidelity for the head and neck complex in sports-related impact tests (Schnebel et al., 2007). Although the ATDs were developed by the automotive industry for use in crash testing (Parent et al., 2017), the influence of their biofidelity on injury risk prediction is unknown.

The goal of this chapter is to identify the missing link between the predicted injury risk based on biomechanical tolerance and the observed field injury rates in a two-fold investigation: First, the proposed IRFs were applied to automotive crash tests and compared with real-world accident analysis. To ensure the general accessibility of the newly developed tissue-level injury risk functions, injury risk functions based on kinematics-based metrics were first developed. Second, to explore the influence of the biofidelity of ATDs on injury prediction, frontal and oblique sled test data using Hybrid III and THOR were analyzed and compared with responses of the post mortem human subjects (PMHS).

9.2 Method

9.2.1 The Link between Tissue Metrics and Kinematics-Based Metrics

FE-derived tissue-level metrics provide the most accurate but most time-consuming method for predicting brain response. In the present state-of-the-art, the newly developed tissue-level IRFs are also model-dependent and cannot be generalized because of the underlying inconsistency between FE models. These disadvantages preclude the practical application of the IRFs and the general accessibility to the scientific community. Kinematics-based metrics can be used as an alternative method to characterize injury tolerances, and recent advancements have demonstrated the good correlation between these kinematics-based metrics (e.g., DAMAGE, UBrIC, CIBIC) with brain strain responses. The kinematics-based metrics selected for the demonstration were DAMAGE and UBrIC (MPS) due to their effectiveness of modeling strain responses. Over 200 human head impacts from the primary injury databases and from published automotive crash tests were simulated and used to establish the correlation between kinematics-based metrics and strain metrics (MPS95) based on a linear regression model (Figure 9-1). Then,

the risk curves for kinematics-based metrics can be obtained from tissue-level risk curves based on the correlation.

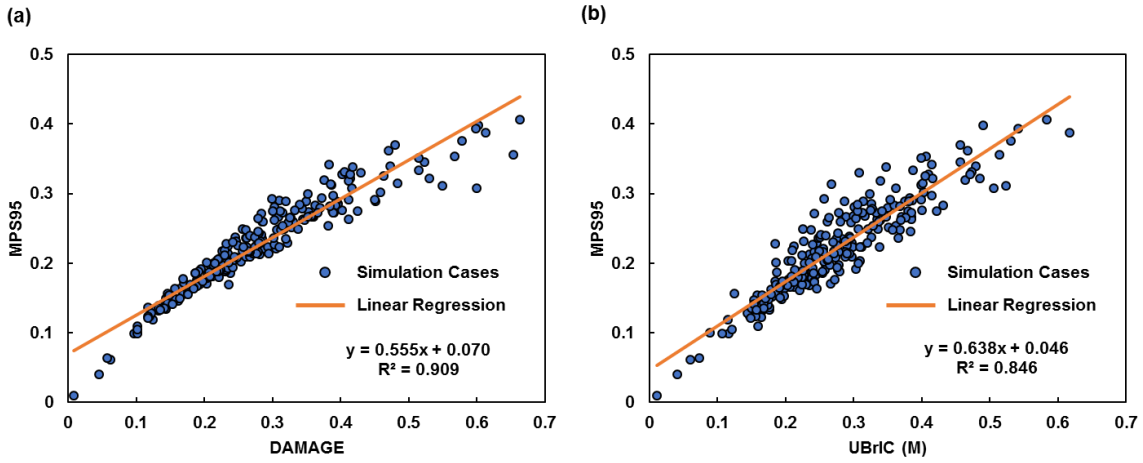

Figure 9-1. Linear regression model between MPS95 and DAMAGE (a), between MPS95 and UBrIC (b).

9.2.2 Evaluation of Injury Risk Functions Using Automotive Field Data

To evaluate the efficiency of risk functions with the observed field injury probabilities, crash test data were utilized to estimate the risk of brain injury and compared with the field injury probability in corresponding crash scenarios. Injury risk functions assessed in this study include the newly developed MPS95, MAS95, VMS95 IRFs, the derived DAMAGE, UBrIC IRFs (based on MPS95 IRF), and injury risk functions (HIC, MPS-based BrIC, and CSDM-based BrIC) proposed by NTHSA (NHTSA, 1995; Takhounts et al., 2013).

Crash Tests

Six-degree-of-freedom (6DOF) head kinematic data from a total of 149 crash tests were used in this study (Table 9-1). These crash tests were performed by NHTSA and IIHS. Kinematics-based injury metrics were derived from head kinematics measured by ATDs, and tissue injury metrics were obtained from computational reconstruction using the axon-based human model subjected to the measured head kinematics.

Table 9-1. Summary of NHTSA and IIHS vehicle databases.

Occupant Location	Impact Direction	Details	Delta-V (km/h)	Surrogate[#]
Driver (114)	Frontal (76)	Full Engagement (38)	56.3 ± 0.30	HYBRID-III
		Small Overlap (20)	64.4 ± 0.00	HYBRID-III
		Moderate Overlap (18)	64.2 ± 1.03	HYBRID-III
	Side (38)	Left-Side (28)	60.5 ± 3.53	EUROSID-2RE
		Left-Side (5)	29.9 ± 1.81	EUROSID-2RE
		Left-Side (5)	32.2 ± 0.04	SID-IIS, F05TH
Front Passenger (34)	Frontal (34)	Full Engagement (21)	56.1 ± 0.36	HYBRID-III
		Full Engagement (13)	56.2 ± 0.28	HYBRID-III, F05TH

[#]50^{TH} Male surrogate unless specified otherwise, head kinematic responses from the small female tests (F05TH) were previously scaled to a 50th percentile male using mass scaling (Gabler et al., 2016).

Field Data Analysis

Cases of real-world crashes were obtained from the National Automotive Sampling System Crashworthiness Data System (NASS-CDS). Cases eligible for NASS-CDS were police-reported incidents involving a harmful event on a public traffic way. Field researchers inspect the scene and the vehicle, perform interviews, and review medical records to obtain information regarding crash circumstances, vehicle and occupant characteristics, and the nature and severity of injuries coded subject to the AIS. Each NASS-CDS case was assigned a weighting factor based on the probability of the case being sampled, and the weighting factors are used to scale the sampled cases to generate a national estimate.

To be commensurate with the collected crash tests and yield enough cases for analysis, cases that satisfy the following inclusion criteria in the NASS-CDS database were selected.

- Crash and vehicle model year 2001–2015.
- Passenger cars (including SUV and Wagons, excluding minivan and truck).
- Crash impact directions and Delta-V.
- Seat position: driver or front passenger (not enough samples for backseat passengers).
- Non-ejected and belted occupant.

- Age 16 or higher.
- Occupants with known injury status or fatality.

Commensurate Crash Scenarios

After obtaining the 11,183 NASS cases meeting the above criteria, injuries sustained were categorized into mTBI and sTBI based on the AIS codes, mTBI were documented as a concussion, while sTBI were documented as DAI and ICH. A table with the injury category assigned to each seven-digit AIS code is provided in Appendix G (Antona-Makoshi et al., 2018). The remaining assessments were based on crash configurations and injury severity. Corresponding to the crash tests, four crash configurations were identified based on seat locations, impact directions, and Delta-V:

- The driver, frontal impact, high speed (50 – 70 km/h)
- The driver, near side impact, low speed (25 – 35 km/h)
- The driver, near side impact, high speed (50 – 70 km/h)
- The passenger, frontal impact, high speed (50 – 70 km/h)

For the first configuration (*driver, frontal impact, high speed*), driver side small overlap, driver side moderate overlap, and full engagement crashed were identified based on the Collision Deformation Classification (CDC) and photographs of vehicle damage (example in Appendix G). A broader bin of high-speed crashes (40 – 80 km/h) was assigned to yield more crashes for analysis. Vehicles with damage originating from the right side of the vehicle, or narrow center damage (pole) were excluded because of their dissimilarity to corresponding crash tests.

The real-world mTBI injury rate was calculated as the (or weighted) number of occupants with a certain injury divided by the (or weighted) number of occupants with known injury status

(Antona-Makoshi et al., 2018). Each NASS-CDS case contains a weighting factor that was used by the NHTSA to extrapolate the individual cases to the national numbers. For complex events like car crashes, unbiased exposure data are not available, and the inclusion of the weighting factor can be controversial (Prasad et al., 2014). Therefore, the incident rates with and without weighting were provided. The analysis was performed separately for different crash configuration.

9.2.3 Influence of the Biofidelity of Anthropometric Test Dummy

Comparing the predicted injury risk sustained in the crash tests with the injury rates found in the NASS CDS database relies on the biofidelity of ATDs. To evaluate the biofidelity of ATDs in reproducing head kinematics, previously published head kinematics of the ATD and PMHS tests were collected and utilized in the current study.The impact tests were conducted under Gold Standard 2 and 3 (GS2 and GS3) conditions (Acosta et al., 2016). The GS2 test condition was a full frontal 30 km/h impact using a custom 3 kN force-limited shoulder belt. The GS3 test condition was a 30 km/h, 30-degree nearside oblique frontal impact using the same custom 3 kN force-limited shoulder belt. The test conditions approximated those of a belted occupant in an actual full frontal or near-side oblique crash. In all tests, a reverse acceleration sled was used to produce the 9 g acceleration pulse used for each test. Hybrid-III ATD, THOR Metric ATD (Parent et al., 2013), and PMHSs were positioned in similar postures and tested in controlled ‘paired’ conditions. All PMHSs were male and approximated 50th percentile stature and mass. The dataset is summarized in Table 9-2.

Table 9-2. Summary of the sled test database.

Test Conditions	Test ID	Surrogate	Body Mass (kg)	Stature (cm)
GS 2	S0300 – S0301	HYBRID-III	78	175
	S0302	PMHS	68	177
	S0303	PMHS	68	173
	S0028	PMHS	68	178
	S0029	PMHS	70	179
GS 3	S0305 – S0307	HYBRID-III	78	175
	S0309 – S0312	THOR		
	S0314	PMHS	76	172
	S0315	PMHS	64	177

9.3 Results

9.3.1 Field Injury Risk

Table 9-3 contains the resulting NASS analysis for the four test configurations stratified by seat location, impact direction and impact speed. The data indicate the driver was more vulnerable in a side impact than in a frontal impact. The large difference between weighted and unweighted injury rates in certain configurations implies that these cases might not be representative of the population. Table 9-4 contains the data for the three high-speed frontal crash modes: small overlap, moderate overlap, and full engagement. The table indicates that the sample sizes were too small to draw any conclusion about the vulnerability of these frontal modes.

Table 9-3. Head injury in various types of crash configurations in the NASS dataset.

Configuration	Cases involved		Cases injured (mTBI)		Cases injured (sTBI)		Injury rates* (%)	
	Number	Weights	Number	Weights	Number	Weights	mTBI	sTBI
Driver, Front, High	313	33,384	38	2,219	3	225	6.6 (12)	0.67 (0.96)
Driver, Side, Low	275	64,369	57	5,924	12	203	9.2 (21)	0.32 (4.3)
Driver, Side, High	40	2831	13	937	6	571	33 (33)	20.2 (15)
Passenger, Front, High	73	4,870	9	485	0	0	9.9 (12.3)	0 (0)

*Unweighted injury rates in the parentheses.

Table 9-4. Head injury in various high-speed frontal crash modes in the NASS dataset.

Configurations	Cases involved		Cases injured (mTBI)		Cases injured (sTBI)		Injury rates* (%)	
	Number	Weights	Number	Weights	Number	Weights	mTBI	sTBI
Small Overlap	34	3,947	4	99	2	38	2.5 (12)	0.97 (5.9)
Moderate Overlap	144	17,504	16	2,344	1	42	13 (11)	0.24 (0.69)
Full Engagement	479	63,352	44	3,065	3	300	4.8 (9.2)	0.47 (0.63)

*Unweighted injury rates in the parentheses.

9.3.2 Crash Tests

Figure 9-2 shows the distribution of the predicted injury probabilities in the crash tests relative to the NASS Dataset for the first configurations (*driver, frontal impact, high speed*). The results for other configurations are provided in Figure A23 – A25 (in Appendix G). Clearly, the variation of estimated injury probabilities was high. For each configuration, the median value was chosen to represent the distribution of injury probabilities, as the predicted probabilities were not following normal distributions. Finally, the median injury probabilities were compared with the corresponding weighted NASS-based head injury rate (Figure 9-3), and unweighted NASS-based head injury rate (Figure A26 in Appendix G). Mixed results were presented for the newly developed injury risk functions, but in general, the predicted mTBI injury risk in the crash tests were higher than those observed in the NASS database, while the predicted sTBI injury risk in the crash tests was similar to those observed in the NASS database, except for the third configuration (*driver, side impact, high speed*), which yielded a very small sample size (n = 40) based on the NASS database. Notably, the estimates from VMS95 were closer to the real observation for mTBI compared with other metrics. For comparison, the MPS-based BrIC estimated quite different head mTBI risks than those observed in similar real crashes. The estimates from the HIC and the CSDM-based BrIC were close to the real mTBI rates. While very few cases were indicated with sTBI, both the MPS-based and CSDM-based AIS4+ IRFs had larger errors when compared with the

other IRFs. Note that the BrIC AIS4+ IRF was originally defined with biomechanical data, and IRFs of other severities (including AIS2+) were scaled from the AIS4+ IRF.

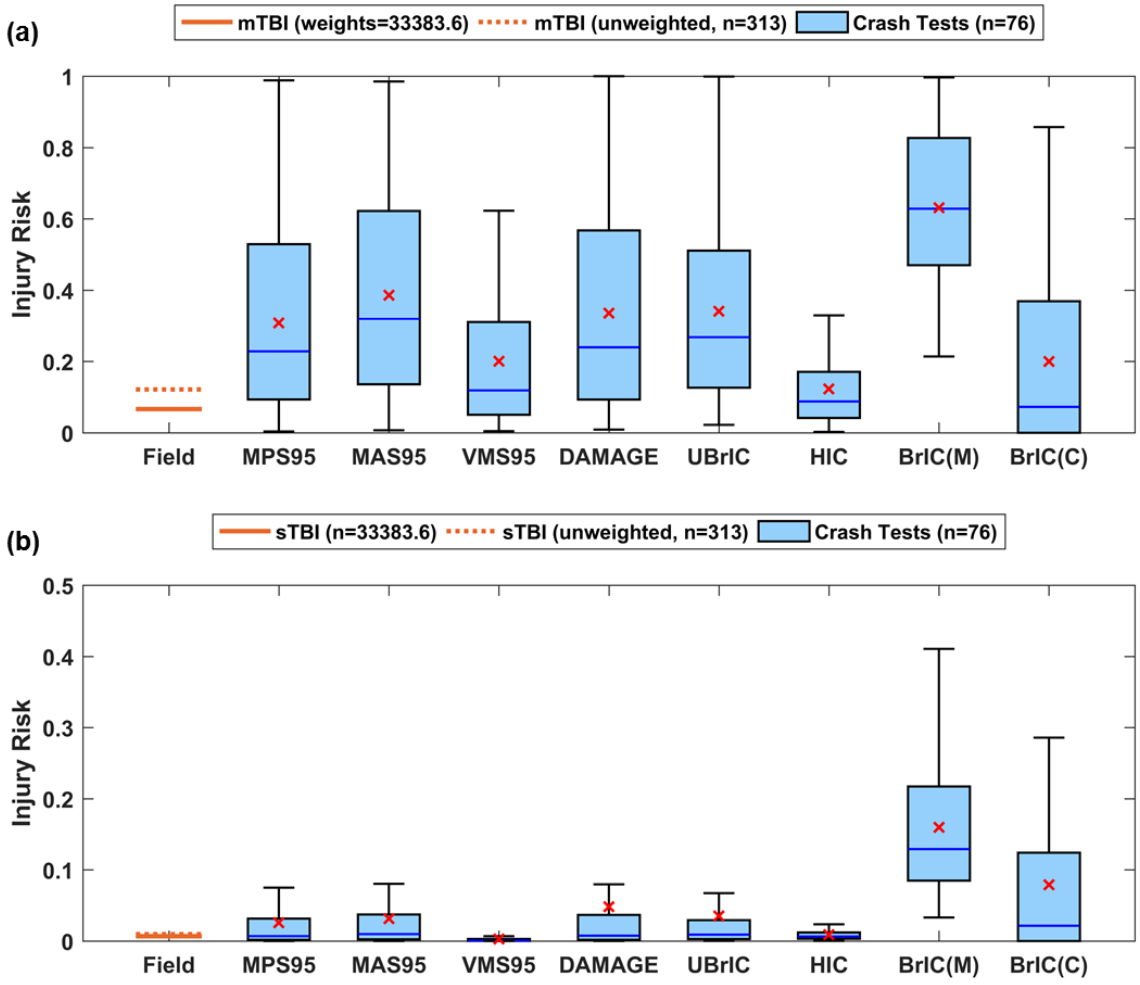

Figure 9-2. Injury risk for mTBI (a) and sTBI (b) sustained by the driver in high-speed frontal crashes in NASS and corresponding crash tests.

A close examination of crash tests was conducted for cases subjected to high predicted injury (>70%) and cases subjected to low predicted injury risk (<10%) based on MPS95 predications. Those tests were grouped for the same crash conditions and similar vehicles (vehicle type and vehicle year), as shown in Table 9-5. The table elucidates the differences between MPS95 (or DAMAGE) and the HIC or BrIC. The HIC was unable to take the angular motion into account, and hard contacts were rare events in the crash tests with the equipment of airbags, and therefore

very low HIC values in the crash tests. The BrIC, developed based on either MPS or CSDM, only accounts for the peak angular velocities, while the MPS actually has a higher correlation with peak angular acceleration ($R^2 = 0.60$) than peak angular velocity ($R^2 = 0.43$) in the current crash dataset (Figure A27 in Appendix G).

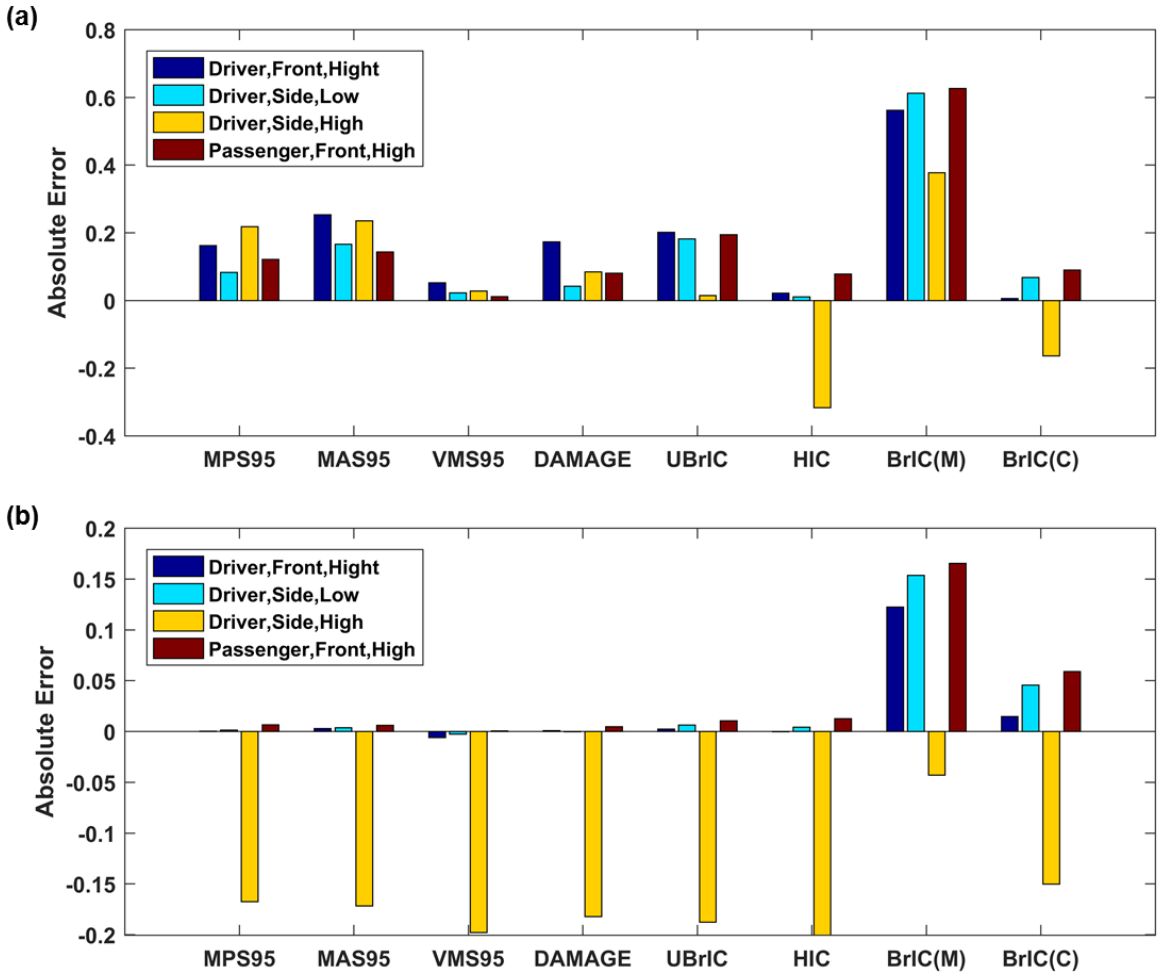

Figure 9-3. Absolute error between predicted Injury risk and weighted field injury rates for mTBI (a) and sTBI (b). Positive values indicate overpredicting injury.

Table 9-5. Predicted injury risk in the frontal crash tests.

Mode (Car)	ID	Basic Kinematics			Predicted Injury Probability				
		a_{max} (g)	ω_{max} (rad/s)	α_{max} (rad/s^2)	MPS95	DAMAGE	HIC	BrIC (M)	BrIC (C)
Full engagement (Compact)	8068-01	62	28	2648	71%	74%	21%	59%	4%
	8071-01	47	42	4443	99%	100%	6%	86%	45%
	8151-01	54	37	3547	96%	99%	10%	86%	43%
	8081-01	43	32	2019	10%	13%	5%	71%	17%
	8156-01	38	28	1630	5%	4%	1%	49%	0%
Full engagement (Mid-size)	8106-01	48	37	3675	74%	73%	8%	80%	31%
	7966-01	53	17	1410	1%	1%	12%	21%	0%
Small overlap (Mid-size)	CEN1229	46	47	3032	85%	100%	6%	100%	95%
	CEN1234	42	41	3113	87%	100%	4%	98%	84%
	CEN1225	27	23	1266	2%	3%	0%	37%	0%
	CEN1230	30	26	2021	4%	4%	1%	53%	1%
	CEN1236	28	25	1252	8%	9%	0%	45%	0%
Full engagement (SUV)	3952-02	87	37	4609	95%	97%	77%	91%	58%
	4223-02	61	30	1883	9%	9%	21%	60%	5%
	4235-02	62	18	1489	9%	10%	24%	45%	0%

Color codes: the cell that holds a ‘severe’ value has the shades of red.

9.3.3 Influence of Anthropometric Test Dummy

Figure 9-4 compares the angular velocity time histories of the ATD head and PMHS head in GS2 and GS3 conditions. The predominant head motion in both frontal and oblique impacts was observed to occur, as expected, within the sagittal plane, but PMHS had substantial out-of-the-plane head motion, while the head of the ATD had very little axial rotation in both conditions. It was also observed that the resultant head displacement (not shown) was greater in the oblique condition. This would indicate that factors associated with the oblique condition allow for greater head motion when compared to that of a standard frontal impact for the same acceleration. The injury risk sustained by ATDs and the injury risk sustained by PMHS were compared in Figure 9-5. Both ATDs substantially underestimated the risk of brain injury under oblique impacts, while

in the frontal impacts, the differences were subtle. Note that the Hybrid-III ATD was unable to differentiate the injury risks between these two conditions.

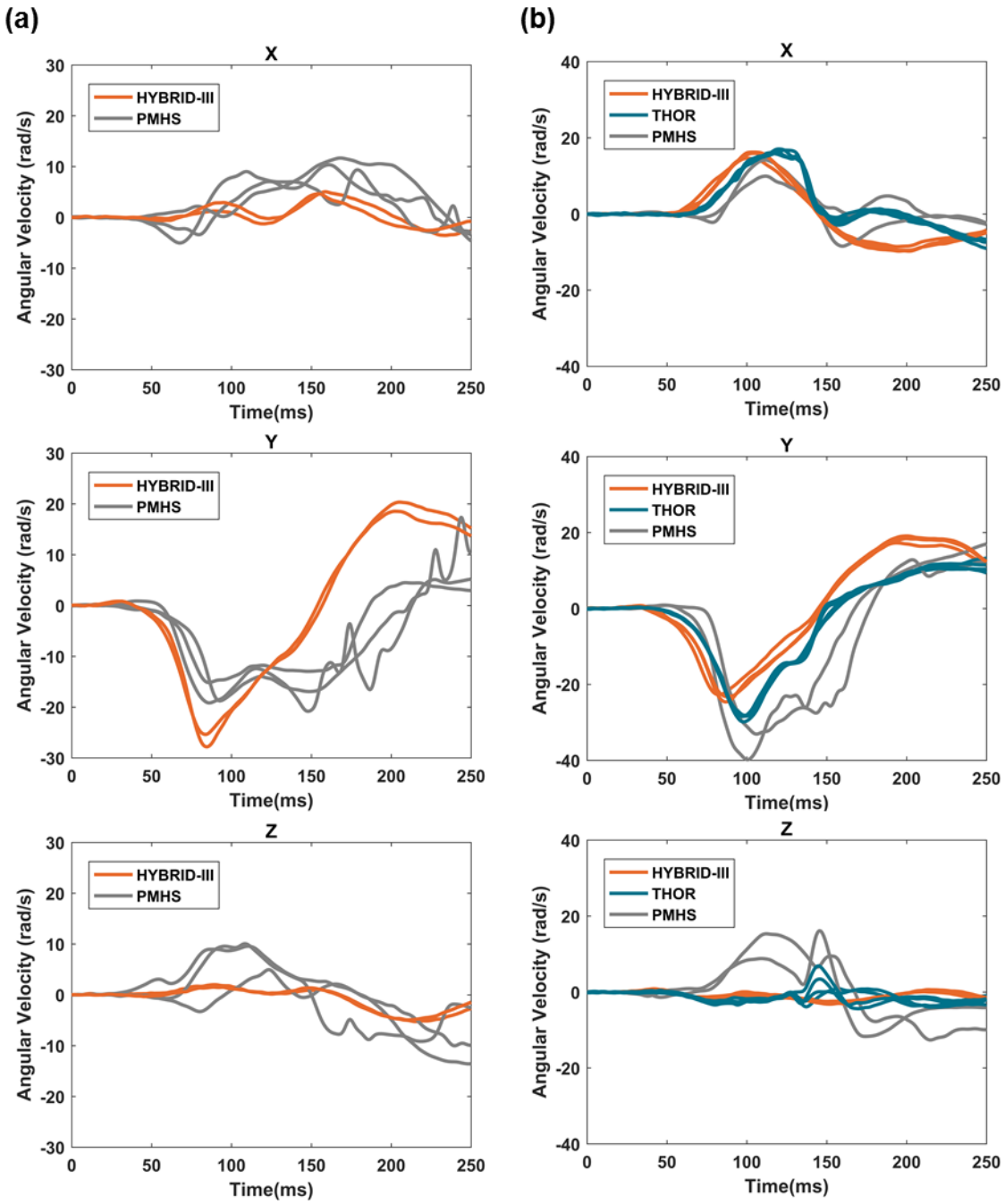

Figure 9-4. Angular velocity time histories of ADTs and PMHS under GS2 conditions (a) and GS3 conditions (b).

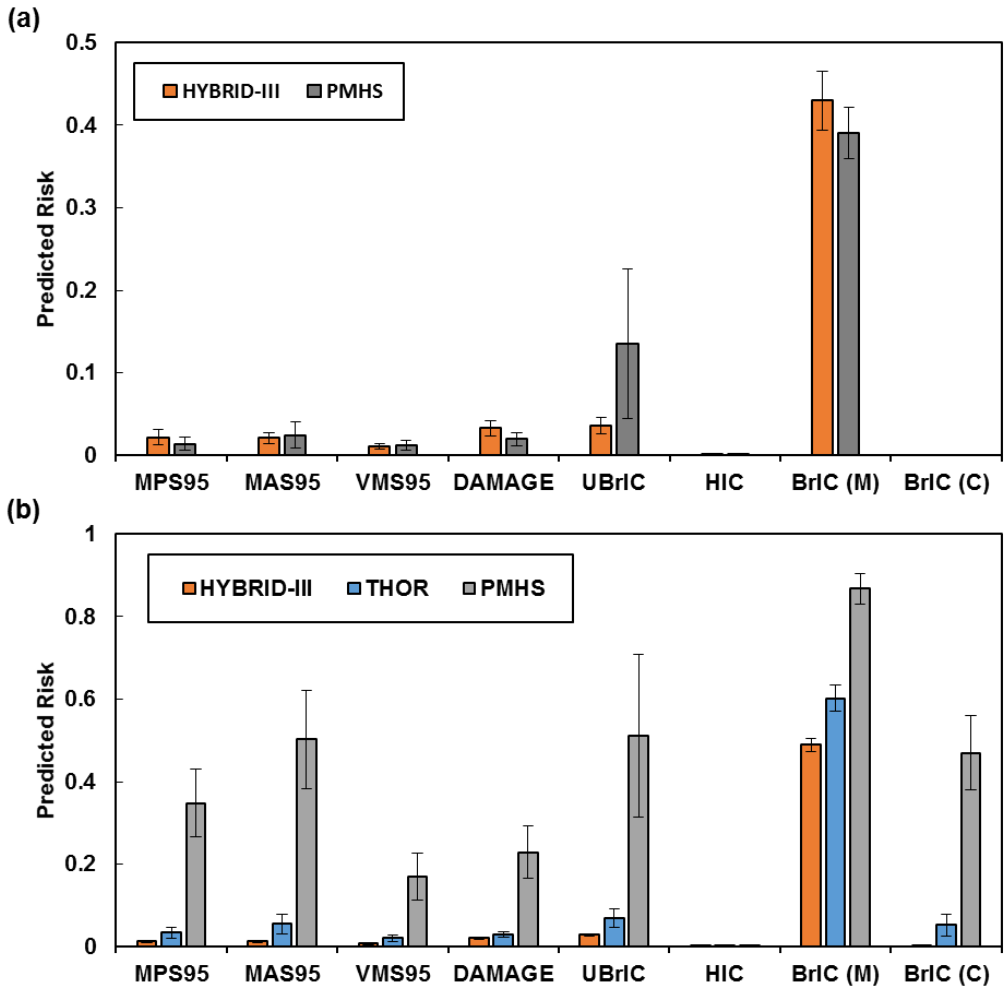

Figure 9-5. Predicted injury probabilities using ADTs and PMHS in GS2 conditions (a) and GS3 conditions (b).

9.4 Discussion

This study applied the newly developed injury risk functions to automotive safety and compared the predicted injury risks in the crash tests with real-world injury rates. Owing to the difficulty of obtaining real-world exposure levels, the problems of evaluating risk functions using epidemiological data come to light. In addition, the error introduced by crash tests using ATDs would substantially influence the prediction of injury vulnerability under certain conditions.

9.4.1 Field Data Analysis

Although the absolute injury rates may not be trustworthy in many configurations due to the small sample size, evaluating the IRFs with real-world crash data provided more insight into the choice of injury metric. Comparing between different crash configuration, the current field analysis revealed the occupants in side crashes are at higher risk (33%) than those in frontal crashes (6.6%) at a similar speed. This observation, consistent with the findings in the literature (Antona-Makoshi et al., 2018), can be explained as occupants in side crashes are located closer to the intruding structure compared to those in frontal crashes, making it difficult for crashworthiness and restraint systems to interact. In the crash tests, as shown in Figure 9-6, this distinct disparity can be detected using the newly development IRFs (MPS95, MAS95, VMS95, DAMAGE, UBrIC), but cannot be reflected through the HIC. BrIC can also differentiate these two configurations to some extent. Several studies (Laituri et al., 2016, 2015; Mueller et al., 2015; Prasad et al., 2014) have assessed brain injury risk functions by comparing predicted injury risk probabilities to real-world injury rates obtained from the NASS. It was commonly found that the AIS 2+ injury rates based on the HIC and CP were more consistent with the real-world injury rates than the MPS-based BrIC injury risk function, but this does not necessarily mean the HIC and CP predicted the real injury risk. For example, the expected mTBI risk values based on CP (sum of the probabilities) was 1.7 in all the 148 crash tests, which might not be realistic.

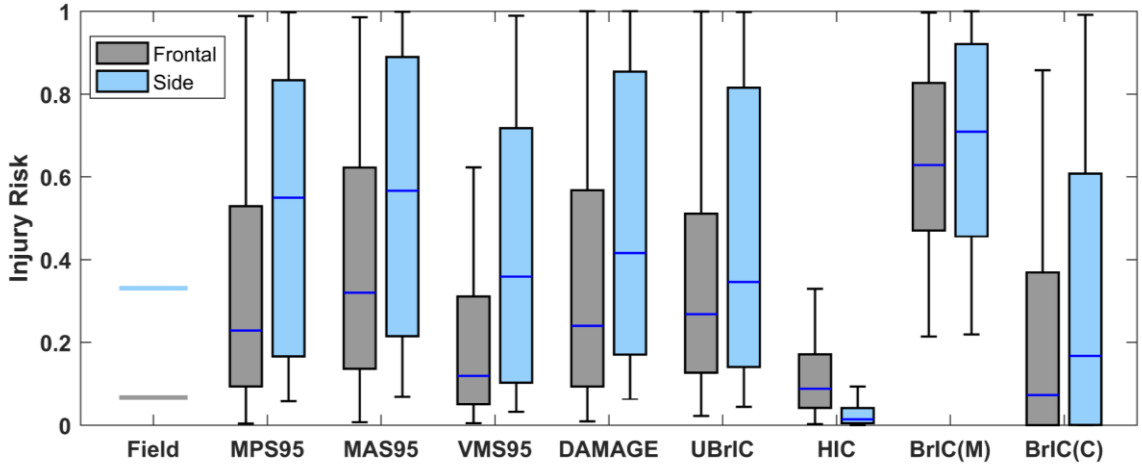

Figure 9-6. Comparison between Injury probabilities in frontal crashes and side crashes.

Crash configuration 1 did not differentiate the same overlap, moderate overlap, and full engagement frontal crashes. The predicted injury risks were similar between these three crash modes (Figure 9-7). This might be partially explained by the observation that the Hybrid III was insensitive to test modes (oblique and frontal). While the weighted injury rates of the full engagement and small overlap shown in the figure were significantly lower than the moderate overlap, the unweighted injury rates of these crashes were similar (9.2%, 11%, and 12%). Using the same NASS dataset, different selection criteria would lead to different conclusions (Table 9-6) as a very small number of injured cases were available. The field injury rates were dependent on Delta-V, as provided in Figure A28 (Appendix G).

Table 9-6. Head and brain injury risk in different frontal crash modes in the literature.

Study	Full Engagement	Moderate Overlap	Small Overlap	Categories	Delta-V
Laituri et al. (2016)	5%	3%	7%	AIS2+	48-64 km/h
	1%	2%	4%	AIS3+	48-64 km/h
Mueller et al., (2015)	--	1.2 %	4.6 %	AIS3+	--
Prasad et al., (2014)	2.09%	1.86%	0.19%	AIS3+ (head/face)	--
Current study*	4.8% (9.2%)	13 % (11%)	2.5% (12%)	mTBI (concussion)	40-80 km/h

*Unweighted injury rates in the parentheses.

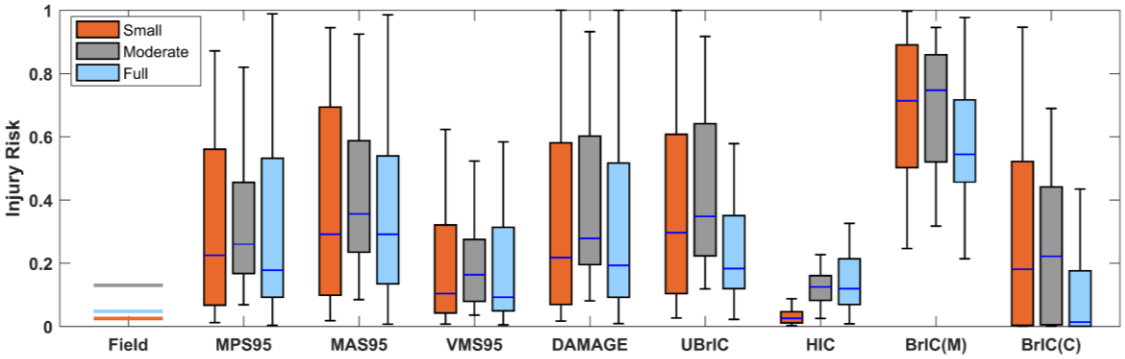

Figure 9-7. Comparison between Injury probabilities in different frontal crash modes.

It is important to note that the field analysis does have several limitations. First, the loading conditions in real-world crashes are complex. Even though the crash conditions were roughly divided based on Delta-V and impact direction, other underlying intrinsic and extrinsic conditions (e.g., vehicle type, principal direction of force, occupant demographics and morphology) could also contribute to injury risk. For example, sex and age are significant contributors to predict the risk of brain injury (Antona-Makoshi et al., 2018). These underlying factors also contribute to the large variation in injury probabilities observed in crash tests in certain crash modes. Second, because the crash test data and the NASS-CDS data satisfying the inclusion criteria were not random samples, the current analysis was limited by the small sample size. A large disparity between weighted and unweighted injury risk was exhibited in some configurations. The crashes selected in NASS CDS were a probability sample of all crashes occurring in the survey year, the data from these crashes were "weighted" to produce national estimates. Weights were resulted from the stages of selection, reflecting that crash's probability of selection. Since the selection criteria used by NASS was different with the current criteria used in this study, whether the weighting factors are still suitable is difficult to determine and requires rigorous investigation in the future.

9.4.2 Biofidelity of the Anthropometric Test Dummy

Since the head kinematics in real-world crashes were not available, using crash tests to estimate real-world injury risk could also be affected by the biofidelity of ATDs. The fidelity of the football reconstruction data that was used to develop the IRFs was also dependent on the biofidelity of ATDs (Hybrid III).

The biofidelity of the Hybrid III ATD was previously evaluated for sports injury scenarios in the laboratory. The Hybrid III ATD reconstructions produced similar peak accelerations for concussive impacts but generated higher rotational velocities under blunt impact (Schnebel et al., 2007). While in the gold standard 3 condition the ATDs significantly produced lower rotational velocities. This is consistent with the findings of a study using a similar dataset (Parent et al., 2017). But the ATD does not necessarily underpredict injury in real-world conditions. The main caveat to this finding was that the "gold standard" setup did not include airbags, thus the head response in this condition exhibited completely free motion, which was unlikely to occur in a frontal and oblique crash in a vehicle with adequate airbag coverage. In addition to the gold standard tests (Shaw et al., 2009), Parent et al. (2017) also evaluated the biofidelity of Hybrid III and THOR in a Far Side Oblique conditions, which represents a more realistic occupant environment in an Oblique Moving Deformable Barrier (OMDB) (NHTSA, 2015) crash test and includes a standard vehicle seat, a three-point seat belt with a pretensioner and load limiter, and a front passenger airbag. The correlation between the head responses of the ATDs and those of the PMHS in this condition were lower than those in the gold standard conditions (Parent et al., 2017). The effect of the head kinematics differences (Figure A29 in Appendix G) in terms of injury probability was actually small, as shown in Figure 9-8. Nevertheless, the variation in the head kinematics of those tests was much larger. It was expected that as the similarity of the test condition

to the real-world conditions increases, the ability of the ATDs to reproduce the biofidelic head response decreases. Further on, the ATDs were designed to replicate the PMHS responses, and the differences between *in vivo* subjects and the PMHS also needs to be considered. For example, the head motion would be affected by the condition of the brain, which may have deteriorated when the tests were conducted. The axial rotation of the head in the GS tests (Figure 9-4) might not be realistic for in vivo subject because of the lack of active musculature (Thunnissen et al., 1995). All those factors would contribute to the discrepancy observed between the predicted injury risk and the field injury rates.

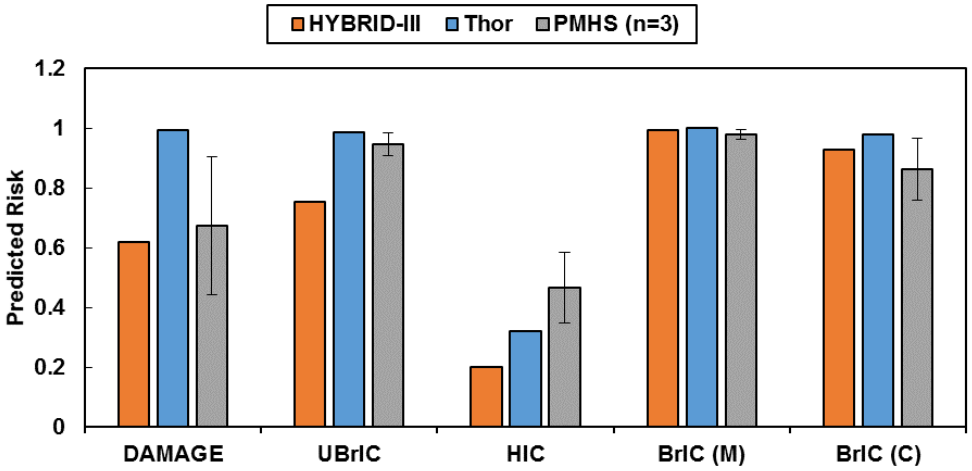

Figure 9-8. Predicted injury probabilities using ADTs and PMHS in far side oblique condition.

Taken together, the newly developed injury risk functions predicted reasonable injury probabilities compared with the field observation in similar automotive crash conditions. They generally showed better capability over the current criteria (e.g., HIC) to positively distinguish the risk sustained in different crash scenarios (frontal impact versus side impact). In this Chapter, it has also been mentioned that evaluating the risk functions with real-world accident analysis is challenging, predicting the actual injury risk requires the accurate characterization of the exposure data, which is not currently available. The test dummies used to predict the head exposure data at certain crash configuration have questions in biofidelity. The crash tests, normally designed to

evaluate the safety of cars, were performed at high severity conditions, which only represent a small number of crashes in the current NASS CDS database. The real injury risk determined by those samples in the NASS CDS database was also implausible since those highly influential weighting factors in the NASS database can skew the distribution of injuries. The risk functions should be rigorously evaluated in the future when the aforementioned questions were better addressed with new information and biomechanical data. For the current data, the developed risk functions show improved predictability and sensitivity to different crash configurations, thus could be considered as foundations to create a feasible incentive for the industry to improve the level of head protection to beyond what is achievable with the current criteria (e.g., HIC).

CHAPTER 10 : CONCLUSIONS

Traumatic brain injuries are a significant public health burden occurring in automotive crash, accidents, sports, and in military training and combat. There is a significant interest in understanding the tolerance of human brain to external mechanical loads with the ultimate objective of mitigation and prevention of TBI. Early TBI research focused on understanding the injury mechanisms in animals, and the latest research focus has been on collecting exposure data in humans that routinely experience head impacts to quantify injury risks. Both research approaches have major limitations when studied in isolation, but when integrated they may provide a complete picture on TBI mechanisms and risk. One of the biggest challenges to forming a more comprehensive understanding of TBI risk is the applicability of animal brain injury data to humans.

The objective of this dissertation was to integrate human and animal brain injury data to establish a well-characterized brain injury dataset that would be used to develop tissue-level brain injury risk functions. To do achieve this goal, novel methods were developed from state-of-the-art computational models of human and animal brains to bridge the interspecies gap between human and NHP injury data, assuming the equivalence of tissue-level metrics across primates. The work from this dissertation is expected to have a substantial impact to the field of brain injury biomechanics. The results and the novel methods in the work have the potential of facilitating the development of advanced injury assessment tools and are a valuable overarching framework for technical innovation to mitigate brain injury.

10.1 Major Contributions

The main contribution of this dissertation will be the two innovative methodologies to develop tissue-level injury risk functions.

1. Methodology for interspecies brain injury data integration.

This work provided an overarching framework for understanding human brain injury mechanism and tolerance using human and animal data. The novelty of this work lies in the application of harmonized computational models to integrate brain injury responses at the tissue level (Chapter 8). The tissue level metrics were independent of the size and shape of the brain and were applicable in any loading conditions. This is an efficient technique for combining interspecies injury data. The utilization of harmonized tools alleviate the deficits involved with physical models (gel-filled skull) or cadaveric models, neither of which currently have the desired spatial resolution for the measured nodal responses to investigate tissue-level metrics. This method can be utilized to enhance the current injury risk functions when new *in vivo* injury data are collected in the future.

This methodology was demonstrated by integrating the primate data in the development of tissue-level injury risk functions. Extension of this concept to another primate (e.g., chimpanzee) and animal model of different size and physiologies is promising, contingent on a better understanding of the interspecies difference in physiological responses and mechanical properties of brain tissue in the future. Even when the (physiological and mechanical) prerequisite was not fulfilled, correlating the biomechanical responses will be the first step to correlating animal injury data to human injury.

2. Cross-species brain injury scaling method

The novelty of this dissertation also lies in proposing a new cross-species scaling method (Chapter 6) to facilitate the usage of animal brain injury data in human TBI study. Although animal data can be correlated with data from humans through FE simulations, the simulation of animal tests was not available in many situations (e.g., harmonized computational models were not

available, or legacy animal studies did not provide time history data of head kinematics). In that case, scaling methods are crucial in the development of both tissue-level and kinematics-based injury risk functions. The merit of the scaling method also gives an explicit relationship to find the equivalent biomechanical loads between different species that result in similar tissue-level mechanical responses. Particularly, the frequency scaling, inspired by characterizing biomechanical responses using simply mechanical systems (Mertz, 1984), addresses limitations with traditional scaling methods by accounting for the anatomical and morphological complexity of the brains of different species. A new (ellipsoidal) method was further developed to apply the direction-dependent frequency scaling factors to complex, three-dimensional head motions.

The scaling relations developed in this study provided a reasonable method for correlating the biomechanical response of the brain of different species. Although more injury data is required to validate this scaling relation, application of the scaling model to the current *in vivo* injury data suggested a similar tolerance of human and NHP brain injury (Chapter 8). The approach used to develop the scaling relations can be extended to other animal models of different size and physiologies with computational tools or even experimental data if available.

10.2 Other Contributions

The significance of this work also lies in the following:

1. *This work developed a new modeling technique to explicitly incorporate mesoscopic axonal tractography in multi-scale finite element brain models.*

In Chapter 3, an anisotropic and heterogeneous brain model was developed by explicitly incorporating axonal fibers as embedded cable elements into the previously validated brain model. The updated model demonstrated good biofidelity when simulating the latest human brain

deformation data (Chapter 4). Although a fixed coupling between the axonal tracts and the ground substance was assumed in this work partly due to the lack of experimental reference, the mathematical formulation of this approach allows us to include slip behavior on to the axonal fibers. As the focus of this work was to evaluate axonal strain, slipping conditions were not expected to affect the results as it probably just shifts the axonal strain level. While this work focuses on evaluating global axonal strain as an injury predictor, the approach described (and the model developed) enables scientists to track the mechanical response of the mesoscale structure (axonal fiber tracts) of the brain. For example, investigation of the mechanical disruption of certain axonal tracts in the neural networks might provide us with new insights into the symptoms (e.g., the memory and attention deficits) observed in mild TBI subjects. The framework presented here can also be generalized to include other mesoscopic anatomical details in finite element models without additional mesh generation.

2. *This work developed a series of harmonized FE models and established a model calibration and evaluation procedure.*

This contribution was presented in Chapter 3, 4, and 5. Human, baboon, and macaque brain FE models were improved through harmonized modeling techniques and mesoscale axonal tracts. The development of the human brain started from the accurate constitutive characterization (calibration) of brain tissue and completed with evaluation of brain deformation. The calibration and evaluation were conducted in various modes to ensure the model's applicability in a broad range of relevant loading conditions. It was one of the first studies to compare three-dimensional brain responses in a FE model to *in situ* brain deformation. The procedure used in this study can guide the continual development of FE models. The developed FE models may be leveraged in future TBI studies for a broad range of applications.

3. *This work reviewed the pros and cons of existing in vivo injury data in the literature and collected a dataset suitable for the development of injury risk functions.*

The work in Chapter 7 summarized sixty years of *in vivo* brain injury data, and this study pointed out that the selection of certain injury data should be oriented towards the objectives to study specific types of brain injuries because of the huge disparities in test protocols, loading conditions, and the resulting types of injuries. A dataset of 300 cases, with a diverse spectrum of clinical outcomes spanning from no injury to severe diffuse injuries, was collected and prepared for simulation. These data and other collected data (but discarded due to different injury types) may be leveraged in future studies for investigating other types of brain injury (e.g., brainstem injury and hematoma) and the evaluation of brain injury risk functions.

4. *This work demonstrated the importance of considering the resonance behavior of the brain under the rotational motion in studying traumatic brain injury.*

The findings in Chapter 6 and Chapter 8 explored an intriguing hypothesis that the deformation responses of the brain-skull system could be simplified as a mass-spring-damping mechanical system. The deformation was sensitive to the frequency/duration of the loading pulses. As stated by Holbourn (1943) '*for blows of long duration, the injury is proportional to the (angular) acceleration, on the other hand for very short blows the injury is proportional to the (angular) velocity*'. What was unknown from Holbourn's work was the critical values that distinguish a certain blow as being a long-duration pulse or short-duration pulse. In this study, the calculated natural frequency from the well-validated axon-based models ranges from 50 Hz to 75 Hz depending on the rotation directions. Compared with the natural frequency of the brain, most head kinematics in automotive crashes with restraint system and even in some helmeted football impacts have a lower frequency. Thus, angular accelerations correlated better with injury than the

angular velocity did. This corroborated the results in Chapter 8 and those in the literature. The most practical meaning of this finding was creating a feasible incentive for the automotive industry to improve the level of head protection beyond what is achievable with the widely used HIC and BrIC criterion, as an effective countermeasure should aim at reducing the force at impact which is directly related to the angular acceleration.

5. *This work developed a set of injury risk functions for mild and severe brain injury.*

The addition of this dissertation provided a series of tissue-level injury risk functions for mild and severe TBI (Chapter 8). The utility of these results is the potential for the injury risk functions (developed or based on) in this dissertation to be used in crashworthiness and helmet safety evaluation. Kinematics-based injury risk functions can be derived based on the correlation between associated kinematics-based metrics and tissue-level metrics (Chapter 9). The developed injury risk functions were applied to automotive crash scenarios, and the missing link between biomechanical tolerance and the field injury risk was identified. Those results are expected to influence car safety regulations, provide guidelines for helmet design and development of other head safety equipment.

10.3 Assumptions, Limitations, and Applicability

The sections below discussed the important assumptions, some of the limitations, and the range of applicability of the developed methods.

1. *Cellular compositions.*

The important assumption for this work is that equal tissue-level stimulus would cause similar severities of injury for both animal and human. To fulfill this assumption, animal and human should have a similar cellular composition of the brain. There is substantial variability in

neuronal densities per milligram of brain tissue across mammalian species (Herculano-Houzel and Dos Santos, 2018). At an average of 86 billion neurons and 85 billion nonneuronal cells, the human brain has the same overall 1:1 nonneuronal/neuronal ratio as other generic primates, but outliers in the primates exist. For example, common squirrel monkey (*Saimiri sciureus*) has an overall 1:1.6 nonneuronal/neuronal ratio. Some non-primate species (e.g., ferret) also have an overall 1:1 nonneuronal/neuronal ratio as humans. This prerequisite should be carefully examined before the extension and application of this work to other species.

2. Proportions and relative size.

Apart from the consideration of cellular composition across species, other neuroanatomical differences between animals and humans would likely influence the tissue-level equivalence as only global measures of the injury metrics were considered. For example, a power law relation was found between the volumes of gray and white matters across mammalian species with an exponent around 1.22 – 1.32 (Ventura-Antunes et al., 2013; Zhang and Sejnowski, 2000). This difference of volume ratio between gray and white matters across species would result in a different interpretation of the global tissue-level metrics across species. In other words, if the gray matter and white matters are not equally vulnerable to TBI, the same values of the tissue-level injury metrics would indicate different impairments to the brains of different species as the proportions of injured white matter or gray matter are different. A similar argument would apply to the interspecies difference in the proportions of the cerebrum in the brain, which varies in relative size from 42% (in the mouse) to 82% of brain mass (in the human) (Herculano-Houzel, 2009). So, another limitation in this work was that brain injury tolerance is not region-specific.

3. Mild brain injury diagnosis and other associated injuries.

This study restricted the brain injuries to closed-head diffuse-type injuries. Other types of brain injuries (e.g., brainstem/spinal cord injury and focal injuries) were not considered due to the limited capabilities of current FE head models and the possible existence of alternative mechanisms. The diagnosis of diffuse-type mild brain injuries was ambiguous and has changed over time. This ambiguity in the mTBI diagnosis might introduce error into the developed mTBI injury risk functions. Particularly, the symptoms induced by cervical spine injuries are often similar to those listed for mTBI, which leads to confusion for the medical diagnosis (Morin et al., 2016). There is a lack of sound evidence in the literature on the involvement of the cervical spine in mTBI. Biofidelic coupling of the brain model with a neck model would improve the understanding of the cervical spine injury and its relations with TBI.

4. Other unaddressed aspects.

Other limitations include the lack of considering the influence of age and sex on brain injury, unvalidated NHP brain FE models, out-of-date injury diagnosis methods, and other bias and ambiguity in the existing injury data (Chapter 7 and 8). Some of these limitations were likely to be addressed in the near future and discussed in detail in the following section.

10.4 Future Work

Following this dissertation, some recommended research topics include:

1. In situ brain deformation of the animal models under rotational motion.

The application of the tissue equivalence approach relies heavily on the biofidelity of the brain FE models. While our understanding of human brain deformations under rotational head motion has been greatly increased by recent advances in *in vivo* and *in situ* experimental studies

(Alshareef et al., 2018; Chan et al., 2018), unfortunately, data for validating animal brain FE model is still extremely limited. These data are more demanding and much-needed to translate animal brain injury findings to humans. *In situ* brain deformation experiments would also improve the understanding of the resonance of the human brain under head rotation, which was critical for selecting suitable kinematics-based metrics for certain application in this dissertation.

2. Traumatic cerebral vascular injury.

In addition to concussion and DAI, vascular brain injury is also frequent in automotive crashes (Antona-Makoshi et al., 2018). When it comes to modeling the complex cerebral vasculature structure, the embedded element technique adopted to incorporate FE meshes of highly complex structures into the brain mesh provide advantages over the traditional mesh method that generate shared nodes between elements. The novel method could address the caveat that requires cumbersome mesh generation processes and provide more options for modeling the connection between the blood vessel and brain tissue other than a fixed connection (Ho and Kleiven, 2007). This method will help us study vascular injury under relevant loading scenarios.

3. Additional in vivo injury studies with animal models.

The legacy non-human primate data were conducted in the 1960s to the 1980s, the understanding of brain injury has been improved since then, as have the techniques for measuring head kinematics, as well as imaging and histopathology techniques. In addition to deriving tolerance of human brain injury, animal models provide a unique opportunity to examine cellular and molecular responses using histological assessment, which can give important insights into the mechanism associated with the evolution of brain injury.

4. Advances in the computational brain model.

Although the head and brain FE models have been continuously improving, some issues still hamper their application in studying brain injury and needed to be resolved. As recognized (Giudice et al., 2018), few existing models, if any, was able to produce a converged strain response at conditions relevant to injury. Biofidelic coupling of the brain model with a neck model including muscles and spinal cord is also desired to study brainstem injury. The boundary conditions (e.g., CSF and membranes) of the brain tissue, which were shown to affect the brain response in computational models significantly, also require accurate characterization and need to be explored in a rigorous manner in the future.

10.5 Summary

The public health burden of TBI is substantial, affecting the lives of millions and millions worldwide. The key public health strategy to reduce the burden and cost of this injury is prevention and mitigation, which requires a thorough understanding the mechanism and risk of TBI. This study has demonstrated the effectiveness of interspecies data integration to address some of the limitations using previous TBI data, the findings in this study could be immediately useful as tentative guidelines for designing and evaluating countermeasures at preventing TBI in automotive and sports industry, but more research is needed before conclusive guidelines can be identified because of the complex nature of TBI. The long-term vision, of which this dissertation is a small part, is the thorough understanding of the TBI mechanism through the combining multifaceted innovations in animal models, real-time field head injury data acquisition, biomarkers, medical imaging, and pathology techniques. The two methodologies (harmonized species-specific computational simulation and interspecies scaling) developed in this study could provide the biomechanical foundation towards revealing the true mechanism of TBI.

REFERENCES

Abel, J.M., Gennarelli, T.A., Segawa, H., 1978. Incidence and severity of cerebral concussion in the rhesus monkey following sagittal plane angular acceleration. SAE Transactions 3144–3150.

Acosta, S.M., Ash, J.H., Lessley, D.J., Shaw, C.G., Heltzel, S.B., Crandall, J.R., 2016. Comparison of Whole Body Response in Oblique and Full Frontal Sled Tests, in: Proceedings of IRCOBI Conference.

Adluru, N., Zhang, H., Fox, A.S., Shelton, S.E., Ennis, C.M., Bartosic, A.M., Oler, J.A., Tromp, D.P., Zakszewski, E., Gee, J.C., others, 2012. A diffusion tensor brain template for rhesus macaques. Neuroimage 59, 306–318.

Afshari, J., Haghpanahi, M., Kalantarinejad, R., 2017. Developing new brain injury criteria for predicting the intracranial response by calculating von Mises stress, coup pressure and contrecoup pressure. Journal of the Brazilian Society of Mechanical Sciences and Engineering 39, 3729–3741.

Akaike, H., 1974. A new look at the statistical model identification, in: Selected Papers of Hirotugu Akaike. Springer, pp. 215–222.

Alshareef, A., Giudice, J.S., Forman, J., Salzar, R.S., Panzer, M.B., 2018. A Novel Method for Quantifying Human In Situ Whole Brain Deformation under Rotational Loading Using Sonomicrometry. Journal of Neurotrauma 35, 780–789. https://doi.org/10.1089/neu.2017.5362

Anderson, R.W., Brown, C.J., Blumbergs, P.C., McLean, A.J., Jones, N.R., 2003. Impact mechanics and axonal injury in a sheep model. Journal of neurotrauma 20, 961–974.

Antona-Makoshi, J., 2016. Traumatic brain injuries: animal experiments and numerical simulations to support the development of a brain injury criterion. Chalmers University of Technology Gothenburg, Sweden.

Antona-Makoshi, J., Davidsson, J., Ejima, S., Ono, K., 2012. Reanalysis of monkey head concussion experiment data using a novel monkey finite element model to develop brain tissue injury reference values, in: Proceeding of the 2012 International IRCOBI Conference on the Biomechanics of Impact.

Antona-Makoshi, J., Davidsson, J., Ejima, S., Ono, K., Brolin, K., Anata, K., 2013. Correlation of global head and brain tissue injury criteria to experimental concussion derived from monkey head trauma experiments, in: IRCOBI Conference. pp. 509–522.

Antona-Makoshi, J., Mikami, K., Lindkvist, M., Davidsson, J., Schick, S., 2018. Accident analysis to support the development of strategies for the prevention of brain injuries in car crashes. Accident Analysis & Prevention 117, 98–105.

Arbogast, K.B., Margulies, S.S., 1997. Regional differences in mechanical properties of the porcine central nervous system. SAE Technical Paper.

Atlan, L.S., Smith, C., Margulies, S.S., 2018. Improved prediction of direction-dependent, acute axonal injury in piglets. Journal of neuroscience research 96, 536–544.

Atsumi, N., Nakahira, Y., Tanaka, E., Iwamoto, M., 2018. Human brain modeling with its anatomical structure and realistic material properties for brain injury prediction. Annals of biomedical engineering 46, 736–748.

Azevedo, F.A., Carvalho, L.R., Grinberg, L.T., Farfel, J.M., Ferretti, R.E., Leite, R.E., Filho, W.J., Lent, R., Herculano-Houzel, S., 2009. Equal numbers of neuronal and nonneuronal cells make the

human brain an isometrically scaled-up primate brain. Journal of Comparative Neurology 513, 532–541.

Bain, A.C., Meaney, D.F., 2000. Tissue-level thresholds for axonal damage in an experimental model of central nervous system white matter injury. Journal of biomechanical engineering 122, 615–622.

Bandak, F.A., Eppinger, R.H., 1994. A three-dimensional finite element analysis of the human brain under combined rotational and translational accelerations. SAE transactions 1708–1726.

Bermejo, M., Santos, A.P., Goicolea, J.M., 2017. Development of practical finite element models for collapse of reinforced concrete structures and experimental validation. Shock and Vibration 2017.

Bilston, L.E., Liu, Z., Phan-Thien, N., 2001. Large strain behaviour of brain tissue in shear: some experimental data and differential constitutive model. Biorheology 38, 335–345.

Bowden, D., Dubach, M., 2000. Applicability of the template atlas to various primate species. Primate Brain Maps: Structure of the Macaque Brain. Elsevier, New York.

Brands, D.W., Bovendeerd, P.H., Peters, G.W., Wismans, J.S., Paas, M.H., van Bree, J.L., 1999. Comparison of the dynamic behavior of brain tissue and two model materials. SAE Technical Paper.

Braun, J., Guo, J., Lützkendorf, R., Stadler, J., Papazoglou, S., Hirsch, S., Sack, I., Bernarding, J., 2014. High-resolution mechanical imaging of the human brain by three-dimensional multifrequency magnetic resonance elastography at 7T. Neuroimage 90, 308–314.

Browne, K.D., Chen, X.-H., Meaney, D.F., Smith, D.H., 2011. Mild traumatic brain injury and diffuse axonal injury in swine. Journal of neurotrauma 28, 1747–1755.

Budday, S., Nay, R., de Rooij, R., Steinmann, P., Wyrobek, T., Ovaert, T.C., Kuhl, E., 2015. Mechanical properties of gray and white matter brain tissue by indentation. Journal of the mechanical behavior of biomedical materials 46, 318–330.

Budday, S., Sommer, G., Birkl, C., Langkammer, C., Haybaeck, J., Kohnert, J., Bauer, M., Paulsen, F., Steinmann, P., Kuhl, E., others, 2017. Mechanical characterization of human brain tissue. Acta biomaterialia 48, 319–340.

Cater, H.L., Sundstrom, L.E., Morrison III, B., 2006. Temporal development of hippocampal cell death is dependent on tissue strain but not strain rate. Journal of biomechanics 39, 2810–2818.

CDC, 2015. Report to congress on traumatic brain injury in the United States: epidemiology and rehabilitation. National Center for Injury Prevention and Control 1–72.

Cernak, I., 2010. The importance of systemic response in the pathobiology of blast-induced neurotrauma. Frontiers in neurology 1, 151.

Chan, D.D., Knutsen, A.K., Lu, Y.-C., Yang, S.H., Magrath, E., Wang, W.-T., Bayly, P.V., Butman, J.A., Pham, D.L., 2018. Statistical Characterization of Human Brain Deformation During Mild Angular Acceleration Measured In Vivo by Tagged Magnetic Resonance Imaging. Journal of Biomechanical Engineering 140, 101005.

Chatelin, S., Constantinesco, A., Willinger, R., 2010. Fifty years of brain tissue mechanical testing: from in vitro to in vivo investigations. Biorheology 47, 255–276.

Chatelin, S., Deck, C., Willinger, R., 2013. An anisotropic viscous hyperelastic constitutive law for brain material finite-element modeling. Journal of biorheology 27, 26–37.

Clayton, E.H., Genin, G.M., Bayly, P.V., 2012. Transmission, attenuation and reflection of shear waves in the human brain. Journal of The Royal Society Interface 9, 2899–2910.

Cloots, R.J., Van Dommelen, J., Kleiven, S., Geers, M., 2013. Multi-scale mechanics of traumatic brain injury: predicting axonal strains from head loads. Biomechanics and modeling in mechanobiology 12, 137–150.

Coats, B., Eucker, S.A., Sullivan, S., Margulies, S.S., 2012. Finite element model predictions of intracranial hemorrhage from non-impact, rapid head rotations in the piglet. International Journal of Developmental Neuroscience 30, 191–200.

COST, 2001. Motorcycle safety helmets. European Co-operation in the field of Scientific and Technical research (COST) project (.

Cullen, D.K., Harris, J.P., Browne, K.D., Wolf, J.A., Duda, J.E., Meaney, D.F., Margulies, S.S., Smith, D.H., 2016. A porcine model of traumatic brain injury via head rotational acceleration, in: Injury Models of the Central Nervous System. Springer, pp. 289–324.

Davis, M.L., Koya, B., Schap, J.M., Gayzik, F.S., 2016. Development and full body validation of a 5th percentile female finite element model. SAE Technical Paper.

de Rooij, R., Kuhl, E., 2016. Constitutive modeling of brain tissue: current perspectives. Applied Mechanics Reviews 68, 010801.

De, S., Rosen, J., Dagan, A., Hannaford, B., Swanson, P., Sinanan, M., 2007. Assessment of tissue damage due to mechanical stresses. The International Journal of Robotics Research 26, 1159–1171.

Deck, C., Willinger, R., 2008. Improved head injury criteria based on head FE model. International Journal of Crashworthiness 13, 667–678.

Duhaime, A.-C., 2006. Large animal models of traumatic injury to the immature brain. Developmental neuroscience 28, 380–387.

Duma, S.M., Manoogian, S.J., Bussone, W.R., Brolinson, P.G., Goforth, M.W., Donnenwerth, J.J., Greenwald, R.M., Chu, J.J., Crisco, J.J., 2005. Analysis of real-time head accelerations in collegiate football players. Clinical Journal of Sport Medicine 15, 3–8.

Elkin, B.S., Morrison, B., 2007. Region-specific tolerance criteria for the living brain. SAE Technical Paper.

Eppinger, R., Sun, E., Bandak, F., Haffner, M., Khaewpong, N., Maltese, M., Kuppa, S., Nguyen, T., Takhounts, E., Tannous, R., others, 1999. Development of improved injury criteria for the assessment of advanced automotive restraint systems–II. National Highway Traffic Safety Administration 1–70.

Estes, M., McElhaney, J., 1970. Response of brain tissue to compressive loading, in: Mechanical Engineering. Asme-Amer Soc Mechanical Eng 345 E 47TH ST, NEW YORK, NY 10017, p. 58.

Ewing, C.L., Thomas, D.J., 1972. Human Head and Neck Response to Impact Acceleration. Naval Aerospace Medical RESEARCH Lab Pensacola Fl.

Fallenstein, G., Hulce, V.D., Melvin, J.W., 1969. Dynamic mechanical properties of human brain tissue. Journal of biomechanics 2, 217–226.

Faul, M., Coronado, V., 2015. Epidemiology of traumatic brain injury, in: Handbook of Clinical Neurology. Elsevier, pp. 3–13.

Feng, Y., Abney, T.M., Okamoto, R.J., Pless, R.B., Genin, G.M., Bayly, P.V., 2010. Relative brain displacement and deformation during constrained mild frontal head impact. Journal of The Royal Society Interface 7, 1677–1688.

Feng, Y., Okamoto, R.J., Namani, R., Genin, G.M., Bayly, P.V., 2013. Measurements of mechanical anisotropy in brain tissue and implications for transversely isotropic material models of white matter. Journal of the mechanical behavior of biomedical materials 23, 117–132.

Fernandes, F.A., Tchepel, D., Alves de Sousa, R.J., Ptak, M., 2018. Development and validation of a new finite element human head model: Yet another head model (YEAHM). Engineering Computations 35, 477–496.

Fievisohn, E.M., 2015. TRAUMATIC BRAIN INJURY MECHANISMS IN THE GOTTINGEN MINIPIG IN RESPONSE TO TWO UNIQUE INPUT MODES (PhD Thesis). Virginia Tech.

Fish, J., 1992. The s-version of the finite element method. Computers & Structures 43, 539–547.

Fung, Y., 2013. Biomechanics: mechanical properties of living tissues. Springer Science & Business Media.

Funk, J.R., Duma, S.M., Manoogian, S.J., Rowson, S., 2007. Biomechanical risk estimates for mild traumatic brain injury. Annu Proc Assoc Adv Automot Med 51, 343–361.

Funk, J.R., Rowson, S., Daniel, R.W., Duma, S.M., 2012. Validation of concussion risk curves for collegiate football players derived from HITS data. Annals of biomedical engineering 40, 79–89.

Gabler, L.F., Crandall, J.R., Panzer, M.B., 2018a. Development of a Metric for Predicting Brain Strain Responses Using Head Kinematics. Annals of biomedical engineering 1–14.

Gabler, L.F., Crandall, J.R., Panzer, M.B., 2018b. Development of a Second-Order System for Rapid Estimation of Maximum Brain Strain. Annals of biomedical engineering 1–11.

Gabler, L.F., Crandall, J.R., Panzer, M.B., 2016. Assessment of kinematic brain injury metrics for predicting strain responses in diverse automotive impact conditions. Annals of biomedical engineering 44, 3705–3718.

Gabler, L.F., Joodaki, H., Crandall, J.R., Panzer, M.B., 2018c. Development of a single-degree-of-freedom mechanical model for predicting strain-based brain injury responses. Journal of biomechanical engineering 140, 031002.

Gadd, C.W., 1966. Use of a weighted-impulse criterion for estimating injury hazard. SAE Technical Paper.

Galbraith, J., Thibault, L., Matteson, D., 1993. Mechanical and electrical responses of the squid giant axon to simple elongation. Journal of biomechanical engineering 115, 13–22.

Galford, J.E., McElhaney, J.H., 1970. A viscoelastic study of scalp, brain, and dura. Journal of biomechanics 3, 211–221.

Ganpule, S., Daphalapurkar, N.P., Ramesh, K.T., Knutsen, A.K., Pham, D.L., Bayly, P.V., Prince, J.L., 2017. A three-dimensional computational human head model that captures live human brain dynamics. Journal of neurotrauma 34, 2154–2166.

Garimella, H.T., Kraft, R.H., 2017. Modeling the mechanics of axonal fiber tracts using the embedded finite element method. International journal for numerical methods in biomedical engineering 33, e2823.

Garo, A., Hrapko, M., Van Dommelen, J., Peters, G., 2007. Towards a reliable characterisation of the mechanical behaviour of brain tissue: the effects of post-mortem time and sample preparation. Biorheology 44, 51–58.

Gasser, T.C., Ogden, R.W., Holzapfel, G.A., 2006. Hyperelastic modelling of arterial layers with distributed collagen fibre orientations. Journal of the royal society interface 3, 15–35.

Geddes, D.M., Cargill, R.S., LaPlaca, M.C., 2003. Mechanical stretch to neurons results in a strain rate and magnitude-dependent increase in plasma membrane permeability. Journal of neurotrauma 20, 1039–1049.

Gehre, C., Gades, H., Wernicke, P., 2009. Objective rating of signals using test and simulation responses, in: International Technical Conference on the Enhanced Safety of Vehicles. National Highway Traffic Safety Administration.

Gennarelli, T.A., Thibault, L., Ommaya, A.K., 1972. Pathophysiologic responses to rotational and translational accelerations of the head. SAE Technical Paper.

Gennarelli, T.A., Thibault, L.E., Adams, J.H., Graham, D.I., Thompson, C.J., Marcincin, R.P., 1982. Diffuse axonal injury and traumatic coma in the primate. Annals of Neurology: Official Journal of the American Neurological Association and the Child Neurology Society 12, 564–574.

Gennarelli, T.A., Thibault, L.E., Tomei, G., Wiser, R., Graham, D., Adams, J., 1987. Directional dependence of axonal brain injury due to centroidal and non-centroidal acceleration. SAE Technical Paper.

Gennarelli, T.A., Wodzin, E., 2006. AIS 2005: a contemporary injury scale. Injury 37, 1083–1091.

Ghajari, M., Hellyer, P.J., Sharp, D.J., 2017. Computational modelling of traumatic brain injury predicts the location of chronic traumatic encephalopathy pathology. Brain 140, 333–343.

Giordano, C., Cloots, R., Van Dommelen, J., Kleiven, S., 2014. The influence of anisotropy on brain injury prediction. Journal of biomechanics 47, 1052–1059.

Giordano, C., Kleiven, S., 2016. Development of an unbiased validation protocol to assess the biofidelity of finite element head models used in prediction of traumatic brain injury. SAE Technical Paper.

Giordano, C., Kleiven, S., 2014a. Evaluation of axonal strain as a predictor for mild traumatic brain injuries using finite element modeling. SAE Technical Paper.

Giordano, C., Kleiven, S., 2014b. Connecting fractional anisotropy from medical images with mechanical anisotropy of a hyperviscoelastic fibre-reinforced constitutive model for brain tissue. Journal of The Royal Society Interface 11, 20130914.

Giudice, J.S., Zeng, W., Wu, T., Alshareef, A., Shedd, D.F., Panzer, M.B., 2018. An Analytical Review of the Numerical Methods used for Finite Element Modeling of Traumatic Brain Injury. Annals of biomedical engineering 1–18.

Golman, A., Wickwire, A., Harrigan, T., Iwaskiw, A., Armiger, R., Merkle, A., 2013. Hierarchical model validation of the falx cerebri and tentorium cerebelli, in: Proceedings of the Forty First International Workshop. pp. 41–3.

Gray, J., Ritchie, J., 1954. Effects of stretch on single myelinated nerve fibres. The Journal of physiology 124, 84–99.

Gurdjian, E.S., Roberts, V., Thomas, L.M., 1966. Tolerance curves of acceleration and intracranial pressure and protective index in experimental head injury. Journal of Trauma and Acute Care Surgery 6, 600–604.

Hardy, W.N., Foster, C.D., Mason, M.J., Yang, K.H., King, A.I., Tashman, S., 2001. Investigation of head injury mechanisms using neutral density technology and high-speed biplanar X-ray. SAE Technical Paper.

Hardy, W.N., Mason, M.J., Foster, C.D., Shah, C.S., Kopacz, J.M., Yang, K.H., King, A.I., Bishop, J., Bey, M., Anderst, W., Tashman, S., 2007. A study of the response of the human cadaver head to impact. Stapp car crash journal 51, 17–80.

Hay, J.R., Johnson, V.E., Young, A.M., Smith, D.H., Stewart, W., 2015. Blood-brain barrier disruption is an early event that may persist for many years after traumatic brain injury in humans. Journal of neuropathology and experimental neurology 74, 1147–1157.

Herculano-Houzel, S., 2009. The human brain in numbers: a linearly scaled-up primate brain. Frontiers in human neuroscience 3, 31.

Herculano-Houzel, S., Dos Santos, S., 2018. You Do Not Mess with the Glia. Neuroglia 1, 193–219.

Hernandez, F., Giordano, C., Goubran, M., Parivash, S., Grant, G., Zeineh, M., Camarillo, D., 2019. Lateral impacts correlate with falx cerebri displacement and corpus callosum trauma in sports-related concussions. Biomechanics and modeling in mechanobiology 1–19.

Hernandez, F., Wu, L.C., Yip, M.C., Laksari, K., Hoffman, A.R., Lopez, J.R., Grant, G.A., Kleiven, S., Camarillo, D.B., 2015. Six degree-of-freedom measurements of human mild traumatic brain injury. Annals of biomedical engineering 43, 1918–1934.

Ho, J., Kleiven, S., 2007. Dynamic response of the brain with vasculature: a three-dimensional computational study. Journal of biomechanics 40, 3006–3012.

Ho, J., von Holst, H., Kleiven, S., 2009. Automatic generation and validation of patient-specific finite element head models suitable for crashworthiness analysis. International journal of crashworthiness 14, 555–563.

Ho, J., Zhou, Z., Li, X., Kleiven, S., 2017. The peculiar properties of the falx and tentorium in brain injury biomechanics. Journal of Biomechanics 60, 243–247.

Holbourn, A., 1943. Mechanics of head injuries. The Lancet 242, 438–441.

Holzapfel, G.A., Ogden, R.W., 2017. On Fiber Dispersion Models: Exclusion of Compressed Fibers and Spurious Model Comparisons. Journal of Elasticity 129, 49–68. https://doi.org/10.1007/s10659-016-9605-2

Holzapfel, G.A., Ogden, R.W., 2015. On the tension–compression switch in soft fibrous solids. European Journal of Mechanics - A/Solids 49, 561–569. https://doi.org/10.1016/j.euromechsol.2014.09.005

Horgan, T.J., Gilchrist, M.D., 2003. The creation of three-dimensional finite element models for simulating head impact biomechanics. International Journal of Crashworthiness 8, 353–366.

Hrapko, M., Van Dommelen, J., Peters, G., Wismans, J., 2006. The mechanical behaviour of brain tissue: large strain response and constitutive modelling. Biorheology 43, 623–636.

Ibrahim, N.G., Ralston, J., Smith, C., Margulies, S.S., 2010. Physiological and pathological responses to head rotations in toddler piglets. Journal of neurotrauma 27, 1021–1035.

Jean, A., Nyein, M.K., Zheng, J.Q., Moore, D.F., Joannopoulos, J.D., Radovitzky, R., 2014. An animal-to-human scaling law for blast-induced traumatic brain injury risk assessment. Proceedings of the National Academy of Sciences 111, 15310–15315.

Ji, S., Zhao, W., Ford, J.C., Beckwith, J.G., Bolander, R.P., Greenwald, R.M., Flashman, L.A., Paulsen, K.D., McAllister, T.W., 2015. Group-wise evaluation and comparison of white matter fiber strain and maximum principal strain in sports-related concussion. Journal of neurotrauma 32, 441–454.

Jin, X., Lee, J.B., Leung, L.Y., Zhang, L., Yang, K.H., King, A.I., 2006. Biomechanical Response of the Bovine Pia-Arachnoid Complex to Tensile Loading at Varying Strain Rates. SAE Technical Paper.

Jin, X., Zhu, F., Mao, H., Shen, M., Yang, K.H., 2013. A comprehensive experimental study on material properties of human brain tissue. Journal of biomechanics 46, 2795–2801.

Johnson, C.L., McGarry, M.D., Gharibans, A.A., Weaver, J.B., Paulsen, K.D., Wang, H., Olivero, W.C., Sutton, B.P., Georgiadis, J.G., 2013. Local mechanical properties of white matter structures in the human brain. Neuroimage 79, 145–152.

Johnson, C.L., Telzer, E.H., 2018. Magnetic resonance elastography for examining developmental changes in the mechanical properties of the brain. Developmental cognitive neuroscience 33, 176–181.

Johnson, V.E., Meaney, D.F., Cullen, D.K., Smith, D.H., 2015. Animal models of traumatic brain injury, in: Handbook of Clinical Neurology. Elsevier, pp. 115–128.

Jones, D.K., Knösche, T.R., Turner, R., 2013. White matter integrity, fiber count, and other fallacies: the do's and don'ts of diffusion MRI. Neuroimage 73, 239–254.

Joodaki, H., Bailey, A., Lessley, D., Funk, J., Sherwood, C., Crandall, J., 2019. Relative motion between the helmet and head in football impact test. Journal of biomechanical engineering.

Kahane, C.J., 2015. Lives saved by vehicle safety technologies and associated Federal Motor Vehicle Safety Standards, 1960 to 2012–Passenger cars and LTVs–With reviews of 26 FMVSS and the effectiveness of their associated safety technologies in reducing fatalities, injuries, and crashes. Report No. DOT HS 812, 069.

Kanda, R., Nakamura, N., Sekino, H., Sakai, H., Masuzawa, H., MII, K., AOYAGI, N., ARUGA, T., KONO, H., SUGIMORI, T., others, 1981. Experimental Head Injury in Monkeys. Neurologia medico-chirurgica 21, 645–656.

Kang, H.-S., Willinger, R., Diaw, B.M., Chinn, B., 1997. Validation of a 3D anatomic human head model and replication of head impact in motorcycle accident by finite element modeling. SAE transactions 3849–3858.

Kikuchi, A., 1982. Human head tolerance to lateral impact deduced from experimental head injuries using primates, in: Proc. 9th International Technical Conference on Experimental Safety Vehicles. pp. 251–261.

Kimpara, H., Nakahira, Y., Iwamoto, M., Miki, K., Ichihara, K., Kawano, S., Taguchi, T., 2006. Investigation of anteroposterior head-neck responses during severe frontal impacts using a brain-spinal cord complex FE model. SAE Technical Paper.

King, A.I., Yang, K.H., Zhang, L., Hardy, W., Viano, D.C., 2003. Is head injury caused by linear or angular acceleration, in: IRCOBI Conference. Lisbon, Portugal.

King, D., Hume, P.A., Brughelli, M., Gissane, C., 2015. Instrumented mouthguard acceleration analyses for head impacts in amateur rugby union players over a season of matches. The American journal of sports medicine 43, 614–624.

King, D.A., Hume, P.A., Gissane, C., Clark, T.N., 2016. Similar head impact acceleration measured using instrumented ear patches in a junior rugby union team during matches in comparison with other sports. Journal of Neurosurgery: Pediatrics 18, 65–72.

Kleiven, S., 2007. Predictors for traumatic brain injuries evaluated through accident reconstructions. SAE Technical Paper.

Kleiven, S., 2006. Evaluation of head injury criteria using a finite element model validated against experiments on localized brain motion, intracerebral acceleration, and intracranial pressure. International Journal of Crashworthiness 11, 65–79. https://doi.org/10.1533/ijcr.2005.0384

Kleiven, S., von Holst, H., 2002. Consequences of head size following trauma to the human head. Journal of biomechanics 35, 153–160.

Knutsen, A.K., Magrath, E., McEntee, J.E., Xing, F., Prince, J.L., Bayly, P.V., Butman, J.A., Pham, D.L., 2014. Improved measurement of brain deformation during mild head acceleration using a novel tagged MRI sequence. Journal of biomechanics 47, 3475–3481.

Korenczuk, C.E., Votava, L.E., Dhume, R.Y., Kizilski, S.B., Brown, G.E., Narain, R., Barocas, V.H., 2017. Isotropic failure criteria are not appropriate for anisotropic fibrous biological tissues. Journal of biomechanical engineering 139, 071008.

Kruse, S.A., Rose, G.H., Glaser, K.J., Manduca, A., Felmlee, J.P., Jack Jr, C.R., Ehman, R.L., 2008. Magnetic resonance elastography of the brain. Neuroimage 39, 231–237.

Laituri, T.R., El-Jawahri, R.E., Henry, S., Sullivan, K., 2015. Field-based assessments of various AIS2+ head risk curves for frontal impact. SAE Technical Paper.

Laituri, T.R., Henry, S., Pline, K., Li, G., Frankstein, M., Weerappuli, P., 2016. New risk curves for NHTSA's brain injury criterion (BrIC): Derivations and assessments. SAE Technical Paper.

Laksari, K., Wu, L.C., Kurt, M., Kuo, C., Camarillo, D.C., 2015. Resonance of human brain under head acceleration. Journal of The Royal Society Interface 12, 20150331.

Langhaar, H., 1951. Dimensional Analysis and Theory of Models. John Willy Sons. Inc New York.

LaPlaca, M.C., Cullen, D.K., McLoughlin, J.J., Cargill II, R.S., 2005. High rate shear strain of three-dimensional neural cell cultures: a new in vitro traumatic brain injury model. Journal of biomechanics 38, 1093–1105.

Latorre, M., Montáns, F.J., 2016. Stress and strain mapping tensors and general work-conjugacy in large strain continuum mechanics. Applied Mathematical Modelling 40, 3938–3950.

Letcher, F.S., Corrao, P.G., Ommaya, A.K., 1973. Head injury in the champanzee: Part 2: Spontaneous and evoked epidural potentials as indices of injury severity. Journal of neurosurgery 39, 167–177.

Lippert, S.A., Rang, E.M., Grimm, M.J., 2004. The high frequency properties of brain tissue. Biorheology 41, 681–691.

Longhitano, D., Burke, C., Bean, J., Watts, D., Fakhry, S., Meissner, M., Ivarsson, J., Sherwood, C., Crandall, J., Takahashi, Y., others, 2005. Application of the CIREN methodology to the study of pedestrian crash injuries, in: 19th International Technical Conference on the Enhanced Safety of Vehicles (ESV), Washington, DC, June. pp. 6–9.

Love, S.A., Marie, D., Roth, M., Lacoste, R., Nazarian, B., Bertello, A., Coulon, O., Anton, J.-L., Meguerditchian, A., 2016. The average baboon brain: MRI templates and tissue probability maps from 89 individuals. NeuroImage 132, 526–533.

Löwenhielm, P., 1975. Mathematical simulation of gliding contusions. Journal of biomechanics 8, 351–356.

Lu, Y.-C., Daphalapurkar, N.P., Knutsen, A., Glaister, J., Pham, D., Butman, J., Prince, J., Bayly, P., Ramesh, K., 2019. A 3D Computational Head Model Under Dynamic Head Rotation and Head Extension Validated Using Live Human Brain Data, Including the Falx and the Tentorium. Annals of biomedical engineering 1–18.

Maier-Hein, K.H., Neher, P.F., Houde, J.-C., Côté, M.-A., Garyfallidis, E., Zhong, J., Chamberland, M., Yeh, F.-C., Lin, Y.-C., Ji, Q., others, 2017. The challenge of mapping the human connectome based on diffusion tractography. Nature communications 8, 1349.

Mao, H., Zhang, L., Jiang, B., Genthikatti, V.V., Jin, X., Zhu, F., Makwana, R., Gill, A., Jandir, G., Singh, A., others, 2013. Development of a finite element human head model partially validated with thirty five experimental cases. Journal of biomechanical engineering 135, 111002.

Mao, H., Zhang, L., Yang, K.H., King, A.I., 2006. Application of a finite element model of the brain to study traumatic brain injury mechanisms in the rat. SAE Technical Paper.

Margulies, S.S., 1987. Biomechanics of traumatic coma in the primate (head injury).

Margulies, S.S., Thibault, L.E., 1992. A proposed tolerance criterion for diffuse axonal injury in man. Journal of biomechanics 25, 917–923.

Margulies, S.S., Thibault, L.E., 1989. An analytical model of traumatic diffuse brain injury. Journal of biomechanical engineering 111, 241–249.

Margulies, S.S., Thibault, L.E., Gennarelli, T.A., 1990. Physical model simulations of brain injury in the primate. Journal of biomechanics 23, 823–836.

Mata-Mbemba, D., Mugikura, S., Nakagawa, A., Murata, T., Ishii, K., Kushimoto, S., Tominaga, T., Takahashi, S., Takase, K., 2018. Traumatic midline subarachnoid hemorrhage on initial computed tomography as a marker of severe diffuse axonal injury. Journal of neurosurgery 129, 1317–1324.

Mata-Mbemba, D., Mugikura, S., Nakagawa, A., Murata, T., Kato, Y., Tatewaki, Y., Li, L., Takase, K., Ishii, K., Kushimoto, S., others, 2015. Intraventricular hemorrhage on initial computed tomography as marker of diffuse axonal injury after traumatic brain injury. Journal of neurotrauma 32, 359–365.

McAllister, T.W., Ford, J.C., Ji, S., Beckwith, J.G., Flashman, L.A., Paulsen, K., Greenwald, R.M., 2012. Maximum principal strain and strain rate associated with concussion diagnosis correlates with changes in corpus callosum white matter indices. Annals of biomedical engineering 40, 127–140.

McElhaney, J.H., Melvin, J.W., Roberts, V.L., Portnoy, H.D., 1973. Dynamic characteristics of the tissues of the head, in: Perspectives in Biomedical Engineering. Springer, pp. 215–222.

McMurry, T.L., Poplin, G.S., 2015. Statistical considerations in the development of injury risk functions. Traffic injury prevention 16, 618–626.

Meaney, D.F., Smith, D.H., 2011. Biomechanics of concussion. Clinics in sports medicine 30, 19–31.

Meaney, D.F., Smith, D.H., Shreiber, D.I., Bain, A.C., Miller, R.T., Ross, D.T., Gennarelli, T.A., 1995. Biomechanical analysis of experimental diffuse axonal injury. Journal of neurotrauma 12, 689–694.

Mellor, A., 2000. Formula one accident investigations. SAE Technical Paper.

Mendis, K., 1992. Finite element modeling of the brain to establish diffuse axonal injury criteria (PhD Thesis). The Ohio State University.

Mertz, H.J., 1984. A procedure for normalizing impact response data. SAE transactions 351–358.

Mertz, H.J., Prasad, P., Nusholtz, G., 1996. Head injury risk assessment for forehead impacts. SAE Technical Paper.

Miller, L.E., Urban, J.E., Stitzel, J.D., 2017. Validation performance comparison for finite element models of the human brain. Computer methods in biomechanics and biomedical engineering 20, 1273–1288.

Miller, L.E., Urban, J.E., Stitzel, J.D., 2016. Development and validation of an atlas-based finite element brain model. Biomechanics and modeling in mechanobiology 15, 1201–1214.

Mori, S., Crain, B.J., Chacko, V.P., Van Zijl, P.C., 1999. Three-dimensional tracking of axonal projections in the brain by magnetic resonance imaging. Annals of Neurology: Official Journal of the American Neurological Association and the Child Neurology Society 45, 265–269.

Morin, M., Langevin, P., Fait, P., 2016. Cervical spine involvement in mild traumatic brain injury: a review. Journal of Sports Medicine 2016.

Morrison, B., Cater, H.L., Wang, C.C., Thomas, F.C., Hung, C.T., Ateshian, G.A., Sundstrom, L.E., 2003. A tissue level tolerance criterion for living brain developed with an in vitro model of traumatic mechanical loading. SAE Technical Paper.

Mueller, B., MacAlister, A., Nolan, J., Zuby, D., 2015. Comparison of HIC and BRIC head injury risk in IIHS frontal crash tests to real-world head injuries, in: Proceedings of the 24th International Technical Conference on the Enhanced Safety of Vehicles.

Munsch, M., Anderson, R.W., Deck, C., Ludes, B., Willinger, R., 2009. Influence of head boundary conditions in pedestrian real world head trauma simulations, in: Proceedings of the International Research Council on the Biomechanics of Injury Conference. International Research Council on Biomechanics of Injury, pp. 287–299.

Nahum, A.M., Smith, R., Ward, C.C., 1977. Intracranial pressure dynamics during head impact. SAE Technical Paper.

Nakadate, H., Kurtoglu, E., Furukawa, H., Oikawa, S., Aomura, S., Kakuta, A., Matsui, Y., 2017. Strain-rate Dependency of Axonal Tolerance for Uniaxial Stretching. Stapp car crash journal 61, 53–65.

Namjoshi, D.R., Cheng, W.H., Bashir, A., Wilkinson, A., Stukas, S., Martens, K.M., Whyte, T., Abebe, Z.A., McInnes, K.A., Cripton, P.A., others, 2017. Defining the biomechanical and biological threshold of murine mild traumatic brain injury using CHIMERA (Closed Head Impact Model of Engineered Rotational Acceleration). Experimental neurology 292, 80–91.

Ng, L.J., Volman, V., Gibbons, M.M., Phohomsiri, P., Cui, J., Swenson, D.J., Stuhmiller, J.H., 2017. A mechanistic end-to-end concussion model that translates head kinematics to neurologic injury. Frontiers in neurology 8, 269.

NHTSA, 2015. Laboratory Test Procedure for Oblique Offset Moving Deformable Barrier Impact Test. Docket ID NHTSA-2015-0119-0017. Docket ID NHTSA-2015-0119-0017.

NHTSA, 1995. Final economic assessment, FMVSS No. 201, upper interior head protection (NHTSA docket 1996-1762-0003). Office of Regulatory Analysis.

Nicolle, S., Lounis, M., Willinger, R., 2004. Shear properties of brain tissue over a frequency range relevant for automotive impact situations: new experimental results. SAE Technical Paper.

Nilsson, M., Lätt, J., St\a ahlberg, F., van Westen, D., Hagslätt, H. akan, 2012. The importance of axonal undulation in diffusion MR measurements: a Monte Carlo simulation study. NMR in Biomedicine 25, 795–805.

Ning, X., Zhu, Q., Lanir, Y., Margulies, S.S., 2006. A transversely isotropic viscoelastic constitutive equation for brainstem undergoing finite deformation. Journal of biomechanical engineering 128, 925–933.

Nolte, J., 2002. The human brain: an introduction to its functional anatomy.

Nusholtz, G.S., Kaiker, P.S., Lehman, R.J., 1986. Critical limitations on significant factors in head injury research. SAE Technical Paper.

O'Connor, K.L., Rowson, S., Duma, S.M., Broglio, S.P., 2017. Head-impact–measurement devices: a systematic review. Journal of athletic training 52, 206–227.

Olszko, A.V., Beltran, C.M., Vasquez, K.B., McGhee, J.S., Chancey, V.C., Yoganandan, N., Pintar, F.A., Baisden, J.L., 2018. Initial analysis of archived non-human primate frontal and rear impact data from the biodynamics data resource. Traffic injury prevention 19, S44–S49.

Ommaya, A., Hirsch, A., 1971. Tolerances for cerebral concussion from head impact and whiplash in primates. Journal of biomechanics 4, 13–21.

Ommaya, A.K., Corrao, P., Letcher, F.S., 1973. Head injury in the chimpanzee: Part 1: Biodynamics of traumatic unconsciousness. Journal of neurosurgery 39, 152–166.

Ommaya, A.K., Gennarelli, T., 1974. Cerebral concussion and traumatic unconsciousness: correlation of experimental and clinical observations on blunt head injuries. Brain 97, 633–654.

Ommaya, A.K., Hirsch, A.E., Yarnell, P., Harris, E.H., 1967. Scaling of experimental data on cerebral concussion in sub-human primates to concussion threshold for man. DAVID W TAYLOR NAVAL SHIP RESEARCH AND DEVELOPMENT CENTER BETHESDA MD ….

Ono, K., Kikuchi, A., Nakamura, M., Kobayashi, H., Nakamura, N., 1980. Human Head Tolerance to Sagittal Impact—Reliable Estimation Deduced from Experimental Head Injury Using Subhuman Primates and Human Cadaver Skulls. SAE Transactions 3837–3866.

Panzer, M.B., 2012. Numerical Simulation of Primary Blast Brain Injury (PhD Thesis). Duke University.

Panzer, M.B., Myers, B.S., Bass, C.R., 2013. Mesh considerations for finite element blast modelling in biomechanics. Computer methods in biomechanics and biomedical engineering 16, 612–621.

Panzer, M.B., Myers, B.S., Capehart, B.P., Bass, C.R., 2012. Development of a finite element model for blast brain injury and the effects of CSF cavitation. Annals of biomedical engineering 40, 1530–1544.

Panzer, M.B., Wood, G.W., Bass, C.R., 2014. Scaling in neurotrauma: how do we apply animal experiments to people? Experimental neurology 261, 120–126.

Parent, D., Craig, M., Moorhouse, K., 2017. Biofidelity Evaluation of the THOR and Hybrid III 50 th Percentile Male Frontal Impact Anthropomorphic Test Devices. SAE Technical Paper.

Parent, D.P., Craig, M., Ridella, S.A., McFadden, J.D., 2013. Thoracic biofidelity assessment of the THOR Mod Kit ATD, in: Proceedings of the 23rd International Technical Conference on the Enhanced Safety of Vehicles (ESV).

Park, G., Kim, T., Forman, J., Panzer, M.B., Crandall, J.R., 2017. Prediction of the structural response of the femoral shaft under dynamic loading using subject-specific finite element models. Computer methods in biomechanics and biomedical engineering 20, 1151–1166.

Patton, D.A., McIntosh, A.S., Kleiven, S., Frechede, B., 2012. Injury data from unhelmeted football head impacts evaluated against critical strain tolerance curves. Proceedings of the Institution of Mechanical Engineers, Part P: Journal of Sports Engineering and Technology 226, 177–184.

Pellman, Elliot J, Viano, D.C., Tucker, A.M., Casson, I.R., Waeckerle, J.F., 2003. Concussion in professional football: reconstruction of game impacts and injuries. Neurosurgery 53, 799–814.

Pellman, Elliot J., Viano, D.C., Tucker, A.M., Casson, I.R., Waeckerle, J.F., 2003. Concussion in professional football: reconstruction of game impacts and injuries. Neurosurgery 53, 799–814.

Peng, Y., Deck, C., Yang, J., Otte, D., Willinger, R., 2013. A study of adult pedestrian head impact conditions and injury risks in passenger car collisions based on real-world accident data. Traffic injury prevention 14, 639–646.

Pervin, F., Chen, W.W., 2009. Dynamic mechanical response of bovine gray matter and white matter brain tissues under compression. Journal of biomechanics 42, 731–735.

Peters, G., Meulman, J., Sauren, A., 1997. The applicability of the time/temperature superposition principle to brain tissue. Biorheology 34, 127–138.

Petitjean, A., Trosseille, X., 2011. Statistical simulations to evaluate the methods of the construction of injury risk curves. SAE Technical Paper.

Petitjean, A., Trosseille, X., Praxl, N., Hynd, D., Irwin, A., 2012. Injury Risk Curves for the WorldSID 50 th Male Dummy. SAE Technical Paper.

Posada, D., Buckley, T.R., 2004. Model selection and model averaging in phylogenetics: advantages of Akaike information criterion and Bayesian approaches over likelihood ratio tests. Systematic biology 53, 793–808.

Prange, M.T., Margulies, S.S., 2002. Regional, directional, and age-dependent properties of the brain undergoing large deformation. Journal of biomechanical engineering 124, 244–252.

Prasad, P, Dalmotas, D., German, A., 2014. An examination of crash and NASS data to evaluate the field relevance of IIHS small offset tests. SAE International journal of transportation safety 2, 326–335.

Prasad, Priya, Dalmotas, D., German, A., 2014. The field relevance of NHTSA's oblique research moving deformable barrier tests. SAE Technical Paper.

Ren, L., Baumgartner, D., Davidsson, J., Yang, J., Willinger, R., 2014. Effect of the inhomogeneous brain mechanical characteristic on dynamic responses of head under trauma, in: Proceeding of the 2014 International IRCOBI Conference on the Biomechanics of Impact.

Rowson, S., Brolinson, G., Goforth, M., Dietter, D., Duma, S., 2009. Linear and angular head acceleration measurements in collegiate football. Journal of biomechanical engineering 131, 061016.

Rowson, S., Duma, D., Stefan M., 2013a. Brain injury prediction: Assessing the combined probability of concussion using linear and rotational head acceleration. Ann. Biomed. Eng. 41, 873–882.

Rowson, S., Duma, S.M., 2013b. Brain injury prediction: assessing the combined probability of concussion using linear and rotational head acceleration. Annals of biomedical engineering 41, 873–882.

Rowson, S., Duma, S.M., Beckwith, J.G., Chu, J.J., Greenwald, R.M., Crisco, J.J., Brolinson, P.G., Duhaime, A.-C., McAllister, T.W., Maerlender, A.C., 2012a. Rotational head kinematics in football impacts: an injury risk function for concussion. Annals of biomedical engineering 40, 1–13.

Rowson, S., Duma, S.M., Beckwith, J.G., Chu, J.J., Greenwald, R.M., Crisco, J.J., Brolinson, P.G., Duhaime, A.C., McAllister, T.W., Maerlender, A.C., 2012b. Rotational head kinematics in football impacts: An injury risk function for concussion. Annals of Biomedical Engineering 40, 1–13. https://doi.org/10.1007/s10439-011-0392-4

Sabet, A.A., Christoforou, E., Zatlin, B., Genin, G.M., Bayly, P.V., 2008. Deformation of the human brain induced by mild angular head acceleration. Journal of biomechanics 41, 307–315.

Sahoo, D., Deck, C., Willinger, R., 2016. Brain injury tolerance limit based on computation of axonal strain. Accident Analysis & Prevention 92, 53–70.

Sahoo, D., Deck, C., Willinger, R., 2014. Development and validation of an advanced anisotropic visco-hyperelastic human brain FE model. journal of the mechanical behavior of biomedical materials 33, 24–42.

Sakai, H., Nakamura, N., Sekino, H., Kanda, R., Taguchi, Y., KANEKO, D., MASUZAWA, H., MII, K., AOYAGI, N., ARUGA, T., others, 1982. Experimental head injury with lateral impact using monkeys (preliminary report). Neurologia medico-chirurgica 22, 491–498.

Salzar, R.S., Treichler, D., Wardlaw, A., Weiss, G., Goeller, J., 2017. Experimental investigation of cavitation as a possible damage mechanism in blast-induced traumatic brain injury in post-mortem human subject heads. Journal of neurotrauma 34, 1589–1602.

Sanchez, E.J., Gabler, L.F., Good, A.B., Funk, J.R., Crandall, J.R., Panzer, M.B., 2018. A reanalysis of football impact reconstructions for head kinematics and finite element modeling. Clinical biomechanics.

Sanchez, E.J., Gabler, L.F., McGhee, J.S., Olszko, A.V., Chancey, V.C., Crandall, J.R., Panzer, M.B., 2017. Evaluation of head and brain injury risk functions using sub-injurious human volunteer data. Journal of neurotrauma 34, 2410–2424.

Santiago, L.A., Oh, B.C., Dash, P.K., Holcomb, J.B., Wade, C.E., 2012. A clinical comparison of penetrating and blunt traumatic brain injuries. Brain Injury 26, 107–125.

Sauerbeck, A., Fanizzi, C., Kim, J., Gangolli, M., Bayly, P., Wellington, C., Brody, D., Kummer, T., 2018. modCHIMERA: a novel murine closed-head model of moderate traumatic brain injury. Scientific reports 8, 7677.

Schnebel, B., Gwin, J.T., Anderson, S., Gatlin, R., 2007. In vivo study of head impacts in football: a comparison of National Collegiate Athletic Association Division I versus high school impacts. Neurosurgery 60, 490–496.

Sekino, H., Nakamura, N., Yuki, K., Satoh, J., Kikuchi, K., SANADA, S., 1981. Brain lesions detected by CT scans in cases of minor head injuries. Neurologia medico-chirurgica 21, 677–683.

Seok, J., Warren, H.S., Cuenca, A.G., Mindrinos, M.N., Baker, H.V., Xu, W., Richards, D.R., McDonald-Smith, G.P., Gao, H., Hennessy, L., others, 2013. Genomic responses in mouse models poorly mimic human inflammatory diseases. Proceedings of the National Academy of Sciences 110, 3507–3512.

Shaw, G., Parent, D., Purtsezov, S., Lessley, D., Crandall, J., Kent, R., Guillemot, H., Ridella, S.A., Takhounts, E., Martin, P., 2009. Impact response of restrained PMHS in frontal sled tests: skeletal deformation patterns under seat belt loading. SAE Technical Paper.

Shen, F., Tay, T., Li, J., Nigen, S., Lee, P., Chan, H., 2006. Modified Bilston nonlinear viscoelastic model for finite element head injury studies. Journal of biomechanical engineering 128, 797–801.

Shultz, S.R., McDonald, S.J., Haar, C.V., Meconi, A., Vink, R., van Donkelaar, P., Taneja, C., Iverson, G.L., Christie, B.R., 2017. The potential for animal models to provide insight into mild traumatic brain injury: translational challenges and strategies. Neuroscience & Biobehavioral Reviews 76, 396–414.

Somers, J.T., Granderson, B., Melvin, J.W., Tabiei, A., Lawrence, C., Feiveson, A., Gernhardt, M., Ploutz-Snyder, R., Patalak, J., 2011. Development of head injury assessment reference values based on NASA injury modeling. SAE Technical Paper.

Stalnaker, R.L., Roberts, V.L., McElhaney, J.H., 1973. Side impact tolerance to blunt trauma. SAE Technical Paper.

Strich, S.J., 1956. Diffuse degeneration of the cerebral white matter in severe dementia following head injury. Journal of neurology, neurosurgery, and psychiatry 19, 163.

Stukel, T.A., 1988. Generalized logistic models. Journal of the American Statistical Association 83, 426–431.

Sullivan, S., Eucker, S.A., Gabrieli, D., Bradfield, C., Coats, B., Maltese, M.R., Lee, J., Smith, C., Margulies, S.S., 2015. White matter tract-oriented deformation predicts traumatic axonal brain

injury and reveals rotational direction-specific vulnerabilities. Biomechanics and modeling in mechanobiology 14, 877–896.

Tabatabaei, S., Lomov, S.V., 2015. Eliminating the volume redundancy of embedded elements and yarn interpenetrations in meso-finite element modelling of textile composites. Computers & Structures 152, 142–154.

Takahashi, Y., Yanaoka, T., 2017. A Study of Injury Criteria for Brain Injuries in Traffic Accidents, in: International Technical Conference on the Enhanced Safety of Vehicles. National Highway Traffic Safety Administration.

Takhounts, Erik G., Craig, C., Matthew J., Moorhouse, K., McFadden, J., Hasija, V., 2013. Development of brain injury criteria (BrIC). Stapp Car Crass J 57, 243–266.

Takhounts, Erik G, Craig, M.J., Moorhouse, K., McFadden, J., Hasija, V., 2013. Development of brain injury criteria (BrIC). SAE Technical Paper.

Takhounts, E.G., Eppinger, R.H., Campbell, J.Q., Tannous, R.E., Power, E.D., Shook, L.S., 2003. On the development of the SIMon finite element head model, in: SAE CONFERENCE PROCEEDINGS P. SAE; 1999, pp. 107–134.

Takhounts, E.G., Ridella, S.A., Hasija, V., Tannous, R.E., Campbell, J.Q., Malone, D., Danelson, K., Stitzel, J., Rowson, S., Duma, S., 2008. Investigation of traumatic brain injuries using the next generation of simulated injury monitor (SIMon) finite element head model. SAE Technical Paper.

Tang-Schomer, M.D., Patel, A.R., Baas, P.W., Smith, D.H., 2010. Mechanical breaking of microtubules in axons during dynamic stretch injury underlies delayed elasticity, microtubule disassembly, and axon degeneration. The FASEB Journal 24, 1401–1410.

Taylor, C.A., Bell, J.M., Breiding, M.J., Xu, L., 2017. Traumatic Brain Injury-Related Emergency Department Visits, Hospitalizations, and Deaths-United States, 2007 and 2013. Morbidity and mortality weekly report. Surveillance summaries (Washington, DC: 2002) 66, 1–16.

Thibault, K.L., Margulies, S.S., 1998. Age-dependent material properties of the porcine cerebrum: effect on pediatric inertial head injury criteria. Journal of biomechanics 31, 1119–1126.

Thibault, L.E., Gennarelli, T.A., 1990. Brain injury: an analysis of neural and neurovascular trauma in the nonhuman primate, in: Association for the Advancement of Automotive Medicine (AAAM), Conference, 34th, 1990, Scottsdale, Arizona, USA.

Thunnissen, J., Wismans, J., Ewing, C., Thomas, D., 1995. Human volunteer head-neck response in frontal flexion: a new analysis. SAE Technical Paper.

Trosseille, X., Tarriere, C., Lavaste, F., Guillon, F., Domont, A., 1992. Development of a FEM of the human head according to a specific test protocol. SAE Technical Paper.

Ueno, K., Melvin, J.W., Li, L., Lighthall, J.W., 1995. Development of tissue level brain injury criteria by finite element analysis. Journal of neurotrauma 12, 695–706.

Velardi, F., Fraternali, F., Angelillo, M., 2006. Anisotropic constitutive equations and experimental tensile behavior of brain tissue. Biomechanics and modeling in mechanobiology 5, 53–61.

Ventura-Antunes, L., Mota, B., Herculano-Houzel, S., 2013. Different scaling of white matter volume, cortical connectivity, and gyrification across rodent and primate brains. Frontiers in neuroanatomy 7, 3.

Versace, J., 1971. A review of the severity index. SAE Technical Paper.

Viano, D.C., Casson, I.R., Pellman, E.J., Zhang, L., King, A.I., Yang, K.H., 2005. Concussion in professional football: brain responses by finite element analysis: part 9. Neurosurgery 57, 891–916.

von Bartheld, C.S., Bahney, J., Herculano-Houzel, S., 2016. The search for true numbers of neurons and glial cells in the human brain: A review of 150 years of cell counting. Journal of Comparative Neurology 524, 3865–3895.

Wagenmakers, E.-J., Farrell, S., 2004. AIC model selection using Akaike weights. Psychonomic bulletin & review 11, 192–196.

Wang, H.C., Wineman, A., 1972a. A mathematical model for the determination of viscoelastic behavior of brain in vivo—II relaxation response. Journal of biomechanics 5, 571–580.

Wang, H.C., Wineman, A.S., 1972b. A mathematical model for the determination of viscoelastic behavior of brain in vivo—I Oscillatory response. Journal of biomechanics 5, 431–446.

Ward, C., Chan, M., Nahum, A., 1980. Intracranial pressure—a brain injury criterion. SAE Transactions 3867–3880.

Weerappuli, P., Chiu, E., Barbat, S., Prasad, P., 2002. CART impact recorder data analysis using mathematical modeling, in: ASME 2002 International Mechanical Engineering Congress and Exposition. American Society of Mechanical Engineers, pp. 207–233.

Wood, G.W., Panzer, M.B., Cox, C.A., Bass, C.R., 2018. Interspecies scaling in blast pulmonary trauma. Human Factors and Mechanical Engineering for Defense and Safety 2, 3.

Wright, R.M., Post, A., Hoshizaki, B., Ramesh, K.T., 2013. A multiscale computational approach to estimating axonal damage under inertial loading of the head. Journal of neurotrauma 30, 102–118.

Xiong, Y., Mahmood, A., Chopp, M., 2013. Animal models of traumatic brain injury. Nature Reviews Neuroscience 14, 128.

Yang, B., Tse, K.-M., Chen, N., Tan, L.-B., Zheng, Q.-Q., Yang, H.-M., Hu, M., Pan, G., Lee, H.-P., 2014. Development of a finite element head model for the study of impact head injury. BioMed research international 2014.

Yang, K.H., Hu, J., White, N.A., King, A.I., Chou, C.C., Prasad, P., 2006. Development of numerical models for injury biomechanics research: a review of 50 years of publications in the Stapp Car Crash Conference. SAE Technical Paper.

Yao, J., Yang, J., Otte, D., 2008. Investigation of head injuries by reconstructions of real-world vehicle-versus-adult-pedestrian accidents. Safety science 46, 1103–1114.

Yeh, F.-C., Panesar, S., Fernandes, D., Meola, A., Yoshino, M., Fernandez-Miranda, J.C., Vettel, J.M., Verstynen, T., 2018. Population-averaged atlas of the macroscale human structural connectome and its network topology. NeuroImage 178, 57–68.

Yoganandan, N., Banerjee, A., Hsu, F.-C., Bass, C.R., Voo, L., Pintar, F.A., Gayzik, F.S., 2016. Deriving injury risk curves using survival analysis from biomechanical experiments. Journal of biomechanics 49, 3260–3267.

Zhang, J., Green, M.A., Sinkus, R., Bilston, L.E., 2011. Viscoelastic properties of human cerebellum using magnetic resonance elastography. Journal of biomechanics 44, 1909–1913.

Zhang, K., Sejnowski, T.J., 2000. A universal scaling law between gray matter and white matter of cerebral cortex. Proceedings of the National Academy of Sciences 97, 5621–5626.

Zhang, L., Yang, K.H., Dwarampudi, R., Omori, K., Li, T., Chang, K., Hardy, W.N., Khalil, T.B., King, A.I., 2001. Recent advances in brain injury research: a new human head model development and validation. Stapp Car Crash J 45, 369–394.

Zhang, L., Yang, K.H., King, A.I., 2004. A proposed injury threshold for mild traumatic brain injury. Journal of biomechanical engineering 126, 226–236.

Zhao, W., Choate, B., Ji, S., 2018. Material properties of the brain in injury-relevant conditions–Experiments and computational modeling. Journal of the mechanical behavior of biomedical materials 80, 222–234.

Zhao, W., Ji, S., 2019. Mesh Convergence Behavior and the Effect of Element Integration of a Human Head Injury Model. Annals of biomedical engineering 47, 475–486.

Zhao, W., Ji, S., 2018. White matter anisotropy for impact simulation and response sampling in traumatic brain injury. Journal of neurotrauma.

Zhao, W., Ruan, S., Ji, S., 2015. Brain pressure responses in translational head impact: a dimensional analysis and a further computational study. Biomechanics and modeling in mechanobiology 14, 753–766.

Zhou, Z., Li, X., Kleiven, S., Shah, C.S., Hardy, W.N., 2018. A reanalysis of experimental brain strain data: implication for finite element head model validation. Stapp car crash journal 62, 293–318.

Zou, H., Kleiven, S., Schmiedeler, J.P., 2007. The effect of brain mass and moment of inertia on relative brain–skull displacement during low-severity impacts. International journal of crashworthiness 12, 341–353.

APPENDIX A: EVALUATION OF HUMAN BRAIN FE MODELS

This section provides details on the evaluation of the axon-based and GHBMC brain models using the NDT impact data and sonomicrometry data. Individual nodal displacement plots comparing simulation results with experimental measurements are shown in Figure A1 – A5 under impact condition (Chapter 3) and in Figure A6 under pure rotational motion (Chapter 4). The model performance assessed with sonomicrometry data were quantified using CORA scores; the scores are provided in Table A1.

Evaluation of Brain Deformation with NDT Impact Data

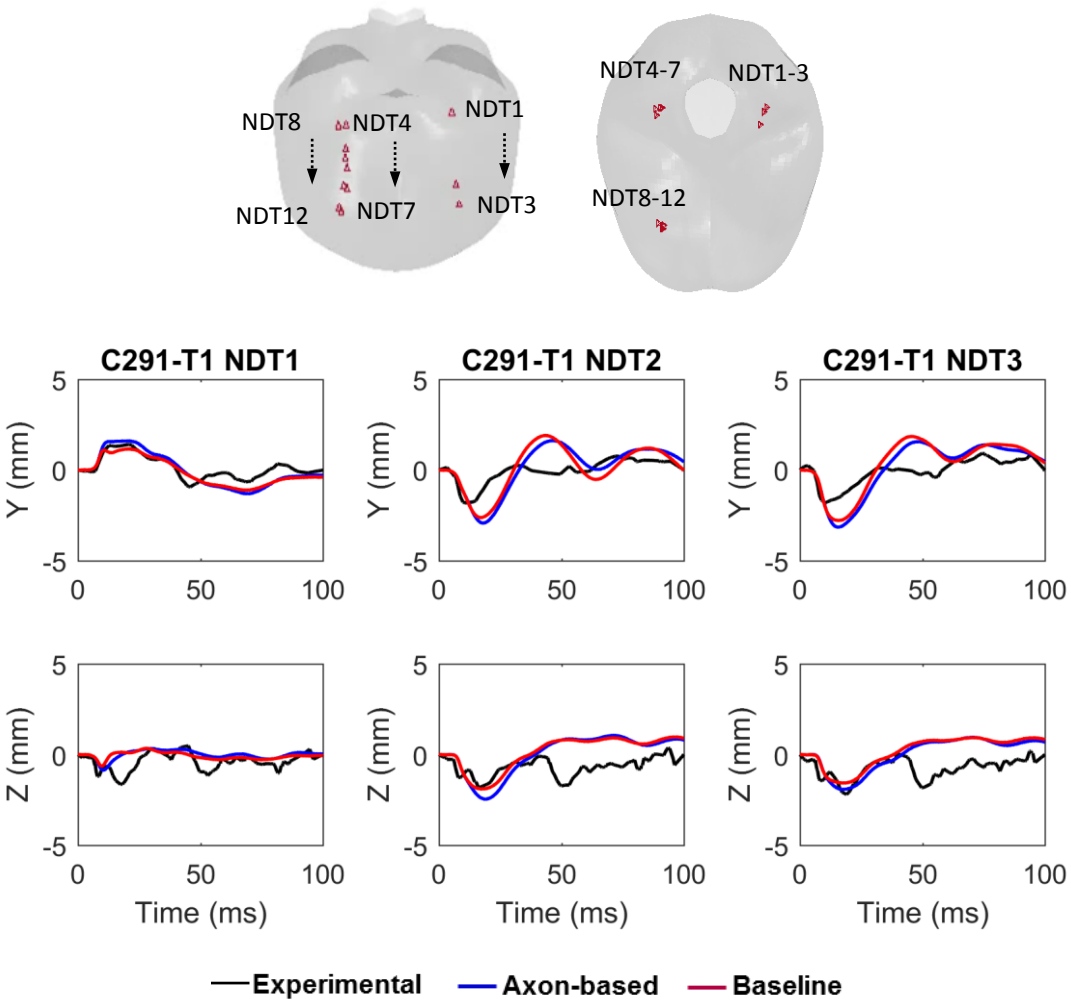

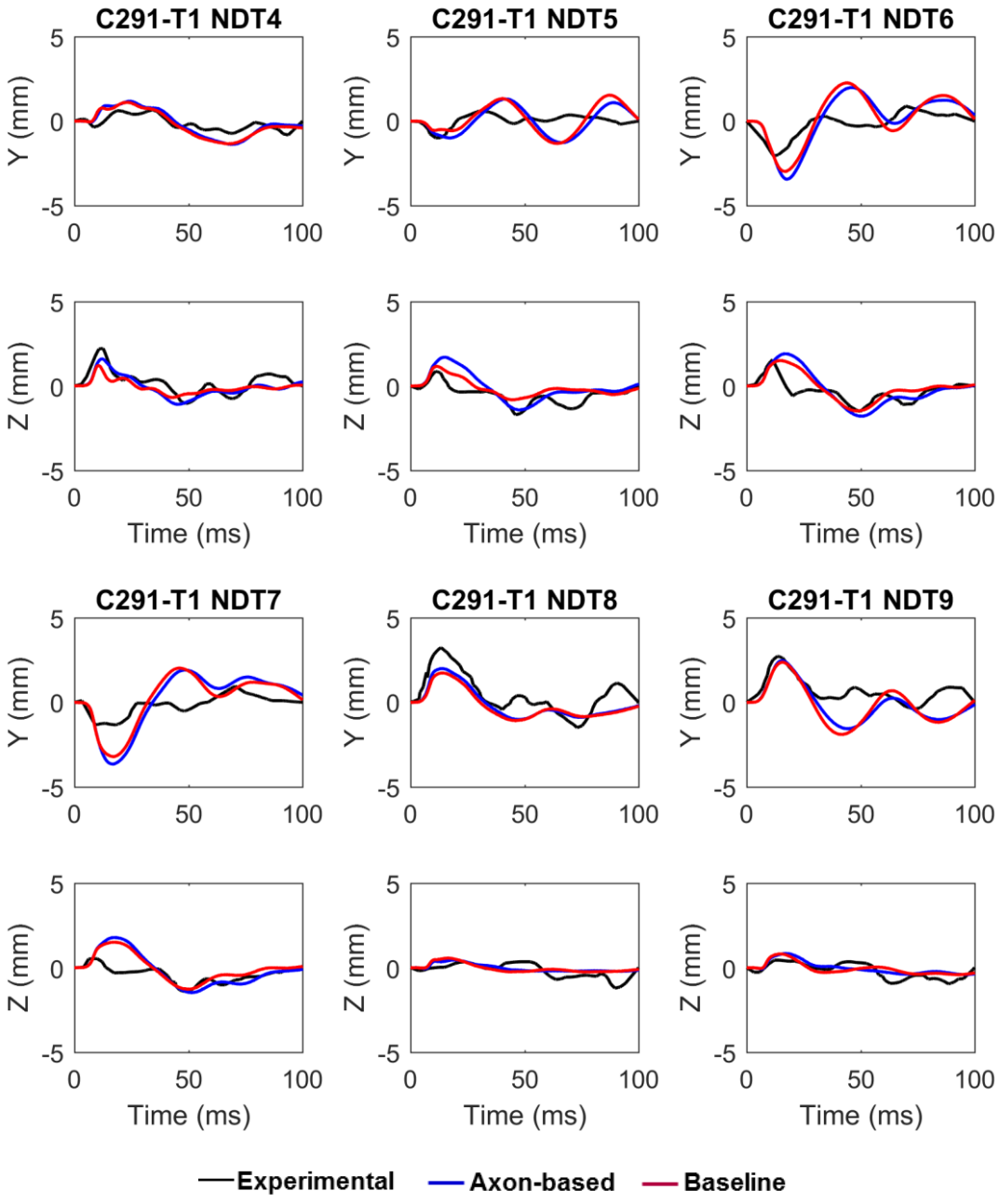
C291-T1 NDT4
C291-T1 NDT5
C291-T1 NDT6
C291-T1 NDT7
C291-T1 NDT8
C291-T1 NDT9
Y (mm)
Z (mm)
Time (ms)
5
0
-5
0
50
100
Experimental
Axon-based
Baseline

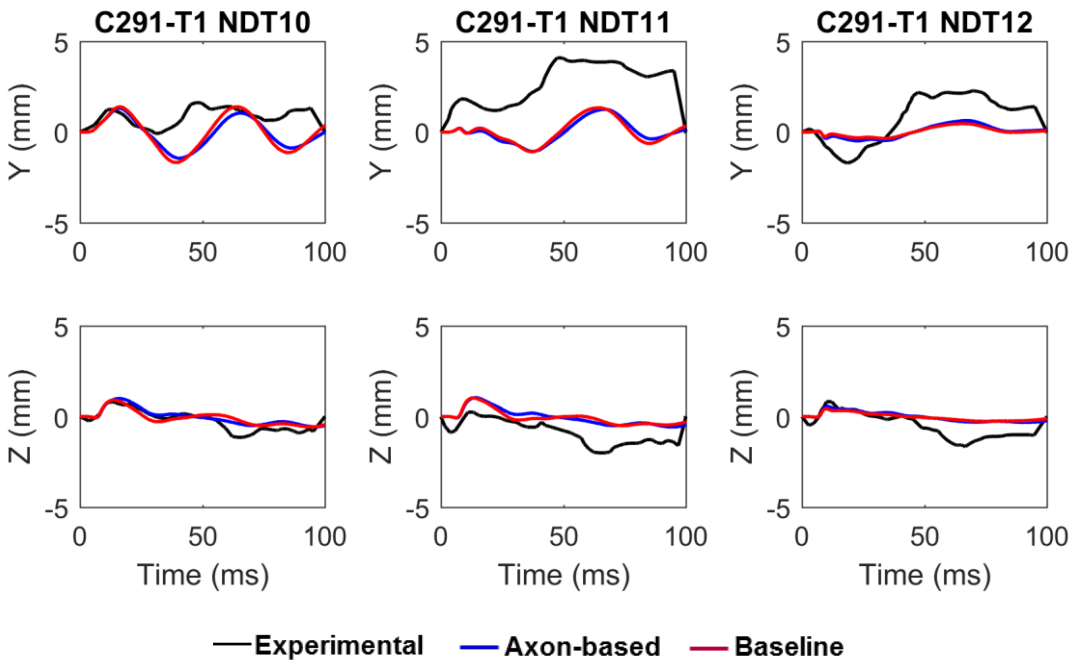

Figure A1. Nodal displacements comparisons for NDT291-T1.

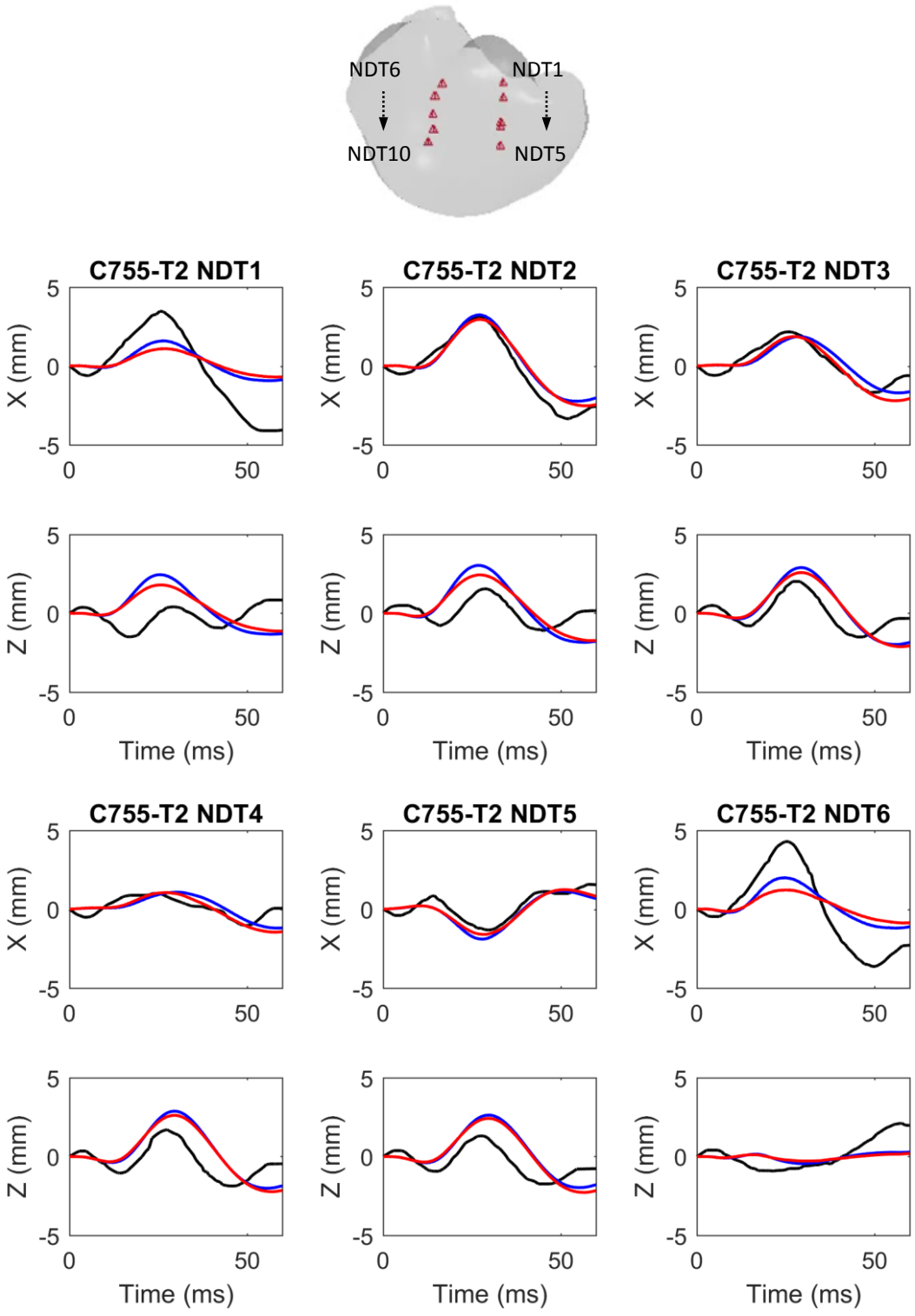
NDT6
NDT1
NDT10
NDT5
C755-T2 NDT1
C755-T2 NDT2
C755-T2 NDT3
C755-T2 NDT4
C755-T2 NDT5
C755-T2 NDT6
X (mm)
Z (mm)
Time (ms)
5
0
-5
0
50

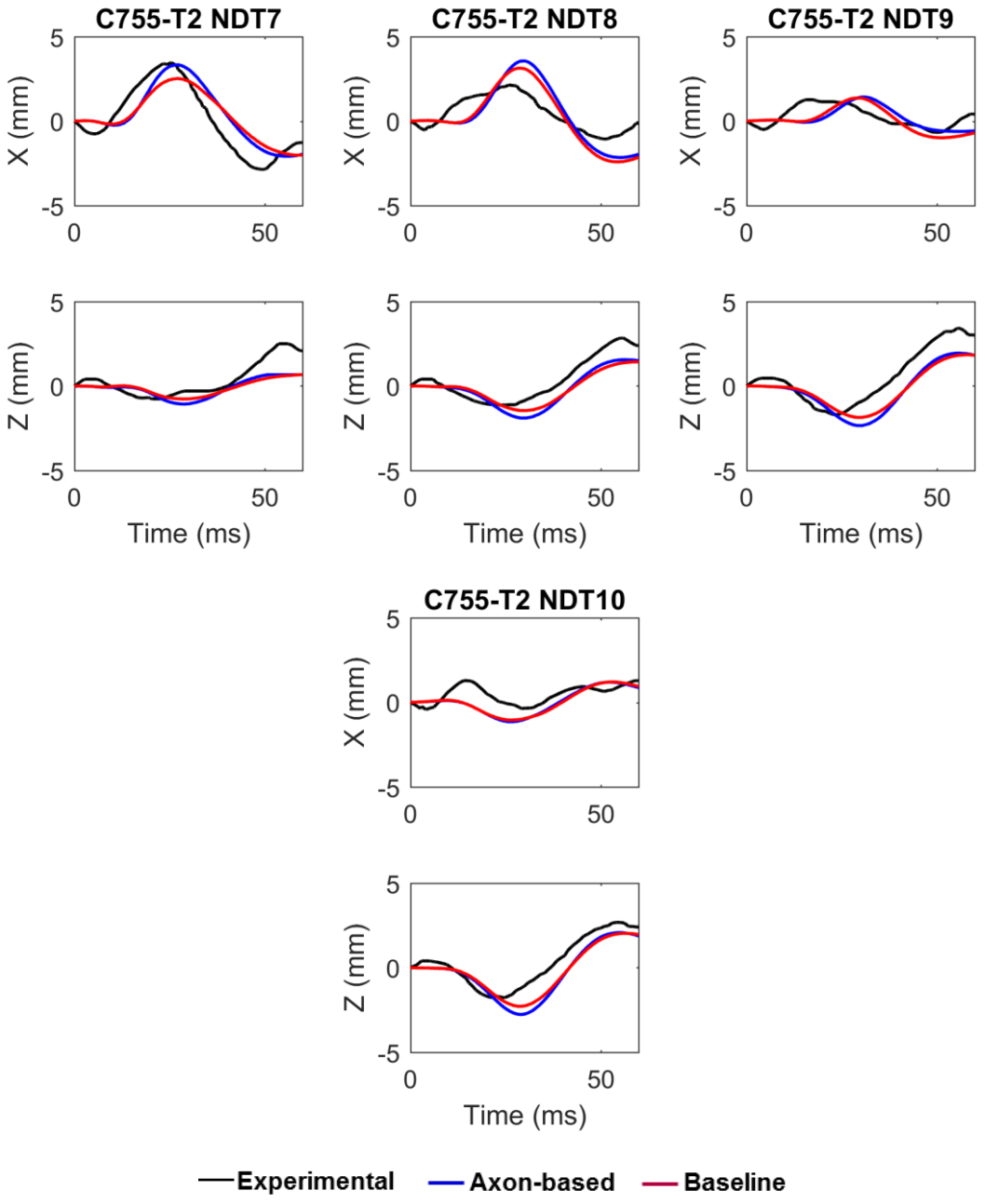

Figure A2. Nodal displacements comparisons for NDT755-T2.

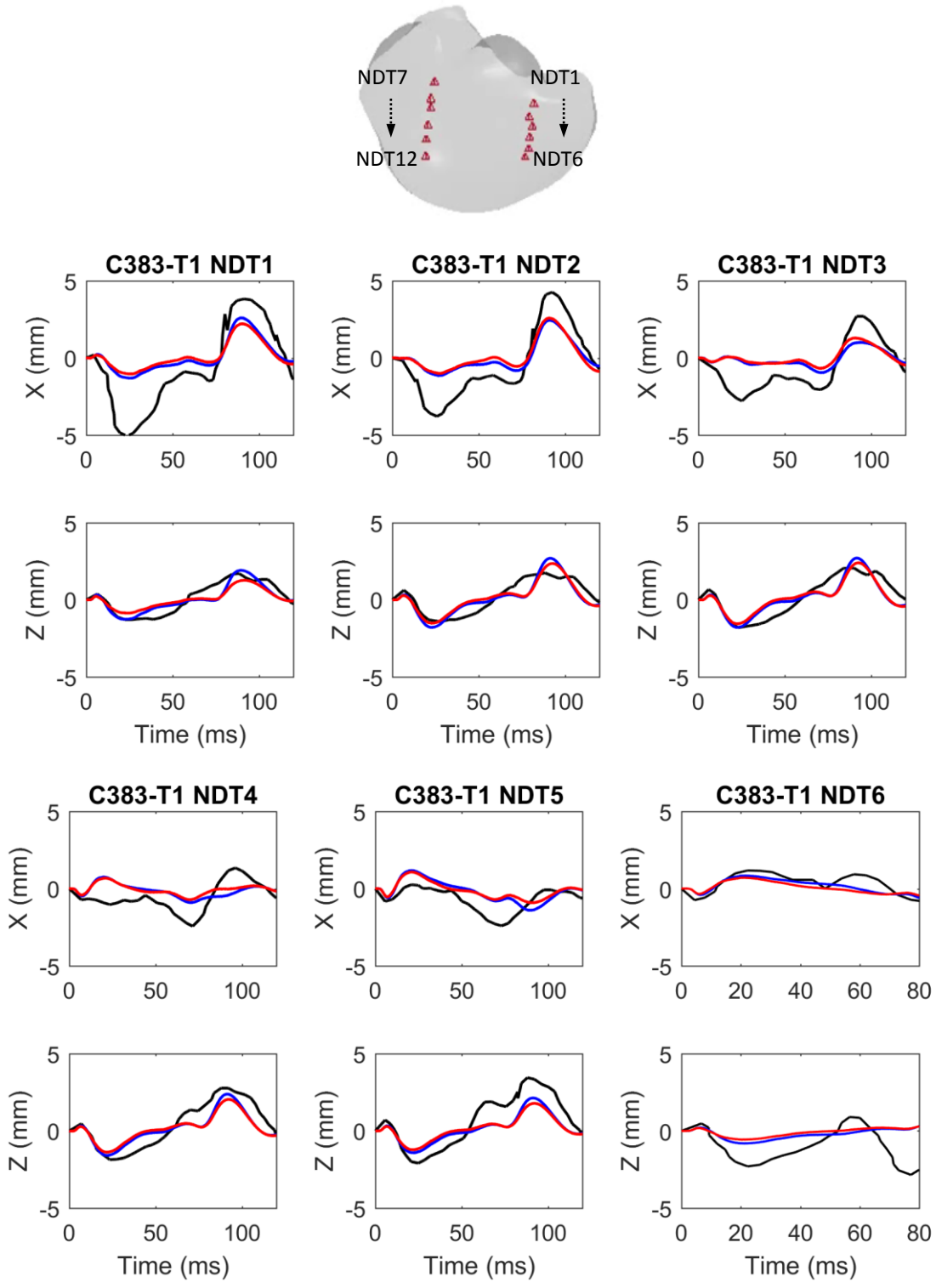
NDT7
NDT1
NDT12
NDT6
C383-T1 NDT1
C383-T1 NDT2
C383-T1 NDT3
C383-T1 NDT4
C383-T1 NDT5
C383-T1 NDT6
X (mm)
Z (mm)
Time (ms)

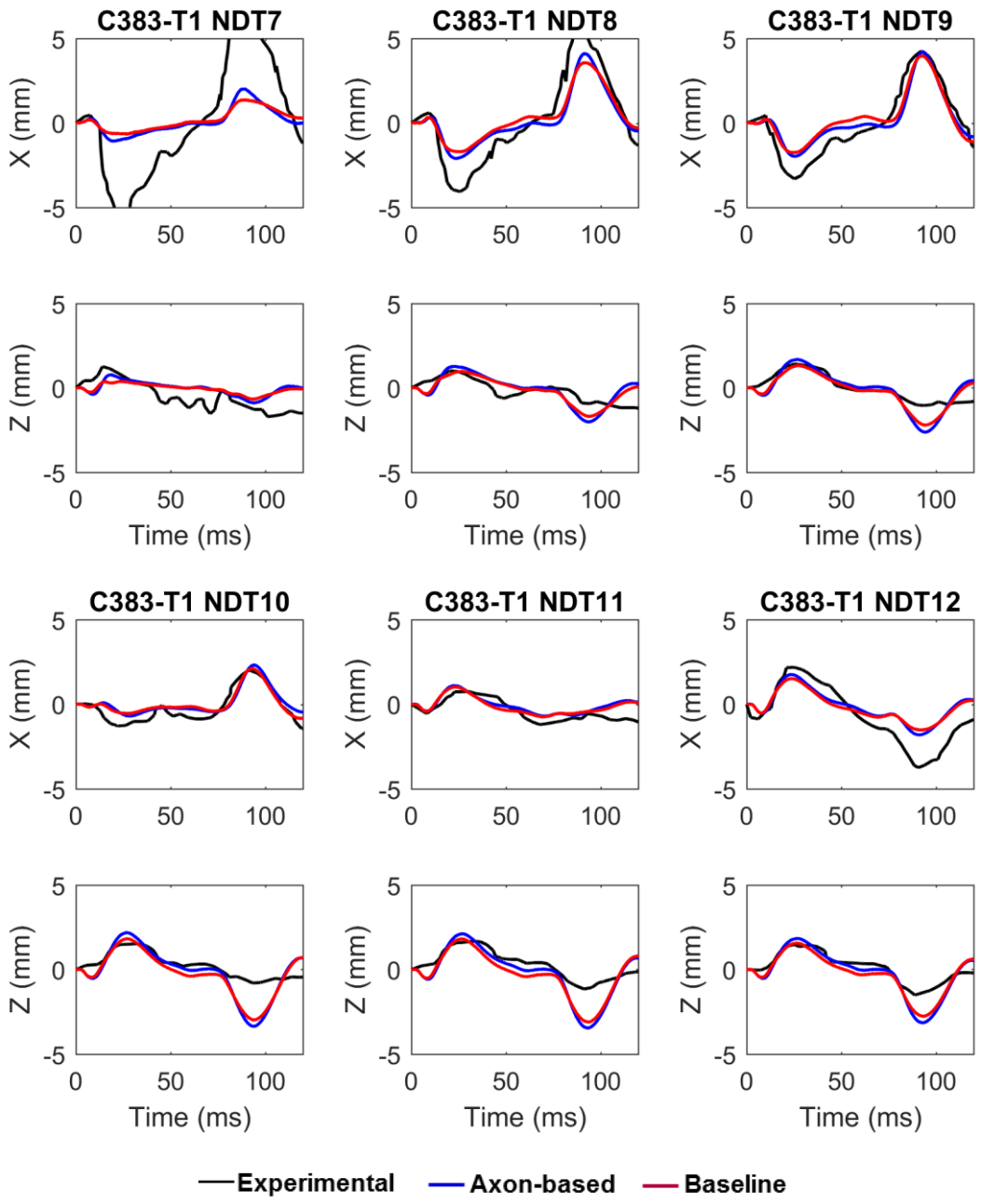

Figure A3. Nodal displacements comparisons for NDT383-T1.

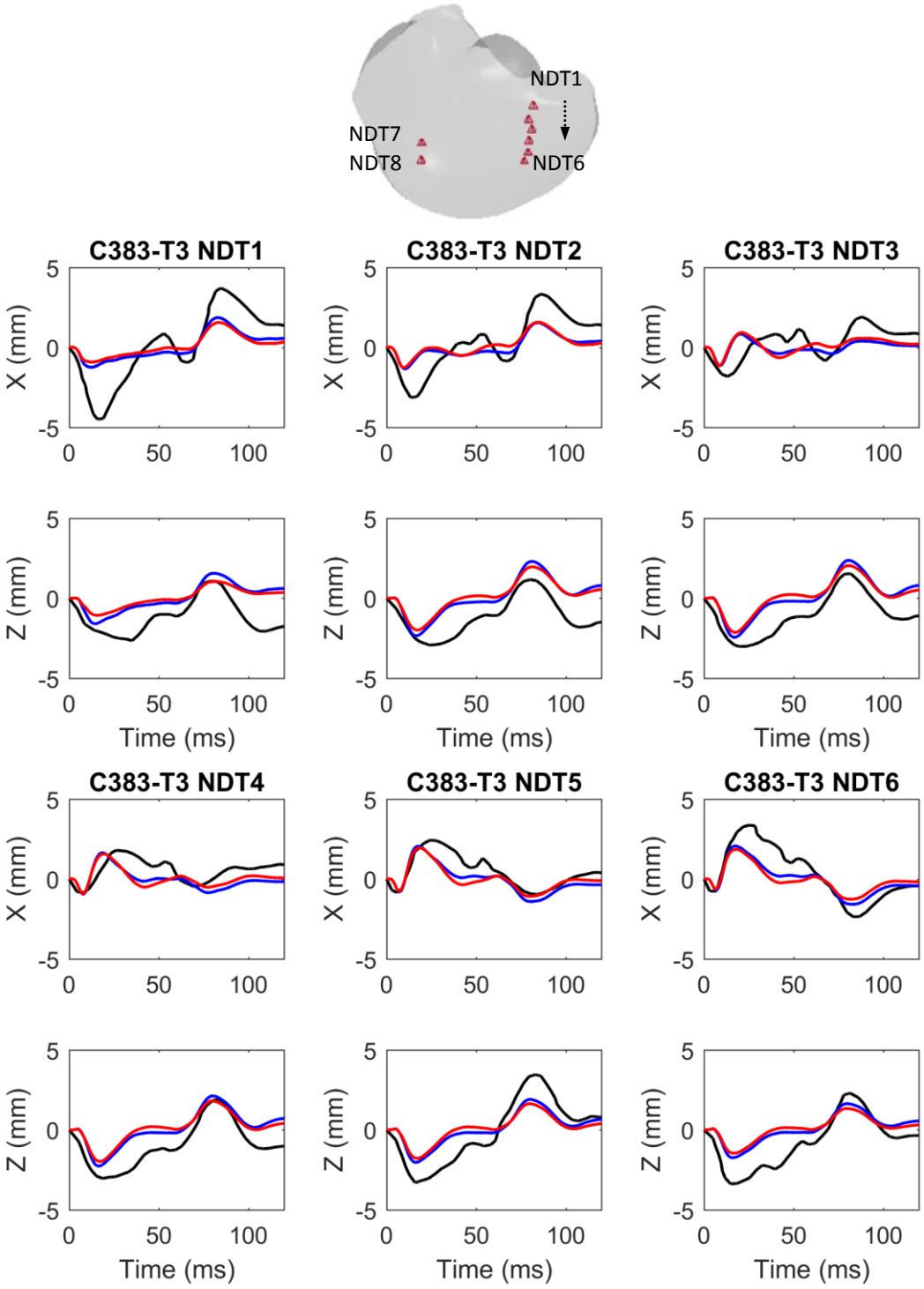
NDT1
NDT7
NDT8
NDT6
C383-T3 NDT1
C383-T3 NDT2
C383-T3 NDT3
C383-T3 NDT4
C383-T3 NDT5
C383-T3 NDT6
X (mm)
Z (mm)
Time (ms)
5
0
-5
0
50
100

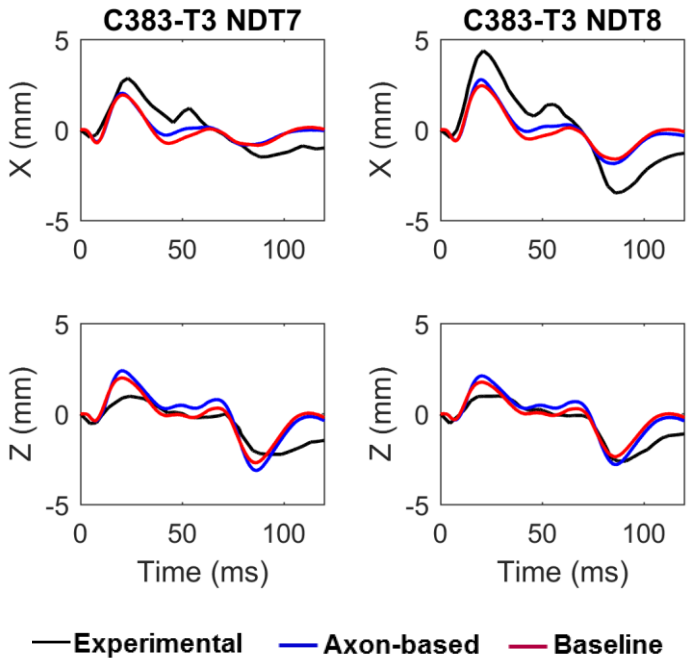

Figure A4. Nodal displacements comparisons for NDT383-T3.

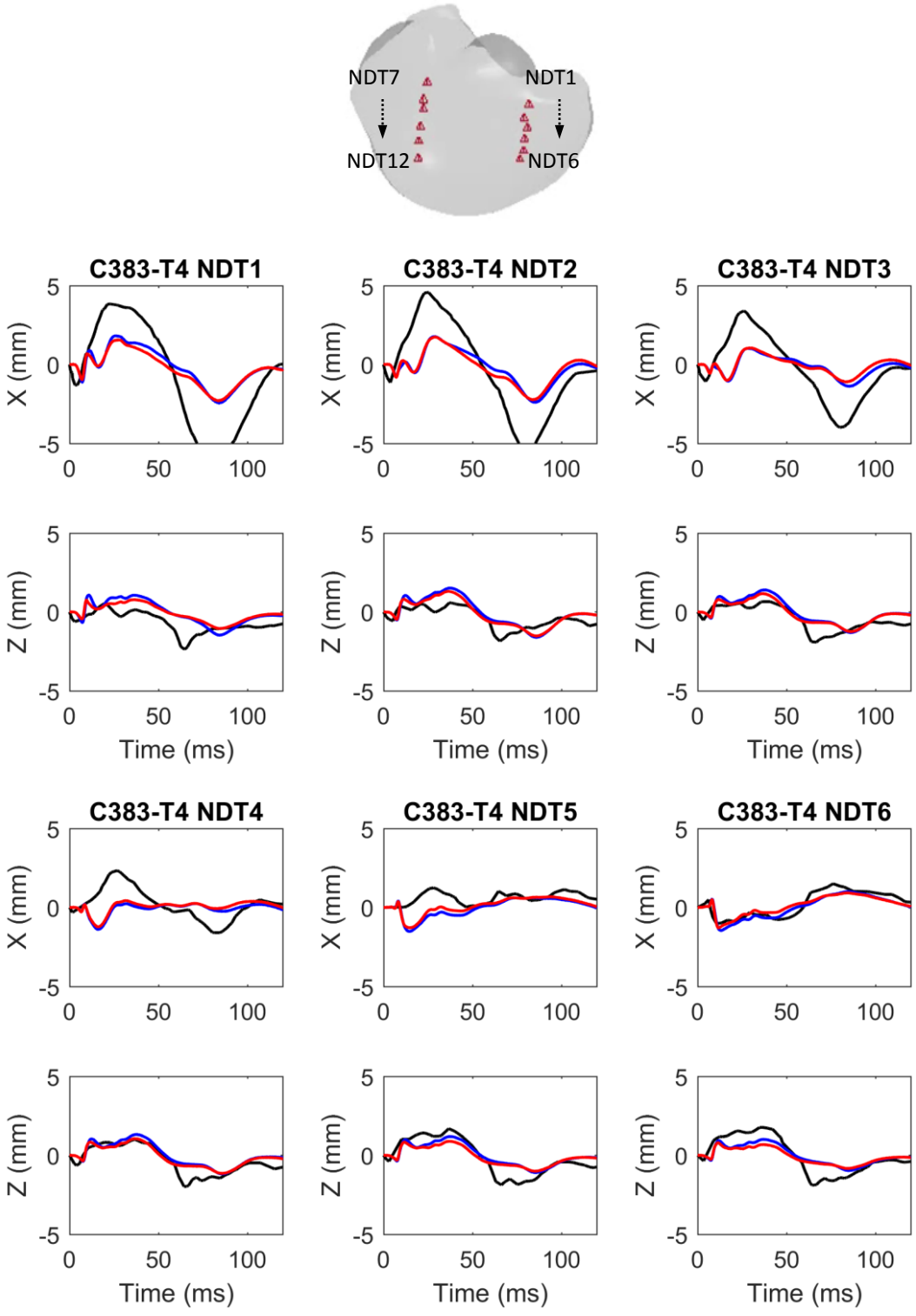
NDT7
NDT1
NDT12
NDT6
C383-T4 NDT1
C383-T4 NDT2
C383-T4 NDT3
C383-T4 NDT4
C383-T4 NDT5
C383-T4 NDT6
X (mm)
Z (mm)
Time (ms)
5
0
-5
0
50
100

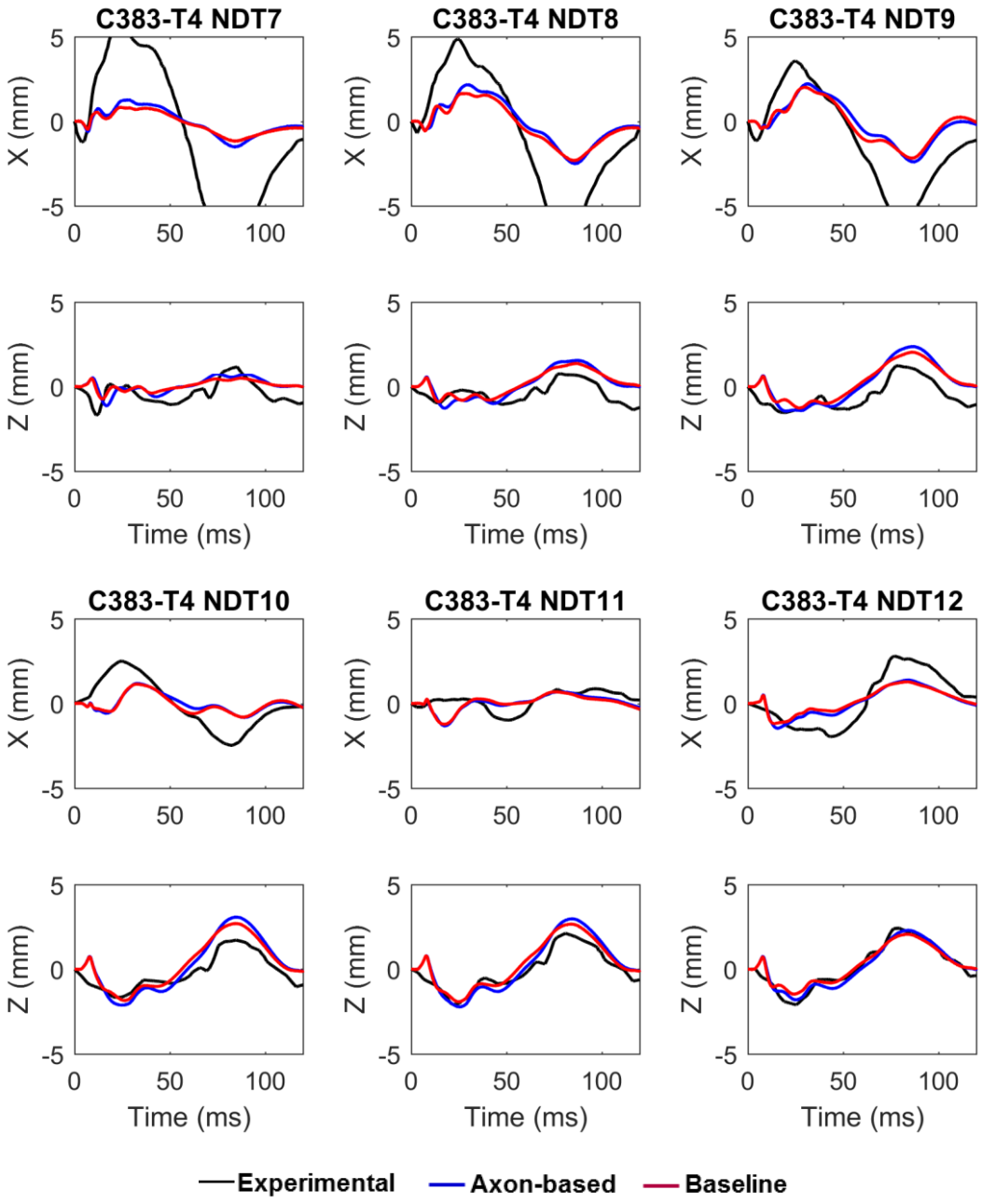

Figure A5. Nodal displacements comparisons for NDT383-T4.

Evaluation of Brain Deformation with Sonomicrometry Data

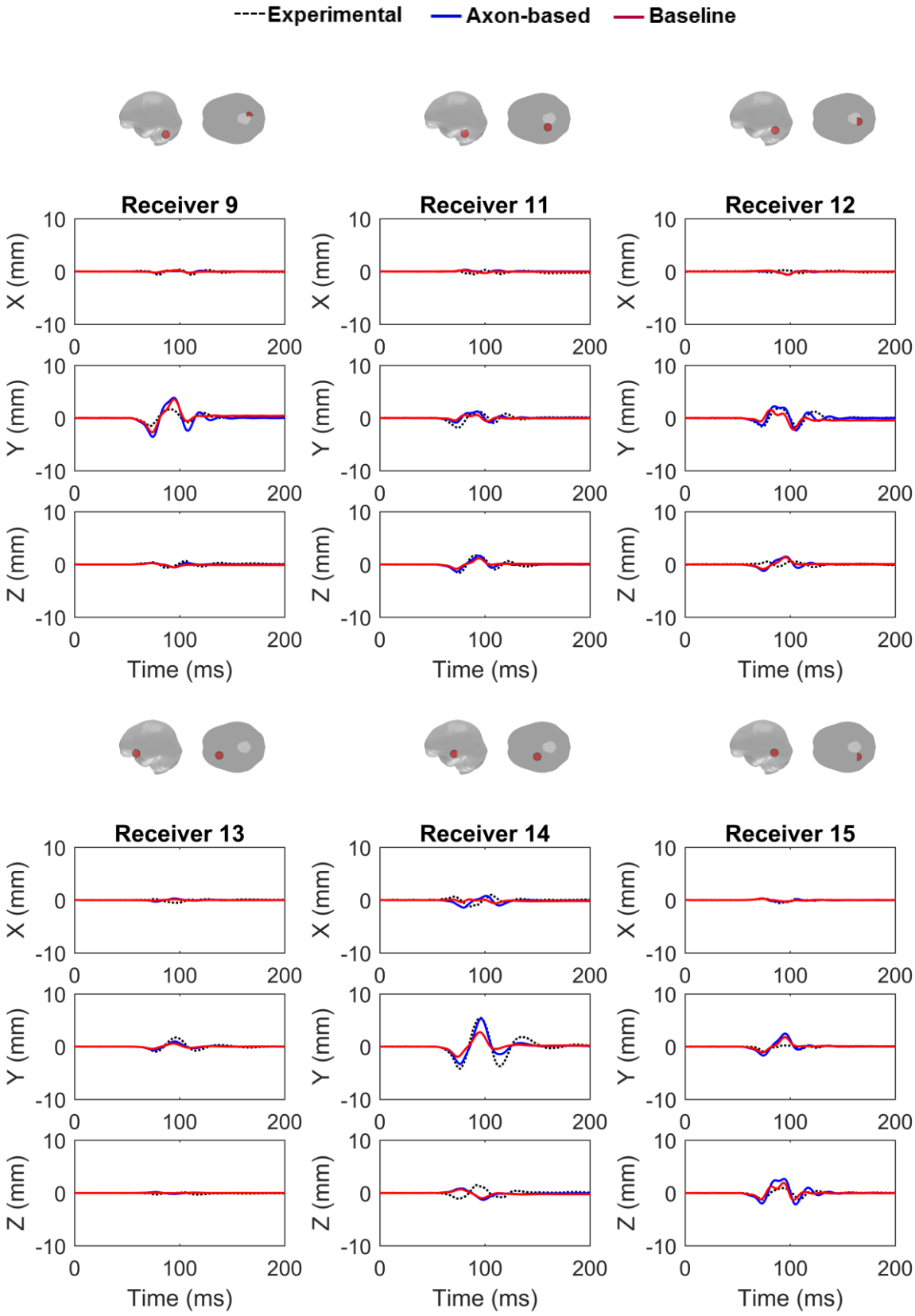
Experimental
Axon-based
Baseline
Receiver 9
Receiver 11
Receiver 12
Receiver 13
Receiver 14
Receiver 15
X (mm)
Y (mm)
Z (mm)
Time (ms)
10
0
-10
0
100
200

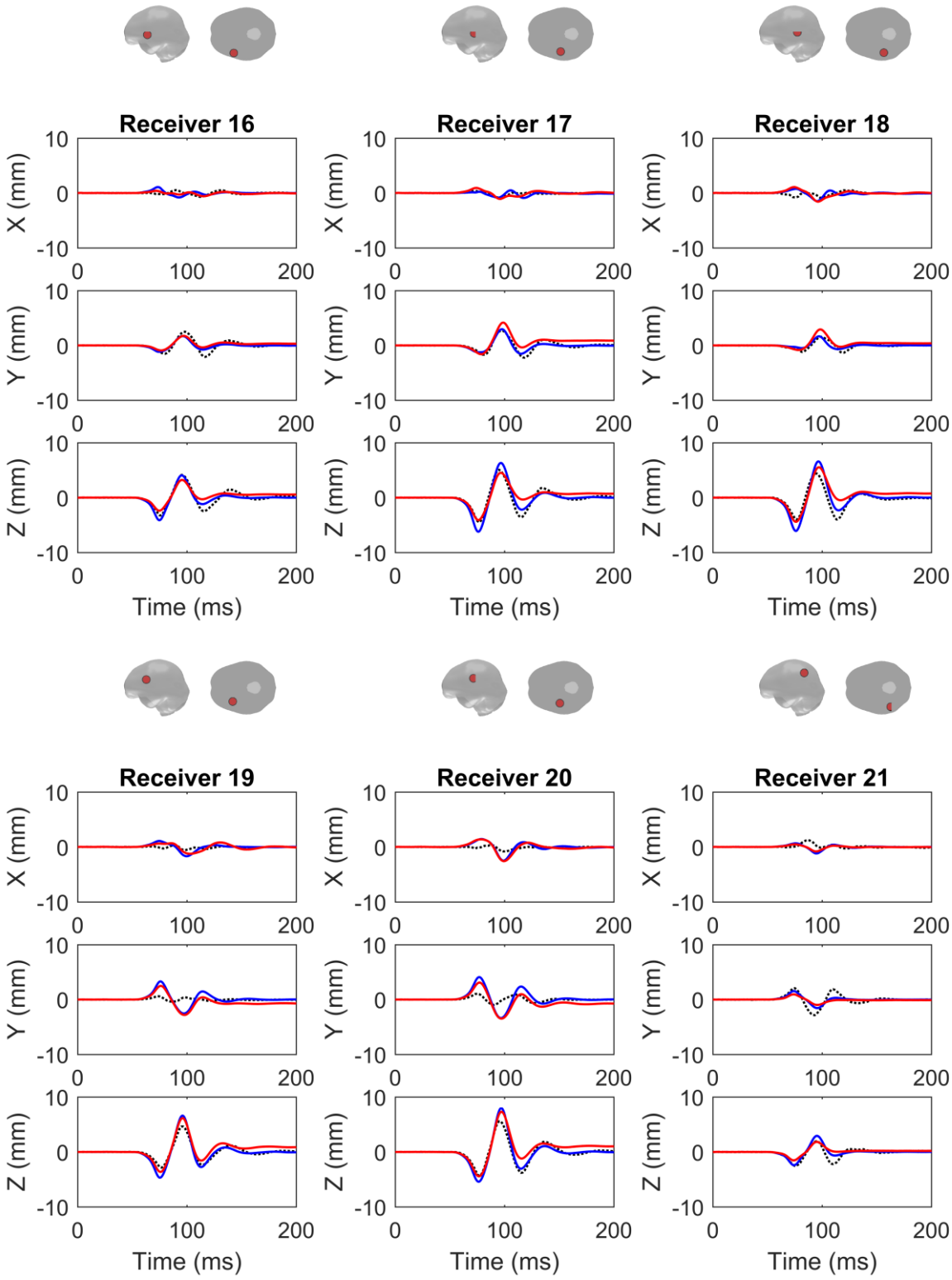
Receiver 16
Receiver 17
Receiver 18
Receiver 19
Receiver 20
Receiver 21
X (mm)
Y (mm)
Z (mm)
Time (ms)
10
0
-10
0
100
200

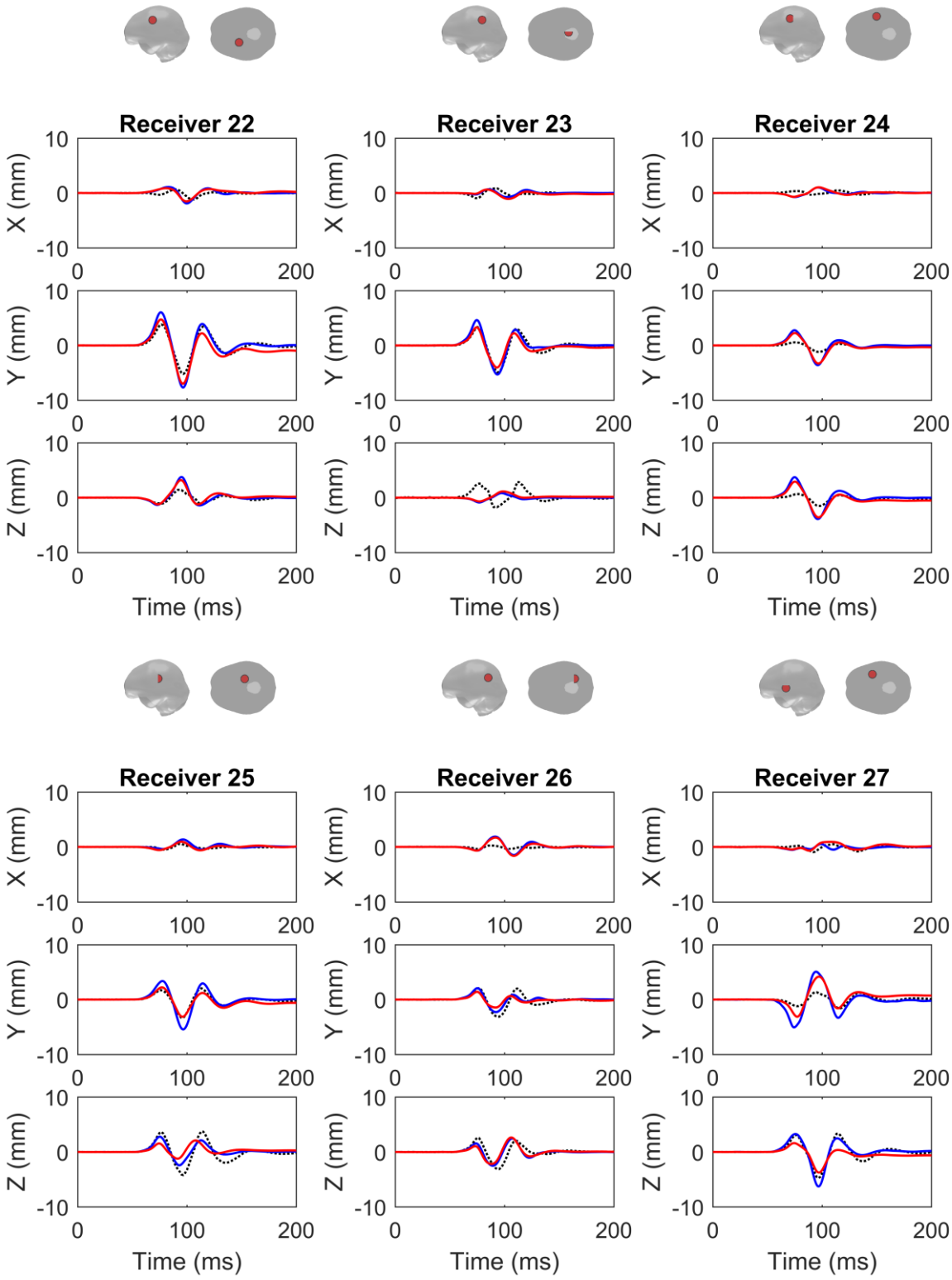
Receiver 22
Receiver 23
Receiver 24
Receiver 25
Receiver 26
Receiver 27
X (mm)
Y (mm)
Z (mm)
Time (ms)
10
0
-10
0
100
200

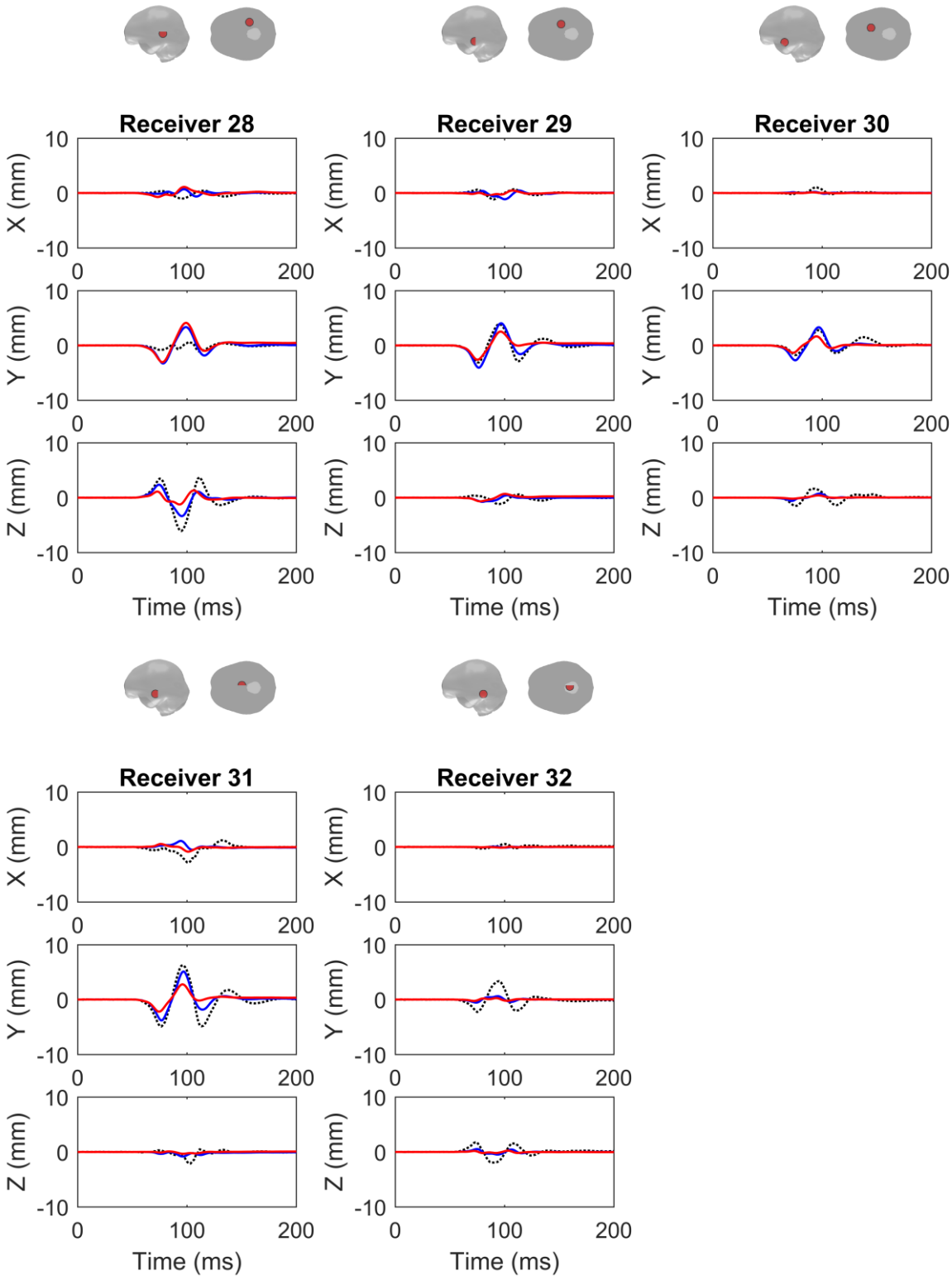

Figure A6. Nodal displacements comparisons for SONO 904, X: 40-30.

Table A1. Quantitative evaluation results of the baseline and axon-based human model for the sonomicrometry data.

Subject	Case	Baseline		Axon-based		Subject	Case	Baseline		Axon-based	
		mWCORA	wWCORA	mWCORA	wWCORA			mWCORA	wWCORA	mWCORA	wWCORA
846	X:20-60	0.543	0.587	0.570	0.627	902	X:20-60	0.600	0.629	0.639	0.663
	X:20-30	0.539	0.572	0.579	0.613		X:20-30	0.622	0.640	0.659	0.676
	X:40-60	0.564	0.609	0.587	0.647		X:40-60	0.581	0.598	0.630	0.646
	X:40-30	0.547	0.581	0.585	0.627		X:40-30	0.621	0.631	0.693	0.702
	Y:20-60	0.557	0.589	0.585	0.616		Y:20-60	0.498	0.507	0.544	0.557
	Y:20-30	0.587	0.626	0.604	0.640		Y:20-30	0.523	0.535	0.569	0.583
	Y:40-60	0.586	0.612	0.613	0.642		Y:40-60	0.513	0.529	0.571	0.591
	Y:40-30	0.551	0.569	0.569	0.585		Y:40-30	0.478	0.486	0.554	0.574
	Z:20-60	0.488	0.552	0.548	0.621		Z:20-60	0.495	0.524	0.517	0.543
	Z:20-30	0.505	0.573	0.563	0.638		Z:20-30	0.494	0.512	0.535	0.546
	Z:40-60	0.524	0.582	0.567	0.630		Z:40-60	0.377	0.402	0.438	0.464
	Z:40-30	0.473	0.511	0.511	0.557		Z:40-30	0.533	0.553	0.620	0.642
896	X:20-60	0.554	0.561	0.609	0.623	903	X:20-60	0.574	0.644	0.634	0.714
	X:20-30	0.535	0.540	0.595	0.605		X:20-30	0.569	0.628	0.631	0.702
	X:40-60	0.526	0.550	0.583	0.602		X:40-60	0.592	0.642	0.649	0.698
	X:40-30	0.507	0.511	0.570	0.574		X:40-30	0.584	0.630	0.639	0.692
	Y:20-60	0.570	0.596	0.620	0.650		Y:20-60	0.505	0.548	0.540	0.584
	Y:20-30	0.546	0.562	0.609	0.625		Y:20-30	0.500	0.551	0.549	0.601
	Y:40-60	0.548	0.562	0.603	0.616		Y:40-60	0.515	0.578	0.571	0.631
	Y:40-30	0.496	0.497	0.563	0.557		Y:40-30	0.527	0.595	0.613	0.680
	Z:20-60	0.512	0.560	0.582	0.637		Z:20-60	0.538	0.612	0.567	0.647
	Z:20-30	0.454	0.488	0.538	0.582		Z:20-30	0.564	0.643	0.603	0.688
	Z:40-60	0.478	0.513	0.555	0.599		Z:40-60	0.479	0.560	0.553	0.641
	Z:40-30	0.440	0.454	0.531	0.560		Z:40-30	0.463	0.526	0.533	0.589
900	X:20-60	0.635	0.680	0.692	0.735	904	X:20-60	0.467	0.478	0.518	0.525
	X:20-30	0.630	0.657	0.696	0.730		X:20-30	0.479	0.491	0.521	0.534
	X:40-60	0.619	0.668	0.653	0.711		X:40-60	0.475	0.493	0.540	0.558
	X:40-30	0.610	0.635	0.672	0.713		X:40-30	0.460	0.479	0.573	0.593
	Y:20-60	0.547	0.561	0.594	0.600		Y:20-60	0.558	0.577	0.619	0.635
	Y:20-30	0.567	0.566	0.602	0.597		Y:20-30	0.570	0.583	0.648	0.667
	Y:40-60	0.550	0.561	0.602	0.620		Y:40-60	0.572	0.585	0.633	0.649
	Y:40-30	0.579	0.588	0.667	0.680		Y:40-30	0.562	0.571	0.656	0.672
	Z:20-60	0.534	0.554	0.613	0.636		Z:20-60	0.509	0.537	0.537	0.558
	Z:20-30	0.564	0.582	0.625	0.649		Z:20-30	0.529	0.567	0.557	0.597
	Z:40-60	0.525	0.539	0.607	0.634		Z:40-60	0.526	0.555	0.564	0.600
	Z:40-30	0.530	0.533	0.626	0.642		Z:40-30	0.493	0.518	0.554	0.590

APPENDIX B: DIMENSIONAL ANALYSIS AND SCALING

The scaling technique, which forms the basis for dimensional analysis (Langhaar, 1951) , was widely used in biomechanics in an attempt to account for the effect of various sizes on the biomechanical responses. The essential idea of dimensional analysis assumes geometric similarity between the two objects scaled from and to, the relationship of the biomechanical responses between these two objects can thus be derived from the ratios of their fundamental properties (Table A2). In biomechanics, the three basic quantities are usually taken as length, mass density, and Young's modulus. Constant mass density ($\lambda_\rho = 1$) was normally assumed for biological material. When using the notion of scaling in biomechanics, another underlying assumption was that the structures demonstrate linear stress-strain behavior up to the point of injury/failure. This latter assumption is of course not strictly fulfilled considering that very few, if any, biological tissues demonstrate perfectly linear stress-strain behavior, but was regarded as reasonable approximation considering the large variability associated with the testing of biological tissues.

Table A2. Scaling Factors Derived from Dimensional Analysis.

Physical quantities	**Scaling factor**
Characteristic Length (basic quantities)	λ_l
Young's Modulus (basic quantities)	λ_E
Density (basic quantities)	$\lambda_\rho = 1$
Angle	*1*
Force	$\lambda_F = {\lambda_l}^2 \lambda_E$
Moment	$\lambda_M = {\lambda_l}^3 \lambda_E$
Deflection	λ_l
Stiffness	$\lambda_k = \lambda_l \lambda_E$
Time	$\lambda_t = \lambda_l (\lambda_E)^{-1/2}$
Kinetic Energy	$\lambda_{KE} = (\lambda_l)^3 \lambda_E$
Velocity	$\lambda_v = (\lambda_E)^{1/2}$
Angular acceleration	$\lambda_\alpha = \lambda_E (\lambda_l)^{-2}$
Angular velocity	$\lambda_\omega = (\lambda_E)^{1/2} (\lambda_l)^{-1}$

Mass Scaling

In biomechanical application, the most conventional scaling approach is a simplification of dimensional analysis by assuming constant linear material properties and deriving a direction-independent characteristic length from mass, $\lambda_l = (\lambda_m)^{1/3}$. The scaling relationship of other physical quantities between two subjects can be simply derived by knowing the mass ratios based on this method, the so-called mass scaling.

Frequency Scaling Principles: Dimensional Analysis of the sDOF Model.

In the case of interspecies scaling, the geometric similarity between brains of different species is dubious, but their tissue responses with respect to a broad range of loading conditions can be characterized using simple mechanical systems. The similarity between the mechanical systems can be fulfilled, and it can be shown that the response of a pair of sDOF systems (equal in ζ and β) can be scaled based on the ratio of natural frequency, which is the alternative basic quantity incorporating length and Young's modulus, as detailed in the followings.

A pair of damped, sDOF mechanical systems with base excitation (Figure A7) was applied to imitate the maximum brain deformation under rotation head motion.

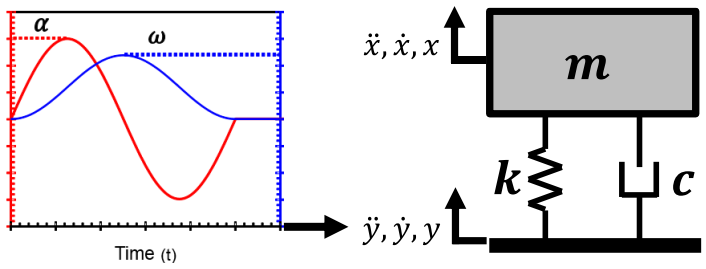

Figure A7. A sDOF mechanical system with sinusoid acceleration base excitation.

The equation of motion for this system is given by the following expression:

$$m\ddot{y} + c\dot{y} + ky = c\dot{x} + kx \quad (1)$$

Where y and x are the displacements of the base and mass, and m, c, and k are the system parameters for the mass, damping, and stiffness, respectively. The relative base-mass displacement, $\delta = x - y$, was assumed to be an analog for brain deformation due to the rotational head motion. Substituting parameters for the system natural frequency, $\omega_n = \sqrt{k/m}$, and damping ratio, $\zeta = c/\sqrt{4mk}$, Eq. (1) can be rewritten in the following form:

$$\ddot{\delta}(t) + 2\zeta\,\omega_n\dot{\delta}(t) + \omega_n^2\delta = \ddot{y}(t) \quad (2)$$

In which $\ddot{y}(t)$ is a pulse base excitation that is fully defined by the parameters α (angular acceleration) and ω(angular velocity). The maximum magnitude of the relative displacement variable, $\delta_m = \max(\delta(t))$, was assumed to be an analog (correlate) for maximum brain deformation. Further details on the analytical solution to Eq. (2) were provided in Gabler et al. (2018). Here we provide a proof with rigorous dimensional analysis to show that the δ_m responses of the paired systems (equal damping ratios) with different natural frequencies can be scaled based on the ratio of natural frequency in the following manner:

$$\text{Angular velocity: } \omega_h = \lambda_\omega\omega_a = \frac{\omega_{nh}}{\omega_{na}}\omega_a \quad (3)$$

$$\text{Angular acceleration: } \alpha_h = \lambda_\alpha\alpha_a = \left(\frac{\omega_{nh}}{\omega_{na}}\right)^2\alpha_a \quad (4)$$

The maximum relative displacement of the sDOF model, δ_m is a function of the coefficients of the mechanical system (ω_n, ζ), and the characteristics of the pulse (α, ω), giving

$$\delta_m = f(\omega_n, \zeta, \alpha, \omega) \quad (5)$$

In the case of Eq. 5, the five variables involve only two independent dimensions (r = 2), that of length [L] and time [T]. According to Buckingham's Π-theorem, the number of independent dimensionless Π-products is equal to the number of physical variables appearing in Eq. 5 (five

variables) minus the number of reference dimensions (two). Therefore, for a sDOF system subjected to an acceleration pulse, we have $5-2=3$ Π-terms. Since we are focusing on the response to pulse-type motions, the obvious choices for the repeating variables are the characteristics of the pulse α, and ω, which gives $\Pi_1=\delta_m\frac{\omega^2}{\alpha}$, $\Pi_2=\frac{\omega_n}{\omega}$ and $\Pi_3=\zeta$. With the three Π-terms established, Eq. (5) reduces to

$$\delta_m\frac{\omega^2}{\alpha}=f(\frac{\omega_n}{\omega},\zeta) \tag{6}$$

A pair of sDOF systems can be defined by a set of parameters $(\omega_{n1},\zeta_1,\alpha_1,\omega_1,\delta_{m1})$ and $(\omega_{n2},\zeta_2,\alpha_2,\omega_2,\delta_{m2})$ respectively. Given $\omega_{n2}=\lambda\omega_{n1}$ and $\zeta_2=\zeta_1$, then according to Eq. (6), the first system follows that

$$\delta_{m1}\frac{{\omega_1}^2}{\alpha_1}=f(\frac{\omega_{n1}}{\omega_1},\zeta_1) \tag{7}$$

The second system follows that

$$\delta_{m2}\frac{{\omega_2}^2}{\alpha_2}=f(\frac{\omega_{n2}}{\omega_2},\zeta_2) \tag{8}$$

Which can be rewritten as

$$\delta_{m2}\frac{{\omega_2}^2}{\alpha_2}=f(\frac{\lambda\omega_{n1}}{\omega_2},\zeta_1) \tag{9}$$

If the excitation of the second system satisfies the following relationship $\omega_2=\lambda\omega_1$ and $\alpha_2=\lambda^2\alpha_1$, where $\lambda=\omega_{n2}/\omega_{n1}$, then Eq. (9) can be rewritten as

$$\delta_{m2}\frac{{\omega_1}^2}{\alpha_1}=f(\frac{\lambda\omega_{n1}}{\omega_1},\zeta_1) \tag{10}$$

We can induct that $\delta_{m2}=\delta_{m1}$ by comparing Eq. (10) with Eq. (7).

Fitted values for the uniaxial parameters of the paired sDOF models.

Table A3. Fitted values for the uniaxial parameters of the paired sDOF models.

Species	Parameters	MPS (95th)			MAS (95th)		
		Coronal	Sagittal	Axial	Coronal	Sagittal	Axial
All	R^2	0.974	0.973	0.914	0.950	0.975	0.891
	ζ	0.900	0.950	0.600	0.750	0.880	0.550
	β	0.189	0.197	0.126	0.336	0.471	0.276
Macaque	f_m (Hz)	194.1	155.2	219.2	213.9	131.4	194.7
Baboon	f_b (Hz)	148.0	116.3	167.2	162.9	100.0	149.4
Human	f_h (Hz)	56.6	49.8	74.9	62.4	41.9	68.6

Comparison of Scaled Response Surfaces under Uniaxial Rotations

Figure A8 – A10 illustrate the scaled animal response surfaces using different scaling methods and the comparison between them with the human responses.

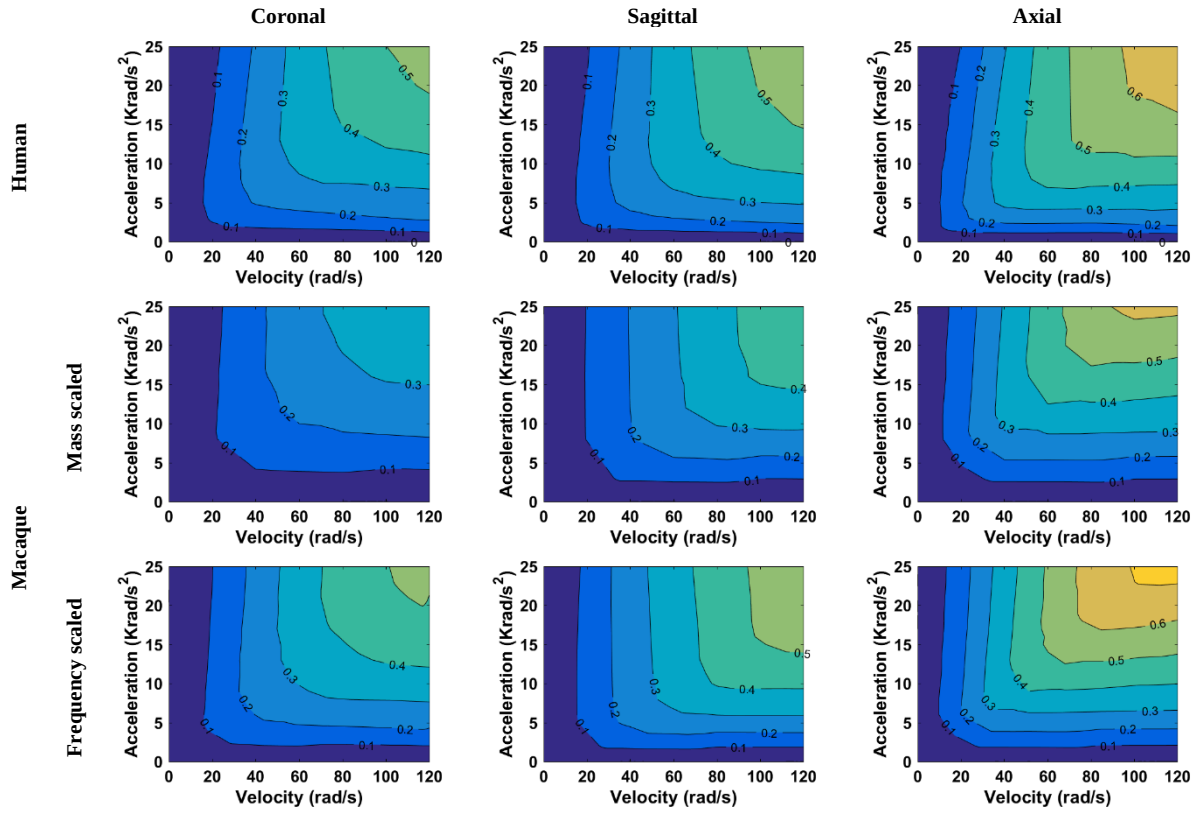

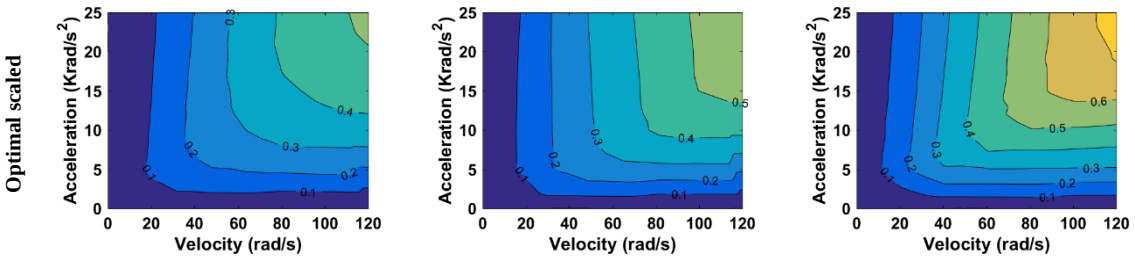

Figure A8. Scaled Macaque MPS (95th) response surfaces.

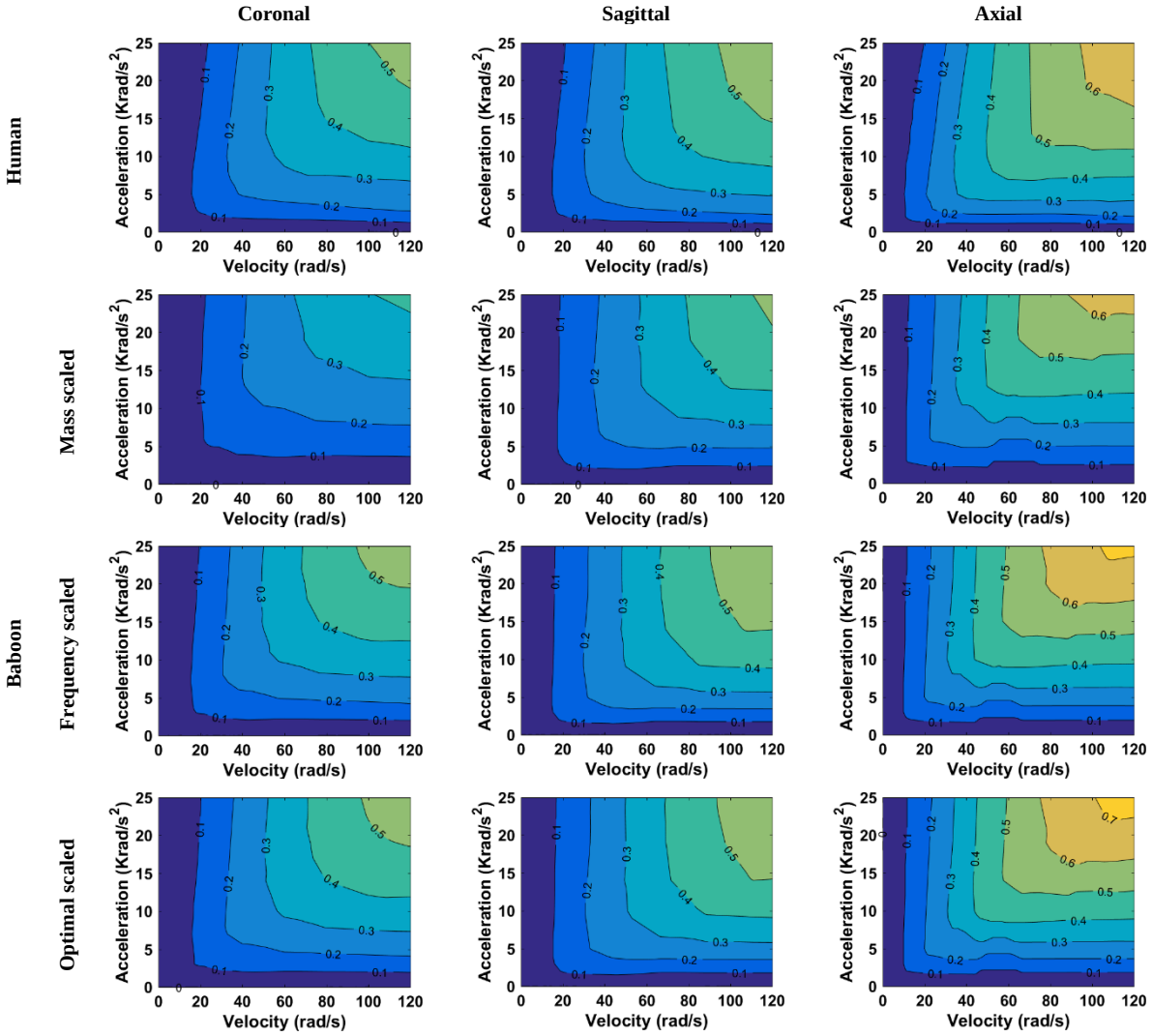

Figure A9. Scaled Baboon MPS (95th) response surfaces.

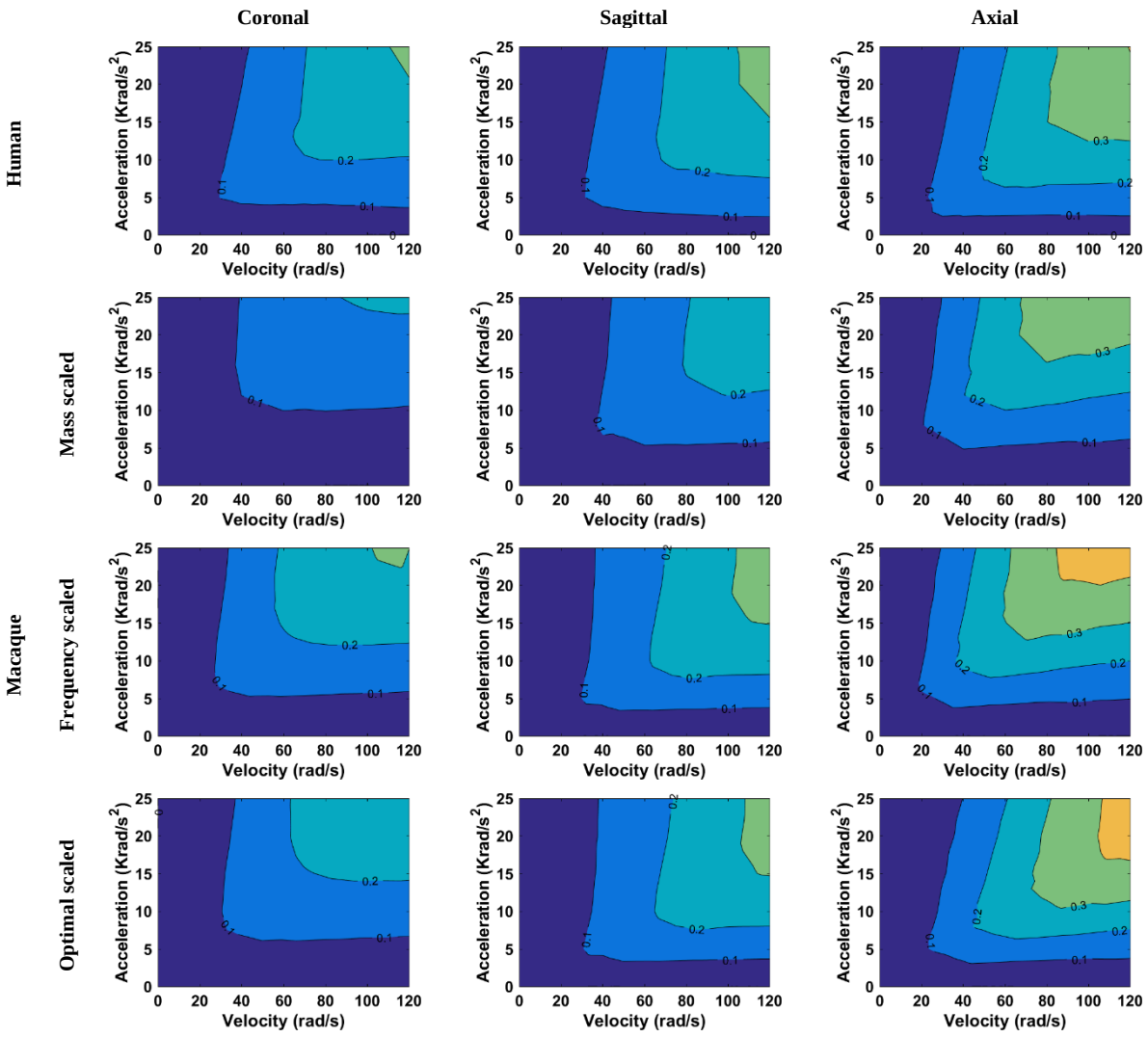

Figure A10. Scaled macaque MAS (95th) response surfaces.

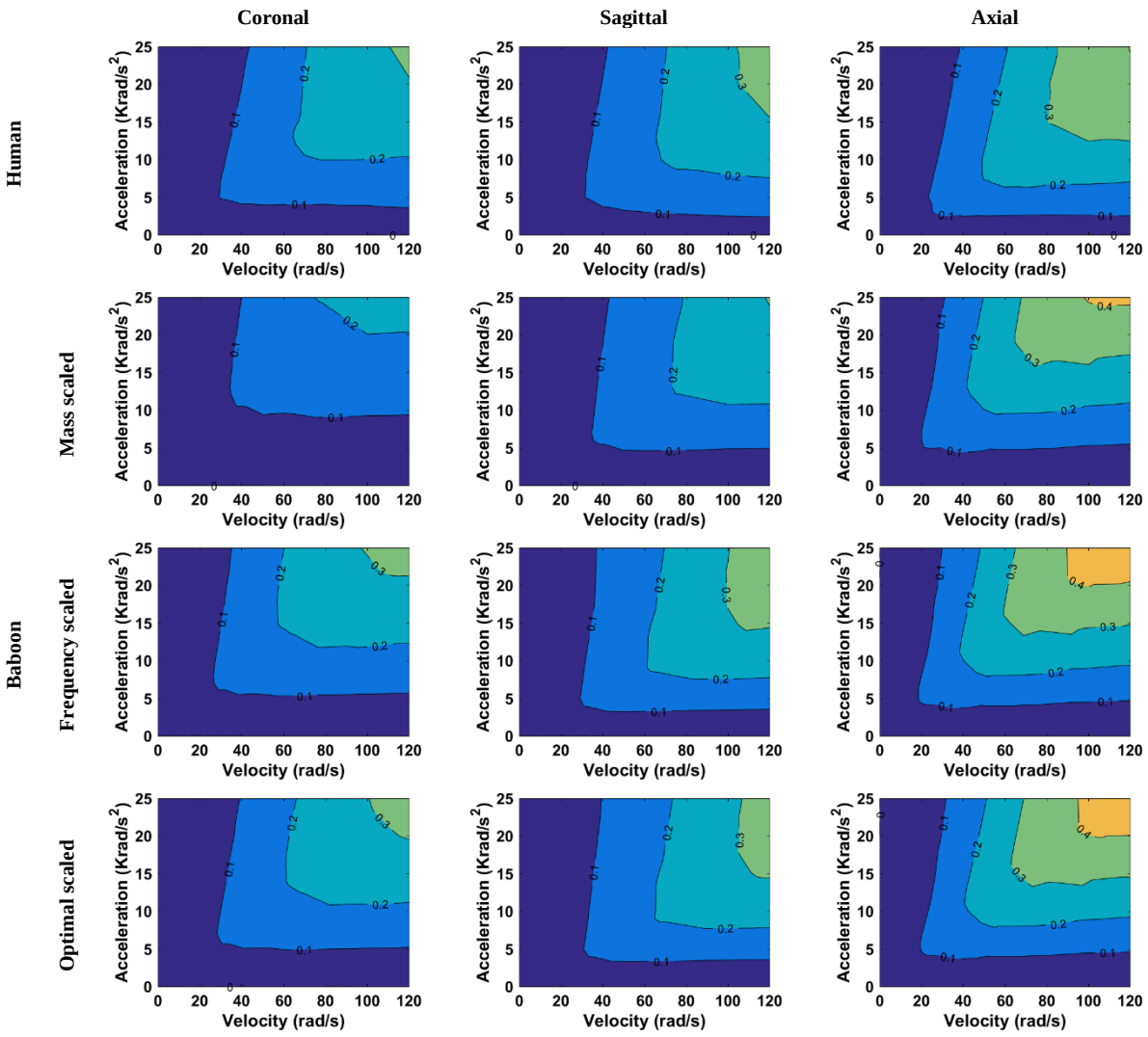

Figure A11. Scaled baboon MAS (95th) response surfaces.

Robustness of the Scaling Methods

To test the robustness of the frequency scaling method and the optimal scaling method discussed in Chapter 6, 100 subsets were randomly sampled (10 human cases, 10 baboon cases) from the whole dataset (57 human cases, 58 baboon cases) to calculate the scaling factors. If the methodology is robust, the scaling factors obtained using the subsets, and the whole dataset should be similar. The smaller variations of frequency-based factors show the better robustness of this scaling method (Figure A12).

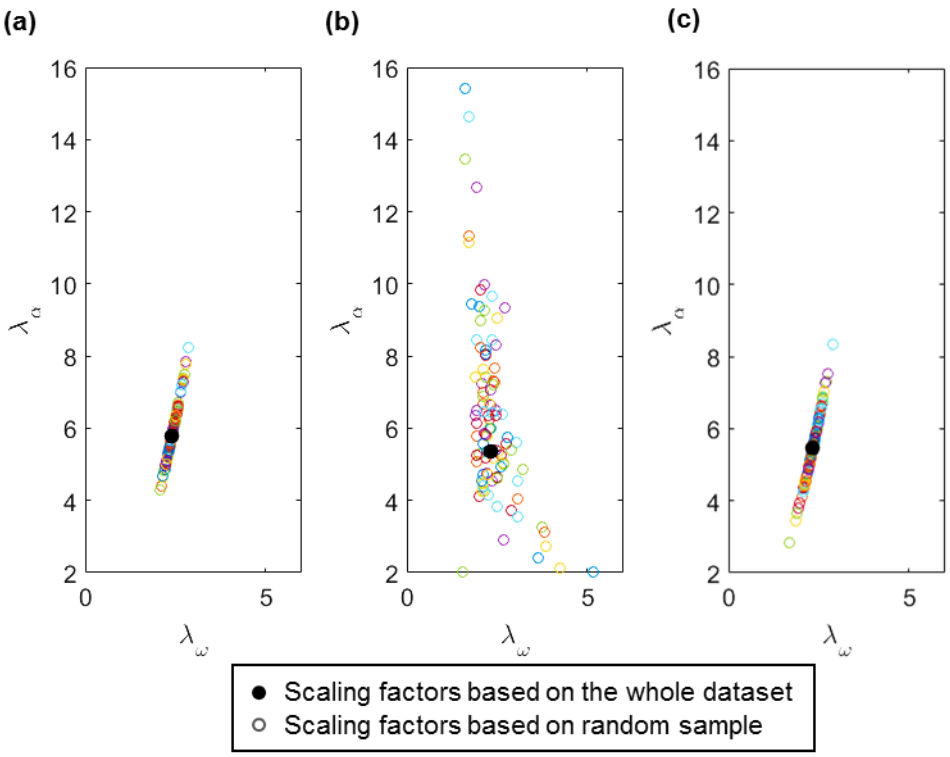

Figure A12. Scaling factors (under sagittal rotation) calculated based on different scaling methods. (a) frequency scaling, (b) optimal scaling method, and (c) constrained optimal scaling method.

APPENDIX C: BIOMECHANICAL INJURY DATA

Table A4. Non-Human primate injury data used in this dissertation.

ID	Source	Species	Brain Mass (grams)	Injury Description	AIS Coding	Severity	Symptoms
2-004	UMTRI	rhesus	88	no injury	0	no injury	No
3-012	UMTRI	rhesus	81	concussion	2	mild	Unconscious < 15 minutes
2-013	UMTRI	rhesus	88	no injury	0	no injury	Slight dazed*
2-014	UMTRI	rhesus	86	Dead, ICH	6	severe	Dead
2-015	UMTRI	rhesus	88	no injury	0	no injury	No*
2-019	UMTRI	cynomolgus	64	no injury	0	no injury	No*
2-020	UMTRI	cynomolgus	54	Concussion	2	mild	Unconscious < 15 minutes
2-024	UMTRI	rhesus	111	Concussion	2-3	mild	Dazed 2 min
2-025	UMTRI	rhesus	105	concussion, skull fracture	2-3	mild	Unconscious < 15 minutes
2-027	UMTRI	rhesus	100	contusion, DAI	4	severe	Unconscious > 15 minutes
2-030	UMTRI	rhesus	112	concussion, skull fracture	2	mild	Dazed 1 min
2-031	UMTRI	rhesus	112	concussion, skull fracture	2	mild	Unconscious < 15 minutes
2-089	UMTRI	cynomolgus	57	DAI, ICH	5	severe	Unconscious > 15 minutes
2-090	UMTRI	cynomolgus	57	concussion, skull fracture	3	mild	Unconscious < 15 minutes
2-092	UMTRI	cynomolgus	67	ICH	3	mild	Unconscious < 15 minutes
2-093	UMTRI	cynomolgus	78	fracture, ICH	5-6	severe	Unconscious < 15 minutes
2-096	UMTRI	baboon	163	fracture, ICH	5	Severe	Unconscious > 15 minutes
402	JARI	Japanese macaque	107	no injury	0	no injury	No*
542	JARI	Japanese macaque	110	no injury	0	no injury	No*
541	JARI	Japanese macaque	111	no injury	0	no injury	No*
529	JARI	Japanese macaque	130	no injury	0	no injury	No*
539	JARI	cynomolgus	71	no injury	0	no injury	No*
B01	UPenn	baboon	143	DAI	4-5	severe	N/A**
B10	UPenn	baboon	160	DAI	4-5	severe	N/A**
B100	UPenn	baboon	134	DAI	4-5	severe	N/A**

B101	UPenn	baboon	130	DAI	4-5	severe	N/A**
B11	UPenn	baboon	153	DAI	4-5	severe	N/A**
B20	UPenn	baboon	112	DAI	4-5	severe	N/A**
B23	UPenn	baboon	139	DAI	4-5	severe	N/A**
B30	UPenn	baboon	169	DAI	4-5	severe	N/A**
B32	UPenn	baboon	124	DAI	4-5	severe	N/A**
B33	UPenn	baboon	149	DAI	4-5	severe	N/A**
B35	UPenn	baboon	125	DAI	4-5	severe	N/A**
B37	UPenn	baboon	150	DAI	4-5	severe	N/A**
B92	UPenn	baboon	156	DAI	4-5	severe	N/A**
BB2	UPenn	baboon	116	DAI	4-5	severe	N/A**
BB3	UPenn	baboon	105	DAI	4-5	severe	N/A**
BB6	UPenn	baboon	128	DAI	4-5	severe	N/A**
BB7	UPenn	baboon	139	DAI	4-5	severe	N/A**
BB8	UPenn	baboon	136	DAI	4-5	severe	N/A**
BB9	UPenn	baboon	126	DAI	4-5	severe	N/A**
RR18	UPenn	baboon	81	DAI	4-5	severe	N/A**
RR21	UPenn	baboon	101	DAI	4-5	severe	N/A**
RR22	UPenn	baboon	96	DAI	4-5	severe	N/A**
1098	UPenn	rhesus	80	DAI	4-5	severe	N/A**
1106	UPenn	baboon	115	DAI	4-5	severe	N/A**
1108	UPenn	baboon	140	DAI	4-5	severe	N/A**
1109	UPenn	baboon	160	DAI	4-5	severe	N/A**
1112	UPenn	baboon	155	DAI	4-5	severe	N/A**
1114	UPenn	baboon	170	DAI	4-5	severe	N/A**
1115	UPenn	baboon	160	DAI	4-5	severe	N/A**
1116	UPenn	baboon	140	DAI	4-5	severe	N/A**
1121	UPenn	baboon	152	DAI	4-5	severe	N/A**
1125	UPenn	baboon	124	DAI	4-5	severe	N/A**

1126	UPenn	baboon	149	DAI	4-5	severe	N/A**
1127	UPenn	baboon	129	DAI	4-5	severe	N/A**
1131	UPenn	baboon	140	DAI	4-5	severe	N/A**
1135	UPenn	baboon	135	DAI	4-5	severe	N/A**
1136	UPenn	baboon	138	DAI	4-5	severe	N/A**
1137	UPenn	baboon	140	DAI	4-5	severe	N/A**
1139	UPenn	baboon	149	DAI	4-5	severe	N/A**
1140	UPenn	baboon	147	DAI	4-5	severe	N/A**
1141	UPenn	baboon	152	DAI	4-5	severe	N/A**
1142	UPenn	baboon	140	DAI	4-5	severe	N/A**
1143	UPenn	baboon	163	DAI	4-5	severe	N/A**
1144	UPenn	baboon	140	DAI	4-5	severe	N/A**
1145	UPenn	baboon	140	DAI	4-5	severe	N/A**
1149	UPenn	baboon	148	DAI	4-5	severe	N/A**
1154	UPenn	baboon	126	DAI	4-5	severe	N/A**
1156	UPenn	baboon	140	DAI	4-5	severe	N/A**
1157	UPenn	baboon	140	DAI	4-5	severe	N/A**
1158	UPenn	baboon	130	DAI	4-5	severe	N/A**
1159	UPenn	baboon	134	DAI	4-5	severe	N/A**
1160	UPenn	baboon	140	DAI	4-5	severe	N/A**
1161	UPenn	baboon	140	DAI	4-5	severe	N/A**
1162	UPenn	baboon	140	DAI	4-5	severe	N/A**
1163	UPenn	baboon	140	DAI	4-5	severe	N/A**
1164	UPenn	baboon	140	DAI	4-5	severe	N/A**

*No symptom, or very minor symptom, which might be caused by invasive instrumentation instead of impact.

** The histopathological identification of DAI was dependent upon the visualization of abnormal axonal profiles, but Individual information is unavailable.

APPENDIX D: KINEMATICS-BASED INJURY METRICS

The kinematics-based head and brain injury metrics included in this study are summarized in Table A4 with corresponding constraints and critical values. A brief description of each metric is provided in the following sections.

Table A5. Existing kinematic-based brain injury metrics and recommended critical values.

Metrics	Formulation	Constraints and Critical Values
$\mathbf{a_{max}}$	Peak resultant linear acceleration	--
$\boldsymbol{\omega_{max}}$	Peak resultant angular velocity	--
$\boldsymbol{\alpha_{max}}$	Peak resultant angular acceleration	--
HIC	Eq. (11)	t_1 - $t_2 \leq$ 15 ms
CP	Eq. (12)	β_0 = -10.2, β_1 = 4.33E-2, β_2 = 8.73E-4, β_3 = -9.20E-7.
BrIC	Eq. (13)	ω_{xcr} = 66.25, ω_{ycr} = 56.45, ω_{zcr} = 42.87.
CIBIC	Eq. (14) A standard linear solid model (Maxwell)	k_{1x} = 12.76, k_{1y} = 16.39, k_{1z} = 17.04, k_{2x} = 22.67, k_{2y} = 31.63, k_{2z} = 47.52, c_x = 129.1, c_y = 120.4, c_z = 74.4, B_x = 0.00313, B_y = 0.00395, B_z = 0.00494.
UBRIC	Eq. (15)	ω_{xcr} = 211, α_{xcr} = 20× 10^3, ω_{ycr} = 171, α_{ycr} = 10.3 × 10^3, ω_{zcr} = 115, α_{zcr} = 7.76× 10^3.
DAMAGE	A three-degree-of-freedom, coupled 2nd-order system	k_x = 32819.8 N/m, k_y = 23658.6 N/m, k_z = 17080.8 N/m, k_{xy} = 0, k_{yz} = 0, k_{zx} = 1815.8 N/m, $a1$ = 5.6 ms, B = 2.995 1/m.

Head Injury Criterion (HIC)

Head injury criterion (HIC), originally proposed by Versace (1971) and later adopted by NTHSA, is by far the most widely used measure of the risk of injury to the brain from a blunt impact to the head. Early cadaver experiments formed the basis for the development of the HIC, as a passing reference to the linear acceleration required to produce linear fractures on the skull was found. Using the HIC as an indication of the brain injury is a considerable extrapolation from the original tests, depending on an unlikely assumption that a linear skull fracture was probably accompanied by a concussion.

$$\mathrm{HIC} = \max_{(t_1,t_2)} \left\{ (t_2 - t_1) \left[\frac{1}{t_2 - t_1} \int_{t_1}^{t_2} |\boldsymbol{a}(t)| dt \right]^{2.5} \right\} \tag{11}$$

Combined Probability of Concussion (CP)

CP was an injury risk function developed by Rowson and Duma (2013) to predict the risk of concussion experienced by football athletes. The formulation of the kinematic metric (Eq. 12) is the result of a multivariate logistic regression analysis considering maximum resultant linear and angular acceleration as predictors. In developing this risk curve, the weighting between the sub-concussive and concussive data distributions was adjusted to consider concussion incidence rates experienced in football and the rates of undiagnosed concussions.

$$CP = \beta_0 + \beta_1 a_{max} + \beta_2 \alpha_{max} + \beta_3 a_{max} \alpha_{max} \tag{12}$$

Brain Injury Criterion (BrIC)

BrIC, proposed by Takhounts et al. (2013), is formulated using the maximum magnitudes of the three orthogonal head angular velocity components:

$$BrIC = \sqrt{\left(\frac{\omega_x}{\omega_{xcr}}\right)^2 + \left(\frac{\omega_y}{\omega_{ycr}}\right)^2 + \left(\frac{\omega_z}{\omega_{zcr}}\right)^2} \tag{13}$$

where $\omega_{icr}, (i = x, y, z)$ are directionally dependent critical values that were determined using FE modeling.

Convolution of Impulse Response for Brain Injury Criterion (CIBIC)

CIBIC was also proposed based on the analogy between a simple mechanical system (Figure A13) and the rotational response of a human FE head-brain model by the following formula.

$$\text{CIBIC} = \max\left\{\sqrt{\sum_{i=1}^{3}\left\{\int_0^t x_i(t-\tau)\alpha_i(\tau)d\tau\right\}^2}\right\} \quad (14)$$

Where $i = 1,2,3$ represent the x, y and z axis and α_i is rotational acceleration.

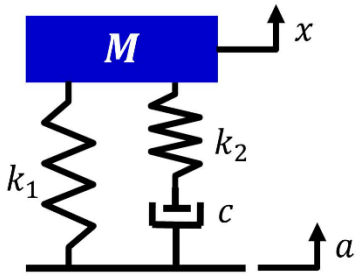

Figure A13. 1D (standard linear solid) model (Takahashi and Yanaoka, 2017).

Universal Brain Injury Criterion (UBrIC)

Based on the governing relationship between excitation and maximum deformation of a second-order system, the UBrIC was proposed by Gabler et al. (2018):

$$UBrIC = \left\{\sum_i \left[\omega_i^* + (\alpha_i^* - \omega_i^*)e^{-\frac{\alpha_i^*}{\omega_i^*}}\right]^2\right\}^{\frac{1}{2}} \quad (15)$$

where ω_i^* and α_i^* are the directionally dependent $(i = x, y, z)$ maximum magnitudes of head angular velocity and angular acceleration each normalized by a critical value (cr); $\omega_i^* = \omega_i/\omega_{icr}$ and $\alpha_i^* = \alpha_i/\alpha_{icr}$. The critical values normalize the metric to maximum brain strain and control the transition between velocity and acceleration dependent deformations.

Diffuse Axonal Multi-Axial General Evaluation (DAMAGE)

The second rotational-based brain injury criterion proposed by Gabler et al. (2019) was DAMAGE. DAMAGE is based on a three-degree-of-freedom, coupled 2nd-order multibody (MB)

system (Figure A14) The MB model predicts maximum brain strain (or DAMAGE value) using the directionally dependent (triaxial) angular acceleration time-histories from a head impact as inputs based on the equations of motion. The internal parameters for the MB model (including the effective mass, stiffness, and damping parameters, Table A4) were determined using simplified rotational pulses which were applied multiaxially to a 50th percentile adult human male finite element model (GHBMC). The MB model can predict global tissue-level strain responses with the accuracy similar to an FE model while maintaining the computational simplicity of a kinematic-based metric.

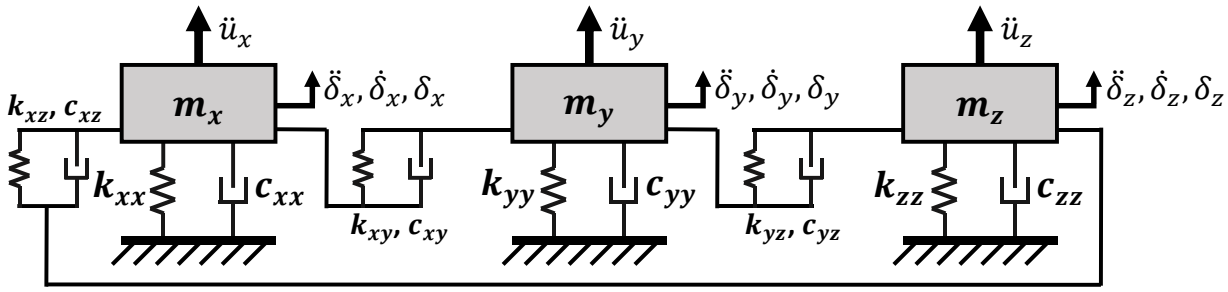

Figure A14. The mechanical analog to the second-order system used to formulate the DAMAGE metric (Gabler et al., 2018b).

APPENDIX E: INJURY RISK FUNCTIONS

This section provides details on the developed tissue-level injury risk functions (Table A5) and existing injury risk functions (Table A6) referred to in this dissertation.

Table A6. Coefficients of newly developed injury risk functions.

Metrics	Unit	mTBI				sTBI			
		Scale	Shape	50% Risk	Figure	Scale	Shape	50% Risk	Figure
MPS95	--	0.276	6.057	0.26	A15	0.391	8.707	0.37	A16
MAS95	--	0.132	5.452	0.12	A17	0.198	7.970	0.19	A18
VMS95	kPa	3.217	3.397	2.89	A19	8.234	4.750	7.62	A20

Table A7. Summary of existing injury risk functions and injury tolerances referred to in this dissertation.

Metric	Reference	Injury Assessment Type	Data Source for Development	Equation	Coefficients or tolerances*
$\boldsymbol{\alpha_{max}}$	Pellman et al., (2003)	Concussion	Football reconstructions	16	β_0 = -4.90; β_1 = 6.06E-2
$\boldsymbol{\alpha_{max}}$	Rowson et al., (2012)	Concussion	Football impacts measured with wearable sensors	16	β_0 = -12.5; β_1 = 2.00E-3
$\boldsymbol{\omega_{max}}$	Rowson et al., (2012)	Concussion	Football impacts measured with wearable sensors	16	β_0 = -12.5; β_1 = 4.42E-1
HIC	NHTSA, (1995)	Skull Fracture, TBI, AIS2+	Human cadavers	18	β_0 = -2.49; β_1 = -200; β_2 = 4.83E-3
HIC	NHTSA, (1995)	Skull Fracture, TBI, AIS4+	Human cadavers	18	β_0 = -4.9; β_1 = -200; β_2 = 3.51E-3
CP	Rowson & Duma, (2013)	Concussion	Football impacts measured with wearable sensors	19	β_0 = -10.2; β_1 = 4.33E-2; β_2 = 8.73E-4; β_3 = -9.20E-7
BrIC (MPS)	Takhounts et al., (2013)	Concussion, AIS2+	Scaled animal impact data	17	b = 0; λ = 0.602; k = 2.84
BrIC (MPS)	Takhounts et al., (2013)	DAI, AIS4+	Scaled animal impact data	17	b = 0; λ = 1.204; k = 2.84
BrIC (CSDM)	Takhounts et al., (2013)	Concussion, AIS2+	Scaled animal impact data	17	b = 0.523; λ = 0.324; k = 1.8
BrIC (CSDM)	Takhounts et al., (2013)	DAI, AIS4+	Scaled animal impact data	17	b = 0.523; λ = 0.647; k = 1.8

*Adapted from (Sanchez et al., 2017)

$$P(x) = \frac{1}{1 + e^{-(\beta_0 + \beta_1 x)}} \tag{16}$$

$$P(x) = 1 - e^{-\left(\frac{x-b}{\lambda}\right)^k} \tag{17}$$

$$P(x) = \frac{1}{1 + e^{-(\beta_0 + \beta_1 HIC^{-1} + \beta_2 HIC)}} \tag{18}$$

$$P(x) = \frac{1}{1 + e^{-(\beta_0 + \beta_1 a_{max} + \beta_2 \alpha_{max} + \beta_3 a_{max} \alpha_{max})}} \tag{19}$$

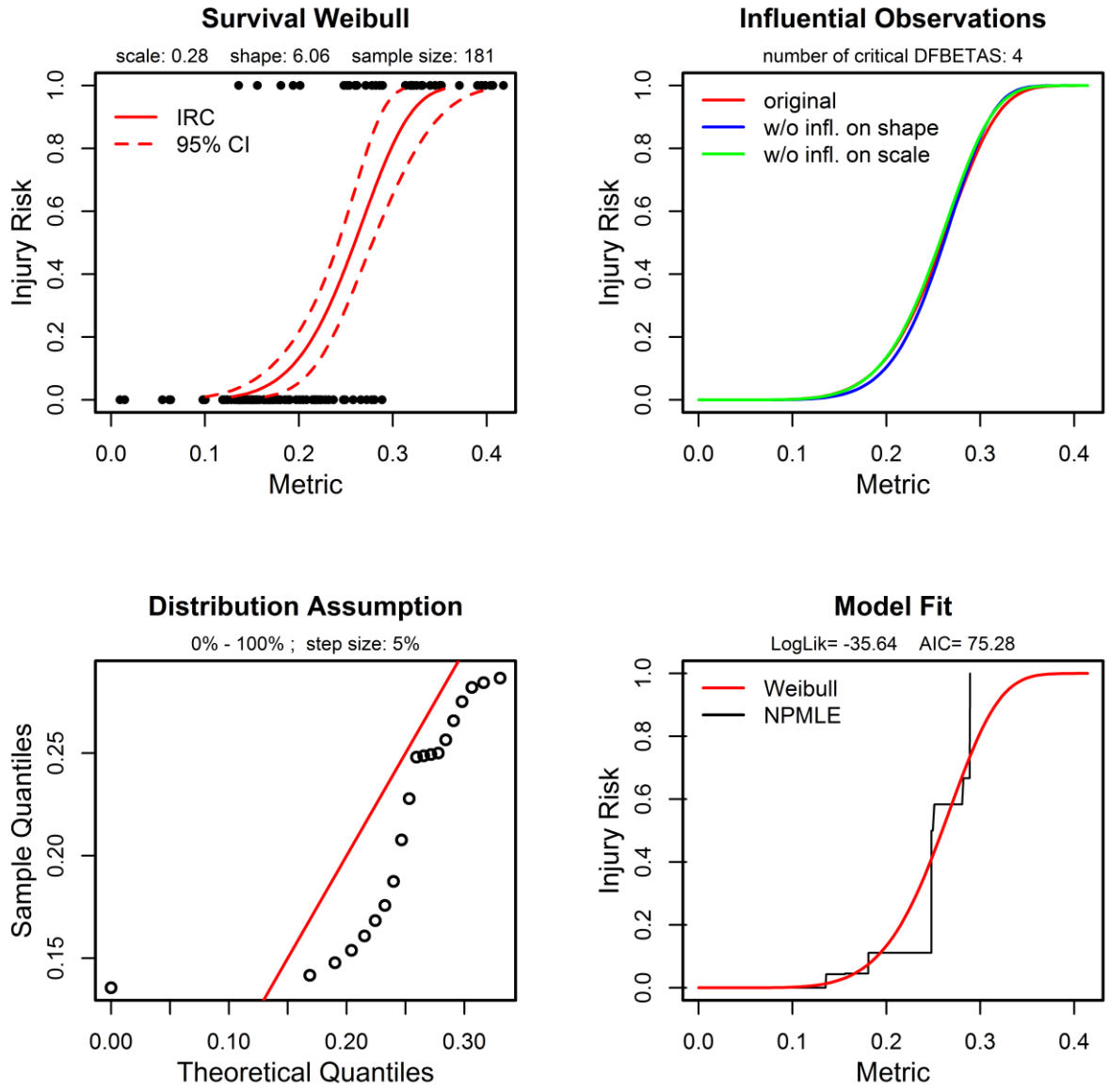

Figure A15. Mild brain injury risk curves based on MPS95.

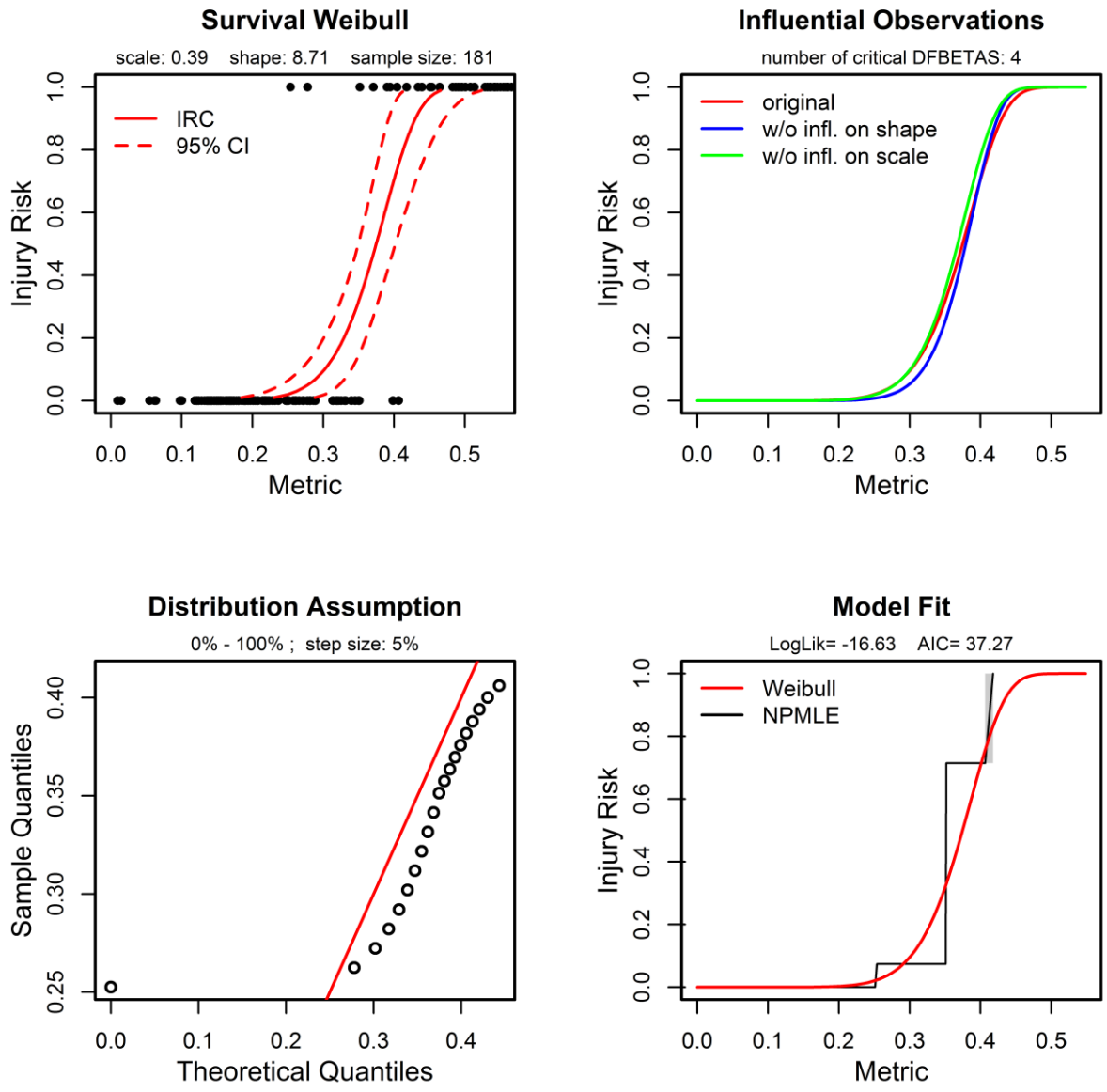

Figure A16. Severe brain injury risk curves based on MPS95.

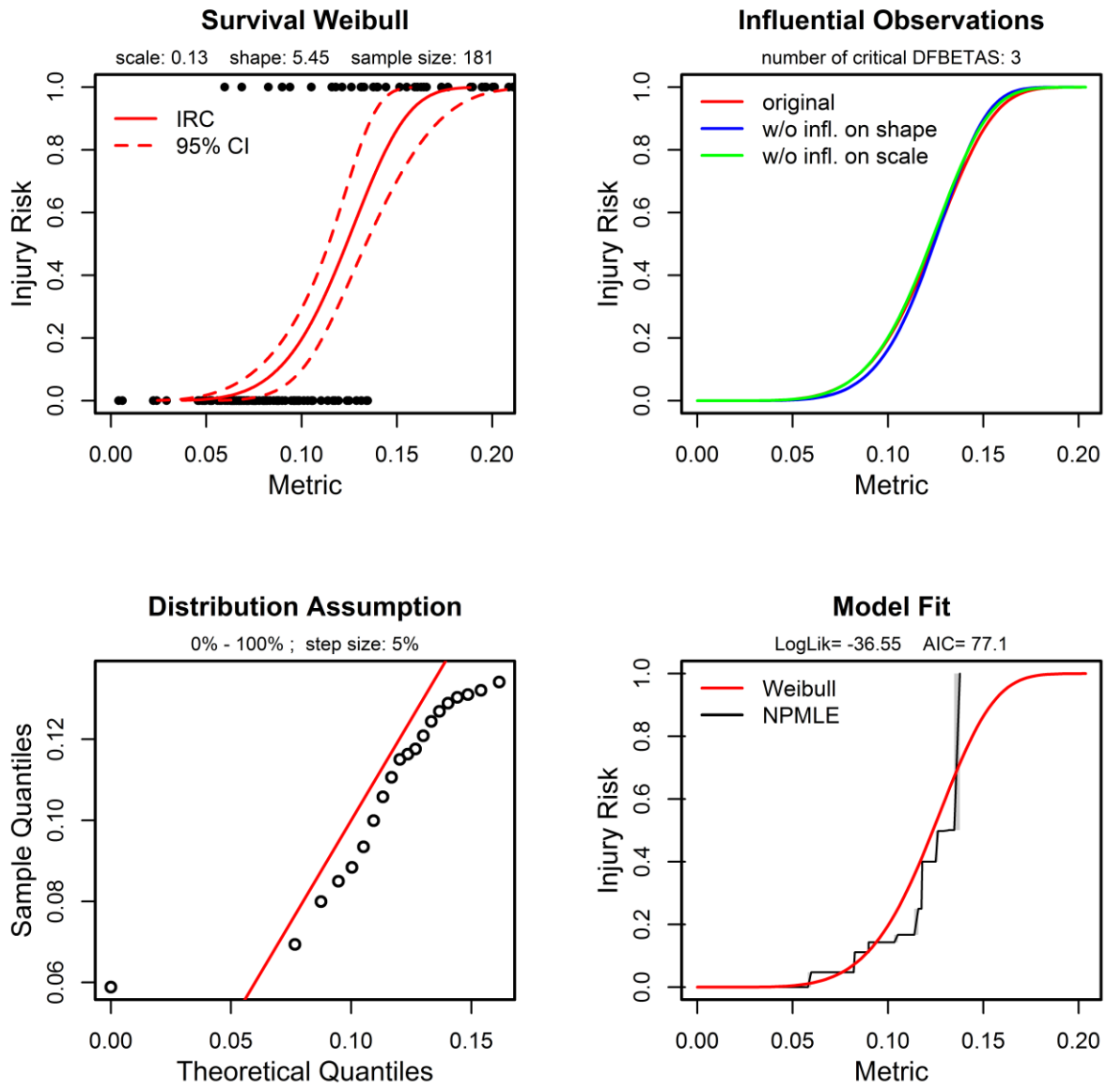

Figure A17. Mild brain injury risk curves based on MAS95.

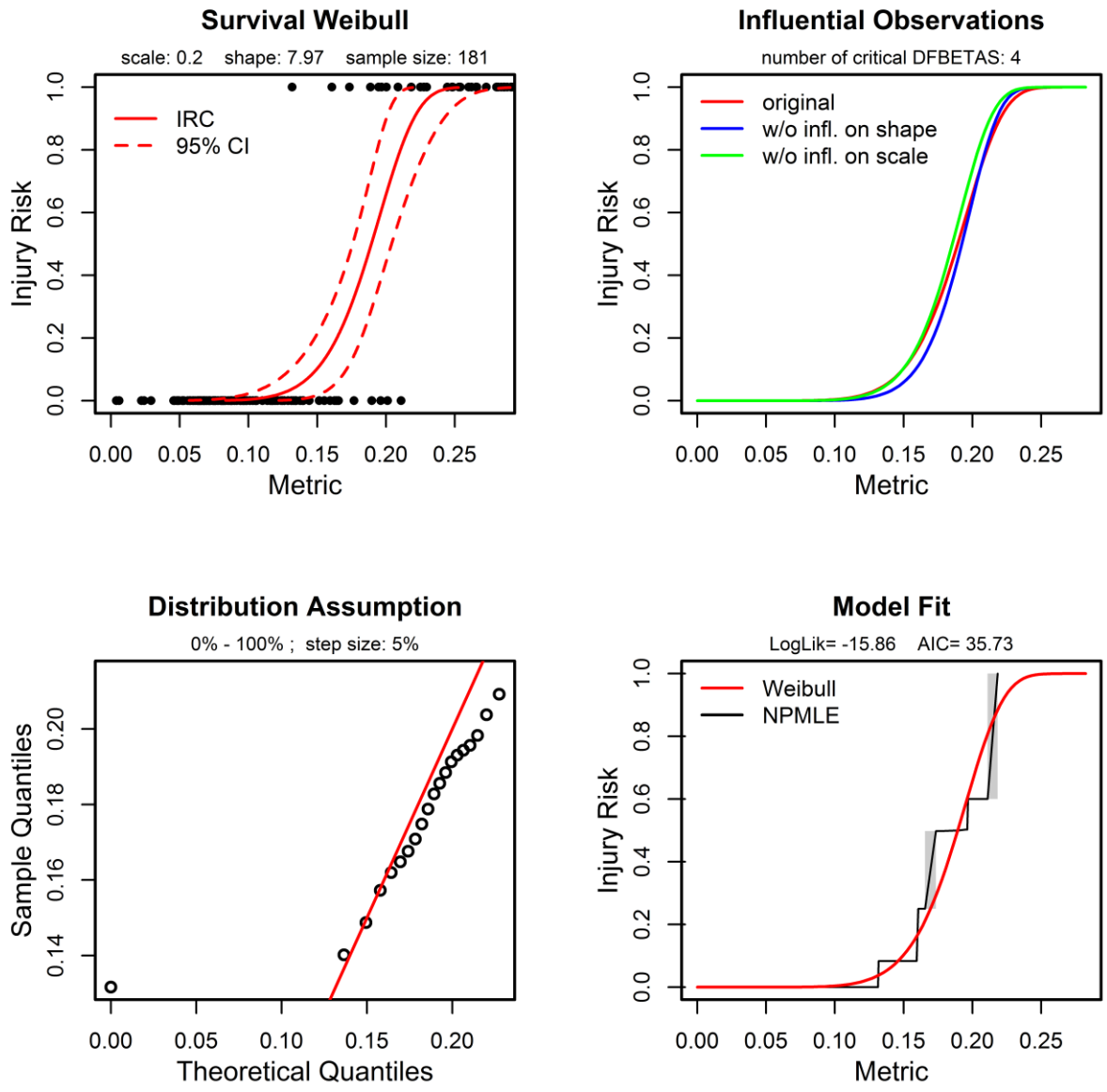

Figure A18. Severe brain injury risk curves based on MAS95.

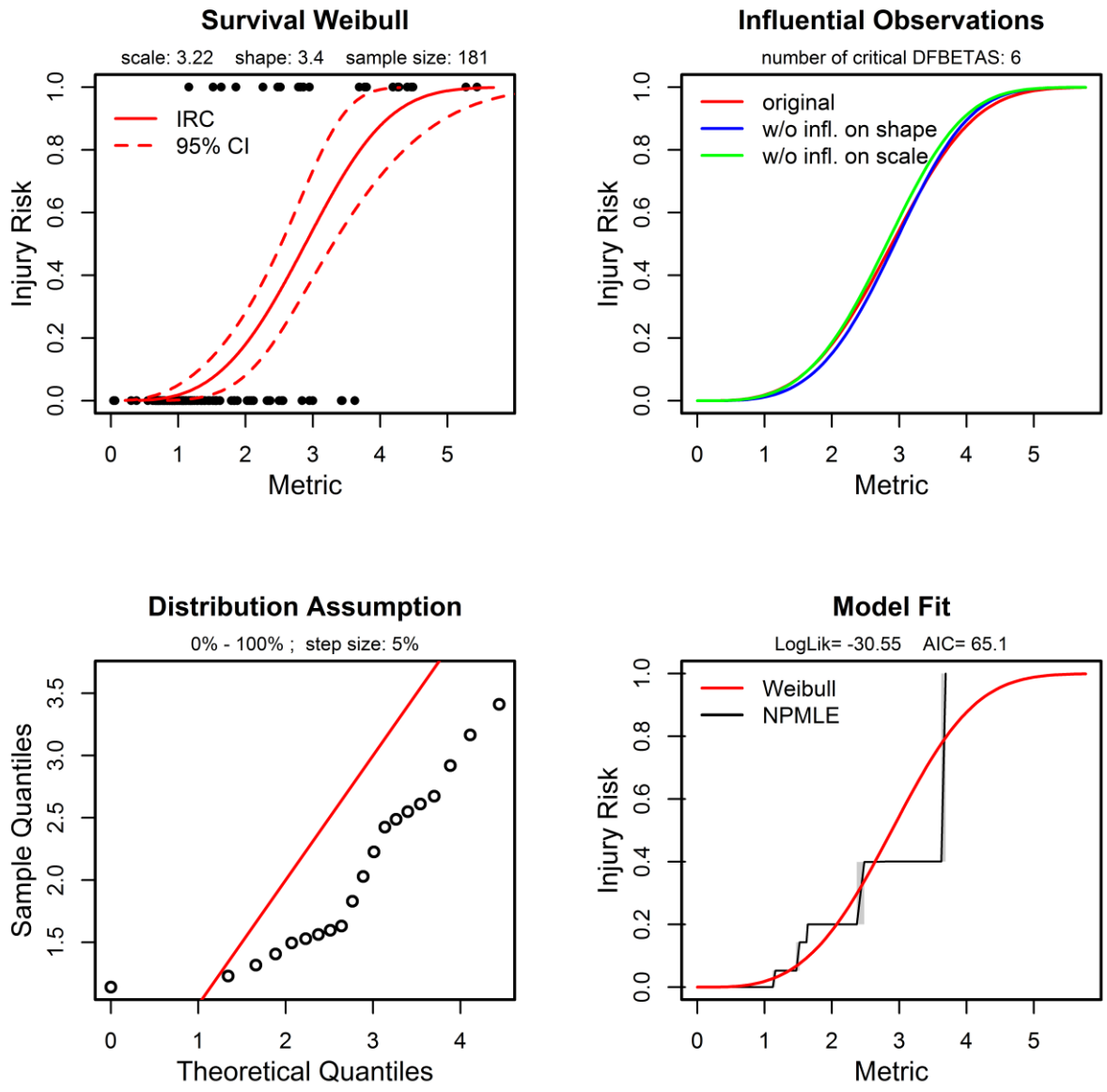

Figure A19. Mild brain injury risk curves based on VMS95.

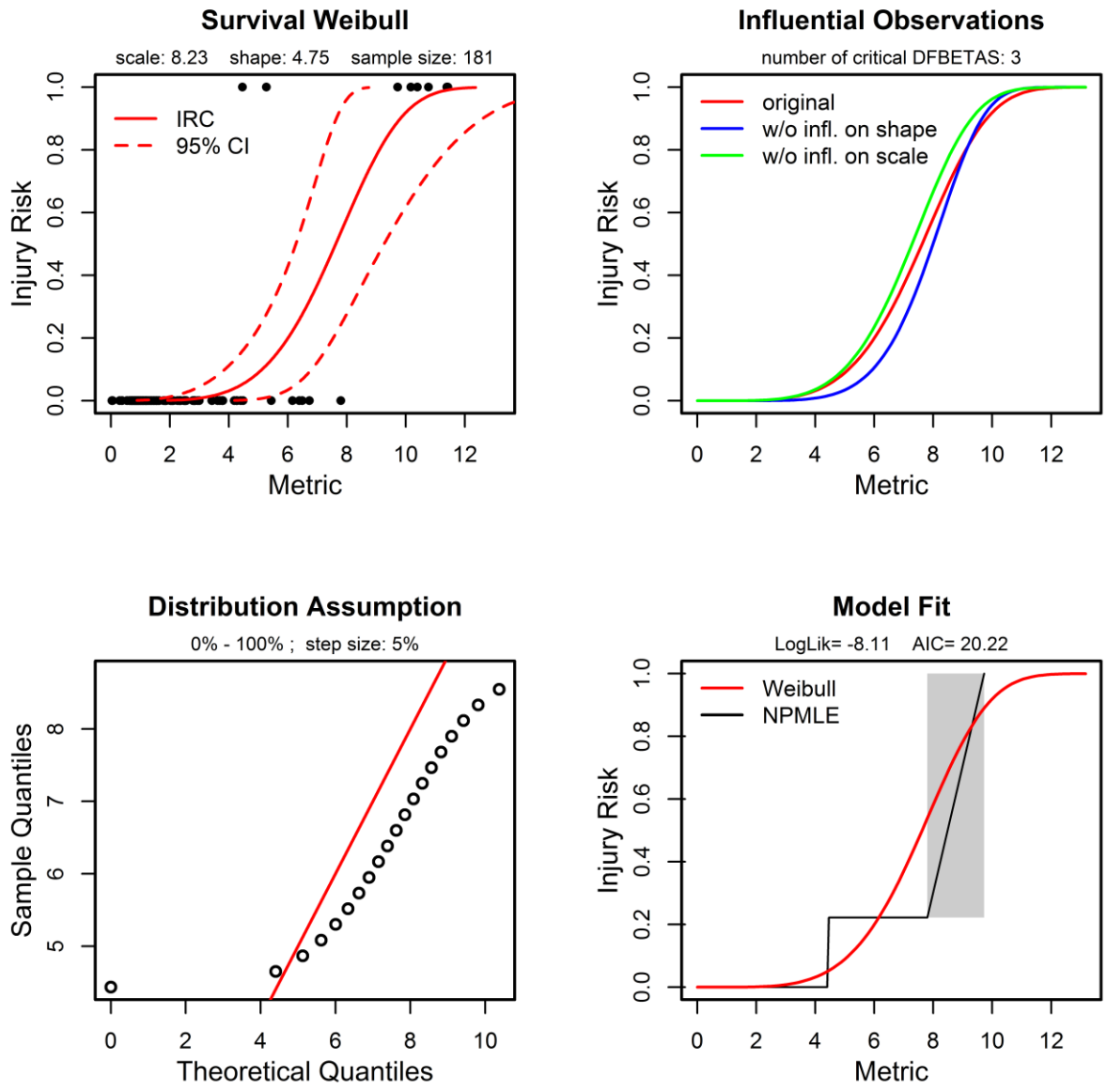

Figure A20. Severe brain injury risk curves based on VMS95.

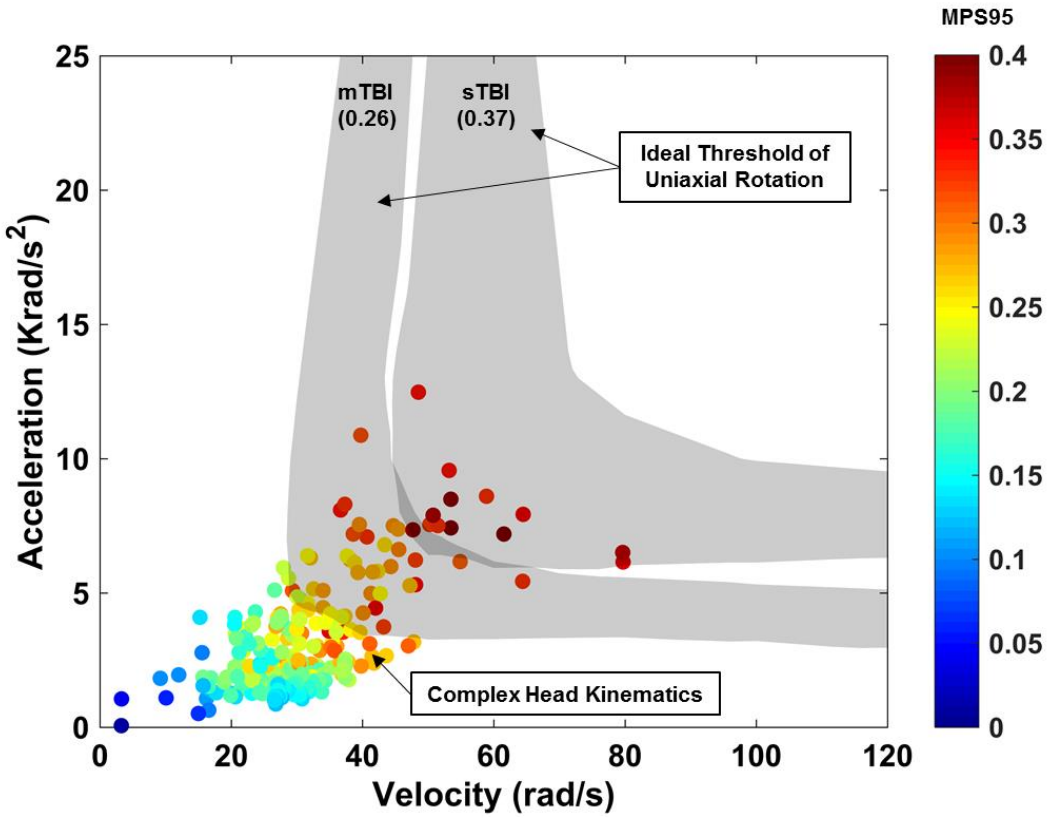

Complex head kinematics collected from automotive impacts, football impacts, and volunteer tests.

Figure A21. MPS95 results of complex head kinematics compared with the results of idealized uniaxial motion.

APPENDIX F: HEAD KINEMATICS DATABASE

Table A8. Complex head kinematics to evaluate frequency scaling in Chapter 6.

ID	Impact Condition	Surrogate[#]
Case059HD01*	helmet to helmet dummy reconstruction of on-field football impact; the striking player	H-III
Case069HD01*	helmet to helmet dummy reconstruction of on-field football impact; the striking player	H-III
Case071HD02MTBI*	helmet to helmet dummy reconstruction of on-field football impact; struck player	H-III
Case084HD02MTBI*	helmet to helmet dummy reconstruction of on-field football impact; struck player	H-III
Case092HD02MTBI*	helmet to helmet dummy reconstruction of on-field football impact; struck player	H-III
Case098HD02MTBI*	helmet to helmet dummy reconstruction of on-field football impact; struck player	H-III
SUV P1**	vehicle sled laterally into a pedestrian	PMHS, F
CEN1325**	vehicle into a barrier at 0deg, 25% offset, small overlap, an occupant on the left front seat	H-III
CEN1328**	vehicle into a barrier at 0deg, 25% offset, small overlap, an occupant on the left front seat	H-III
CEN1507**	vehicle into a barrier at 0deg, 25% offset, small overlap, an occupant on the left front seat	H-III
7429-01**	impactor into a vehicle at 15deg, 35% offset, left front seat	THOR
H03-93-A**	padded linear impactor into the helmeted head, oblique facemask	H-III
H11-93-UT**	padded linear impactor into the helmeted head, side of facemask	H-III
H3-5-22**	padded pendulum impactor at 0 deg into head CG	H-III, F

Reference: * (Sanchez et al., 2018); **(Gabler et al., 2018a).

[#]50^{TH} Male surrogate unless specified otherwise.

Table A9. Head kinematics in automotive conditions.

Sources	ID	Type	Vehicle	Details	Seat*	Surrogate#	ΔV (km/h)
NHTSA	4303-01	frontal	2003 HONDA PILOT	full overlap	01	H-III	55.9
NHTSA	4273-01	frontal	2002 MINI COOPER	full overlap	01	H-III	56.2
NHTSA	4198-01	frontal	2002 SATURN VUE	full overlap	01	H-III	56.3
NHTSA	3916-01	frontal	2002 TOYOTA SEQUOIA	full overlap	01	H-III	56.3
NHTSA	4250-01	frontal	2002 KIA SPECTRA	full overlap	01	H-III	55.7
NHTSA	4251-01	frontal	2002 SUBARU LEGACY	full overlap	01	H-III	56.8
NHTSA	4090-01	frontal	2002 MITSUBISHI LANCER	full overlap	01	H-III	56.3
NHTSA	4264-01	frontal	2002 SUBARU IMPREZA	full overlap	01	H-III	55.6
NHTSA	4215-01	frontal	2002 NISSAN ALTIMA	full overlap	01	H-III	56.3
NHTSA	4259-01	frontal	2003 CADILLAC CTS	full overlap	01	H-III	56.7
NHTSA	3987-01	frontal	2002 LEXUS ES300	full overlap	01	H-III	56.6
NHTSA	4235-01	frontal	2002 LAND ROVER DISCOVERY II	full overlap	01	H-III	55.7
NHTSA	3901-01	frontal	2002 CHEVROLET BLAZER	full overlap	01	H-III	55.9
NHTSA	4241-01	frontal	2002 ISUZU RODEO	full overlap	01	H-III	56.5
NHTSA	5287-01	frontal	2005 SUZUKI VERONA	full overlap	01	H-III	55.8
NHTSA	5567-01	frontal	2006 HUMMER H3	full overlap	01	H-III	56.3
NHTSA	5595-01	frontal	2006 SUZUKI GRAND VITARA	full overlap	01	H-III	56.8
NHTSA	5609-01	frontal	2006 TOYOTA 4RUNNER	full overlap	01	H-III	56.3
NHTSA	7966-01	frontal	2013 NISSAN ALTIMA	full overlap	01	H-III	56.2
NHTSA	7977-01	frontal	2013 BMW X5	full overlap	01	H-III	56.1
NHTSA	7978-01	frontal	2013 VOLKSWAGEN TIGUAN	full overlap	01	H-III	56.4
NHTSA	7989-01	frontal	2013 CADILLAC XTS	full overlap	01	H-III	56.2
NHTSA	8000-01	frontal	2013 HYUNDAI SANTA FE SPORT	full overlap	01	H-III	56.3
NHTSA	8024-01	frontal	2013 AUDI A4	full overlap	01	H-III	56.2
NHTSA	8035-01	frontal	2013 HONDA ACCORD	full overlap	01	H-III	56.3
NHTSA	8045-01	frontal	2013 CADILLAC ATS	full overlap	01	H-III	56.2
NHTSA	8048-01	frontal	2013 DODGE CHALLENGER	full overlap	01	H-III	56.4
NHTSA	8055-01	frontal	2013 LEXUS IS250	full overlap	01	H-III	56.2
NHTSA	8064-01	frontal	2013 VOLKSWAGEN BEETLE	full overlap	01	H-III	56.8
NHTSA	8068-01	frontal	2013 NISSAN SENTRA	full overlap	01	H-III	56.2
NHTSA	8071-01	frontal	2013 FORD CMAX HYBRID	full overlap	01	H-III	56.4
NHTSA	8077-01	frontal	2013 FORD FUSION HYBRID	full overlap	01	H-III	56.3
NHTSA	8081-01	frontal	2013 FORD FOCUS BEV	full overlap	01	H-III	56.4
NHTSA	8091-01	frontal	2013 MERCEDES ML350	full overlap	01	H-III	56.2
NHTSA	8106-01	frontal	2013 TOYOTA PRIUS V	full overlap	01	H-III	56.6
NHTSA	8153-01	frontal	2013 TOYOTA PRIUS C	full overlap	01	H-III	55.7
NHTSA	8151-01	frontal	2013 FORD CMAX ENERGI	full overlap	01	H-III	56.4
NHTSA	8156-01	frontal	2013 HONDA CIVIC	full overlap	01	H-III	56.2

Sources	ID	Type	Vehicle	Details	Seat*	Surrogate#	ΔV (km/h)
IIHS	CEN1219	frontal	2012 HYUNDAI SONATA	small overlap	01	H-III	64.4
IIHS	CEN1220	frontal	2012 MAZDA 6	small overlap	01	H-III	64.4
IIHS	CEN1221	frontal	2012 SUZUKI KIZASHI	small overlap	01	H-III	64.4
IIHS	CEN1222	frontal	2013 FORD ESCAPE	small overlap	01	H-III	64.4
IIHS	CEN1223	frontal	2012 HONDA CR-V	small overlap	01	H-III	64.4
IIHS	CEN1224	frontal	2012 NISSAN ROGUE	small overlap	01	H-III	64.4
IIHS	CEN1225	frontal	2012 KIA OPTIMA	small overlap	01	H-III	64.4
IIHS	CEN1226	frontal	2012 JEEP PATRIOT	small overlap	01	H-III	64.4
IIHS	CEN1227	frontal	2012 MITSUBISHI OUTLANDER SPORT	small overlap	01	H-III	64.4
IIHS	CEN1228	frontal	2013 SUBARU LEGACY	small overlap	01	H-III	64.4
IIHS	CEN1229	frontal	2013 HONDA ACCORD	small overlap	01	H-III	64.4
IIHS	CEN1230	frontal	2012 NISSAN MAXIMA	small overlap	01	H-III	64.4
IIHS	CEN1231	frontal	2013 NISSAN ALTIMA	small overlap	01	H-III	64.4
IIHS	CEN1232	frontal	2012 VOLKSWAGEN PASSAT	small overlap	01	H-III	64.4
IIHS	CEN1233	frontal	2012 VOLKSWAGEN JETTA	small overlap	01	H-III	64.4
IIHS	CEN1234	frontal	2013 HONDA ACCORD	small overlap	01	H-III	64.4
IIHS	CEN1235	frontal	2013 JEEP WRANGLER	small overlap	01	H-III	64.4
IIHS	CEN1236	frontal	2013 FORD FUSION	small overlap	01	H-III	64.4
IIHS	CEN1515	frontal	2015 NISSAN MURANO	small overlap	01	H-III	64.4
IIHS	CEN1518	frontal	2015 AUDI Q5	small overlap	01	H-III	64.4
NHTSA	6370-01	frontal	2007 FORD FIVE HUNDRED	moderate overlap	01	H-III	59.9
IIHS	CEF1206	frontal	2013 FORD ESCAPE	moderate overlap	01	H-III	64.4
IIHS	CEF1207	frontal	2013 DODGE DART	moderate overlap	01	H-III	64.4
IIHS	CEF1208	frontal	2013 NISSAN ALTIMA	moderate overlap	01	H-III	64.4
IIHS	CEF1301	frontal	2014 MAZDA 6	moderate overlap	01	H-III	64.4
IIHS	CEF1302	frontal	2013 BMW X1	moderate overlap	01	H-III	64.4
IIHS	CEF1303	frontal	2013 BUICK ENCORE	moderate overlap	01	H-III	64.4
IIHS	CEF1304	frontal	2014 FIAT 500L	moderate overlap	01	H-III	64.4
IIHS	CEF1305	frontal	2014 JEEP CHEROKEE	moderate overlap	01	H-III	64.4
IIHS	CEF1306	frontal	2013 CHEVROLET SPARK	moderate overlap	01	H-III	64.4

Sources	ID	Type	Vehicle	Details	Seat*	Surrogate#	ΔV (km/h)
IIHS	CEF1307	frontal	2014 MASERATI GHIBLI	moderate overlap	01	H-III	64.4
IIHS	CEF1308	frontal	2014 MITSUBISHI MIRAGE	moderate overlap	01	H-III	64.4
IIHS	CEF1402	frontal	2014 NISSAN ROUGE	moderate overlap	01	H-III	64.4
IIHS	CEF1403	frontal	2015 SUBARU WRX	moderate overlap	01	H-III	64.4
IIHS	CEF1404	frontal	2014 FORD C-MAX HYBRID	moderate overlap	01	H-III	64.4
IIHS	CEF1405	frontal	2014 MAZDA 5	moderate overlap	01	H-III	64.4
IIHS	CEF1406	frontal	2014 HYUNDAI VELOSTER	moderate overlap	01	H-III	64.4
IIHS	CEF1501	frontal	2016 AUDI Q3	moderate overlap	01	H-III	64.4
NHTSA	3818-01	side	1999 SAAB 9-5	pole	01	ES 2RE	28.5
NHTSA	4497-01	side	2000 SAAB 9-5	pole	01	ES 2RE	32.3
NHTSA	3820-01	side	1999 VOLVO S80	pole	01	ES 2RE	28.6
NHTSA	4498-01	side	1999 VOLVO S80	pole	01	ES 2RE	31.9
NHTSA	3802-01	side	1999 MERCURY COUGAR	pole	01	ES 2RE	28.2
NHTSA	7955-01	side	2013 NISSAN ALTIMA	pole	01	SID-IIS, F	32.2
NHTSA	7979-01	side	2013 VOLKSWAGEN TIGUAN	pole	01	SID-IIS, F	32.2
NHTSA	7988-01	side	2013 CADILLAC XTS	pole	01	SID-IIS, F	32.2
NHTSA	7997-01	side	2013 HYUNDAI SANTA FE SPORT	pole	01	SID-IIS, F	32.1
NHTSA	8052-01	side	2013 DODGE CHALLENGER	pole	01	SID-IIS, F	32.2
NHTSA	4551-01	side	2002 CHEVROLET IMPALA	left-side pure	01	ES 2RE	53.1
NHTSA	4547-01	side	2001 FORD FOCUS	left-side pure	01	ES 2RE	52.6
NHTSA	4292-01	side	1999 CHEVROLET PRIZM	left-side pure	01	ES 2RE	52.6
NHTSA	4482-01	side	1999 CHEVROLET PRIZM	left-side pure	01	ES 2RE	53.1
NHTSA	5461-01	side	2005 SATURN ION	left-side pure	01	ES 2RE	53.3
NHTSA	7967-01	side	2013 NISSAN ALTIMA	left-side pure	01	ES 2RE	62.2
NHTSA	7984-01	side	2013 VOLKSWAGEN TIGUAN	left-side pure	01	ES 2RE	62.5
NHTSA	7990-01	side	2013 CADILLAC XTS	left-side pure	01	ES 2RE	62.4
NHTSA	7998-01	side	2013 HYUNDAI SANTA FE SPORT	left-side pure	01	ES 2RE	62.4
NHTSA	8033-01	side	2013 HONDA ACCORD	left-side pure	01	ES 2RE	62.5
NHTSA	8047-01	side	2013 CADILLAC ATS	left-side pure	01	ES 2RE	62
NHTSA	8053-01	side	2013 DODGE CHALLENGER	left-side pure	01	ES 2RE	62.6
NHTSA	8054-01	side	2013 LEXUS IS250	left-side pure	01	ES 2RE	61.9
NHTSA	8069-01	side	2013 FORD CMAX HYBRID	left-side pure	01	ES 2RE	62.2
NHTSA	8072-01	side	2013 NISSAN SENTRA	left-side pure	01	ES 2RE	62
NHTSA	8078-01	side	2013 FORD FUSION HYBRID	left-side pure	01	ES 2RE	62.2
NHTSA	8079-01	side	2013 MERCEDES-BENZ C-CLASS	left-side pure	01	ES 2RE	62
NHTSA	8082-01	side	2013 FORD FOCUS BEV	left-side pure	01	ES 2RE	61.7

Sources	ID	Type	Vehicle	Details	Seat*	Surrogate#	ΔV (km/h)
NHTSA	8092-01	side	2013 MERCEDES ML350	left-side pure	01	ES 2RE	62.2
NHTSA	8102-01	side	2013 HONDA ACCORD	left-side pure	01	ES 2RE	62
NHTSA	8108-01	side	2013 TOYOTA PRIUS V	left-side pure	01	ES 2RE	61.5
NHTSA	8149-01	side	2013 TOYOTA PRIUS C	left-side pure	01	ES 2RE	62.2
NHTSA	8157-01	side	2013 HONDA CIVIC	left-side pure	01	ES 2RE	62.4
NHTSA	8150-01	side	2013 FORD CMAX ENERGI	left-side pure	01	ES 2RE	62.2
NHTSA	4380-01	side	2002 CHEVROLET IMPALA	left-side pure	01	ES 2RE	62.1
NHTSA	4456-01	side	2001 FORD FOCUS	left-side pure	01	ES 2RE	61.8
NHTSA	3799-01	side	2001 FORD FOCUS	left-side pure	01	ES 2RE	62.1
NHTSA	3803-01	side	2002 CHEVROLET IMPALA	left-side pure	01	ES 2RE	61.6
NHTSA	4205-02	frontal	2002 FORD THUNDERBIRD	full overlap	02	H-III	56.2
NHTSA	4266-02	frontal	2003 TOYOTA COROLLA	full overlap	02	H-III	55.9
NHTSA	4264-02	frontal	2002 SUBARU IMPREZA	full overlap	02	H-III	55.6
NHTSA	3901-02	frontal	2002 CHEVROLET BLAZER	full overlap	02	H-III	55.9
NHTSA	4215-02	frontal	2002 NISSAN ALTIMA	full overlap	02	H-III	56.3
NHTSA	4237-02	frontal	2002 NISSAN FRONTIER	full overlap	02	H-III	56.2
NHTSA	4090-02	frontal	2002 MITSUBISHI LANCER	full overlap	02	H-III	56.3
NHTSA	4223-02	frontal	2002 FORD EXPLORER SPORT	full overlap	02	H-III	55.6
NHTSA	4267-02	frontal	2002 ISUZU AXIOM	full overlap	02	H-III	55.8
NHTSA	4242-02	frontal	2002 HONDA ODYSSEY	full overlap	02	H-III	56.5
NHTSA	4255-02	frontal	2003 ACURA 3.2 TL	full overlap	02	H-III	55.8
NHTSA	4235-02	frontal	2002 LAND ROVER DISCOVERY II	full overlap	02	H-III	55.7
NHTSA	4265-02	frontal	2002 TOYOTA HIGHLANDER	full overlap	02	H-III	55.8
NHTSA	4249-02	frontal	2002 NISSAN XTERRA	full overlap	02	H-III	55.8
NHTSA	4259-02	frontal	2003 CADILLAC CTS	full overlap	02	H-III	56.7
NHTSA	4198-02	frontal	2002 SATURN VUE	full overlap	02	H-III	56.3
NHTSA	3915-02	frontal	2002 TOYOTA TUNDRA	full overlap	02	H-III	56.2
NHTSA	3952-02	frontal	2002 BUICK RENDEZVOUS	full overlap	02	H-III	56.6
NHTSA	5301-02	frontal	2005 DODGE DAKOTA	full overlap	02	H-III	56.5
NHTSA	5594-02	frontal	2006 NISSAN TITAN	full overlap	02	H-III	56.5
NHTSA	5595-02	frontal	2006 SUZUKI GRAND VITARA	full overlap	02	H-III	56.8
NHTSA	7977-02	frontal	2013 BMW X5	full overlap	02	H-III, F	56.1
NHTSA	7989-02	frontal	2013 CADILLAC XTS	full overlap	02	H-III, F	56.2
NHTSA	8035-02	frontal	2013 HONDA ACCORD	full overlap	02	H-III, F	56.3
NHTSA	8045-02	frontal	2013 CADILLAC ATS	full overlap	02	H-III, F	56.2
NHTSA	8055-02	frontal	2013 LEXUS IS250	full overlap	02	H-III, F	56.2
NHTSA	8064-02	frontal	2013 VOLKSWAGEN BEETLE	full overlap	02	H-III, F	56.8
NHTSA	8068-02	frontal	2013 NISSAN SENTRA	full overlap	02	H-III, F	56.2
NHTSA	8080-02	frontal	2013 MERCEDES-BENZ C-CLASS	full overlap	02	H-III, F	56.2

Sources	ID	Type	Vehicle	Details	Seat*	Surrogate#	ΔV (km/h)
NHTSA	8081-02	frontal	2013 FORD FOCUS BEV	full overlap	02	H-III, F	56.4
NHTSA	8104-02	frontal	2013 HONDA ACCORD	full overlap	02	H-III, F	55.7
NHTSA	8106-02	frontal	2013 TOYOTA PRIUS V	full overlap	02	H-III, F	56.6
NHTSA	8153-02	frontal	2013 TOYOTA PRIUS C	full overlap	02	H-III, F	55.7
NHTSA	8156-02	frontal	2013 HONDA CIVIC	full overlap	02	H-III, F	56.2

*Occupant seat position code, 01: driver; 02: front driver.

#50^{TH} Male surrogate unless specified otherwise.

APPENDIX G: FIELD DATA ANALYSIS

The supplemental material presented in this section was to support the field data analysis in Chapter 9.

Table A10. Injury definitions and classification applied in the field analysis.

AIS Code	Injury Description*	Injury Definition**	Classification
1404065	Cerebellum diffuse axonal injury (white matter shearing)	DAI	sTBI
1404264	Cerebellum hematoma/hemorrhage intracerebellar NFS	ICH	sTBI
1404304	Cerebellum hematoma/hemorrhage intracerebellar small	ICH	sTBI
1404345	Cerebellum hematoma/hemorrhage intracerebellar large	ICH	sTBI
1406285	Cerebrum diffuse axonal injury (white matter shearing)	DAI	sTBI
1406384	Cerebrum hematoma/hemorrhage intracerebral NFS	ICH	sTBI
1406404	Cerebrum hematoma/hemorrhage intracerebral small	ICH	sTBI
1406424	Cerebrum hematoma/hemorrhage intracerebral small petechial hemorrhage(s)	ICH	sTBI
1406444	Cerebrum hematoma/hemorrhage intracerebral small subcortical hemorrhage	ICH	sTBI
1406465	Cerebrum hematoma/hemorrhage intracerebral bilateral	ICH	sTBI
1406485	Cerebrum hematoma/hemorrhage intracerebral large	ICH	sTBI
1406784	Cerebrum intraventricular hemorrhage/intracerebral hematoma in ventricular system	ICH	sTBI
1602022	LOU <1 hr.	Concussion	mTBI
1602043	LOU known to be <1 hr. with neurological deficit	Concussion	mTBI
1602063	LOU known to be 1-6 hrs.	Concussion	mTBI
1602084	LOU known to be 1-6 hrs. with neurological deficit	DAI	
1602104	LOU known to be 6-24 hrs.	DAI	sTBI
1602125	LOU known to be 6-24 hrs. with neurological deficit	DAI	sTBI
1602145	LOU known to be > 24 hrs.	DAI	sTBI
1604042	APR on Admis. or Initial Observ. at Scene (GCS15) no prior unconsciousness with neurological deficit	Concussion	mTBI
1604062	APR on Admis. or Initial Observ. at Scene (GCS15) prior unconsciousness, but length of time NFS	Concussion	mTBI
1604083	APR on Admis. or Initial Observ. at Scene (GCS15) prior unconsciousness with neurological deficit	Concussion	mTBI
1604102	APR on Admis. or Initial Observ. at Scene (GCS15) amnesia	Concussion	mTBI
1604123	APR on Admis. or Initial Observ. at Scene (GCS15) amnesia with neurological deficit	Concussion	mTBI
1604142	APR on Admis. or Initial Observ. at Scene (GCS15) unconsciousness known to be <1 hr.	Concussion	mTBI
1604163	APR on Admis. or Initial Observ. at Scene (GCS15) unconsciousness known to be <1 hr. with neurological deficit	Concussion	mTBI
1606022	LSO post resuscitation on Admis. or Initial Observ. at Scene (GCS9-14) no prior unconsciousness	Concussion	mTBI
1606043	LSO post resuscitation on Admis. or Initial Observ. at Scene (GCS9-14) no prior unconsciousness with neurological deficit	Concussion	mTBI
1606062	LSO post resuscitation on Admission or Initial Observ. at Scene (GCS9-14) prior unconsciousness, but length of time NFS	Concussion	mTBI
1606083	LSO post resuscitation on Admis. or Initial Observ. at Scene (GCS9-14) prior unconsciousness, but length of time NFS with neurological deficit	Concussion	mTBI

1606102	LSO post resuscitation on Admis. or Initial Observ. at Scene (GCS9-14) unconsciousness known to be <1 hr.	Concussion	mTBI
1606123	LSO post resuscitation on Admis. or Initial Observ. at Scene (GCS9-14) unconsciousness known to be <1hr. with neurological deficit	Concussion	mTBI
1606143	LSO post resuscitation on Admis. or Initial Observ. at Scene (GCS9-14) 1-6 hrs. unconsciousness	Concussion	mTBI
1606164	LSO post resuscitation on Admis. or Initial Observ. at Scene (GCS9-14) 1-6 hrs. unconsciousness with neurological deficit	DAI	sTBI
1606992	LSO post resuscitation on Admission or Initial Observ. at Scene (GCS9-14) NFS	Concussion	mTBI
1608023	UPR on Admis. or Initial Observ. at Scene (GCS<9) LOU NFS	Concussion	mTBI
1608044	UPR on Admis. or Initial Observ. at Scene (GCS<9) LOU NFS with neurological deficit	DAI	sTBI
1608063	UPR on Admis. or Initial Observ. at Scene (GCS<9) <1 hr.	Concussion	mTBI
1608084	UPR on Admis. or Initial Observ. at Scene (GCS<9) <1 hr. with neurological deficit	DAI	sTBI
1608103	UPR on Admis. or Initial Observ. at Scene (GCS< 9) 1-6 hrs.	Concussion	mTBI
1608124	UPR on Admis. or Initial Observ. at Scene (GCS<9) 1-6 hrs. with neurological deficit	DAI	sTBI
1608144	UPR on Admis. or Initial Observ. at Scene (GCS<9) 6-24 hrs.	DAI	sTBI
1608165	UPR on Admis. or Initial Observ. at Scene (GCS<9) 6-24 hrs. with neurological deficit	DAI	sTBI
1608185	UPR on Admis. or Initial Observ. at Scene (GCS<9) >24 hrs.	DAI	sTBI
1608204	UPR on Admis. or Initial Observ. at Scene (GCS<9) appropriate movements with painful stimuli no matter length of time	DAI	sTBI
1608225	UPR on Admis. or Initial Observ. at Scene (GCS<9) appropriate movements with painful stimuli no matter LOU with neurological deficit	DAI	sTBI
1608245	UPR on Admis. or Initial Observ. at Scene (GCS<9) inappropriate movements no matter LOU	DAI	sTBI
1608993	UPR on Admis. or Initial Observ. at Scene (GCS<9) NFS	Concussion	mTBI
1610002	Cerebral Concussion	Concussion	mTBI

*LOU = Length Of Unconsciousness, APR = Awake Post Resuscitation, Admis. = Admission, GCS = Glasgow Coma Scale, LSO = Lethargic, Stuporous, Obtunded, UPR = Unconscious Post Resuscitation, NFS = No Further Specified
** Adapted from (Antona-Makoshi et al., 2018).

Figure A22. Crush profiles for small overlap (a), moderate overlap (b), and full engagement (c) frontal crashes.

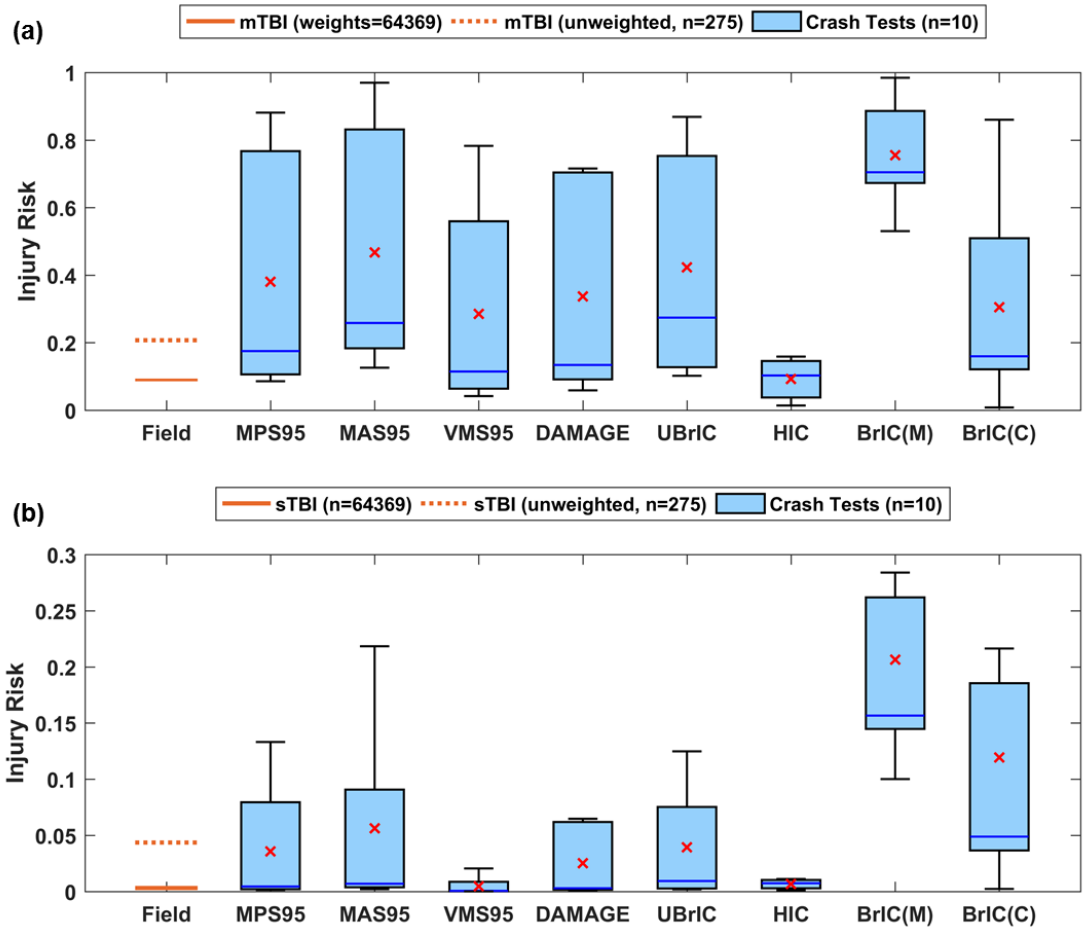

Figure A23. Injury risk for mTBI (a) and sTBI (b) sustained by the driver in low-speed side crashes in NASS and corresponding crash tests.

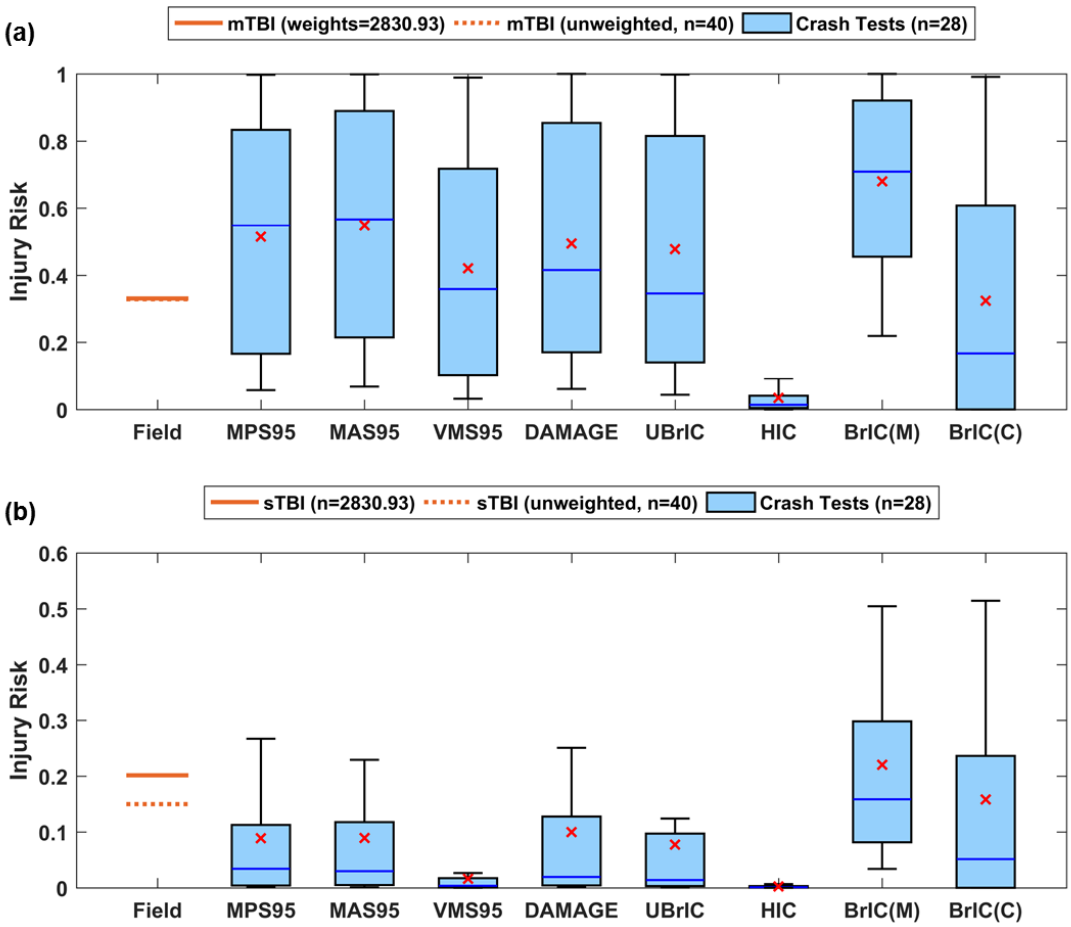

Figure A24. Injury risk for mTBI (a) and sTBI (b) sustained by the driver in high-speed side crashes in NASS and corresponding crash tests.

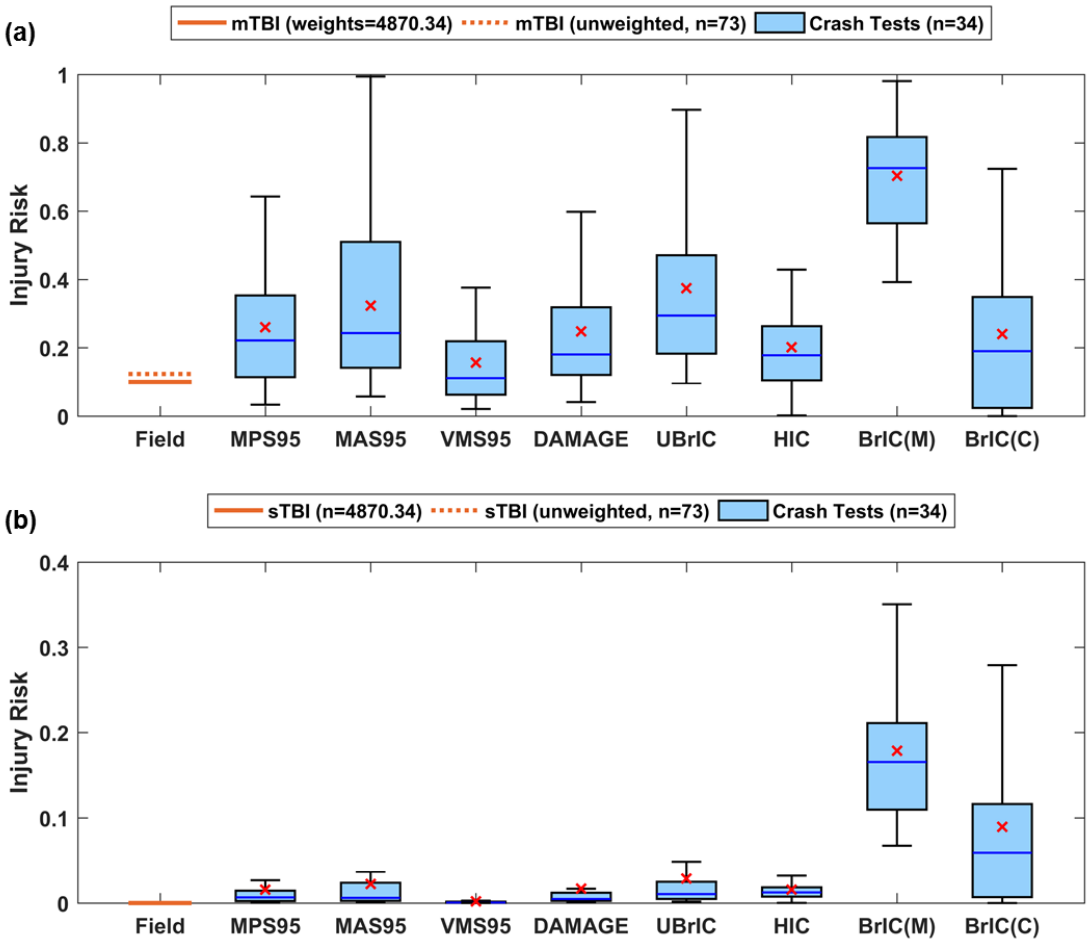

Figure A25. Injury risk for mTBI (a) and sTBI (b) sustained by the passenger in high-speed side crashes in NASS and corresponding crash tests.

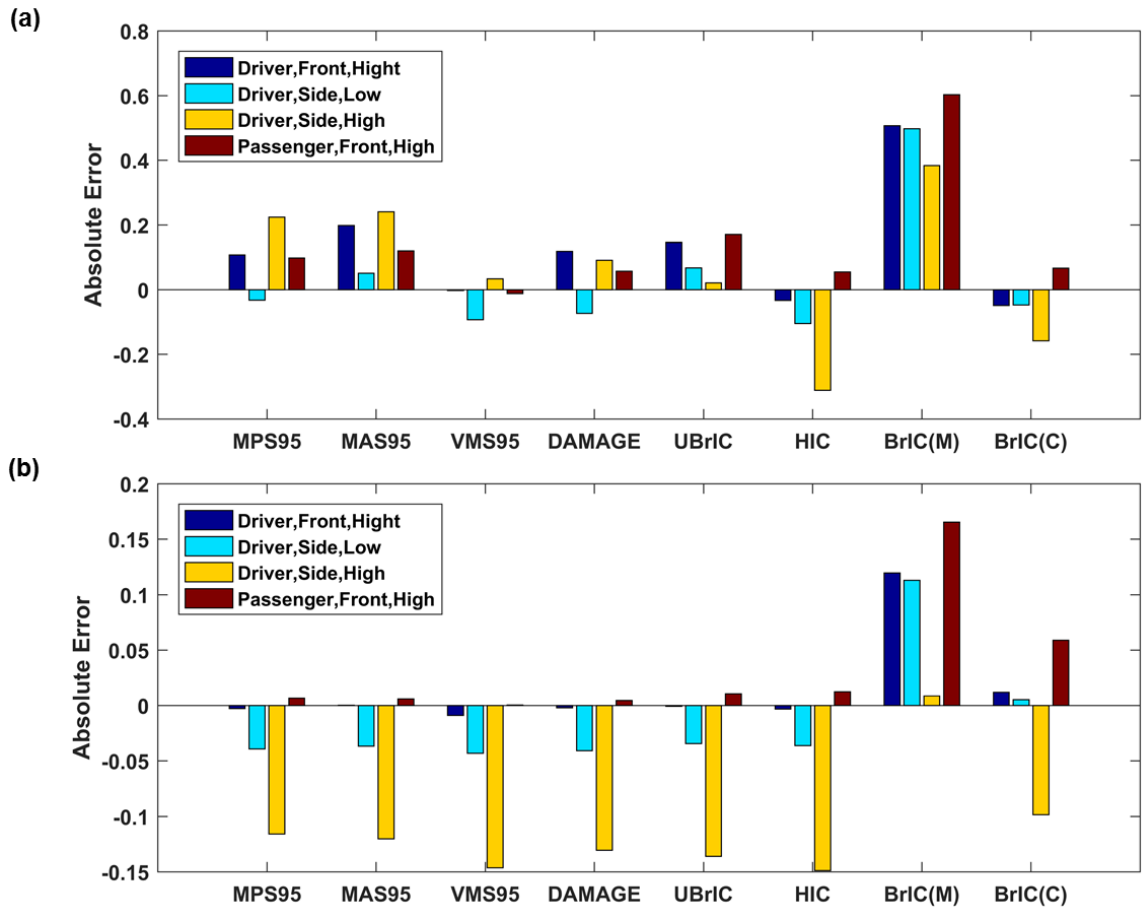

Figure A26. The absolute error between predicted Injury risk and <u>unweighted</u> field injury rates for mTBI (a) and sTBI (b). Positive values indicate overpredicting injury.

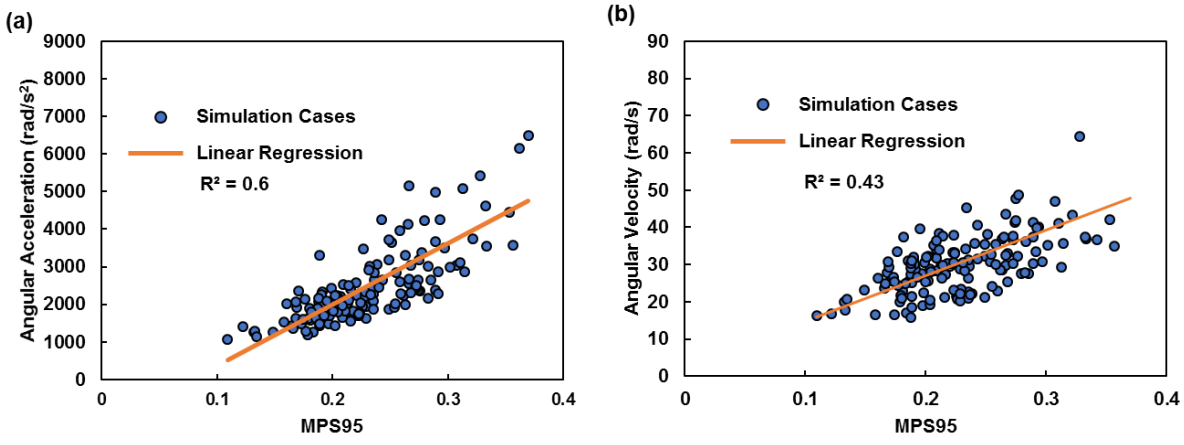

Figure A27. Correlation between MPS95 and peak resultant angular accelerations (a) and angular velocities (b) in the crash tests.

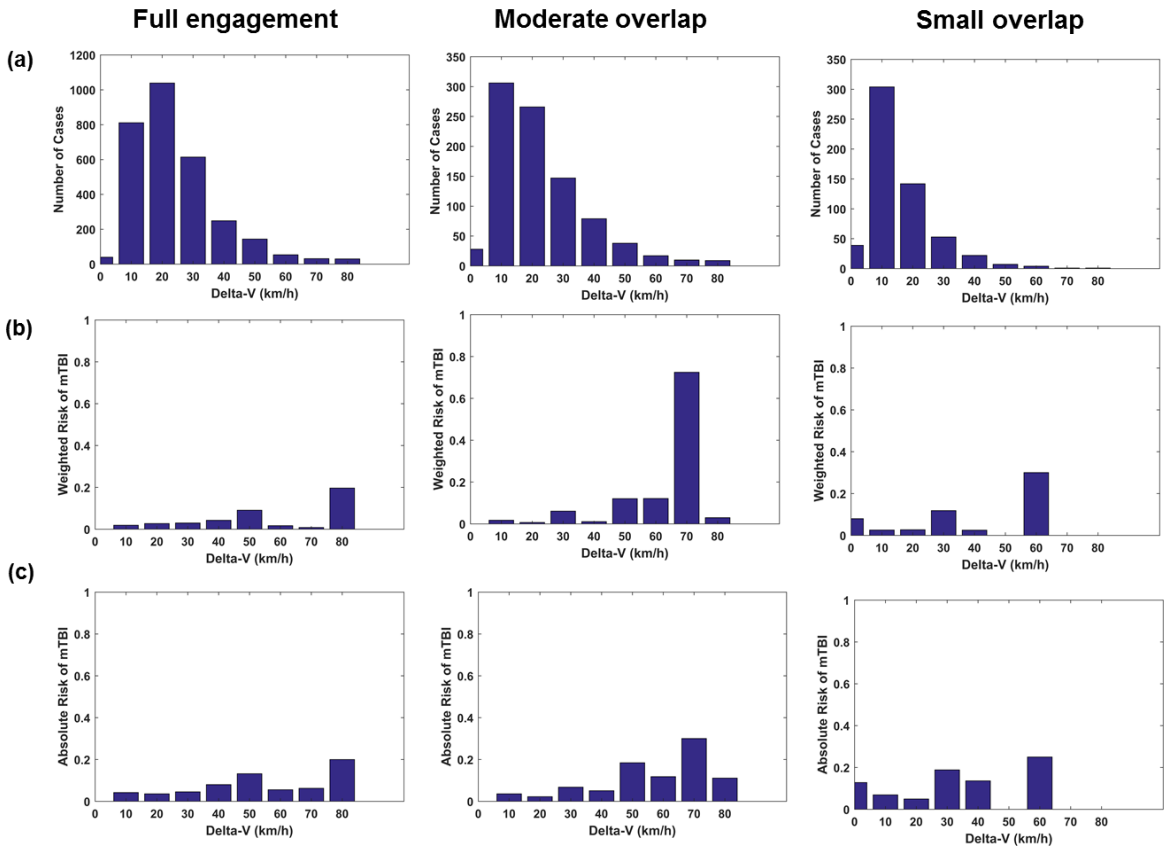

Figure A28. Distribution of Delta-V (a), weighted mTBI risks (b), and unweighted mTBI risks (b) in different frontal impact modes.

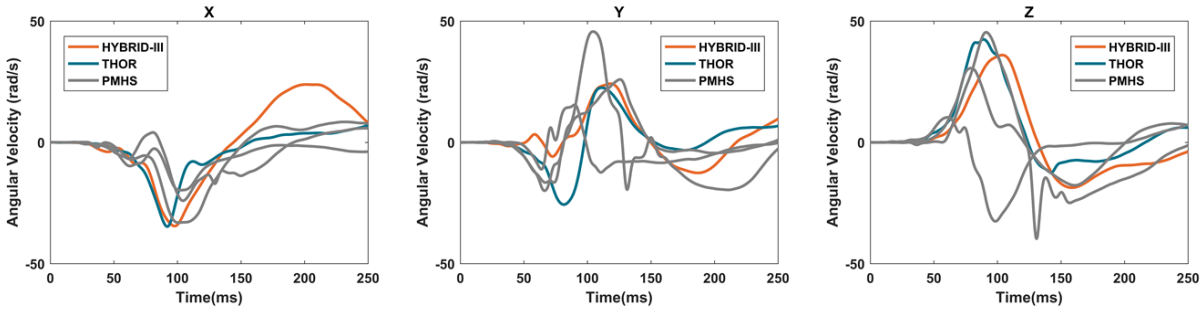

Figure A29. Head angular velocities of the ATDs and PMHS in far side oblique condition.